VELOCITY VARIATIONS IN CROSS-HOLE SONIC LOGGING SURVEYS

Causes and Impacts in Drilled Shafts

U.S. Department of Transportation

Federal Highway Administration

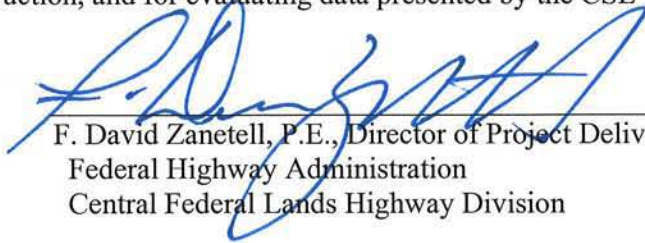**Federal Lands Highway**

Commitment to Excellence

Central Federal Lands Highway Division
12300 West Dakota Avenue
Lakewood, CO 80228

FOREWORD

The Federal Lands Highway (FLH) of the Federal Highway Administration (FHWA) promotes development and deployment of applied research and technology applicable to solving transportation related issues on Federal Lands. The FLH provides technology delivery, innovative solutions, recommended best practices, and related information and knowledge sharing to Federal agencies, Tribal governments, and other offices within the FHWA.

This study evaluated the effectiveness of cross-hole sonic logging (CSL) for non-destructive evaluation of concrete drilled-shaft bridge foundations using numerical analysis. Effects of tube material, tube bending, concrete curing, hydration, heat transfer, residual stress, surrounding ground conditions, cracking, internal rebar support, and external loading on the seismic velocity CSL measurements are shown. This project provides designers, inspectors, and contractors with a basis for understanding basic principles of the chemistry, physics, and mechanics involved in the process of drilled shaft construction, and for evaluating data presented by the CSL technique.

F. David Zanetell, P.E., Director of Project Delivery
Federal Highway Administration
Central Federal Lands Highway Division

Technical Report Documentation Page

1. Report No. FHWA-CFL/TD-08-009	2. Government Accession No.	3. Recipient's Catalog No.	
4. Title and Subtitle *Velocity Variations in Cross-Hole Sonic Logging Surveys* *Causes and Impacts in Drilled Shafts*		5. Report Date September 2008	
		6. Performing Organization Code	
7. Author(s) Alan D. Rock, Runing Zhang, Ph.D., P.E., David Wilkinson, Ph.D.		8. Performing Organization Report No.	
9. Performing Organization Name and Address Summit Peak Technologies, LLC 6121 N. Powell Road Parker, CO 80134		10. Work Unit No. (TRAIS)	
		11. Contract or Grant No. DTFH68-05-P-00056, DTFH68-05-P-00089, and DTFH68-06-P-00105	
12. Sponsoring Agency Name and Address Federal Highway Administration Central Federal Lands Highway Division 12300 W. Dakota Avenue, Suite 210 Lakewood, CO 80228		13. Type of Report and Period Covered Final Report March 2005 – March 2007	
		14. Sponsoring Agency Code HFTS-16.4	

15. Supplementary Notes
COTR: Khamis Haramy, FHWA-CFLHD. Advisory Panel Members: Michael Peabody and Roger Surdahl, FHWA-CFLHD; Matt Greer, FHWA-CO Division. and Frank Jalinoos, FHWA-TFHRC. This project was funded under the FHWA Federal Lands Highway Technology Deployment Initiatives and Partnership Program (TDIPP).

16. Abstract

Drilled shafts are popular deep foundation supports, as they can be constructed in a wider range of ground conditions with less noise and vibration than driven piles. Quality assurance and quality control of drilled shafts has become a concern due to difficulties in locating defects and determining load bearing capacity. Various non-destructive evaluation (NDE) techniques have been developed to estimate the integrity of the concrete. While NDE techniques provide a powerful tool and have been widely accepted, many variables and unknowns can affect the measurement results. Results are more difficult to interpret, leading to unnecessary litigation over shaft integrity. In addition, influences of surrounding ground, stress states under different load conditions, and crack development during concrete curing further complicate determination of shaft performance.

This study identifies various conditions that affect the load bearing capacity of drilled shafts by modeling various conditions and analyzing them with numerical methods. The analysis first identifies design criteria and construction procedures, and reviews NDE techniques. This analysis uses results based on principles and theorems from engineering mechanics, geotechnical engineering, concrete chemistry, and geophysical engineering, which are analyzed numerically by the Geostructural Analysis Package (GAP.) GAP combines numerical methods of Discrete Element Method, Particle Flow Method, Material Point Method, and Finite Differencing, together with engineering mechanics constitutive models, concrete chemistry models, thermodynamics models, and geophysical tomography and holography for geotechnical engineering application. GAP has also been used successfully for ground characterization in highway engineering and mining operations.

This study explores many concerns recently raised for drilled shaft design, construction and maintenance. Conclusions and recommendations offer engineers more information for a better understanding of drilled shaft foundations to revolutionize foundation design, concrete mix design, construction techniques, NDE measurement, and defect evaluation, to improve performance and efficiency.

17. Key Words **CROSS-HOLE SONIC LOGGING (CSL), DRILLED SHAFTS, DEEP FOUNDATION, GEOPHYSICAL SURVEY, TOMOGRAPHY, VELOCITY, ANOMALIES**		18. Distribution Statement No restriction. This document is available to the public from the sponsoring agency at the website http://www.cflhd.gov.	
19. Security Classif. (of this report) Unclassified	20. Security Classif. (of this page) Unclassified	21. No. of Pages 180	22. Price

Form DOT F 1700.7 (8-72)   **Reproduction of completed page authorized**

SI* (MODERN METRIC) CONVERSION FACTORS

APPROXIMATE CONVERSIONS TO SI UNITS

Symbol	When You Know	Multiply By	To Find	Symbol
		LENGTH		
in	inches	25.4	Millimeters	mm
ft	feet	0.305	Meters	m
yd	yards	0.914	Meters	m
mi	miles	1.61	Kilometers	Km
		AREA		
in^2	square inches	645.2	Square millimeters	mm^2
ft^2	square feet	0.093	Square meters	m^2
yd^2	square yard	0.836	Square meters	m^2
ac	acres	0.405	Hectares	ha
mi^2	square miles	2.59	Square kilometers	km^2
		VOLUME		
fl oz	fluid ounces	29.57	Milliliters	mL
gal	gallons	3.785	Liters	L
ft^3	cubic feet	0.028	cubic meters	m^3
yd^3	cubic yards	0.765	cubic meters	m^3
	NOTE: volumes greater than 1000 L shall be shown in m^3			
		MASS		
oz	ounces	28.35	Grams	g
lb	pounds	0.454	Kilograms	kg
T	short tons (2000 lb)	0.907	megagrams (or "metric ton")	Mg (or "t")
		TEMPERATURE (exact degrees)		
°F	Fahrenheit	5 (F-32)/9 or (F-32)/1.8	Celsius	°C
		ILLUMINATION		
fc	foot-candles	10.76	Lux	lx
fl	foot-Lamberts	3.426	candela/m^2	cd/m^2
		FORCE and PRESSURE or STRESS		
lbf	poundforce	4.45	Newtons	N
lbf/in^2	poundforce per square inch	6.89	Kilopascals	kPa

APPROXIMATE CONVERSIONS FROM SI UNITS

Symbol	When You Know	Multiply By	To Find	Symbol
		LENGTH		
mm	millimeters	0.039	Inches	in
m	meters	3.28	Feet	ft
m	meters	1.09	Yards	yd
km	kilometers	0.621	Miles	mi
		AREA		
mm^2	square millimeters	0.0016	square inches	in^2
m^2	square meters	10.764	square feet	ft^2
m^2	square meters	1.195	square yards	yd^2
ha	hectares	2.47	Acres	ac
km^2	square kilometers	0.386	square miles	mi^2
		VOLUME		
mL	milliliters	0.034	fluid ounces	fl oz
L	liters	0.264	Gallons	Gal
m^3	cubic meters	35.314	cubic feet	ft^3
m^3	cubic meters	1.307	cubic yards	yd^3
		MASS		
g	grams	0.035	Ounces	oz
kg	kilograms	2.202	Pounds	lb
Mg (or "t")	megagrams (or "metric ton")	1.103	short tons (2000 lb)	T
		TEMPERATURE (exact degrees)		
°C	Celsius	1.8C+32	Fahrenheit	°F
		ILLUMINATION		
lx	lux	0.0929	foot-candles	fc
cd/m^2	candela/m^2	0.2919	foot-Lamberts	fl
		FORCE and PRESSURE or STRESS		
N	newtons	0.225	Poundforce	lbf
kPa	kilopascals	0.145	poundforce per square inch	lbf/in^2

*SI is the symbol for the International System of Units. Appropriate rounding should be made to comply with Section 4 of ASTM E380.
(Revised March 2003)

ABBREVIATIONS AND ACRONYMS

Acronym	Definition
ASTM	American Society for Testing and Materials
CSL	Cross-hole Sonic Logging
DEM	Distinct Element Method
DOT	Department of Transportation
FHWA	Federal Highway Administration
GAP	Geostructural Analysis Package
MPM	Material Point Method
NDE	Non Destructive Evaluation
PFC	Particle Flow Code
UPV	Ultrasonic Pulse Velocity

TABLE OF CONTENTS

LIST OF FIGURES

LIST OF TABLES

CHAPTER 1. INTRODUCTION

1.1   Purpose

This study focuses on the evaluation of the structural integrity of drilled shafts using the cross-hole sonic logging method. The objectives are to analyze the effectiveness of cross-hole sonic logging (CSL) surveys to characterize the integrity and bearing capacity of deep-drilled shaft foundations. Numerical analysis will be employed to isolate, control, and measure the effects of various phenomena.

This study simulates CSL surveys under various conditions commonly encountered in the field. The effects of the following factors on velocity propagation are examined:
1.   Access tube-- including tube bending, sensor drift and orientation within the tubes, steel vs. PVC tubes, thermal expansion during concrete hydration, and tube debonding.
2.   Rebar--including CSL signal reflection and dispersion, rebar thermal expansion, and rebar debonding.
3.   Concrete hydration in typical ground conditions and at different curing times, using chemical hydration rates, heat transfer, and thermal stress.
4.   Common defects will be introduced into the models, such as honeycombing, soil intrusion, and thermal cracking. Simulated CSL surveys will be evaluated for effectiveness to detect and classify these defects using simulated waveform analysis.

Next, numerical stress analysis will be performed on defects within the drilled shaft to estimate effects on bearing capacity and structural integrity.

A well-established, comprehensive numerical model based on the Particle Flow Code (PFC) method is used in this study. PFC is a Discrete Element Method (DEM) that uses combinations of small spherical elements bounded by springs of various stiffness to model the larger, more complex elements commonly used in DEM. This modeling method was selected because it supports solids, with effects of friction, interlocking, collisions, and cracking, as well as fluids and solid/fluid interaction. This method also has the capability to model dynamic crack propagation, seismic waves, and static loading in concrete, soil, and other geotechnical materials. The PFC method was also expanded to model a wider range of phenomena, such as concrete curing, heat transfer, thermal cracking, honeycombing, surrounding ground conditions, ground water effects, and corrosion.

The results of this study offer a method to process full-waveform seismic data collected from existing survey techniques and obtain a more accurate and comprehensive estimate of long term drilled shaft performance and structural integrity.

1.2   Cross-hole Sonic Logging (CSL) Surveys of Drilled Shafts

The most commonly used drilled shaft foundation down-hole integrity test is cross-hole sonic logging (CSL), also known as ultrasonic testing (ASTM D 6760-02). The cross-hole sonic logging technique is an indirect, low strain, non-destructive imaging method for detecting defects inside the rebar cage of a drilled shaft or diaphragm wall element. CSL has become a standard

test for most transportation agencies, and is currently performed on most drilled shaft in the United States and other developed countries. Prior to the acceptance of CSL, quality assurance testing in the United States was performed only on a very limited number of drilled shafts primarily using the sonic echo and impulse response test. Gamma-gamma density logging tests are gaining popularity as combination backup tests to CSL for defect identification. Several variations of the CSL equipment and techniques exist, including a source (pulse transmitter) and a receiver simultaneously lowered in the same tube (single hole ultrasonic test, dubbed "SHUT"), a source and a receiver lowered in adjacent tubes, and a source and multiple receivers lowered in separate tubes. The single source and receiver in adjacent tubes is the most commonly used today. CSL has gained credibility based on tests that were successfully conducted in the United States on hundreds of shafts with depths up to 120 m (tested in China).

1.3   CSL Basic Theory

The CSL method is a "derivative" of the ultrasonic pulse velocity test. The basic principle of the CSL test is that ultrasonic pulse velocity through concrete varies proportionally with the material density and elastic constants. A known relationship between fractured or weak zones and measured pulse velocity and signal attenuation is fundamental for these tests. Research has shown that weak zones reduce velocities and increase attenuations. During CSL measurements, the apparent signal travel time between transmitter and receiver are measured and recorded. By measuring the travel times of a pulse along a known distance (between transmitter and receiver), the approximate velocity can be calculated as a function of distance over time. If a number of such measurements are made and compared at different points along the concrete structure, the overall integrity of the concrete can be assessed.

The first-arrival travel times (FAT) recorded during CSL testing are known as compressional, primary, longitudinal, or P-wave arrivals. The P-wave has discrete particle motion in the same direction as the wave is moving. The surface of the constant phase, or the surface on which particles are moving together at a given moment in time, is called the wavefront. An imaginary line perpendicular to the wavefront is called a ray path. It is often assumed that a beam of produced ultrasonic energy travels along the ray path (Robert E. Sheriff and Lloyd P. Geldart, 1995). Basic elements of the emitted wave during CSL testing are presented in Figure 1.1.

The following are definitions of terminology used with CSL analyses (Robert E. Sheriff, 1978):
- wavelength (λ) - distance between successive repetitions of a wavefront,
- amplitude (A) - maximum displacement from equilibrium,
- period (T) - time between successive repetitions of a wavefront,
- frequency (f) - number of waves per unit time,
- velocity (V) - speed at which a seismic wave travels, proportional to the frequency and wavelength ($V=f\lambda$),
- apparent wavelength - distance between successive similar points on a wave measured at an angle to the wavefront, and
- apparent velocity - product of frequency and apparent wavelength.
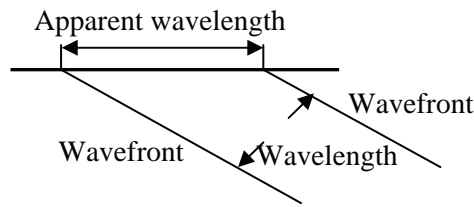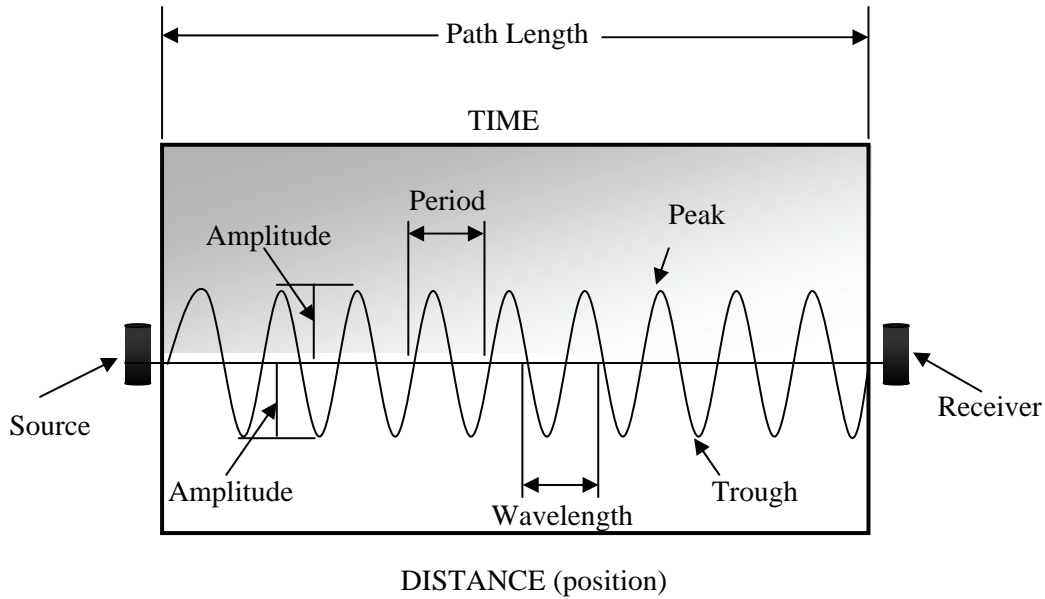
Figure 1.1. Plot. Basic Wave Elements

Velocity of the P-wave in homogenous "isotropic" media is related to the modulus and density of the medium through which the wave travels, and is given as:

$$Vp = \sqrt{\frac{(4/3\mu + k)}{\rho}} \quad \text{where} \tag{1.3}$$

Vp - *velocity of the P-wave*
μ - shear modulus of the medium through which the wave travels,
k - bulk modulus of the medium through which the wave travels,
ρ - density of the medium through which the wave travels.

$$k = \frac{E}{3(1-2\nu)} \tag{1.4}$$

$$\mu = \frac{E}{2(1+\nu)}, \tag{1.5}$$

where
ν is Poisson's ratio of the medium.

The P-wave velocity can then be written as:

$$Vp = \sqrt{\frac{E(1-\nu)}{(1+\nu)(1-2\nu)}} \ , \qquad\qquad (1.6)$$

where
E - dynamic elastic modulus or Young's modulus
During CSL analysis, the first arrival times of the P-wave are picked using an automated picker within the CSL software, and the pulse velocity can be calculated as:

$$PulseVelocity = \frac{PathLength}{TransitTime} \qquad\qquad (1.7)$$

For accurate results, it is recommended that the path lengths and transit times be measured with a precision greater than 1%. Although pulse velocity varies with different concrete mixes, the average pulse velocity of a typical concrete is approximately 4,000 m/s. Knowing the linear distance between the transmitter and receiver (path length), and the pulse transit time (first arrival time of the P-wave), the pulse velocity can then be calculated. If the CSL access tubes are not installed in a near vertical position and the distance between them varies significantly along the length of the shaft, errors in velocity calculations may occur, and the results may be misleading.

The seismic wavelength can be calculated based on the known frequency of the transmitted signal and the calculated pulse velocity as shown in Table 1.1. Table 1.1 suggests that the higher the transmitted frequencies used during CSL testing, the shorter the wavelength, allowing for the detection of smaller defects. However, the tradeoff is that the higher the source signal frequency,

Table 1.1   Numerical Relationship between Path Length (PL), Transit Time (TT), Frequency (f), Period (T=1/f), Velocity (V=PL/TT), and Wavelength (λ=V/f)

PL, (m)	TT x10^{-4}, (s)	1/f, (kHz)	1/f x10^{-5}, (s)	V=(PL/TT), (m/s)	λ = (V/f), (m)
0.6	1.6	35	2.8	3,750	0.1
0.6	1.6	50	2.0	3,750	0.075
0.6	2.4	35	2.8	2,500	0.071
0.6	2.4	50	2.0	2,500	0.05

the greater the signal absorption[1] and the shorter the wavelength. This implies that if higher frequencies are used during the CSL testing, more accurate detection of small defects is permitted, but signal absorption will also be high, limiting the penetration range of the method. Although most CSL systems operate at 35 kHz, frequencies in the range between 30 kHz and 90 kHz are used for CSL tests. At frequencies of about 90 kHz, the wavelength is at about the size

---

[1] Absorption is the process responsible for the gradual and sometimes complete disappearance of wave motion. The elastic energy associated with wave motion passes through the medium, becoming slowly absorbed and transformed into heat (Robert E. Sheriff and Lloyd P. Geldart, 1995).

of the aggregate. At this scale, the concrete can no longer be considered a homogeneous material. Therefore very high frequencies are not recommended.

The energy of an ultrasonic wave is a measure of the motion of the medium as the wave passes through it. Energy per unit volume is called energy density (Robert E. Sheriff and Lloyd P. Geldart, 1995). A wave passing through a medium possesses both kinetic and potential energy. Because the medium oscillates as the wave passes through it, energy is converted back and forth from kinetic to potential forms, but the total energy remains fixed. When the particle has zero displacement, the kinetic energy is at a maximum and its potential energy is zero. Conversely, when maximum displacement of the particle occurs, the kinetic energy is zero, and the total energy is all potential energy. When the total energy equals the maximum value of the kinetic energy, the energy density for a harmonic wave is proportional to the first power of the density of the medium, and to the second power of the frequency and amplitude as shown in the following equation:

$$E = 2\pi^2 \rho f^2 A^2 \tag{1.8}$$

where

$\quad E$ = total energy

$\quad \rho$ = density

$\quad f$ = transmitted frequency

$\quad A$ = wave amplitude

1.4 CSL Test Procedures and Results

CSL testing can be performed on either drilled shaft foundations or pre-cast concrete piles, provided that 50-mm-diameter steel or PVC access tubes capable of holding water are installed (50-mm-diameter holes can be cored, if necessary). These tubes must extend at least 1 m above the top of the shaft to compensate for water displaced by insertion and removal of the transmitter, receiver, and cable. To reduce the chances of tube debonding, steel access tubes are preferred (steel tubes are not suitable if SHUT is to be applied). If schedule 40 PVC tubes are used, the tests must be performed within 10 days after concrete placement to avoid debonding at the PVC/concrete interface. Other factors may also cause debonding:

1) Disturbance of tubes during or shortly after concrete placement.
2) Improperly tying the tubes firmly to the cage.
3) Delays in filling the tubes with water.

To perform CSL testing, two probes, a piezoelectric transmitter, and a receiver are lowered to the bottom of two access tubes. These probes are simultaneously pulled vertically at a constant interval while pulses are created and recorded. During testing, the transmitter and receiver are maintained at the same elevation to create a horizontal signal travel path between the transmitter and the receiver. The cables to the probes pass through a meter-wheel that is connected to the data acquisition control unit. The meter-wheel controls the ultrasonic wave pulse by triggering the pulse generator at predetermined vertical intervals, causing the transmitter probe to emit an ultrasonic pulse. The timer circuit measures the time between pulse emission and subsequent detection by the receiver. Since the number of pulses emitted is a function of meter-wheel rotation and the wheel circumference is known, the depth of the probes can be calculated. All records are automatically stored on the system hardware.

In general, the range of frequencies used for concrete testing is between 20 kHz and 250 kHz, with 35 kHz being most commonly used for field-testing of drilled shafts. Since concrete is a heterogeneous material, high-frequency pulses (short wavelengths of energy) are unsuitable for use because of the considerable amount of energy attenuation. The corresponding wavelength is approximately 200 mm for lower frequencies (20 kHz) and approximately 16 mm for the higher frequencies (250 kHz).

The waveform of the raw data is digitized and continuously displayed with the positive peak of the received pulse presented and the negative peak displayed as blank space. In some CSL systems, the full waveform traces are stacked and displayed in a format representing vertical profiles of the pulse propagation time through the concrete (dubbed "waterfall" profiles) as shown in Figure 1.2(a). Other logs depict the arrival times, apparent velocity, and energy amplitude versus depth, as shown in Figure 1.2(b).
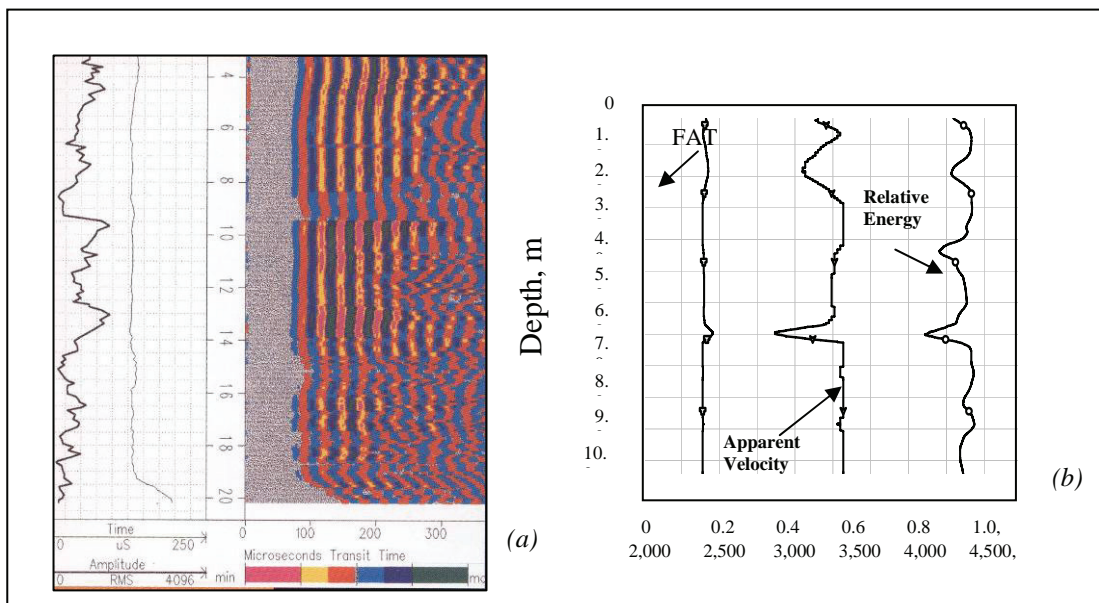
Figure 1.2. Plot. (a) Full Waveform Stacked Traces (InfraSeis, Inc.) and (b) CSL Log Plot – First Arrival Time (FAT), Apparent Velocity and Relative Energy Versus Depth (GRL & Assoc., Inc.)

CSL results can be evaluated on-site immediately following testing. Concrete integrity can be preliminary assessed based on first arrivals and signal amplitude. Good quality concrete is indicated by constant travel time per unit distance and good signal amplitude. Where the pulse velocity is reduced by defects or low modulus material, the propagation time will be longer, and the amplitude will decrease. Several irregularities can be identified at different locations within the same-drilled shaft as shown in Figure 1.3. In some cases, defects can significantly reduce pulse amplitude, causing the signal to be lost completely. Poor bonding between access tubes and the concrete, or de-lamination, can also cause complete signal loss. Steel tubes provide improved bonding with concrete, but the high mechanical impedance of steel may cause attenuation of the signal transmission and the signal may not be as well defined when PVC tubes are used. Since the tubes must be oversized to permit free passage of the probes and to allow for minor bending of the tubes during placement, the probes are somewhat free to move laterally.

6
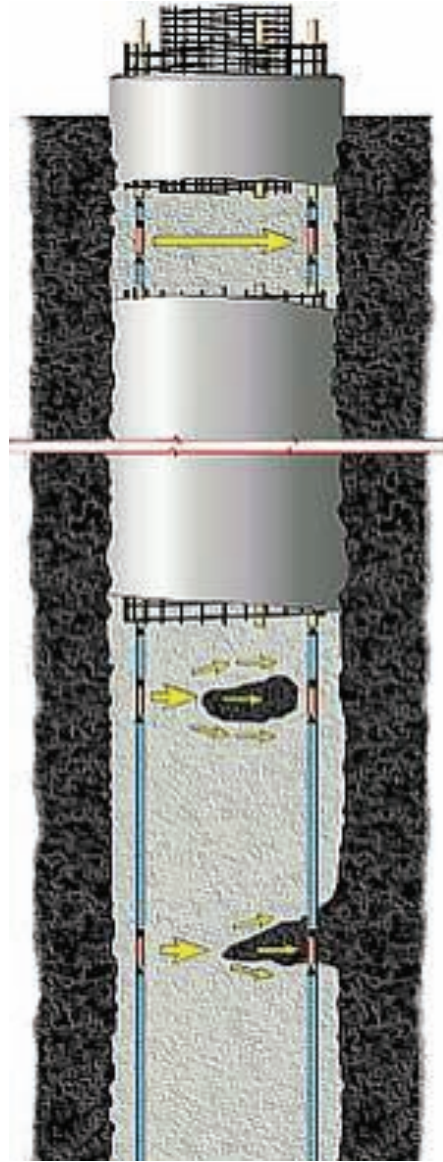
Figure 1.3. Plot. Drilled Shaft with Defects

Consequently, this may cause variation in transmitted pulse strength and received signal amplitude.

The received amplitude of an ultrasonic pulse can also vary depending on aggregate shape, orientation, and local changes in aggregate distribution. Concrete defects such as gravel zones, soil inclusions, bentonite inclusions, or honeycombing have a much lower propagation velocity, and their presence can usually be detected.

Current CSL tests only indicate that an anomaly may exist somewhere between two access tubes. It is, however, difficult to determine the geometry and exact location of the anomaly with the respect to tube location. To better characterize defects in terms of size, geometry, and location, additional CSL tests are performed. Data are collected with several offsets between transmitter

and receiver in adjacent boreholes and used for detailed analysis and cross-hole tomography. A 2-D color tomogram is then plotted to better identify anomaly geometry and location.

1.5 CSL Data Processing and 3-D Tomography

The basic principles of tomography are borrowed from the medical field where imaging of a body is done by multidirectional CAT-scans. Tomography for medical purposes is used to display the loss in intensity of x-rays due to absorptive properties of different body parts. Because x-ray imaging depends entirely on variations in absorption with no refraction or diffraction, medical and seismic tomography are not perfectly analogous. In CAT-scanning, the x-rays travel mostly in straight lines in many directions, whereas in seismic tomography, the ray paths can bend appreciably depending on the velocity contrast within the medium.

The main concept of 3-D seismic tomographic imaging is the creation of color-coded images that provide a clear and detailed representation of property variations within a medium from seismic rays projected through the medium. Travel time tomography involves imaging the seismic properties from the observation of the transmitted compressional first arrival energy (Dines and Lytle, 1979). The relationship between the travel time t_i and the velocity field $v_{(x,y)}$ is given by the line integral for a ray "i":

$$t_i = \int_{R_i} \frac{ds}{v_{(x,y)}}$$ (2.1)

where
ds is the path length,
R_i denotes the curve connecting a source receiver pair that yields the least possible travel time according to Fermat's principle.

Tomography is an attempt to match calculated travel times from model responses to the observed data by inversion of these line integrals. Initially, the region of interest is divided into grids of uniform cells "j" of constant velocity cells and a discrete approximation of the line integral is assumed as:

$$t_i = \sum_j \Delta S_{ij}.n_j$$ (2.2)

where
ΔS_{ij} is the distance traveled by ray "i" in cell "j"
n_j is the slowness (inverse of velocity) within cell "j".
Using a first order Taylor expansion and neglecting residual error, from equations (2.1) and (2.2), the following equation can be written in matrix form as:

$$\overline{y} = A\overline{x}$$ (2.3)

where
$\overline{y}$ is the difference between computed travel times obtained from the model and the observed travel times obtained from the field
$\overline{x}$ is the difference between the true and the modeled slowness
A is the Jacobian matrix.

In travel time tomography, Equation 2.3 is usually solved by two methods: 1)- the matrix inversion approach (e.g. conjugate gradient (CG) matrix inversion technique) (Nolet, 1987; Scales, 1987); and 2)- the "back-projection" inversion technique, adapted from medical tomography (e.g. simultaneous iterative reconstruction technique (SIRT)) (Herman, 1980; Ivanson, 1986).

In both techniques, the acoustic wave-field is initially propagated through a presumed theoretical model, and a set of travel times are obtained by ray tracing through the cells (forward modeling step). The travel time equations are then inverted iteratively to solve for the changes in slowness that produces a best-fit solution with the lowest root mean square (RMS) error between the observed and computed travel times (inversion step). The model is then modified, new ray paths traced, and the process repeated until the slowness distribution matches observations within acceptable tolerances. In practice, an adequate tomographic solution can be obtained if enough ray paths penetrate the medium in multiple directions. To reach this, the recording procedure uses large number of source/receiver locations. Color-coded tomograms of the velocity distribution within the medium are then generated from inversion results as the final step in the tomography data processing. Tomogram interpretation is the next step for defining areas of defects by evaluating velocity changes through the medium (Robert E. Sheriff and Lloyd P. Geldart, 1995).

In velocity tomography, only the first arrival pulses are considered. Therefore, only the signal component that travels through the fastest path is used in the analysis. As the velocity changes through the medium due to energy absorption, the slowness (1/velocity) of any uniform cell of the medium may change not only the travel time, but also the ray path.

A number of software algorithms for performing travel time tomography exist. These algorithms use straight or curved rays, 2-D or 3-D matrix inversion, and 2-D or 3-D graphic packages to display the results. For accurate volumetric imaging of anomalies in drilled shafts, it is critical to use a software package with the following characteristics: a)- curved ray tracing or wave propagation; b)- true 3-D tomographic inversion; c)- 3-D display of data. Two-dimensional tomographic inversion produces defect images in 2-D planes (panels), which is inadequate for reconstructing the size and shape of anomalies in some cases.

The CSL data measured between the three access tubes of abutment 1 shaft 2 were processed for P-wave first arrival times. The data were then processed using the RockVision3D software for generating 3-D velocity tomograms of the shaft interior. The input information for the tomogram generation was; 1) depth of the shaft where the first arrived component of the signal was measured, 2) the first picked arrived time at each depth, and 3) tube separation distance.

The program code is designed to provide multiple iterative reconstructions of path length for calculated seismic velocity determined from measured travel times. Ray paths are calculated by propagating a finite-difference wave front across the surveyed shaft from a known source location. For low velocity contrast, straight rays are often assumed. In higher velocity contrast, the rays bend (refract) resulting in longer ray paths.

A 3-D representation of the shaft interior was constructed and imaged to produce 3-D contours velocities (green areas in the figure) to emphasize areas of "questionable" integrity and 2-D cross-sections between access tubes in Figure 2.2. From these images, three distinct velocity contrast zones are seen: z*one1* with maximum measured velocity (red), which indicates that the concrete is in "good" condition; z*one 2* with middle range velocity (green), indicating velocities 10%-20% lower than the maximum measured velocity, and z*one 3* upper zone (purple) showing the extent of the shaft with the velocities down to 2,000 m/s. This zone shows the top of the shaft where the tubes are outside the concrete and is not an indication of any defects in the upper area of the shaft. The locations, size, and orientation of the anomalies are clearly depicted in these images.

Horizontal cross-sections looking from the top of the shaft at 0.5-m intervals are also plotted and shown in Appendix A. The first image at 5.5 m from the bottom of the shaft shows the portion of the shaft with the velocities down to 2,000 m/s. Going deeper into the shaft, the location of an anomalous zone with the velocities of the concrete showing "questionable" structure condition can be clearly seen. Images were produced to compare the results of the CSL x,y plots with the tomographic imaging maps. By plotting color-coded 3-D tomographic images of the ultrasonic data (CSL), accurate location of anomalous/questionable zones and their geometries can result in more reliable information about the shaft concrete integrity.

1.6 Defect Definition and Drilled Shaft Integrity

Defects, or anomalies that critically affect shaft performance, are difficult to define using results from CSL. This limitation has resulted in serious disputes and litigation. The effect of the size, location, and distribution of anomalies on shaft performance and structural integrity are difficult to quantify apart from numerical analysis. Without advanced numerical analysis tools, defect definition is often arbitrary, exaggerated, and overrated. Certain guidelines have been proposed to constitute a defective shaft, such as a 20% reduction in overall concrete velocity. Errors in tube separation distances could easily result in an invalid shaft rejection. A defective shaft could easily be adjusted to pass acceptance by "correcting" the picks or tube separation distance. This problem will be analyzed in greater depth in the following chapters, to define the relationship between defects and shaft integrity, using numerical analysis tools and techniques.

CHAPTER 2. CONCRETE DEFECTS AND CURING CHEMISTRY

Concrete is basically the product of a mixture of two components: aggregate and paste. The paste consists of cementitious materials, such as pozzolan in Portland cement, water, and entrapped or purposely entrained air. The properties of concrete may be changed by adding chemical admixtures during the batching process. In newly mixed plastic concrete, the coarse and fine aggregates are held in suspension by the paste until the mass hardens into a rigid, homogeneous mixture of components. The semi-fluid mixture hardens into concrete by the chemical action of hydration of cement, not by loss of moisture. Cement hydration will continue to occur, increasing concrete strength with age, provided the concrete is properly cured. Proper curing requires deliberate action, such as using a sealing compound or insulating blankets, to maintain the moisture and temperature conditions in the freshly placed mixture. Concrete strength will continue to increase with age provided that water is available to react with unhydrated cement, a relative humidity above 80% is maintained, the concrete temperature remains above freezing, and sufficient space is available for hydration products to form in the matrix. The chemical composition changes that occur in the concrete during the curing process fundamentally determine the strength and durability capabilities of the final concrete product.

Cement is the binding material that locks the mineral aggregates in a solid structure. While it is not the terminology typically used in the transportation arena, cement is classified as a ceramic material, with typical properties listed in Table 2.1. Perfect ceramic crystals have extremely high tensile strengths, with some ceramic glass fibers having ultimate strengths over 700 MPa. However, ceramic crystals often contain many cracks and other defects, reducing their tensile strengths to near-zero levels. This explains why cement has a high compressive strength, but a relatively low tensile strength. The ceramic cement crystals contain many cracks at the micro-scale, and weaken further as cracking propagates to a larger scale.

Table 2.1 Properties of Typical Ceramics

High melting point
High hardness
High compressive strength
High tensile strength (perfect crystals)
Low ductility (brittleness)
High shear resistance (low slip)
Low electrical conductivity
Low thermal conductivity
High corrosion (acid) resistance
Low coefficient of thermal expansion

The term corrosion is somewhat imprecise, but generally refers to progressive oxidation of metals such as may occur to the reinforcing steel. Ceramics consist of oxidized materials, so they do not oxidize or corrode. Ceramic materials, although not vulnerable to oxidation, are still vulnerable to other chemical processes that react with and break down the material. These processes can be compared with the weathering of rock in nature.

There is a definite impact of the chemical composition of the cured concrete on final shaft performance. The strength of continuous uniform chemical matrices of cement and concrete can be theoretically calculated. In practice, concrete is never a continuous matrix such as plastic or metallic materials. Similar to ceramics, concrete is rigid. Rigid materials can take only a limited amount of stress before cracking. Such stresses are inherently produced by the processes that form the concrete, particularly for large structures. As a result, an extensive body of literature has evolved to study the cracking of concrete.

The stresses that occur in curing concrete are a natural result of the processes that create the rigid concrete structure from the initial fluid concrete mix. The matrix formed has a different structure, and thus a different density, than the original liquid. In addition, a large amount of heat is generated in the hydration process, resulting in an initial rise in temperature. The temperature then gradually declines as the chemical reaction comes to completion and generated heat is conducted outward. This process can vary from a few hours for small structures to many years for very large concrete structures, such as dams. A rise in concrete temperature creates a corresponding expansion, followed by contraction as the concrete cools. Once the concrete has substantially set up into a rigid matrix, expansion or contraction can easily cause cracking.

Structurally, the significance of cracking varies depending on the type of concrete. Concrete inherently is a material with good compressive strength, but has weak tensile strength strongly affected by cracking. Thus, for unreinforced concrete, cracking can seriously affect performance. For reinforced concrete where the steel rebar absorbs tensile load, the effect is controlled. For drilled shafts, where reinforced concrete is used and the major load is compressive, cracking is not a serious problem structurally, especially in the short run. Cracking causes more problems for shafts that experience substantial lateral loads. Cracking does however accelerate environmental attacks on both concrete and rebar over time. Also, high slump concrete mixtures are routinely used for drilled shafts. If placed improperly, especially in smaller diameter drilled shafts, the concrete may segregate or honeycomb. In these cases where the reinforcing steel may prevent unrestricted free fall of the concrete, then chute may be needed.

Successfully modeling the curing process of concrete to predict cracking is an essential part of understanding the processes that lead to CSL velocity variations in drilled shafts.

2.1 Hydration Rates and Heat Generation during Concrete Curing

Modeling the curing process of concrete essentially entails modeling the cement hydration processes, together with the resultant physical effects of hydration. This includes modeling heat generation, temperature dissipation, microstructure formation, and the resulting stiffening or setting of the concrete. The curing process for a typical Portland cement concrete mixture involves four major hardening compounds, together with gypsum, as shown in Table 2.2.

All of the hardening compounds, C_3S, C_2S, C_3A, C_4AF, and CSH_2, hydrate at different rates and generate differing amounts of heat per unit weight, although only the silicates contribute to strength. Exact measurement of heat generation is complicated, but generally the amount of heat

Table 2.2 Compounds Involved in the Hydration Process (Kosmatka 2002)

Chemical Name	Chemical Formula	Shorthand Notation	Percent by Weight
Tricalcium Silicate	$3CaO.SiO_2$	C_3S	50% (37-71%)
Dicalcium Silicate	$2CaO.SiO_2$	C_2S	25% (4-36%)
Tricalcium Aluminate	$3CaO.Al_2O_3$	C_3A	12% (0-14%)
Tetracalcium Aluminoferrite	$4CaO.Al_2O_3.Fe_2O_3$	C_4AF	8% (4-19%)
Gypsum	$CaSO_4.H_2O$	CSH_2	3% (1-7%)

generated is proportional to the hydration of the cement. An example hydration/heat generation curve for a typical cement mixture, generated empirically, is shown in Figure 2.1.
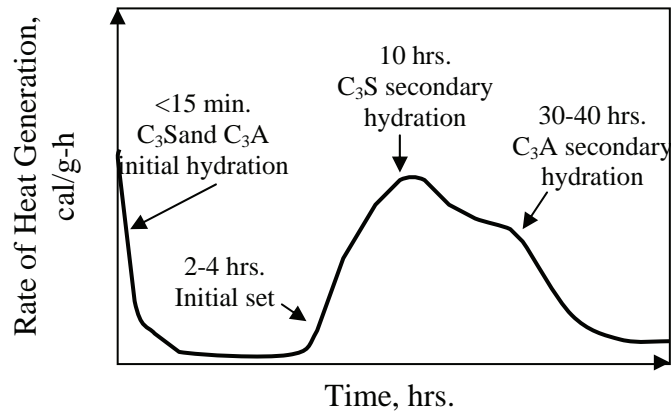
Figure 2.1. Plot.   Typical Rate of Heat Evolution during Cement Hydration

Although a rough approximation, the rate and quantity of heat generation is a function of the following cement parameters (Breugel 1998):

- Cement chemical composition
- Cement fineness and particle size distribution
- Water/cement ratio
- Reaction temperature

The reaction temperature is variable, as the heat generated by the hydration reaction increases the temperature. The degree to which this occurs depends on the size of the concrete sample and insulation from the ambient environment. Essentially all the heat of hydration generated in small un-insulated concrete structures is conducted to the environment, resulting in a temperature isothermally equivalent to that of the environment. By contrast, larger structures such as drilled

13

shafts have an almost adiabatic regime, meaning that generated heat is self-adsorbed, causing a corresponding increase in temperature. In these cases, the temperature may rise 40°C or more, and may require significant time for cooling. Some very large structures such as dams may require years before the heat entirely dissipates. The majority of structures have a temperature regime somewhat between these extreme cases.

The reaction temperature is affected by the heat of hydration, which in turn affects the hydration process. As with most chemical reactions, the rate of reaction increases with temperature. Concrete in warmer, more insulated environments hydrates faster. Also, higher curing temperatures cause changes in the concrete microstructure, reducing the molecular length and size of the hydration structures in the paste. This reduces the strength of the concrete, which in turn increases susceptibility to cracking.

As hydration and concrete setting is highly dependent on curing temperature, modeling the temperature profile in curing concrete is important for estimating resulting properties, performance, and durability of the structure. The ideal case for maximizing concrete performance would be a cool isothermal environment, both at initial placement and during setting, in which all heat generated is conducted out of the concrete, maintaining a cool uniform temperature profile throughout the concrete structure at all times. Unfortunately, this is typically not the case, with regions of increased temperature and steep temperature gradients existing within the structure. Both a general increase in temperature and non-uniformity can negatively affect the properties of the concrete structure. Any measures which can be taken to reduce the impact of heat and heating on concrete structures and improve the structural properties of the concrete is a key part of concrete engineering, and certain aspects are presently active subjects of discussion in civil engineering.

2.2   Curing Chemistry Modeling

Modeling the temperature profile to predict thermally induced mechanical stress and cracking is important to predict concrete performance. These stresses are a byproduct of normal strength development in young concrete. Excessive stress results in cracking. At early stages, significant changes to material properties take place due to chemical hydration reactions in the cement. The remaining properties, such as the thermal and mechanical development of the young hardening concrete, all occur in response to hydration. Therefore it is important to understand and definitively model the hydration process.

The microscopic chemical processes in the developing microstructure are the driving forces behind the development of concrete properties. Mathematical modeling of the thermal and mechanical properties of the concrete can be approached in various ways. The traditional and established approach has been to empirically model the material properties of the concrete mixture from tables and charts. These properties can then be used to model the thermal and mechanical properties that describe the behavior of the hardening concrete mixture as a whole.

To go beyond empiricism requires developing models to link the microstructure of the developing concrete to macroscopic properties. This requires an understanding of how the micro-physics, chemistry, and associated micromechanics translate into microphysical

phenomena such as creep, shrinkage, and fracture of the concrete structure. Up until very recently, this unified material science based approach has been viewed as very difficult, although new approaches are currently under development in these regards.

2.2.1 Empirical Modeling Methods

Empirically based models of concrete properties are focused on the macroscopic properties of the concrete. These models are related to uncertainties created by the variability of concrete curing. Variable parameters are used from tables and charts based on the study of concrete characteristics as a function of temperature, amount and type of cement and admixtures, water, and other variables. Dominant macroscopic characteristics such as the compressive strength or temperature are then used to estimate other macroscopic properties of the concrete.

Within this general category are a broad variety of techniques and formulas. Empirical approaches rely more on studying the material properties of the concrete mixtures from tables and charts. More mathematical approaches attempt to model the behavior of concrete based on formulas derived from modeling a particular aspect of concrete curing, or from analysis of a particular aspect of concrete curing chemistry. Lokhorst describes five of these chief concepts (Lokhorst 1993):
- The porosity concept
- The gel-space ratio concept
- The degree of hydration concept
- Maturity laws (equivalent time laws)
- Chemistry-oriented strength laws

These concepts are used to derive mathematical models for increasing compressive strength with time. These models use empirical coefficients based on different grades of concrete and cement types, and also consider other variables such as hydration and temperature, depending on the equation. The compressive strength in turn provides information on other concrete properties, such as durability, tensile strength and stiffness.

2.2.2 Geostructural Analysis Package Methods (GAP)

Going beyond empiricism requires developing models to link the microstructure of developing concrete to the macroscopic properties. Concrete hardening is the result of a chemical reaction, and therefore going below the macroscopic level requires analyzing and modeling the molecular changes and dynamics that will eventually produce the final mature concrete product. At the molecular level, physical phenomena like the production of heat, formation of new chemical hydration bonds, and use of water are linked to the physical properties of the micro-aggregates that are being formed by concrete hydration.

Micro-modeling of the concrete mixture can be approached in a variety of ways. Most current analyses focuses on the concrete mixture as a mixture of two types of particles: macroscopic-sized particles of aggregate and largely microscopic-solidifying particles of cement paste. Physically, the viscoelastic (i.e. fluid) mixture of the solid component (the aggregate) and the cement/water mixture gradually become more solid.

15

Modeling aggregate particles is fairly straightforward, since during the initial hydration period, the aggregate's chemical reactivity is very slow and physically solid, with a fixed heat capacity and heat conductivity. The aggregate's potential for long term alkali-silica reactivity or alkali-carbonate reactivity is not considered in this model. Modeling cement is more complex, because all the physical, chemical, and structural properties of the particles are in transition. The cement is initially composed of course, dry particles, which start to dissolve and react upon contact with water. Modeling of this dynamic process using the solidification theory has been developed by leading concrete experts such as Bazant and Van Breugal (Bazant 1977).

Using solidification theory, the cement paste mixture is simplified using spherical cement particles divided arbitrarily into two layers: an outer layer of solidity, composed of hydrated cement, and an inner layer constructed of unhydrated fluid cement paste. Over the course of time, the liquid layer recedes while the solid layer propagates into the cement particle, and becomes more rigid.

Use of this solidification theory can allow combination of various physical equations governing and regulating the hydration reactions of concrete, such as temperature, moisture diffusion, and the physical properties of the concrete. However, its application is still under development.

2.3 Thermal Issues for Concrete Construction in the Field

Large and medium-sized concrete structures, such as dams, tunnel linings, and drilled shafts, can generate large amounts of heat internally. High internal temperatures and temperature differentials can form between the interior and exterior of the concrete. This requires active measures to control heat related effects, such as using internal cooling or external insulation. Such measures are commonly used for massive structures, but rarely considered for medium-sized structures. Usually limitations are specified for the maximum allowable temperature difference. Most state DOTs limit the interior/exterior temperature differential to $20\,^{o}C$ ($35\,^{o}F$) (Concrete Construction Magazine 2001).

Limiting the temperature differential is not an issue for relatively small drilled shafts. This becomes a significant challenge for drilled shafts exceeding 2 m in diameter. Internal temperatures may reach levels as high as $90\,^{o}C$. Limiting the temperature difference to $20\,^{o}C$ may be difficult, if not impossible, without special measures, such as internal cooling. This is a topic of recent discussion concerning proper temperature controls for drilled shafts.

2.3.1 General Aspects of Thermal Cracking Analyses

Thermal cracking is the most prominent of adverse temperature effects on concrete structures. Thermal cracking arises from the uneven expansion and contraction of concrete structures during heating and/or subsequent cooling. Thermal cracking refers both to cracking that occurs in concrete at a young age when it is still curing and generating heat, as well as non temperature-induced stress of early age shrinkage. In either case, predicting the likelihood of thermal cracking involves modeling the stresses that arise in the curing concrete. Four main factors must be considered in such modeling – the chemical reactions during the hydration and curing

processes, the temperature development in the concrete element being cast, the mechanical behavior of the young concrete, and any forces acting on the shaft from the surrounding environment as the concrete cures. An independent analysis of both the temperature development and resulting stresses are necessary for a thorough analysis of cracking tendency.

Engineering practice often uses rough estimates to reduce cracking risk, such as the specification of the 20 $^{\circ}$C temperature differential *(ΔT)* limit. The maximum temperature difference in the structure is generally estimated from simple rules of thumb, charts, or temperature simulations. Estimates from such methods often provide an approximation of the actual cracking risk to be encountered in the structure. Such criteria assume a general relationship between ΔT and tensile stress levels in concrete, an assumption not borne out in practice. Tensile stresses are directly correlated with cracking tendency, as cracking in a concrete element generally initiates when the tensile stress exceeds the tensile strength.

A review of Table 2.3 shows the weakness of estimating the cracking risk purely from the temperature differential. Cracking risk can be defined to be the point at which tensile stresses exceed the tensile strength of the concrete. This table concerns a 1.5-m thick concrete structure. Calculations are made of the maximum stress level using a temperature differential from 3 Cases: Case I-winter temperatures with warm initial concrete, Case II-summer temperatures with warm concrete and, Case III- summer temperatures with cool concrete. Case I

Table 2.3 Surface Cracking Risks for a Structure with Concrete Thickness of 1.5 m

	Parameter	**Case I**	**Case II**	**Case III**
Initial Concrete Temperature	T_i	20 $^{\circ}$C	20 $^{\circ}$C	10 $^{\circ}$C
Ambient Air Temperature	T_{air}	5 $^{\circ}$C	20 $^{\circ}$C	20 $^{\circ}$C
Temperature Difference Cross-section	ΔT_{max}	24.5 $^{\circ}$C	18 $^{\circ}$C	14.5 $^{\circ}$C
Cracking Risk – (Max. Stress)l	n_{max}	0.45	0.53	0.54
Cracking Risk – (Temp. Difference)	$\dfrac{\Delta T_{max}}{\Delta T_{cr}}$	1.225	0.90	0.752
Correlation Factor	$\dfrac{\dfrac{\Delta T_{max}}{\Delta T_{cr}}}{n_{max}}$	2.72	1.69	1.39

approximates winter conditions, while Cases II and III correspond to summer temperatures. The cracking risk is lowest for Case I (winter scenario), even though it has the greatest internal/external temperature differential.

The cracking risk factors are from computations by Emborg (1994), of the maximum stress level ($n_{max)}$ the concrete can absorb without cracking, compared to the actual thermal stress encountered. The cracking risk is much less in winter, in spite of a greater ΔT_{max}. A cooler initial concrete temperature reduces the maximum temperature differential, but increases the cracking risk, as shown in Case III. These calculations illustrate the problems with using a maximum temperature differential as the control factor for cracking risk.

2.3.2 Problems with the 20 ^{o}C Limit

As construction of drilled shafts demands larger and larger concrete structures, meeting overly simplistic measures such as the 20° C limit become difficult, expensive, time consuming, and impractical. Using a measure designed for smaller concrete structures on large shafts can adversely affect structural integrity, rather than safeguard it. In some cases, specifying 20 ^{o}C temperature difference limit may be too restrictive, unnecessarily increasing time and cost and may not prevent damage from thermal cracking as intended. As foundation engineering complexity increases, the use of simple "rule of thumb" standards may not adequately meet design requirements. Criterion for better QA/QC during construction may be required. Development of these controls is based on more detailed and thorough planning, modeling, and engineering analysis of the thermal profiles and resulting thermal stresses on the structure. Some of the techniques for such modeling are described below.

2.3.3 The Importance of Thermal Modeling in Concrete Structural Design and NDE

Thermal/chemical modeling of concrete elements is important to evaluate the soundness and integrity of drilled shafts. Controlling thermal development, through careful modeling, is a key aspect to understand concrete curing and to minimize the risk of thermal cracking. Construction of large diameter drilled shafts, 2.5 m or larger for instance, requires a thorough understanding of temperature development during concrete curing. However, thermal cracking may occur when mass concrete begins to exceed 0.6 to 1 m in thickness. Numerical models are useful, not only to provide answers to specific problems, but also to develop a fundamental understanding of interaction between the physical, mechanical, and chemical properties during the curing process.

Thermal modeling is also important for understanding and evaluating CSL data since temperature profiles have direct influence on velocities, and can result in CSL velocity variations. Temperature is generated in the model according to empirical measurements of heat generated from the concrete hydration process. Understanding the temperature history of a structure plays a key role in determining the ultimate integrity of the drilled shaft. The likelihood that velocity variations may be caused by thermal cracking and other temperature related defects in the structure is an important factor to consider when evaluating the CSL profile. Techniques to analyze CSL data for cracking could result in a significant improvement

in determining shaft integrity. As thermal modeling is a critical factor for CSL data, its role will be discussed in more detail in the following section.

2.4 Engineering Practice for Controlling Thermal Issues in Concrete Construction

The physical and chemical properties of the concrete setting process make concrete vulnerable to curing defects. Stresses arising from heat generation during concrete curing lead to thermal stresses and hence concrete cracking. As a result, a substantial research has been conducted in the past to develop construction procedures to reduce concrete cracking. There are two major categories of controls commonly used to control thermal development in concrete. The first sets of controls are designed to reduce the risk of thermal cracking in general. This includes measures that reduce heat build-up by using low-heat concrete, and measures that reduce the harmful effects of heat buildup using aggregate with a low-coefficient of heat expansion. These measures help ameliorate the effects of heat build-up, and generally improve the performance and durability of the finished product. Excessively large heat buildup of temperatures over 38°C for instance, requires strict regulations to control, and may be expensive, time consuming, and impractical. Special controls may include external insulation and internal cooling. However, the effect of such measures may be problematic, regarding the actual performance of the concrete structure.

2.4.1 Temperature Profiling

The temperature of the water in CSL access tubes within a drilled shaft can be measured over time, as shown in Figure 2.2. Since the access tubes are generally at the same radial distance from the center of the shaft, no direct measurement of the higher central temperature is available. The temperature appears to peak at approximately two days, corresponding to the secondary hydration reaction.

2.4.2 Simple and Practical Techniques for Reducing Thermal Concrete Cracking With Standard Construction Techniques

A number of measures can be used to prevent cracking. The degree of susceptibility of a concrete mixture to crack can be quantified by the cracking temperature. A low cracking temperature is an indicator of low cracking tendency, and vice versa for a high cracking temperature.

2.4.2.1 Concrete Placement Temperature

The placement temperature, normally from 10 to 30°C, with respect to the temperature of the surrounding strata is perhaps the most critical factor for cracking in drilled shafts. A high initial temperature causes an increase in temperature within the concrete as it hardens due to the increase in the rate of hydration. This produces a higher peak curing temperature, which reduces concrete tensile strength, increasing cracking susceptibility. The high temperature also creates greater thermal contraction as the concrete cools to ambient temperatures. Therefore, reducing the placement temperature is one of the most effective means of reducing cracking susceptibility.
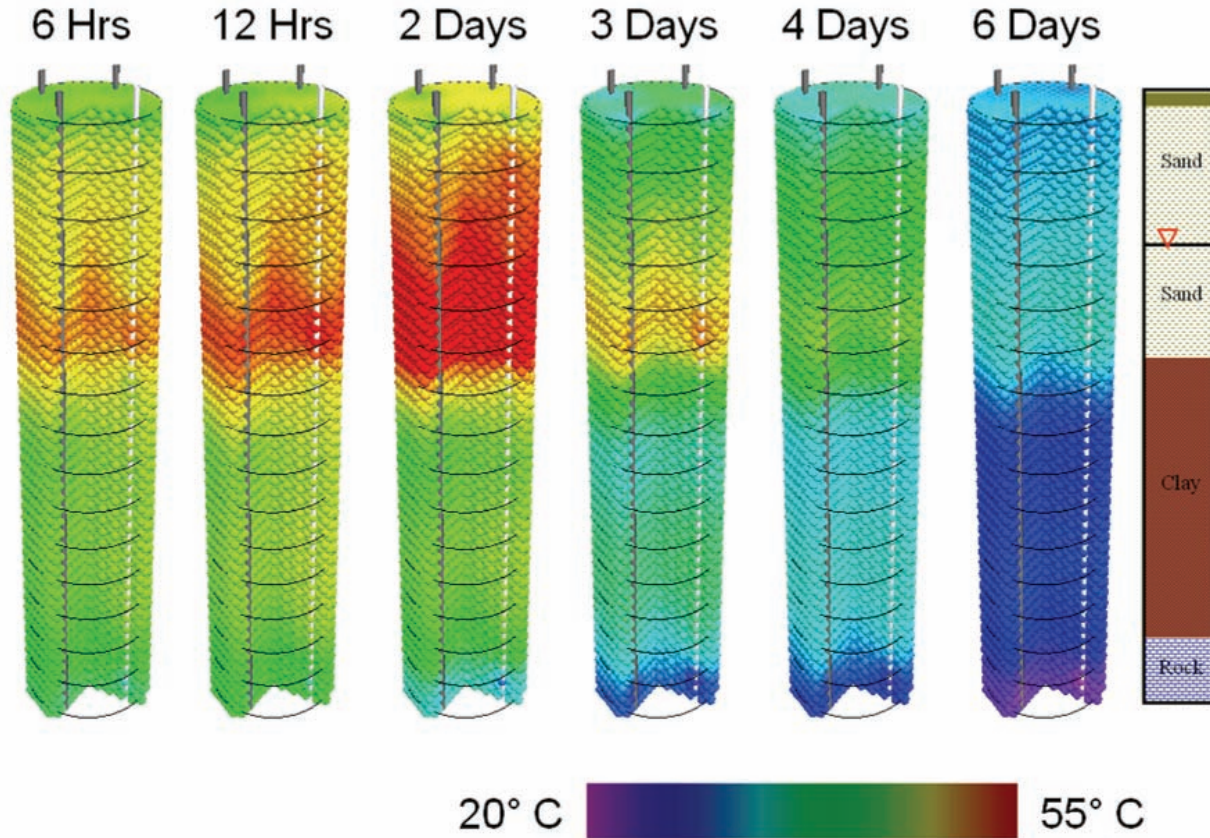
Figure 2.2. Plot. Temperature Plot from Data Progressively Collected from Access Tubes

A reduction in the placing temperature by 10°C can reduce the cracking temperature by 13 to 15°C, a substantial decrease for improving concrete properties. However, unlike concrete pavement, the placement temperature for concrete structures is often not specified.

2.4.2.2 Aggregate Properties

Certain aggregate properties can reduce cracking susceptibility. A low coefficient of thermal expansion reduces thermal contraction. A large aggregate size reduces the amount of cement necessary for workability, reducing cracking susceptibility. Too large an aggregate size can reduce tensile strength, increasing cracking susceptibility. The use of crushed aggregate, with higher fractured faces, increases tensile strength and decreases cracking susceptibility.

2.4.2.3 Cement Properties

Reducing the heat produced by cement during hydration is a good way to reduce cracking susceptibility. Although formulating a good low heat cement mix can be tricky, there are some practical ways to reduce this heat. Reducing cement paste to a minimum reduces cracking susceptibility, as heat generation is reduced. Cement paste can be reduced by substituting a portion of the cement with materials of similar consistency, such as fly ash, with lower heat of hydration.

In air entrained concretes, the tensile strain is typically increased by up to 20%, decreasing the stiffness of the concrete. Air entrainment significantly reduces cracking sensitivity for this reason.

Adjustments to the concrete mix may substantially reduce the overall cracking tendency and thermal stresses. There are intrinsic limits on how far the mix can be adjusted. Measures that reduce the heat output can result in a paradoxical effect. Concrete is a rigid ceramic material, with high compressive strength and a susceptibility to cracking. The rigidity which creates the compressive strength more specifically is a function of the cement, which holds the whole structure in place.

The quantity of cement paste is the most significant factor effecting heat generation in the concrete mixture. This is true whether the actual cement paste is minimized, the water content of the cement is increased, or with the addition of fly ash. Use of air-entraining agents to increase the air quantity also belongs in this category. All these measures reduce cracking, reduce rigidity, and reduce the compressive, shear, and tensile strength of the concrete. Fundamentally, these measures reduce cracking tendency by reducing the factors that give concrete its rigidity and strength. The overall effects of crack sensitivity reduction measures are quantified in Table 2.4.

Table 2.4 Effects on Crack Sensitivity (Springenschmid 1998)

Action	Decrease in Thermal Cracking Coefficient
Reduce fresh concrete temperature from 25°C to 12°C.	15-18K
Use optimum cement type	Up to 20K
Increase maximum aggregate size to 32 mm from 8 mm with corresponding allowable reduction in cement	5-10K
Use aggregates with a low thermal expansion coefficient	Up to 10K
Add air-entraining agents (Air content 3-6%):	3-5K
Use crushed aggregate instead of gravel	3-5K
Replace 20% cement with fly ash	3-5K

2.4.3 Field Measures to Reduce ΔT, Techniques and Implications

Drilled shafts with diameters greater than 2 m generate more heat internally than can be dissipated. Internal temperatures and thermal gradients can rise beyond prescribed limits. Measures to counter the amount of heat generated can include increasing the magnitude of measures presented in the previous section, or special construction measures such as insulation or internal cooling. These measures all have implications on performance and cost.

2.4.3.1   Special Construction Measures

The most direct means of dealing with heat generation involves the use of additional construction measures. Two common measures involve installing insulation on the external surface of the concrete structure, or a method of internal cooling, such as pipes circulating cooling water. Both measures can increase construction time and cost significantly. While both measures reduce the maximum temperature differential, the overall effect on concrete quality is not known, and may have detrimental effects on concrete quality and performance.

Use of Insulation

External insulation reduces the rate of heat conduction from the outer surface of the concrete structure, increasing the temperature of the outer surface and decreasing the temperature gradient. This causes the concrete to cool down slower and reach higher temperatures. Temperatures above a certain limit will have a negative effect on hydration structure, increasing crack susceptibility and decreasing concrete strength. The uniform temperature reduces thermal stresses, offsetting overall crack susceptibility somewhat. Many states have a maximum temperature requirement of 70 $^{\circ}$C (160 $^{\circ}$F) in some cases, which must be considered.

Insulation adds difficulty and expense to construction. The slower cooling rate requires more time for curing. Insulation cannot be removed for several weeks, in some cases. If insulation is removed prematurely, thermal shock can result. Care must be taken to remove insulation sequentially, layer by layer. Longer curing times expose the structure to weather or other external influences which could damage the insulation, resulting in thermal shock. Insulation may help meet temperature differential standards, but this benefit may be offset by potential complications, cost, and delay of construction.

Use of Internal Cooling

Installation of internal cooling is the most direct way of controlling the thermal development of concrete structures, and is also the most complex, expensive, and labor intensive. Special features must be incorporated in the overall engineering design of the structure from inception, requiring continuous and active oversight until the structure is completely set and cooled. There is no other option for controlling heat in massive concrete structures such as dams, where internal cooling has traditionally been applied.

As drilled shafts increase in size, internal cooling may become a consideration. Although internal cooling alleviates extreme temperature gradients, thermal stress will still exist, and differences in thermal expansion between the concrete and cooling pipes will result in cracking. These factors would need to be analyzed and accounted for in the engineering design.

Table 2.5 Comparison of Measures on ΔT , Concrete Strength, and Overall Concrete Quality

Actions calculated by effect on Cracking Temperature (Springenschmid 1998)	Decrease in Thermal Cracking Coefficient	Decrease in ΔT	Effect on Strength	Overall Effect on Quality
Reduce concrete placement temperature from 25°C to 12°C.	15-18K	Strong Decrease	Increase	Strongly Positive
Reduce temperature of placed concrete from 12°C to 1°C.	Problematic	Strong Decrease	Increase	Problematic
Use optimum cement type	Up to 20K	Strong Decrease	Variable Decrease	Positive, if used carefully
Increase maximum aggregate size to 32 mm from 8 mm with corresponding allowable reduction in cement	5-10K	Decrease	Decrease (due to cement decrease)	Positive, if used carefully
Use aggregates with a low thermal expansion coefficient	Up to 10 K	No effect	No effect	Moderately positive
Add air-entraining agents (Air content 3%-6%):	3-5K	No effect	Slight Decrease	Moderately positive
Use crushed aggregate instead of gravel	3-5K	No effect	Slight Increase	Moderately positive
Replace 20% of cement with fly ash	3-5K	Strong decrease	decrease	Moderately positive

2.5   Comparative Evaluation of Thermal Control Measures

A side to side comparison is useful to evaluate the effectiveness of various measures used to control concrete quality in drilled shafts. The respective measures should be evaluated to determine if the net effect in reducing cracking sensitivity is positive or negative on the integrity of drilled shafts. Modest reductions in the concrete placement temperature have the most significant effect, but even this measure has potential for negative effects if not used carefully.

Simple measures can have some positive effects in moderately sized structures. In larger structures, use of simplistic "rules of thumb" can lead to deterioration in the quality of the overall concrete structure. An understanding of the complex interactions of various parameters used in controlling concrete temperature may lead to improved structural integrity of large drilled shafts. The following summarizes the results of the table above:
- Initial effect positive, as both ΔT and T_{max} are reduced.
- Further reduction limited. Table 2.3 shows how cooling cement well below ambient temperatures may actually increase thermal stresses.
- Reduction in cement and increase of water lead to workability problems and voids, so such changes intrinsically decrease the margin for error in concrete mix quantity.
- Most Class F fly ashes, for instance, act as inert cement substitutes, and delay the hydration process. A large increase in Class F fly ash merely reduces the strength and overall rigidity of the concrete.

2.6   Environmental Effects on Curing Chemistry and Concrete Quality

The initial characteristics of the concrete at placement, such as placement temperature and constituents of the mix, determine a large portion of the concrete's quality and cracking tendency. However, the surrounding environment during curing can have a significant effect on the quality and durability of the concrete structure, due to its affect on the curing process.

Since non-uniformity in curing concrete is a major cause of cracking and other quality issues, any substantial local variations and non-uniformity in the curing environment, such as heating by the sun on the surface during the day, can adversely affect concrete quality. However, even assuming a fairly uniform environment, concrete quality is still strongly affected by both moisture and temperature. Excessive effects of moisture, such as a high water table, are usually handled by installing a water-proof barrier around the drilled shaft.

Temperature also strongly affects concrete quality. Low ambient temperatures, especially in combination with high placement temperatures, increase the cracking susceptibility considerably, due to rapid cooling. The difference between the placement temperature and the ambient temperature of the surrounding environment is especially important in regards to surface cracking. Concrete surfaces exposed to the sun are often adversely affected by cracking.

Non-uniform temperature distribution has an especially strong negative effect on concrete quality because of the close relationship between heat of hydration and concrete maturity. Non-

uniform temperature and maturity in concrete create internal stress gradients, potentially increasing the tendency for cracking.

Temperature gradients occur in large concrete structures even in a uniform external environment, due to heat gradients resulting from temperature buildup in the interior portions of the structure. The temperature gradient is reduced by utilizing internal cooling or insulation methods, commonly employed in large structures such as concrete dams.

However, drilled shafts usually do not have a uniform external environment, as the surrounding ground conditions can result in a highly variable and complex environment. As a consequence, a drilled shaft may experience radial, axial, and circumferential, non-linear temperature gradients.

2.6.1 Changes in Ground Water Heat Conductivity

The effect of ground water on the temperature gradient within a drilled shaft can be very pronounced, especially in regions near the water table. Ground water has a large heat capacity and readily absorbs heat generated during the curing phases of the drilled shaft. As a result, ground water is capable of creating a substantial temperature differential in the drilled shaft at the contact surface interface.

The groundwater table usually does not vary significantly in depth over the initial curing process of 3-4 days, except under very unusual circumstances, such as torrential rains or floods. However, horizontal movement of ground water can vary widely depending on conditions. For example, typical groundwater flow velocities lie in the range of 0 to 250 m/day. Lowest flow velocities are in heavy clays, with flow rates increasing with soil permeability, especially with significant head pressure.

Ground water flow should be considered when modeling heat flow into the surrounding soil, due to substantial differences in heat absorption of the environment. Variations in ground conditions surrounding the shaft may also have a substantial effect on the local temperature of the drilled shaft. Different types and consistencies of soils (clay, sand, gravel) or bedrock (shale, sandstone, or granite etc.) have substantial variations in heat capacity and thermal conductivity, both vertically and laterally.

Table 2.6 Ground Water Flow in Soil

Soil Type	Hydraulic Conductivity, K (cm/s)
Clay-like	10^{-9} - 10^{-6}
Silt-like	10^{-7} - 10^{-3}
Sand-like	10^{-5} - 10^{-1}
Gravel-like	10^{-1} - 10^{2}

CHAPTER 3. NUMERICAL MODELING

Modeling has been a useful tool for engineering design and analysis. The definition of modeling may vary depending on the application, but the basic concept remains the same: the process of solving physical problems by appropriate simplification of reality. In engineering, modeling is divided into two major parts: physical/empirical modeling and theoretical/analytical modeling. Laboratory and in situ model tests are examples of physical modeling, from which engineers and scientists obtain useful information to develop empirical or semi-empirical algorithms for tangible application. Theoretical modeling usually consists of four steps. The first step is construction of a mathematical model for corresponding physical problems with appropriate assumptions. This model may take the form of differential or algebraic equations. In most engineering cases, these mathematical models cannot be solved analytically, requiring a numerical solution. The second step is development of an appropriate numerical model or approximation to the mathematical model. The numerical model usually needs to be carefully calibrated and validated against pre-existing data and analytical results. Error analysis of the numerical model is also required in this step. The third step of theoretical modeling is actual implementation of the numerical model to obtain solutions. The fourth step is interpretation of the numerical results in graphics, charts, tables, or other convenient forms, to support engineering design and operation.

With the increase in computational technology, many numerical models and software programs have been developed for various engineering practices. Numerical modeling has been used extensively in industries for both forward problems and inverse problems. Forward problems include simulation of space shuttle flight, ground water flow, material strength, earthquakes, and molecular and medication formulae studies. Inverse problems consist of non-destructive evaluation (NDE), tomography, source location, image processing, and structure deformation during loading tests. Although numerical models enable engineers to solve problems, the potential for abuse and misinformation persists. Colorful impressive graphic presentation of a sophisticated software package doses not necessarily provide accurate numerical results. Fundamental scientific studies and thorough understanding of the physical phenomena provide a reliable and solid guideline for engineering modeling. In this project, the focus is on the thermo effects of drilled shafts after the placement of concrete, and performance under various loading conditions. The numerical models developed in this project are based on well-developed theories and constitutive laws in chemical and civil engineering, as well as numerical methods widely accepted in engineering. The numerical results are also carefully analyzed against existing laboratory test data.

3.1 Establishment of Numerical Model

Modeling is fundamentally the core of engineering. A model is an appropriate simplification of reality. The skill in modeling is to spot the appropriate level of simplification, distinguish important features from those that are unimportant in a particular application, and use engineering judgment. There is a long history of empirical modeling in civil engineering. Due to difficulties in obtaining accurate material properties of in situ earth materials and construction materials, most civil engineering is based on experience--although many techniques are semi-empirical rather than purely empirical. For this reason, the development of more rigorous

modeling tools has lagged behind the demands of industry. In this project, advancements in computational techniques, civil engineering, and material science are incorporated into a theoretical/mathematical numerical model based on the analysis of physical phenomena and constitutive laws for the application of drilled shafts in roadway/highway engineering.

3.2   Theoretical Models

The description of most engineering problems involves identifying key variables and defining how these variables interact. The study of theoretical modeling involves two important steps. In the first step, all the variables that affect the phenomena are identified, reasonable assumptions and approximations are made, and the interdependence of these variables is studied. The relevant physical laws and principles are invoked, and the problem is formulated mathematically. In the second step, the problem is solved using an appropriate approach (in this project, an appropriate numerical approach) and results are interpreted.

The fundamental principles and constitutive laws of material behavior have been thoroughly investigated for engineering purposes. This makes it possible to predict the course of an event before it actually occurs, or to study various aspects of an event mathematically without actually running expensive and time-consuming experiments. Very accurate results to meaningful practical problems can be obtained with relatively little effort by using suitable and realistic mathematical/numerical models. However, the preparation of such models requires an adequate knowledge of the natural phenomena and relevant laws, as well as sound judgment.

Theoretical modeling leads to an analytical solution of the problem. For this reason, engineering problems are often described by differential equations. An engineer often has to choose between a more accurate but complex model, and a simple yet relatively less accurate and over-generalized model. Available computational technology and techniques provide engineers the option of exploring complex numerical models. A numerical solution usually implies the replacement of a continuous description of a problem by one in which the solution is only obtained at a finite number of points in space and time. In this project, the quality of the numerical approach is verified by applying the numerical model to a situation for which an exact solution is known.

However, mathematical/numerical modeling does not eliminate the indispensable experimental approach to physical modeling. The experimental approach provides observations of actual physical phenomena. Physical modeling is fundamental in the development of civil engineering. Many theoretical and empirical models are based on the interpretation of experimental results. Physical modeling validates the theoretical and empirical hypotheses. However, this approach is expensive, time-consuming, and not always practical in engineering.
The theoretical models and technical approaches employed in this project to model the drilled shaft in highway engineering are: a) thermal modeling; b) engineering mechanics; c) numerical model of discrete element method (DEM) and d) validations of numerical models.

3.3   Thermal Modeling

It is well known that the thermal behavior, temperature distribution, and residual stresses/strains in the shaft during concrete placement significantly affect the performance and strength of the support. In this section, heat transfer and the resulting temperature gradient will be discussed. A chemical model and heat transfer model were implemented together with a mechanics constitutive model to simulate conditions of the concrete shaft while curing.

During the concrete curing (hydration) process, heat generates inside of the concrete. This heat transfers from regions of higher temperature to regions of lower temperature, such as the surrounding environment. The non-uniform temperature gradient causes variations in shrinkage strains and generates cracks in the shaft. Common guidelines specify a 20° C (35° F) temperature gradient rule, restricting the maximum temperature difference in the concrete. The 20° C rule may not truly reflect all situations, as the heat of hydration, thermal conductivity, tensile strength, modulus, and density of concrete changes as a function of time. Contractors often find difficulty maintaining high concrete strength by using a higher percentage of cement paste, which generates more heat, and still satisfy the temperature gradient rule. The heat transfer model employed in this project tries to combine curing chemistry, aging, thermal behavior, and mechanical strength of concrete to provide a better understanding of the concrete curing process so that appropriate engineering limits may be developed for temperature and quality control.

The rate of heat generation during concrete curing varies with temperature and time. The temperature inside a shaft varies with time, as well as position. This variation is expressed as:

$$T(\boldsymbol{x},\ t), \tag{3.1}$$

where
 x is the position vector
 t is time

The conductivity of concrete during curing varies with time and position, expressed as:

$$k(\boldsymbol{x},t) \tag{3.2}$$

This case is a typical nonlinear unsteady 3D heat conduction problem. Unfortunately, an analytical solution of the problem does not exist, except for overly simplified conditions. Numerical modeling can provide an efficient technical approach for this problem. In order to accurately model the thermal behavior during the curing process, a modified 3D explicit finite difference model is used as the numerical method in this study. Basic principles of the numerical solution and algorithm are presented in this section. Note that heat transfer by convection is considered, but heat transfer by radiation is not considered in this study.

The 3-dimensional heat conduction equation is expressed as:

$$\nabla(k_i \nabla T) + \dot{g} = \rho c \dot{T} \tag{3.3a}$$

Or, in the rectangular coordinate system as:

$$\frac{\partial}{\partial x} k_x(\mathbf{x},t) \frac{\partial T(\mathbf{x},t)}{\partial x} + \frac{\partial}{\partial y} k_y(\mathbf{x},t) \frac{\partial T(\mathbf{x},t)}{\partial y} + \frac{\partial}{\partial z} k_z(\mathbf{x},t) \frac{\partial T(\mathbf{x},t)}{\partial z} + \dot{g}(\mathbf{x},t) = \rho c \frac{\partial T(\mathbf{x},t)}{\partial t} \tag{3.3b}$$

where

$T(\mathbf{x},\, t)$ is the temperature distribution function with element control volume as *dxdydz*

$k_i(\mathbf{x},t)$ is the thermal conductibility in corresponding directions, respectively

$\dot{g}(\mathbf{x},t)$ is the rate of energy generation in the control volume

ρ is density of the material

c is specific heat (The heat capacity per unit of mass of the object)

$\mathbf{x}$ is position vector variable, explicitly expressed as x, y and z in rectangular coordinates

t is time.

The solution of equation (3.3) gives the temperature distribution in the material at different times. The temperatures obtained are used as input to the concrete curing chemistry model and engineering mechanics model to determine concrete tension/compression strength and thermal stresses/strains. Crack formation occurs when the tension stress is larger than the tension strength at a certain position. Cracks are simulated by breaking the connection between the material points. Micro-cracks develop and propagate inside the concrete as more connections are broken. These defects are taken into account for the concrete shaft loading and performance analysis. The model in this project is developed to represent history dependent material behavior.

Equation (3.3) is a non-linear unsteady heat conduction equation. Various numerical methods have been developed for the finite solution. One of the most popular is the finite difference method, which discretizes the domain into a finite mesh or grid. Equation (3.3) is solved on the mesh nodes together with boundary and initial conditions. The accuracy and efficiency of the solution depend on the discretization method, mesh size, and numerical integration algorithm. Generally, the mesh size is cubic in rectangular coordinates, or curved cubic in cylindrical or spherical coordinates. In this project, a modified finite different solution was developed with mesh nodes connected in a tetrahedral packing form that matches the mechanics numerical analysis algorithm. Figure 3.1 shows a portion of a 2D and 3D thermal resistance network mesh and nodes connection for heat conducting calculations.

The solution algorithm is based on the well known thermal resistance concept in thermal dynamics. Heat conduction is analogous to the relation for electric current flow as shown in Figure 3.1. According to Fourier's law of heat conduction, the rate of heat conduction through a plane layer is proportional to the temperature difference across the layer and the heat transfer area, but is inversely proportional to the thickness of the layer. Assume that at given time the distance between two adjacent nodes is Δx, the temperature difference is ΔT, which equals to the temperature at node 1 (T_1) minus the temperature at node 2 (T_2).
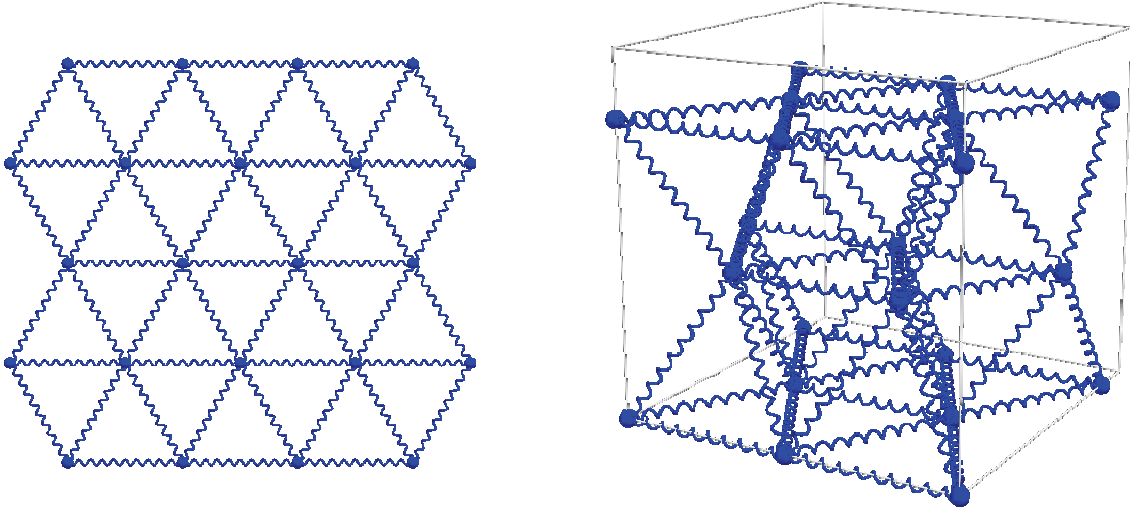
Figure 3.1. Plot. 2D and 3D Thermal Network Mesh for Heat Conducting Calculations

Defining the heat conduction area between two nodes as *A* gives:

$$\dot{q} = kA\frac{\Delta T}{\Delta x} = kA\frac{T_1 - T_2}{\Delta x} \tag{3.4}$$

where
k is thermal conductivity, a function of time and location.

By using the thermal resistance concept, equation (3.4) can be rewritten as:

$$\dot{q} = \frac{\Delta T}{R_{i-n}} = \frac{T_1 - T_2}{R_{i-n}} \tag{3.5}$$

where
R_{i-n} is thermal conduction resistance between node *i* and node *n*:

$$R_{i-n} = \frac{\Delta x}{kA} \tag{3.6}$$

Assuming that the conduction area *A* is constant between two nodes, and the mesh grid size is generated equally so that Δx is constant, R_{i-n} is only a function of *k*. In thermal modeling R_{i-n} is the variable vector of time and position. R_{i-n} is appropriately defined based on the concrete curing chemistry model. For 3D tetrahedral packing connections, each node is connected to twelve other neighbor nodes to form a thermal resistance network covering the model domain.

31

Assuming the initial temperature of concrete at placement is T_0, and assuming the heat generated by a unit concrete mass while curing is q (a function of concrete hydration rate), the temperature raised by unit mass due to the generated heat energy is:

$$\Delta T = \frac{q}{c} \tag{3.7}$$

where

ΔT is the temperature change per unit concrete mass due to the heat generated in hydration

c is the specific of heat of concrete

The specific heat is defined as the energy required to raise the temperature of a unit mass of a substance by one degree. Specific heat is a material property and is physically measured at constant volume (c_v) or constant pressure (c_p). Generally it is a function of temperature, though the change is small. Since concrete changes from a "fluid" state to a solid state while curing, the specific heat also changes correspondingly. For this reason, the specific heat is also a function of hydration. In this study, the change of specific heat is assumed to be linear to the non-linear hydration rate.

After the temperatures at each calculation mesh node are known, equation (3.5) is used to calculate the heat transfer rate between nodes. The heat energy at each node is updated correspondingly, based on the heat transfer rate changes. The new heat energy is then used to update the temperature of each node. Since the numerical modeling is based on a dynamic algorithm, and the temperature of boundary nodes are constrained by boundary conditions, the boundary conditions are correspondingly satisfied in the simulation.

3.4   Engineering Mechanics

In this section, the basics of the engineering mechanics principles involved in the modeling and analysis of this project are briefly presented. Since design philosophies, failure criteria, load capacity evaluation methods, and building codes for drilled shafts have been well defined in highway/roadway and civil engineering in AASHTO publications and other engineering resources, these topics will not be repeated. The focus is on the mechanical properties of concrete and soil, their relation to stress wave propagation in these materials, and the effect of thermal cracking and other defects to the performance of drilled shafts.

When an impact load is applied to a body, the deformation of the body due to the load will gradually spread throughout the body via stress waves. The nature of propagation of stress waves in an elastic medium is extremely important in geotechnical and geophysical engineering. Even though the materials encountered in geotechnical and geophysical engineering can hardly be called "elastic", the theory developed for an elastic medium is very useful and satisfactory in signal processing and inverse problem analysis. It is also widely used to determine material properties such as elastic modulus and shear modulus, and other design parameters of dynamic load-resistant structures.

From continuum mechanics theory, the equation of motion in an elastic medium can be written as:

$$\frac{\partial \sigma_{ij}}{\partial x_j} = \rho \frac{\partial^2 u_i}{\partial t^2} \tag{3.8}$$

where

σ_{ij} is the stress tensor

u_i is the displacement vector

ρ is the density of the material

By substituting the elastic stress-strain relationship into the equation of motion and re-arranging the equations, the elastic compression stress wave equation becomes:

$$\frac{\partial^2 p}{\partial t^2} = c_p^2 \nabla^2 p \tag{3.9}$$

where

p is the pressure

∇^2 is the Laplacian

c_p is the P-wave velocity

The elastic shear stress wave equation can be expressed as:

$$\frac{\partial^2 \omega_i}{\partial t^2} = c_s^2 \nabla^2 \omega_i \tag{3.10}$$

where

ω_i is the rotation vector

c_s is the S-wave velocity

From the above equations, the relationship of P-wave and S-wave velocity and elastic material properties are defined as:

$$c_p = \sqrt{\frac{\lambda + 2G}{\rho}} = \sqrt{\frac{E(1-\mu)}{\rho(1+\mu)(1-2\mu)}} \tag{3.11}$$

$$c_s = \sqrt{\frac{G}{\rho}} = \sqrt{\frac{E}{2(1+\mu)\rho}} \tag{3.12}$$

where

E is the elastic modulus

G is the elastic shear modulus

λ is the Lame constant

μ is the Poisson's ratio

Note that the material constants during concrete curing are a function of time and temperature. The actual values applied for the calculations in this project are based on the concrete curing chemistry modeling results.

The viscoelastic model is considered a better approach to wave propagation in geo-materials since the amplitude of the source wave attenuates with distance. The corresponding viscoelastic wave equation can be derived based on the equation of motion with a damping force:

$$\frac{\partial \sigma_{ij}}{\partial x_j} = \rho \frac{\partial^2 u_i}{\partial t^2} + c \frac{\partial u_i}{\partial t}$$

(3.13)

where
   c is damping coefficient of the medium.

The solutions of equations (3.9) and (3.10) describe wave propagation in an elastic medium. In geophysics, the finite difference method (FD) is the most common numerical method chosen for the solution. Various numerical schemes can be considered for the finite difference solution. For a 3D problem, various schemes include cubic rectilinear, octahedral, interpolated rectilinear, or tetrahedral, depending on the specific problem and desired accuracy. In this project, a non-linear viscoelastic model is used for the wave propagation calculations.

Thermal stress calculations during concrete curing are based on chemistry modeling. The stress depends on curing temperature, concrete strength and strain at different curing stages. The relationship between the rate of change of the temperature and strain with heat conduction is given by:

$$\frac{\partial}{\partial x_i} \left(k_{ij} \frac{\partial T}{\partial x_j} \right) = \rho C_v \frac{\partial T}{\partial t} + T \beta_{ij} \frac{\partial \varepsilon_{ij}}{\partial t}$$

(3.14)

where
   β_{ij} is a material constant proportional to the temperature change

   k_{ij} is the thermal conductivity matrix

   C_v is the specific heat per unit mass measured in the state of constant strain

   ρ is the density of the material

   ε_{ij} is the strain tensor

   T is the temperature

Again the material constants of concrete during curing depend on the temperature and the time. The constant values are obtained from concrete curing chemistry modeling and analysis.

To complete the specification of the mechanical properties of a material, additional constitutive equations are developed for the concrete curing process. The mechanical constitutive equation of a curing concrete specifies the dependence of stress on kinematics variables such as the rate of deformation tensor, temperature and other thermodynamics, electrodynamics, and chemical variables. Since this study focuses on engineering application, more effort is concentrated on the

simplification of currently available theoretical equations, and calibration of numerical models to meet the accuracy of engineering practice. Detailed descriptions of the technical approaches for concrete and soil are presented in the following sections.

3.5 **Discrete Element Method (DEM) Background**

Numerical modeling of the discrete element method and its application is presented. As discussed earlier, most mathematical equations established in theoretical modeling cannot be solved analytically, requiring a numerical solution. The development and selection of an appropriate numerical model is a key step for the successful application. Many numerical methods have been developed to solve different engineering problems, such as the Finite Element Method (FE), Finite Difference Method (FD), Boundary Value Problem (BV), Discrete Element Method (DEM), Material Point Method (MPM), etc. No single numerical method has been shown to be sufficient for all engineering problems. Each method has advantages and limitations for particular problems. The more physical phenomena are understood, the better numerical techniques can be developed and applied. In this project, the discrete element method (DEM) is employed based on the following considerations:

- Simplicity: the algorithm is simple to implement.
- Efficiency: the data structure of DEM is based on a mesh free principle, resulting in efficient computation and memory usage. The numerical model can be run on normal PC environments at high resolution.
- Flexibility: the model is originally designed for dynamics problems, such as wave propagation, contact/impact, and vibration problems. It can be easily modified to solve other problems, such as statics problems with dynamic relaxation, heat transfer problems with thermal resistance, seepage problems with friction losses, etc. The model simplifies generation of different geometrical shapes and boundary conditions.
- Extensibility: the model can be easily extended for geotechnical engineering applications such as slope stability, ground-foundation interactions, rock falls, tunneling/mining operations, avalanche study, as well as granular flow problems in chemical engineering and agricultural industries.

DEM, as well as any other numerical method, has limitations in engineering applications. Since the modeling domain of DEM is discretized into distinct particles which contact each other at their contact faces, the contact constitutive equations between particles determine the global mechanical responses of the whole particle assembly. The simplest contact constitutive model is represented by a spring-dashpot model for a normal contact, and a Coulomb friction model for a shear force, as shown in Figure 3.2. Although these constitutive models do not necessarily have to be linear and elastic, the model currently uses linear and elastic deformation unless the particles are totally detached. For the same discretization scheme of DEM, each individual particle is considered a "rigid" body. There is no deformation for individual particles. If such deformation is desired, a combined approach of DEM with other numerical methods such as FE
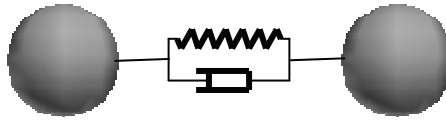
Figure 3.2. Plot.   Viscoelastic Contact Model for DEM

or BV is usually used. The contact constitutive model in this project is based on a non-linear contact mechanics model between two spheres.

3.5.1 Discrete Element Method Definition

The discrete element method (DEM) is a numerical technique designed to solve problems in applied mechanics that exhibit gross discontinuous material and geometrical behavior. DEM is used to analyze multiple interacting rigid or deformable bodies undergoing large dynamic or pseudo static, absolute or relative motion, governed by complex constitutive behavior.

DEM essentially is based on the numerical solution of the equation of motion and the principle of dynamic relaxation. Kinematics equations are established for each discrete body. The velocities, accelerations, and positions of the bodies are updated by calculating the contact forces between them. Depending on different physical problems, DEM programs should at least include the following three aspects:
- Representation of contact, which attempts to establish a correct contact constitutive model between discrete bodies.
- Representation of the properties of materials, which defines the particles or blocks to be rigid or deformable.
- Contact detection and revision of contacts, which attempts to establish certain data structures and algorithms to asses the contacts and the contact types, such as whether the vertex, edge or face of one polyhedron will touch a corresponding entity on a second polyhedron.

The following section discusses the discrete element method specifically related to this project, which discretizes the particles as 3D spheres that contact each other at their surfaces. Some general features of DEM are also included in this section.

3.5.2 Equation of Motion

Figure 3.3 shows two blocks *I* and *II* in contact. Their positions are defined by vectors R_1 and R_2. The blocks have masses m_1 and m_2, linear velocity vectors v_1 and v_2, and angular velocity vectors ω_1 and ω_2.

36

The equation of motion for element i at discretized time step n is:

$$\mathbf{M}_i \mathbf{a}_n^i + \mathbf{C}_i \mathbf{v}_n^i + \mathbf{P}_i \left(\mathbf{x}_n^i \right) = \mathbf{f}_n^i \tag{3.15}$$

where

$\mathbf{x}_n^i$, $\mathbf{v}_n^i$ and $\mathbf{a}_n^i$ are the position, velocity and acceleration vectors of the ith element at the nth time step,

$$\begin{aligned}
\left(\mathbf{x}_n^i \right)^T &= \left[\mathbf{x}_n^i, \mathbf{y}_n^i, \mathbf{z}_n^i, \theta_n^i \right] \\
\left(\mathbf{v}_n^i \right)^T &= \left[\dot{\mathbf{x}}_n^i, \dot{\mathbf{y}}_n^i, \dot{\mathbf{z}}_n^i, \dot{\theta}_n^i \right] \\
\left(\mathbf{a}_n^i \right)^T &= \left[\ddot{\mathbf{x}}_n^i, \ddot{\mathbf{y}}_n^i, \ddot{\mathbf{z}}_n^i, \ddot{\theta}_n^i \right]
\end{aligned} \tag{3.16}$$

where

$\mathbf{M}_i$ and $\mathbf{C}_i$ are the mass and damping matrices.

$\mathbf{P}_i$ and $\mathbf{f}_n^i$ are the resultant contact forces and applied boundary force/body force, respectively.

The formula for contact force depends on the particular constitutive laws applied to the problems. A modified Hertz-Mindlin contact law and viscoelastic contact law are discussed later in "Contact Mechanics".

Numerically solving equation (3.15) in the time domain gives accelerations, velocities, displacements and resultant forces. The stress/strain relationship inside of the discrete assembly is obtained by an averaging method. The *average stress tensor* of the volume V of the *representative of volume element* (RVE) can be obtained by:

$$\overline{\sigma}_{ij} = \frac{1}{V} \sum_{p=1}^{N} \sum_{c=1}^{m_p} \mathbf{x}_i^c \mathbf{F}_j^c \tag{3.17}$$

where

$\mathbf{x}_i^c$ is position vector at contact point c

$\mathbf{F}_j^c$ is contact force vector at contact point c

N is the particle number in RVE

m_p is the number of contact points for particle p

Similarly, the *average strain* of the RVE defined for infinite deformation can be written (by the Average Displacement Gradient Algorithm) as:

$$\overline{\varepsilon}_{ij} = \frac{1}{2} \left(\mathbf{F}_{ij} + \mathbf{F}_{ji} \right) \tag{3.18}$$

where

$\mathbf{F}_{ij}$ is contact force
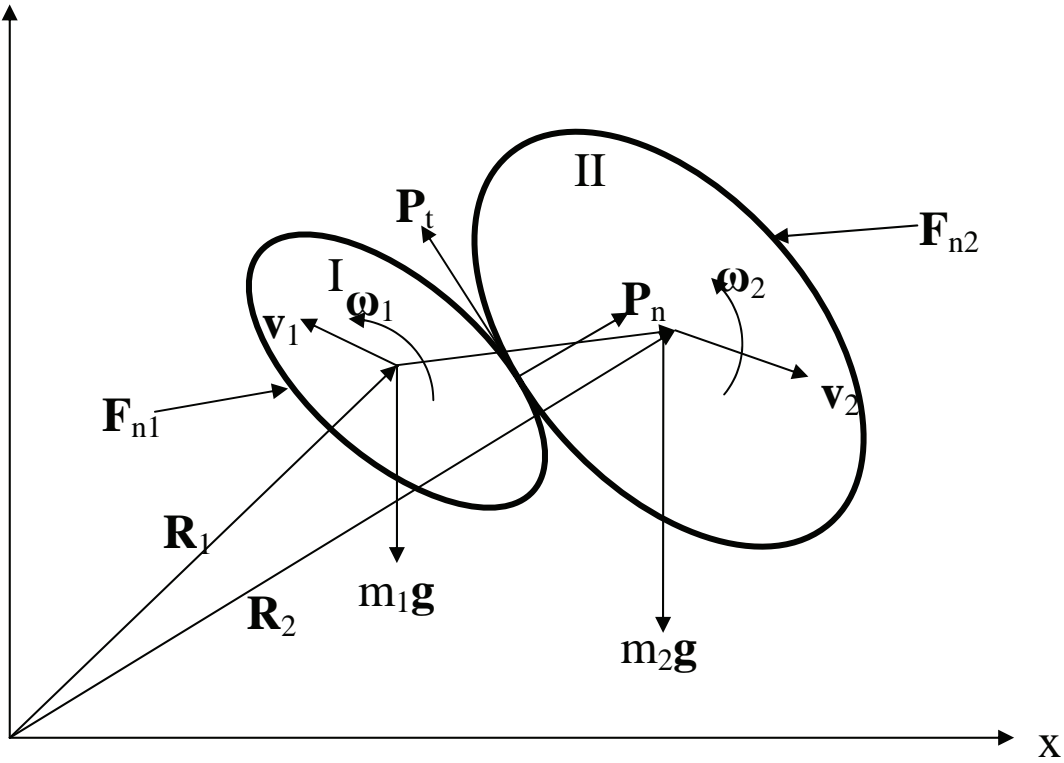
Figure 3.3. Plot.   Blocks in Contact

There are different numerical integration algorithms for solving equation (3.15). The explicit integration algorithm is among the most used schemes in current discrete element analysis. In this project, central different explicit expressions are used for the acceleration at time step interval h for velocity and displacement updates. The velocity update equation is:

$$\mathbf{v}_{n+1/2} = \frac{(M/h - C/2)}{(M/h + C/2)}\mathbf{v}_{n-1/2} + \frac{\mathbf{f}_n - \mathbf{P}}{(M/h + C/2)}$$

(3.19)

and the displacement update equation is:

$$\mathbf{x}_{x+1} = \mathbf{x}_n + h\mathbf{v}_{n+1/2}$$

(3.20)

Where the symbols are the same as in equation (3.15)

The explicit integration algorithm used in DEM analysis is quite simple and straightforward compared to implicit schemes. However, this algorithm is only conditionally stable. The time step must be adequately small to maintain stability conditions.

When the algorithm is used to solve static (or pseudo static) problems, dynamic relaxation procedures (DR) must be performed in order to achieve rapid convergence. To obtain static solutions, one should properly select the damping coefficient C, the time increment step h, and the mass matrix M, to obtain efficient convergence, determining $\mathbf{x}$ such that $\mathbf{P}(\mathbf{x}) = \mathbf{f}$. Several

approaches are available for determining the optimum convergence rate from which the optimum damping parameters will be obtained. These techniques are based on numerical error analysis of calculated value and residual of the solution. One of the approaches is developed by Bardet et al. In this project, a trial and error numerical procedure is developed for fast dynamic relaxation. The procedure is based on the equilibrium principle, when the assembly system is under static state in equilibrium. Numerical tests show that the equilibrium trial and error method is more efficient for static problems such as consolidation of soil, shaft loading tests, and other pseudo static problems.

3.5.3 Contact Mechanics

Since the DEM numerical scheme discretizes the object of interest into individual particles (or blocks) that connect or contact each other through their boundaries, the connecting or contacting forces, and other variables of the particles, must be properly defined to accurately represent physical properties of the object. These variables include the packing form of the particle assembly, particle size distribution, density of the particles, internal configuration of particle mass, and response under different load conditions. The relationship between stress and strain and continuum equivalent of the object may be derived from the study of the force-displacement behavior between the individual particles, by using the averaging method of *the representative volume element* (RVE), as described earlier. The force calculations may vary based on different engineering problems, and may include calculations of normal force, shear force, friction, moment, and torsion of each particle at contact points. Traditionally, the contacts are considered to be elastic, so that the theory of contact of elastic bodies can be invoked to furnish a description the physical phenomena. Elastic models are widely used in DEM because the forces required to crush individual particles are much larger than the forces required to make the whole particle assembly fail, and that deformations of the individual particles are much smaller than that of the whole assembly. A well known non-linear elastic model is the Hertz-Mindlin contact model. The viscoelastic and perfect plastic model are also widely accepted in DEM. Both Hertz-Mindlin and viscoelastic models are described in this section. Note that some plastic incremental models have been proposed in recent years. These models have been very successful to describe contact problems in mechanical engineering. Since these models are stress history dependent and require significant memory to store the history of each contact of the assembly, they are not widely implemented in DEM simulations.

3.5.3.1   Non-Linear Hertz-Mindlin Contact Model

The Hertz-Mindlin model begins by assuming that contacting solids are isotropic and elastic, and that the representative dimensions of the contact area are very small compared to the various radii of curvature of the undeformed bodies. Another assumption of the Hertz-Mindlin model is that the two solids are perfectly smooth. Only the normal pressures that arise during contact are considered (the extensions of Hertz theory for the tangential component of traction will be discussed later). The Hertz-Mindlin contact-force-displacement law is nonlinear elastic, with path dependence and dissipation due to slip, and omits relative roll and torsion between the two spheres. Strictly speaking, the simplified contact force-displacement law is thermodynamically inconsistent (i.e., unphysical), since it permits energy generation at no cost. The law is widely used in engineering because of its simplicity. For the particle assembly, the contact forces and

displacements are infinite, and the approximation satisfies the accuracy of engineering applications.

The normal force-displacement relationship of the Hertz-Mindlin law is:

$$N = \frac{4E_0}{3\sqrt{R_0}} \rho^{3/2} \qquad (3.21)$$

where (as shown in Figure 3.4 and Figure 3.5)

N is normal force

ρ is the relative approach of the sphere (Figure 3.4)

R_0 is the average radius of two contact spheres

$$\frac{1}{R_0} = \frac{1}{R_1} + \frac{1}{R_2} \qquad (3.22)$$

where

R_1 and R_2 are the radii of sphere 1 and sphere 2, respectively

E_0 is the average modulus of the materials of two contact spheres

$$\frac{1}{E_0} = \frac{1-v_1^2}{E_1} + \frac{1-v_2^2}{E_2} \qquad (3.23)$$

where

E_1 and E_2 are Young's modulus

v_1, v_2 are Poisson's ratio of sphere 1 and 2, respectively
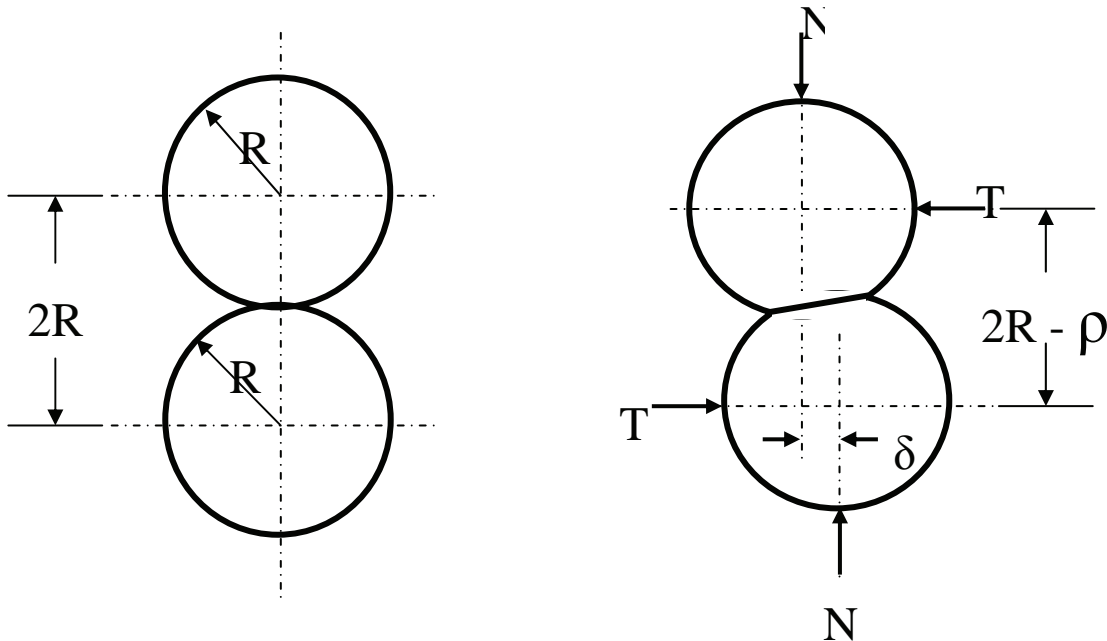
Figure 3.4. Plot. Identical Elastic Rough Spheres in Contact
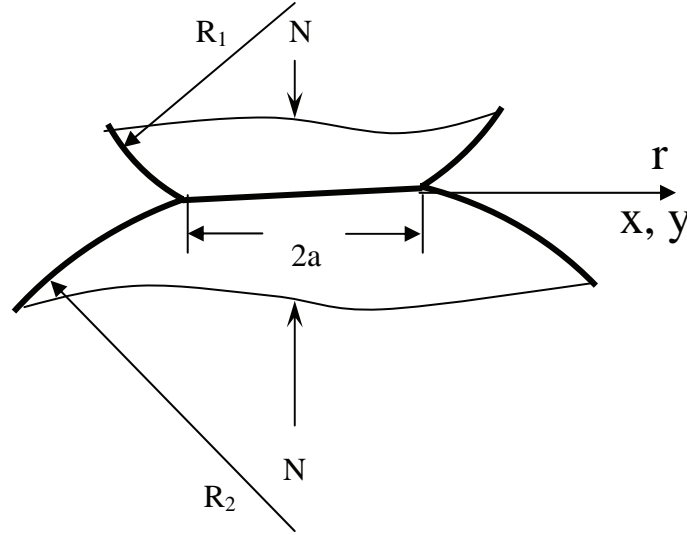
Figure 3.5. Plot. Hertz Contact of Solids of Revolution

Tangential force-displacement is one of the important extensions of the Hertz contact law, which addresses problems involving additional force systems superimposed upon the Hertz normal force. By solving the appropriate boundary-value problem, Cattaneo and Mindlin derived expressions for the tangential component of traction on the contact surface, and the displacement of points on one sphere, remote from the contact, with respect to similarly situated points in the other sphere. Physical experiments show that slip occurs between two contact spheres no matter how small the applied tangential force. When the tangential force is completely removed, the slip does not vanish. A permanent displacement appears. This displacement can be removed only by applying a tangential force in the opposite direction. For this reason, the tangential forces are calculated separately for different cases. Three cases in tangential force-displacement calculations are considered:

- increasing tangential force
- decreasing tangential force
- oscillating tangential force

Case 1. The tangential force-displacement relationship of increasing tangential force with consideration of slip conditions is given by:

$$\delta = \frac{3(2-v)fN}{8Ga}\left[1-\left(1-\frac{T}{fN}\right)^{2/3}\right]$$ (3.24)

where

δ is relative displacement proportional to the tangential applied force
v is Poison's ratio
G is shear modulus of the material
a is contact area of two contact spheres
N is normal force obtained from equation (3.21)
f is coefficient of static friction
T is applied tangential force in contact plane

Case 2. The tangential force-displacement relationship of decreasing tangential force with consideration of slip conditions is given by:

$$\delta_u = \frac{3(2-v)fN}{8Ga}\left[2\left(1-\frac{T_s-T}{2fN}\right)^{2/3} - \left(1-\frac{T_s}{fN}\right)^{2/3} - 1\right] \qquad (3.25)$$

where

δ_u is relative displacement proportional to the unloading tangential applied force

T_s is the tangential force at peak value $0 < T_s < fN$

Case 3 considers oscillating tangential force-displacement relationship. A subsequent increase of T from $-T_s$ to T_s will give rise to identical events as occurring in the course of the reduction of T from T_s to $-T_s$, except for the reversal of sign. The appropriate displacement during this loading process will be $\delta_l = \delta_u(T)$.

3.5.3.2   The Viscoelastic Contact Model

The viscoelastic contact model is the simplest contact model used in DEM simulations. Because of its simplicity, the calculations are very efficient. Usually, the stresses causing the failure of particle assemblies due to the relative friction and slip between the particles are much lower than the stresses required to crush individual particles. The assumption of a linear elastic contact force-displacement relationship between two particles is a good approximation, and is still widely used in engineering. The mechanical model is shown in Figure 3.2.

The normal contact formulation is linear elastic with a viscous damper characterized by two parameters: normal stiffness k_n and viscosity C. The model works for both compression and tension forces based on the relative distance between the two contact points. The normal force is defined by:

$$\mathbf{N} = \begin{cases} \dfrac{1}{2}k_n\varepsilon\cdot\mathbf{n} + C\mathbf{v}_{rn} & \varepsilon \geq 0 \,\|\, \varepsilon \geq -\varepsilon_{max} \\ 0 & \varepsilon < -\varepsilon_{max} \end{cases} \qquad (3.26)$$

where

ε is the penetration distance between two contact points. For two spheres, ε equals the sum of two sphere's radii minus the distance between the two contact sphere centers.

$-\varepsilon_{max}$ is the maximum tension distance two neighboring particles. If negative penetration is larger than this value, the connection between the two neighbors is disconnected, and tension force between these two particles is set to be zero.

$\mathbf{n}$ is the normal unit vector at the contact point

$\mathbf{v}_{rn}$ is the normal relative velocity vector at the contact point

k_n is the normal contact stiffness

C is the viscosity of the material

The tangential force depends on the friction of the material and the relative tangential velocity of the two contact particles. The formula of the tangential force is defined as:

$$\mathbf{T} = \begin{cases} sign(\mathbf{v}_{rs}) \dfrac{1}{2} k_s \varepsilon \cdot \mathbf{s} & \dfrac{1}{2} k_s \cdot \varepsilon < f \mid N \mid \\ sign(\mathbf{v}_{rs}) f \mid \mathbf{N} \mid \mathbf{s} & \dfrac{1}{2} k_s \cdot \varepsilon \geq f \mid N \mid \end{cases} \tag{3.27}$$

where

k_s is the shear contact stiffness

f is the coefficient of static friction

$\mathbf{v}_{rs}$ is the tangential relative velocity vector at the contact point

The direction of the tangential force is the reverse of the tangential relative velocity. The magnitude of tangential force is equal to the maximum static friction force, if it is bigger than the Coulomb friction force, which is the second term of equation (3.27).

The key to successful modeling using DEM is proper selection of the stiffness and damping coefficients. Theoretically, the damping coefficient can be derived from material properties such as the restitution coefficient:

$$C = 2\ln\left(\frac{1}{e}\right)\sqrt{\frac{\dfrac{k_n m_i m_j}{(m_i + m_j)}}{\pi^2 + \left[\ln(1/e)\right]^2}} \tag{3.28}$$

where

m_i and m_j are the masses of particles *i* and *j*, respectively.

e is the restitution coefficient of the material

k_n is the normal contact stiffness

To relate the stiffness to material properties, a number of trial and error numerical tests are performed. The procedures are based on the principle of elastic wave propagation in a medium, which are widely used to determine elastic constants of materials in laboratories. In the numerical tests, the particles are assembled in different packing forms, and elastic stress waves are generated. The wave propagation velocities are measured at different points for different stiffness. The stiffness is checked against the wave velocity obtained from material property manuals and laboratory data. The stiffness is then calibrated correspondingly and saved in a database for future modeling.

3.5.4 Validation of Numerical Models

Before the numerical model is applied to solve engineering problems, it is used to simulate some small scale problems and simple cases for which the results are known or can be easily obtained, for verification. Some constants and parameters must be pre-defined or calibrated based on

material properties and specified conditions. In this project, the validity of the numerical modeling has been checked in three different ways before being used for large scale problems: 1) energy conservation; 2) dynamic relaxation and 3) elastic wave propagation.

3.5.4.1   Energy Conservation

First, an energy method was used to verify dynamic stability of the system. The energy of an individual discrete particle in the system consists of three parts: kinetic energy, potential energy, and gravitational energy. The energy is defined as:

$$e_i = \frac{1}{2} m_i v_i^2 + \frac{1}{2} I_c \omega_i^2 + \frac{1}{2} k (\varepsilon_i / 2)^2 + m_i g z_i \tag{3.29}$$

where

m_i is the mass of the discrete particle

v_i is the translational velocity

ω_i is the angular velocity

I_c is the mass moment of inertia of the discrete particle with respect to the mass center

k is the stiffness of the normal contact (or stretch)

ε_i is the relative approach or stretch distance of two neighboring particles

z_i is the particle altitude relative to the calculation datum

The total energy of the system is the sum of each individual particle:

$$E_{total} = \sum_{i=1}^{n} e_i \tag{3.30}$$

Figure 3.6 shows a stack of spherical elements used for the energy tests. The bottom element is not allowed to move. The remaining elements are stacked with no initial contact forces.

Figure 3.6. Plot. Stack Balls Setup for Energy and Dynamic Relaxation Numerical Tests

If there are no interactions which cause mechanical energy loss, such as damping, friction, etc., and no energy is added to the system, the total energy of the system should be conserved. For the energy test, the stack is assumed to be perfectly elastic. Under the only gravitational force, when the stack is released from the initial position, the elements will push into each other and continue to oscillate up and down forever, conserving total energy. For the stack, the diameters

of all elements are equal to 1 m. The specific weight of the material is 3000 kg/m^3, the mass of each ball is 1.5708 kg and the gravitational acceleration is 9.81 m/s^2. The coordinate of the center of the bottom ball is set at (0, 0, 0). The total energy of the stack at the beginning of the test is only gravitational energy, which equals 554.74 N-m. Figure 3.7 shows, as expected, the total energy of the stack is constant, with some fluctuations due to the numerical approximation.
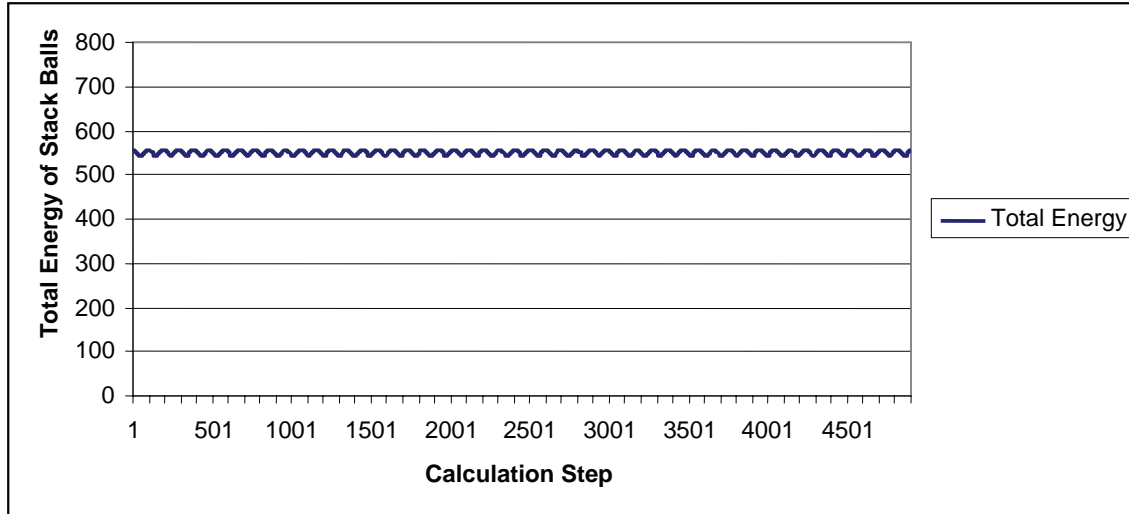

Figure 3.7. Chart. Total Energy of Stack Ball

3.5.4.2   Damping and Dynamic Relaxation (DR) Tests

Damping and dynamic relaxation (DR) are major parameters and procedures in DEM modeling for two reasons. First, the materials in this project are not elastic (i.e. concrete and soil). Stress wave propagating in the materials are attenuated with distance. Second, since DEM is originally designed to solve dynamic problems with explicit integration for static (or pseudo static) problems, dynamic relaxation procedures (DR) must be performed in order to achieve convergence. An excessively small damping coefficient leads to spurious vibrations during the dynamic transition between two static states. This causes changes in the grain arrangement, since frictional material is very sensitive to vibrations. If the damping coefficient is too large, the results will simulate viscous flow, a phenomenon which is more related to Stokes flow of immersed bodies.

The same stack setup for the energy conservation test is used for the damping and DR tests. The diameters of the balls, specific weight, and coordinates are the same as used in the energy test. The validity of static convergence is verified by checking the displacement of the top ball on the stack under gravitation force alone. Three cases were performed for the numerical tests:
▪   The stack was released from the initial position without damping (restitute coefficient is zero). This test is equivalent to the elastic energy test, except that the displacement of the top is recorded.
▪   The same test as above with a restitution coefficient of 0.2 (damping and restitution are related by equation 5.27).

▪   The adaptive numerical equilibrium DR test. This algorithm is a numerical trial and error approach developed for fast convergence and stable solution. The method is based on the equilibrium principle when the assembly system is under static state at equilibrium.
As shown in Figure 3.8, the top element on the stack oscillates around its balance position when the system is released from its initial position without damping. When the normal DR procedure is performed with damping, the vibration attenuates, and the top element position approaches a static position at 7.86 after one thousand iterations. Adaptive equilibrium DR shows that the top ball approaches the same static position faster. The adaptive equilibrium DR has a dramatic advantage in computational efficiency when the system consists of a large number of particles (i.e. thousands or millions particles).
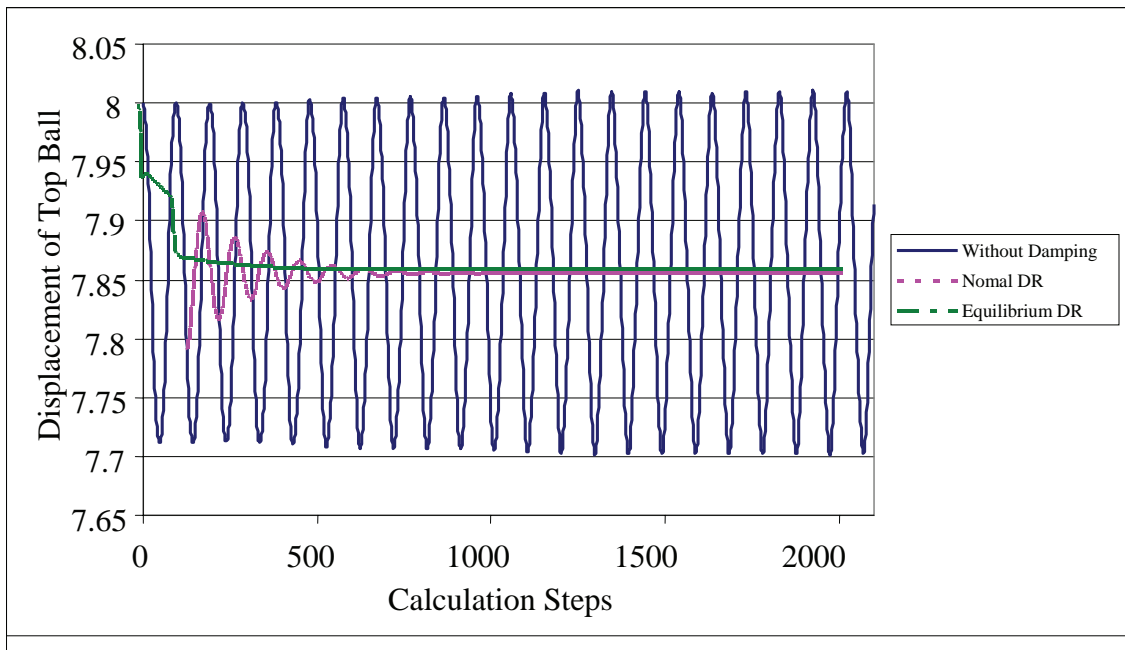
Figure 3.8. Chart. Dynamic Relaxation Test Results

3.5.4.3   Wave Propagation

To validate the wave propagation behavior of the model, the impulse response of a non-linear 1D oscillating system is obtained. The system is similar to the stack as described before, but with more elements, different material properties, and zero gravitational body forces. The system consists of one hundred identical balls with individual mass m connected with nonlinear springs of stiffness k and dashpot c. The model is simple, but useful for analyzing a wide range of dynamic systems, such as ionic polarization at the molecular level, the response of experimental devices such as isolation tables and resonant instruments, the vibration of a foundation, and the seismic response of buildings.

For 1D problems, equation (3.15) can be written as:

$$m \, \ddot{y}_n + c_i \, \dot{y}_n + k_i \, y_n = x_n \tag{3.30}$$

where

x is the time history of the input force. In this numerical test, x is an impulse force.
y is the time history of the displacement response. Dots on y denote first and second derivatives.

The specific weight of the material is 3000 kg/m^3, the mass of each ball is 1.5708 kg, the gravitational acceleration is 0.0 m/s^2, and the restitution coefficient is 0.3 (related to the damping coefficient by equation 5.28).

A vertical impulse force is applied on the top ball at its center, and the bottom ball is not allowed to move. The impulse P-wave propagates down the stack, and the wave reflects when it reaches the bottom element. The acceleration of each ball is recorded in Figure 3.9. A hundred signals are plotted as time vs. receiver distance from the source. This figure clearly shows that the first arrival delay and attenuation with distance. The first arrival is sharp, with higher frequency, for the receivers closer to the source, and flattens with distance. The plot also shows the reflection from the bottom.
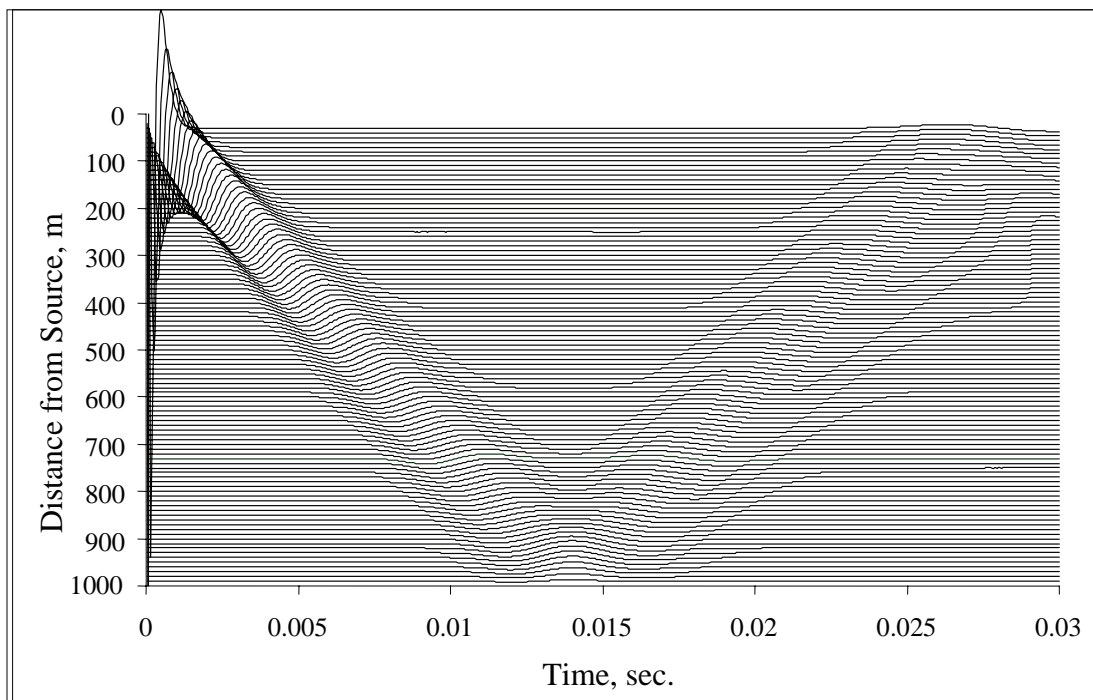
Figure 3.9. Plot. 1-D P-Wave Propagation in a Rod

The test shows that the model is able to successfully propagate waves in different materials with various boundary and initial conditions. The model provides a fundamental and powerful tool for a wide range of geotechnical and civil engineering applications, such as refraction, reflection, reverse time, tomography, and other inverse problems. With the implementation of non-

reflection boundary conditions, the model is also able to simulate wave propagation in semi-infinite or infinite media.

CHAPTER 4.   NUMERICAL MODELING ANALYSIS OF CSL IN DRILLED SHAFTS

Many factors influence the sonic wave velocity and energy in a drilled shaft, such as structural defects, tube bending, tube debonding, and sensor orientation. In this chapter, numerical modeling analysis will be used to evaluate major factors resulting in CSL velocity and energy variations.

4.1   Geostructural Analysis Package (GAP) Model Description

The numerical modeling studies performed in the remainder of this study use the Geostructural Analysis Package (GAP). This method combines well-developed techniques from Discrete Element Method (DEM), Particle Flow Code (PFC), Material Point Method (MPM), and Finite Difference (FD) methods, resulting in efficient simulation of high-resolution dynamic modeling applications. Figure 4.1 shows the material color palettes used in the GAP models. These palettes are used to display various properties, such as velocity, wave compression, average stress, temperature, heat generation, hydration phase, tension strength, modulus, damping, etc. Defects, such as honeycombs, cracking, and debonding, are shown in a graduated red palette. Darker colors on the left represent lower property values. The ranges for each property used in subsequent models, corresponding to material color palettes, are shown in Table 4.1.

The right of Figure 4.1 shows the drilled shaft used in subsequent numerical models. A 1 m reinforced shaft (4.5 m long) is in the center, surrounded by dry sand in the top meter, wet sand in the next meter, two meters of clay, and one meter of rock at the base. The shaft is socketed one half meter in the rock. Portions of the model are hidden for internal viewing. Half of the wet sand and clay are hidden to show the location of the shaft. The concrete in the shaft is hidden from a depth of 1 to 2.5 m, to show the internal rebar, access tubes, and support cage.
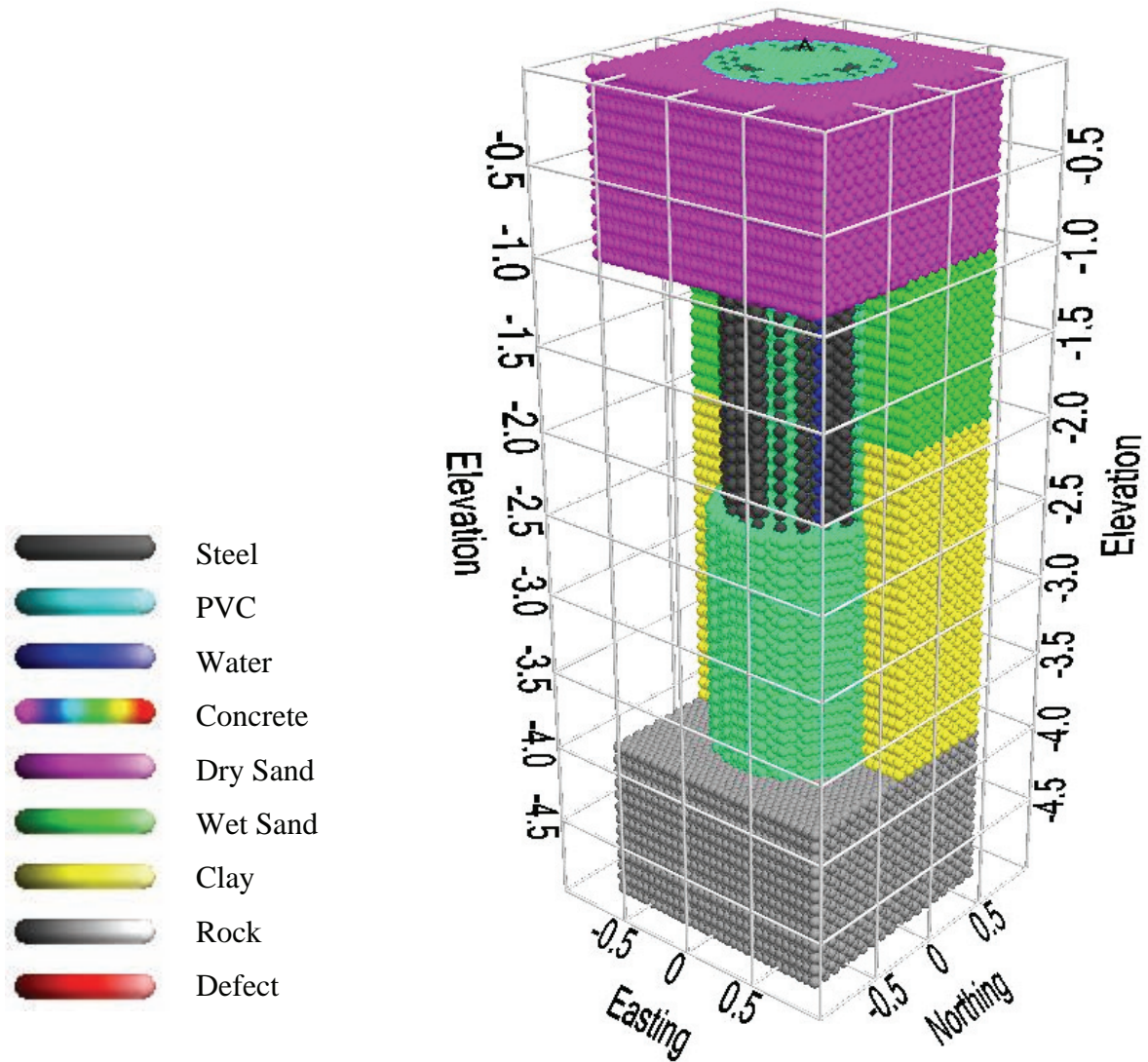
Figure 4.1. Plot. Material Palettes used in GAP Models. Defects Shown in Red Include Honeycombs, Cracking, and Debonding. Darker Colors on the Left Represent Lower Values. These Palettes are used to Display Corresponding Velocity, Wave Compression, Average Stress, Temperature, Heat Generation, Hydration Phase, Tension Strength, Modulus, etc. A Cross-section of the 1 m Drilled Shaft used in the Study is Shown on the Right. The Shaft is in the Center, Surrounded by Dry Sand, Wet Sand, Clay, and Rock. Portions of the Wet Sand, Clay, and Concrete are Hidden to Show the Internals of the Model.

Table 4.1 Property Ranges Corresponding to Material Color Palettes

Property	Minimum	Maximum
Cracking	-25%	25%
Change in Cracking	-25%	25%
Compression Stress Loading (N)	-0.001	0.001
Change in Compression Stress Loading (N)	-0.001	0.001
Temperature (°C)	10	50
Change in Temperature (°C)	-10	10
Hydration	0%	100%
Change in Hydration	-15%	15%
Curing Compression (N)	-1.0×10^{-4}	1.0×10^{-4}
Change in Curing Compression (N)	-1.00×10^{-4}	1.0×10^{-4}
Heat (Cal)	0	0.001
Change in heat (Cal)	-0.001	0.001
Seismic Compression (N)	-1.0×10^{-10}	1.0×10^{-10}
Change in Seismic Compression (N)	-1.0×10^{-10}	1.0×10^{-10}

Table 4.2 Material Properties used in Models

Material	Tension Strength N/m^2	Specific Gravity	Pwave Velocity (m/s)	Coefficient of Restitution	Percent Cracked	Percent Void	Void Material	Thermal Conductivity
Steel	10000	7.85	8000	0.9	0	0		0.99
PVC	50	1.5	1000	0.9	0	0		0.5
Water	1	1	1500	0.9	0	0		0.25
Concrete	150	4	4000	0.3	0	0		0.5
Dry Sand	1	2	400	0.1	90	2		0.6
Wet Sand	50	2.5	600	0.2	30	2	Water	0.7
Clay	100	3	2000	0.2	5	0		0.8
Rock	5000	4	7000	0.4	0	0		0.4
Honeycomb	50	2	3200	0.2	10	20		0.8
Debonding	0	2	10	0.2	90	90		0.8
Cracking	50	4	4000	0.3	90	0		0.5
Void	0	0	0	0	0	100		0

Figure 4.2 shows the location of a sample 2-D slice in the drilled shaft model. Slices may be extracted at different depths depending on surrounding ground conditions, but Figure 4.2 applies to most of the 2-D models throughout this study. The resolution of the 2-D models is 1 cm, meaning that each spherical model element is 1 cm in diameter.

The three access tubes are numbered clockwise, starting from the tube at the top. Access tube #1 is at the top (north), tube #2 is in the lower right (south east), and tube #3 is in the lower left (south west). The access tube material is steel, except for the 3-D model comparing PVC with steel. The tubes are filled with water. The inside tube diameter is 50 mm. The access tubes are 320 mm from the center of the shaft.

The steel rebar cage is represented by 20 rebar distributed around the perimeter, each 50 mm in diameter. The cage diameter is 0.8 m. The rebar is 10 cm in diameter, distributed in three pairs inside the rebar cage. Steel is used for the rebar.

Figure 4.3 shows the location of a sample 3-D section in the drilled shaft model. The resolution of the 3-D CSL models in this chapter, for tube material and tube debonding, is 20 mm. Top portions of the 3-D models are hidden for display purposes. Compression waves are shown in the hidden portions for positive compression values, to show wave propagation in 3-D.

4.2   Factors Affecting CSL Velocity Measurements

Typically, the wave velocity of concrete in a drilled shaft is estimated from the first arrival time obtained during CSL measurements, using the separation distance between the source and receiver tubes at the top of the shaft, assuming the tubes remain vertical throughout the shaft. The first arrival time may correspond to the point at which the signal amplitude first fluctuates, or at the first peak or trough identifiable in the waveform. Uncertainties in source and receiver locations and variations in the definition of the first arrival must be taken into account when interpreting CSL data. Very small changes in source/receiver separation distance and the selection of the first arrival time, called the arrival pick, can result in large velocity variations. Without proper tube bending measurements, sensor alignment, or proper waveform analysis for first arrival determination, CSL data should be used as a relative guide rather than an absolute value.

Tube locations below the top of the shaft are unknown and are typically assumed parallel. The tube distances at the top of the shaft are occasionally adjusted during the CSL data analysis to obtain a tube separation resulting in more "reasonable" velocities. Tube bending near the top of the shaft is common and often used to justify the practice of adjusting arrival picks in this fashion. This practice can introduce apparent velocity variations in good concrete, or remove velocity variations in defective concrete.
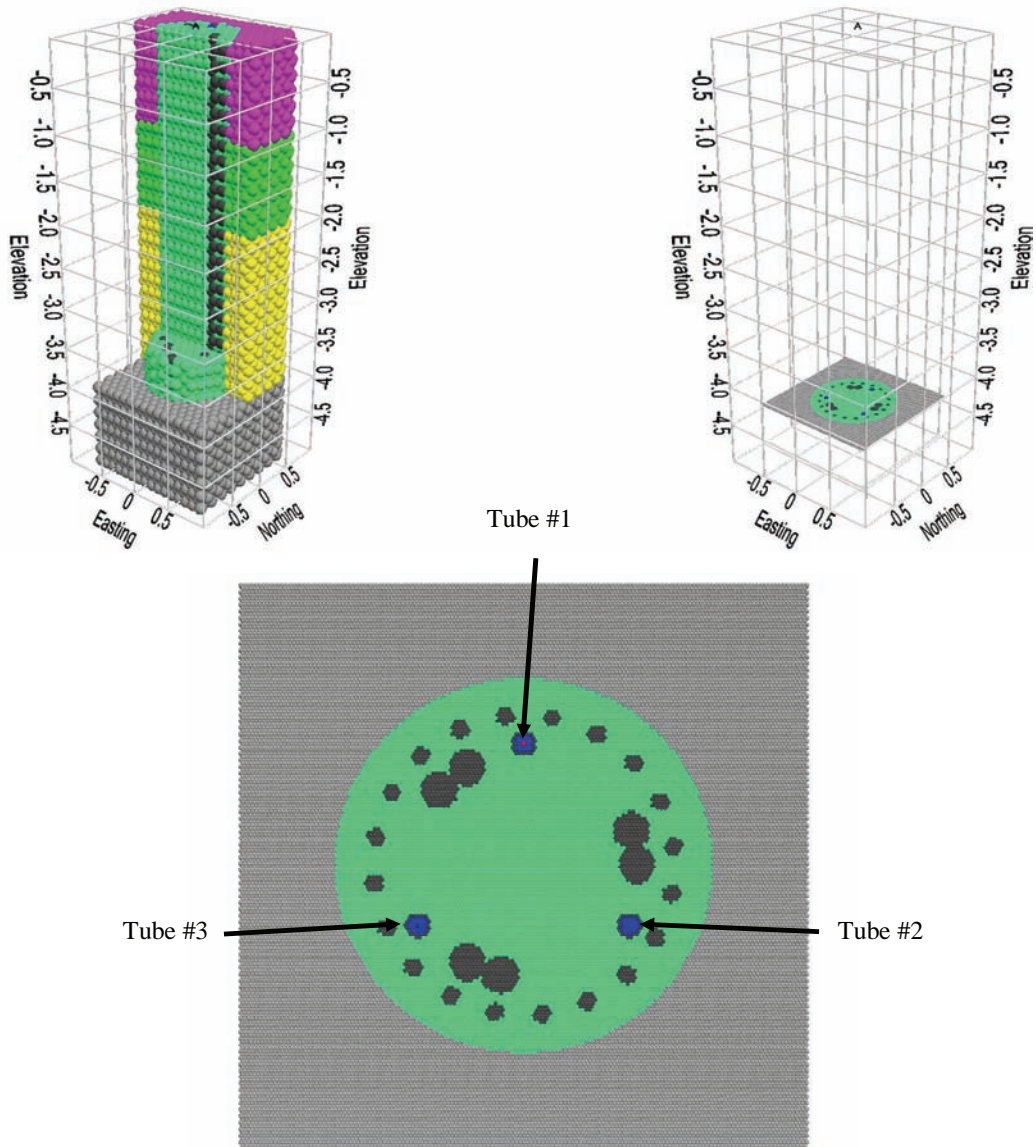
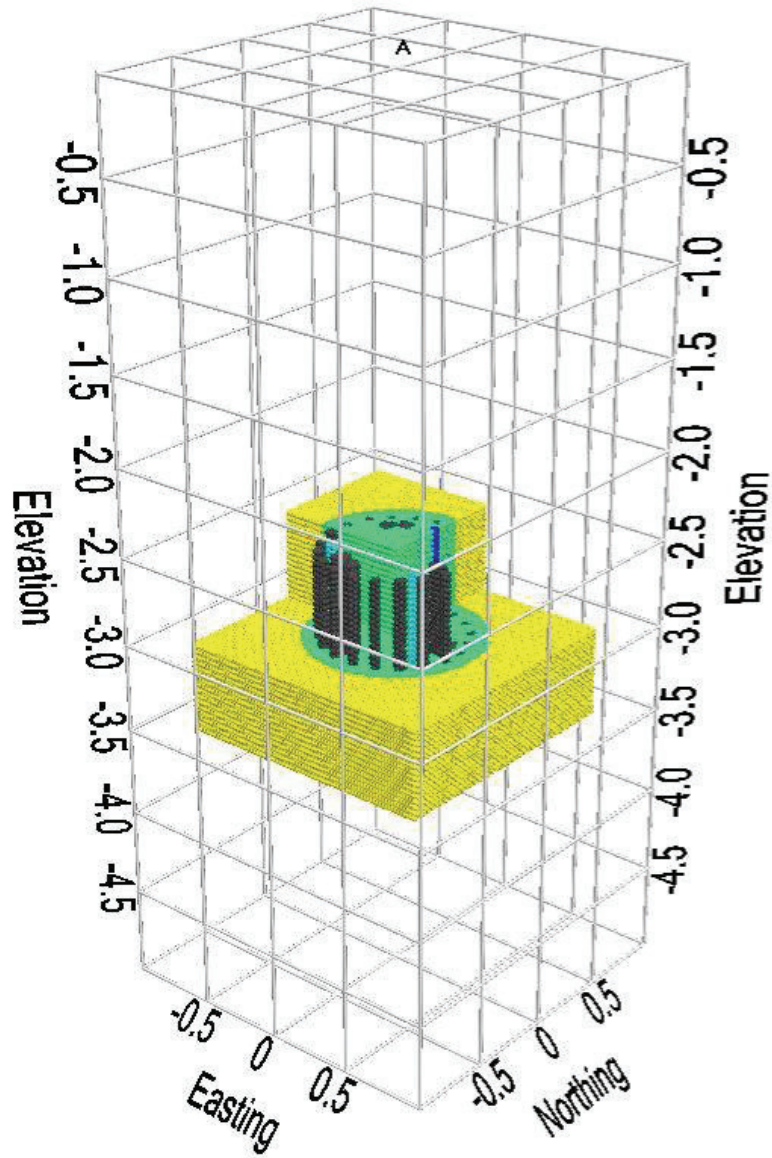**Figure 4.2. Plot. Location of Drilled Shaft Cross-section Surrounded by Rock**

Figure 4.3. Plot. Location of 3D Section within Drilled Shaft

Plots of the signal energy versus depth are often generated in CSL surveys, in addition to plots of first arrival picks. The definition of signal energy often varies from system to system. The signal energy may be determined by summing up the absolute values of a set number of signal samples after the first arrival time, or may be measured from the first major peak after the first arrival, or from the maximum signal amplitude. The energy and velocity plots versus depth are generally used together to indicate regions of compromised concrete quality. Some CSL data collection systems do not attempt to analyze the signal data, but simply plot the waveforms with depth for visual inspection.

CSL velocity variations may indicate zones of lower quality concrete, voids, and honeycombs in a drilled shaft. Actual defects are difficult to detect using CSL data in its present form, because CSL measurements must be assumed accurate and absolute, not approximate, relative, and massaged. When good CSL data is available and reconstructed variations can be trusted as defects, the influence of a defect on foundation performance should be carefully examined. A drilled shaft should not be rejected simply because certain zones suggest a lower concrete quality. Design loads and the load bearing assessment should be taken into consideration relative to the anomaly location within the drilled shaft. For example, an anomaly near the base of a friction shaft may not significantly affect the load carrying capacity. The same anomaly in an end-bearing shaft in very loose soil may be of greater concern, depending on how the loads are applied to the shaft and transferred to the surrounding soil. An end bearing shaft experiences friction with the surrounding ground, as does a friction shaft. Actual loading conditions and load distribution should be evaluated to determine the effect of anomalies on overall shaft performance for defect definition.

CSL is not restricted by shaft length and can detect multiple anomalies within a drilled shaft, with accurate data collection. Combined with tomography and the option to create more signals on angled or offset paths, the size and location of defects can be better estimated. However, CSL is relatively expensive and requires pre-installation of access tubes. Debonding between tubes and concrete can seriously affect the results, corrupting measurements of entire sections of the shaft. Variations in hydration rates during concrete curing can also create anomalies in first arrival times and signal energies, falsely indicating lower quality concrete.

If only first arrival times or signal energy levels are used, no information outside the rebar cage can be obtained from CSL tests. Placing the access tubes outside the reinforcing cage significantly reduces the quality of data and complicates interpretation. Signals attenuate due to thermal cracking and debonding of the concrete in regions adjacent to the rebar cage. In friction shafts, concrete integrity outside the steel-reinforcement cage is more critical to assess than the core of the shaft. This is a serious limitation of the CSL test.

4.3   CSL Velocity Variations

Actual variations in sonic velocity within concrete structures such as drilled shafts originate from two sources, "structural" and "chemical". This division breaks down naturally from the basic nature of concrete structures. Fundamentally concrete structures can be conceptualized as a form of artificial stone, formed from constituent components as a result of a clearly defined chemical process - the hydration of the cement. Water chemically reacts with the cement in the hydration

process. The cement paste does not dry out, and water does not escape into surrounding porous materials or evaporate into the air, as is commonly thought. Defects resulting in a substantial reduction in the strength of concrete structures from its designed capacity may have two origins. Structural defects can be the result of a physical deviation in the process of forming the concrete structure, since structural design assumes a uniform mass of well mixed concrete. Defects may also occur when the concrete mixture is placed in the desired form as intended. These defects come from inherent weakness and variability in the process of the concrete curing itself. From the time concrete is placed to the time it is fully set, many dynamic processes take place. Variations in chemical reactions that form the concrete can result in decreased design strength. A defect in the concrete that decrease the performance of the shaft can be classified as a structural defect.

4.4   Effect of Surrounding Material on CSL Signals

Figures 4.4 – 4.9 compare CSL signals from a drilled shaft surrounded by rock with signals from a shaft surrounded by clay. The full waveforms are shown for each model for comparison, since precise definitions of arrival times and energies are not standardized and difficult at times to quantify. The waveforms for the rock/clay model are shown in Figure 4.9.

Figure 4.4 shows the compression wave propagating from the top access tube (Tube #1) after 20 μs. The surrounding rock is displayed on the left with a gray palette, and the shaft in soil is on the right with a yellow palette. The difference is shown at the bottom, but there is no difference between the compression waves at this stage.

The cross-section shows three water-filled steel access tubes with an impulse source located in the top tube (Tube #1), and receivers located in the center of the two lower tubes (Tubes #2 and #3).

Figure 4.5 shows the compression wave at 60 μs, as the wave first interacts with the surrounding ground. The difference plot shows the reflection, with the same polarity as the source signal. The rock has a higher stiffness than the clay, resulting in a reflection with the same polarity.

The compression wave continues to propagate to the edge of the shaft and encounters the surrounding soil. A portion of the wave propagates into the soil, while another portion reflects back into the concrete shaft. The concrete has a higher stiffness and density than the clay, resulting in a reverse-polarity reflection. However, the rock has higher stiffness than concrete, so results in a reflection with the same polarity.
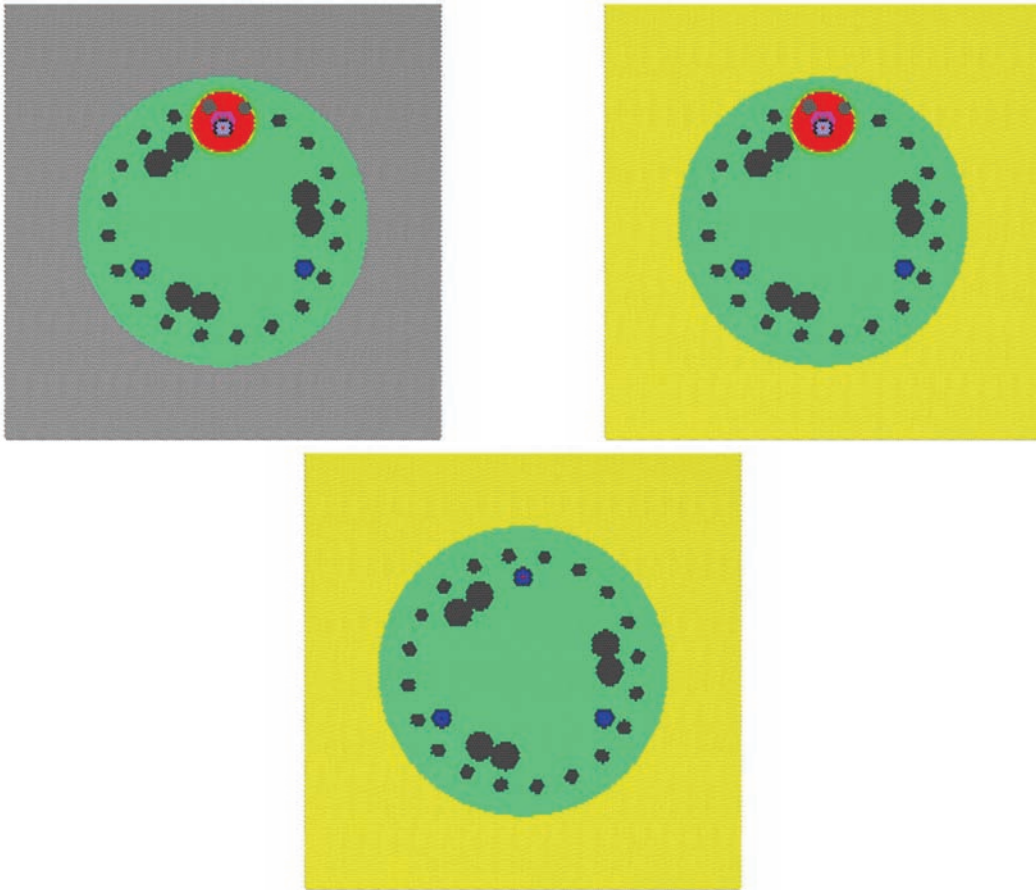
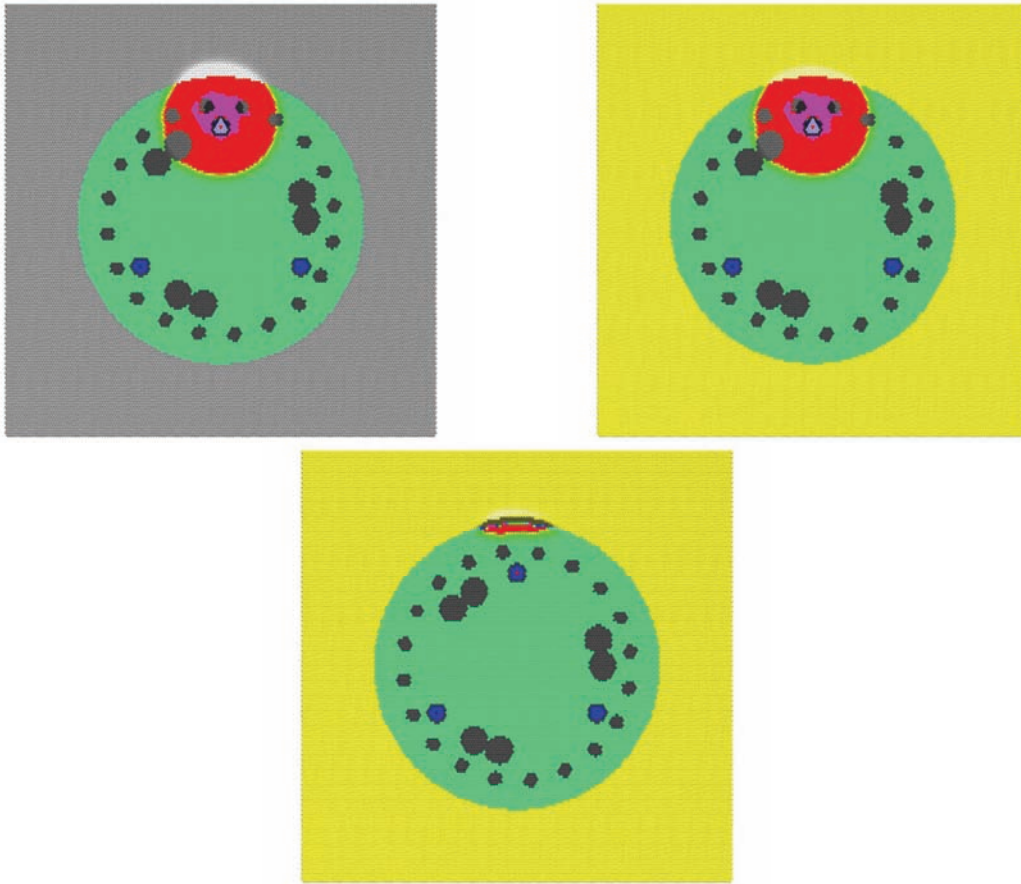**Figure 4.4. Plot. Rock (Top Left) vs. Clay (Top Right) at 20 μs, with Difference (Bottom)**

Figure 4.5. Plot. Rock (Top Left) vs. Clay (Top Right) at 60 μs, with Difference (Bottom)

Figure 4.6 shows the compression wave at 120 µs, as the first tension wave interacts with the surrounding ground. The compression wave travels faster through the rock than through the clay, because of the higher stiffness of the rock. The difference plot shows the reflection bending around the perimeter of the shaft, corresponding to the interaction of the wavefront with the surrounding ground.
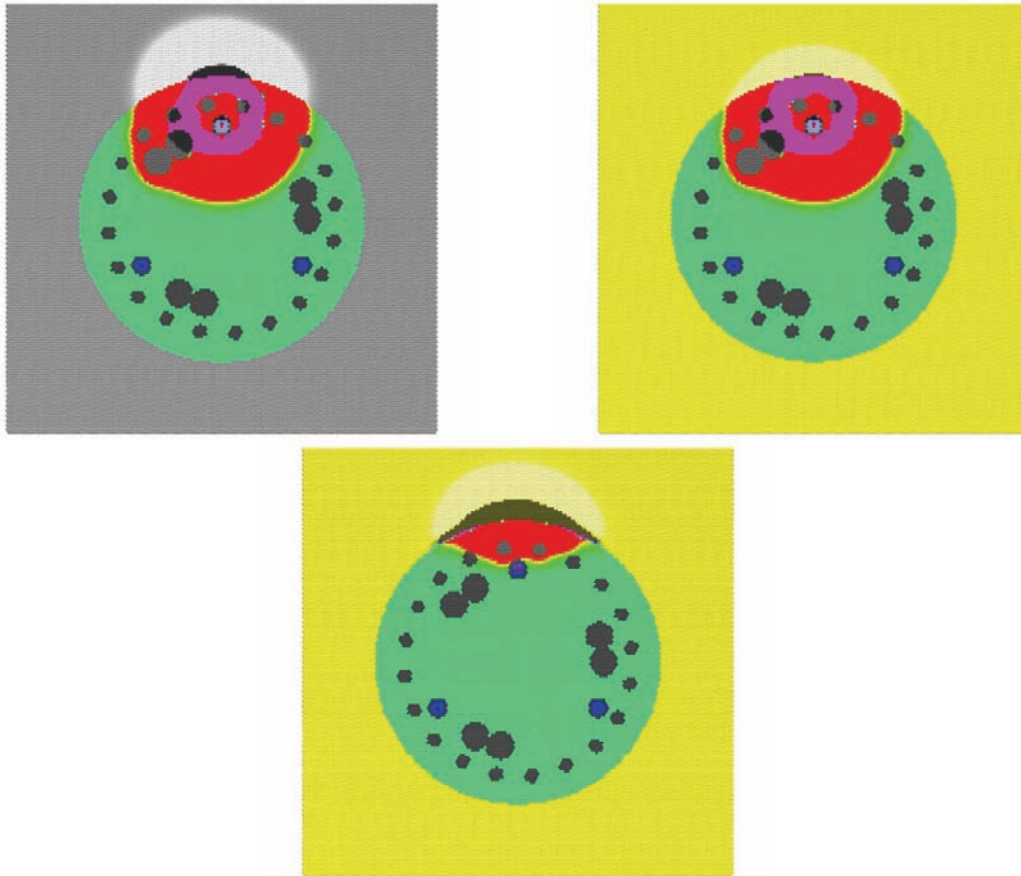

Figure 4.6. Plot. Rock (Top Left) vs. Clay (Top Right) at 120 µs, with Difference (Bottom)

Figure 4.7 shows the compression wave at 300 μs, as the first compression wave reaches the access tubes. The arrival is identical for both access tubes. The difference plot shows the reflection lagging far behind, contributing no effect on the initial waveform.

The sensors in the access tubes measure the compression waves in the water, which may not necessarily correspond to the compression waves in the concrete. Compression in the water is indicated using a gradient blue palette, with lighter blue for positive compression, blue for neutral compression, and dark blue for negative compression, or tension.

The compression wave propagates through the drilled shaft, followed by a tension wave. The wavefront is circular when traveling through a homogenous medium.
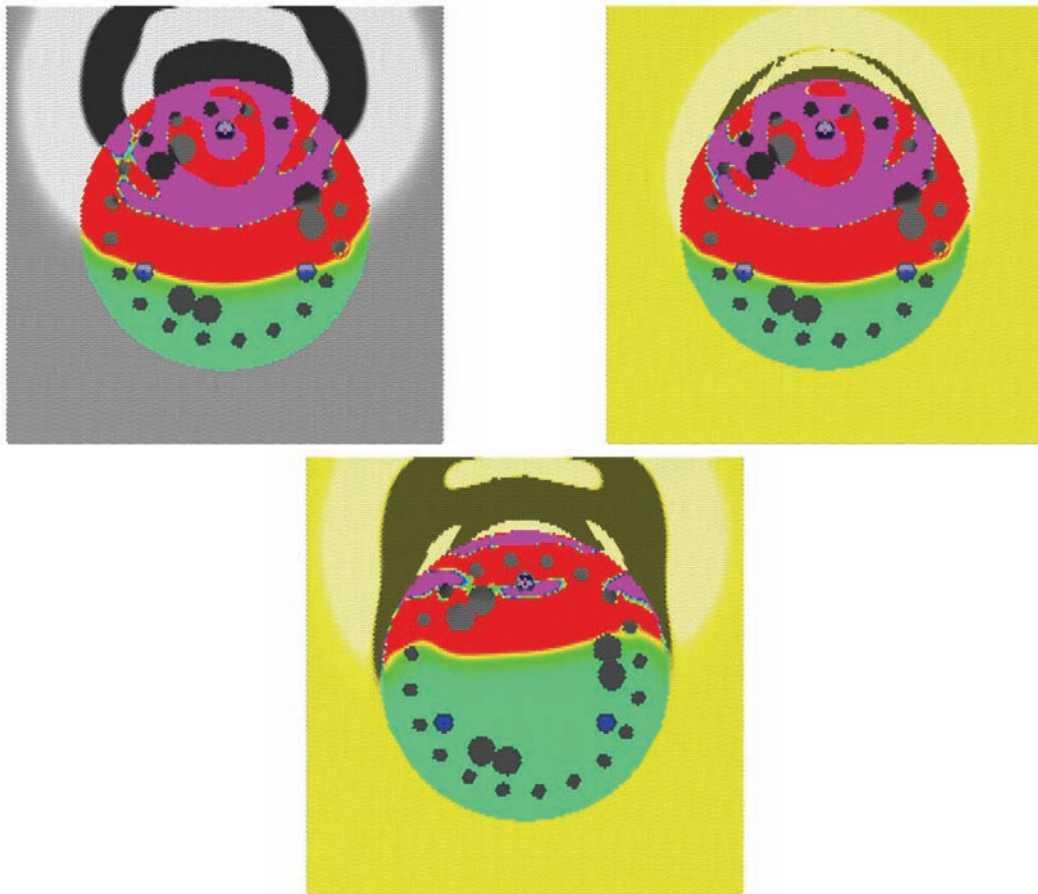

Figure 4.7. Plot. Rock (Top Left) vs. Clay (Top Right) at 300 μs, with Difference (Bottom)

Figure 4.8 shows the compression wave at 500 μs, as the first tension wave reaches the access tubes. This also happens to correspond to the instant when the concrete/ground reflection first reaches the access tubes. The tension wave in the water is lagging behind the tension wave in the concrete.

The compression wave patterns in the access tubes should be noted. The compression wave in the receiver access tube exhibits a slightly delayed arrival due to the lower compression wave velocity of water. As the compression wave first contacts the tube, the wave travels quickly around the tube due to the higher compression wave velocity of steel. However, the water in the tube has a significantly lower compression wave velocity, resulting in a slight delay in arrival time measurements.

The compression waves in the source tube do not necessarily correspond to the compression waves propagating through the concrete due to multiple reflections among the water, steel tube, and concrete interfaces.
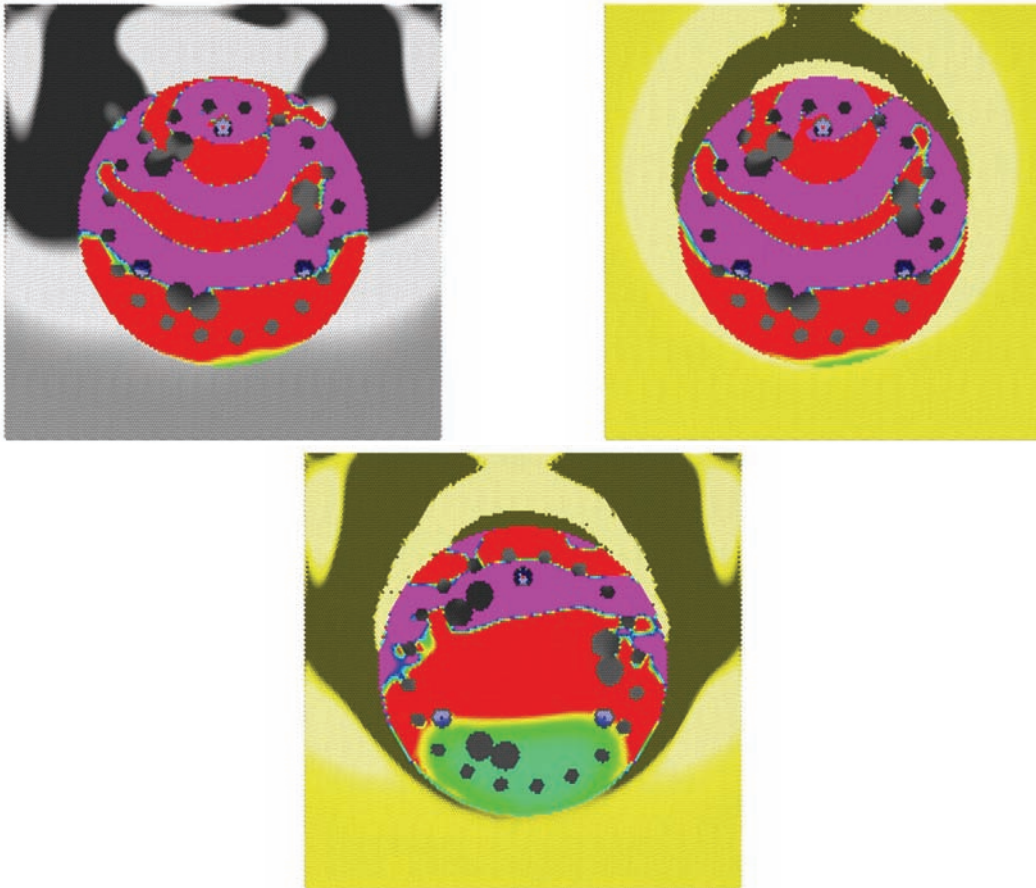

Figure 4.8. Plot. Rock (Top Left) vs. Clay (Top Right) at 500 μs, with Difference (Bottom)

Figure 4.9 compares the waveforms collected in the access tubes. The waveform in the top graph refers to the signal collected in the shaft surrounded by rock and clay, with the source in access tube #1, and the receiver in tube #2. The x-axis is plotted in milliseconds, and the y-axis is average compression force, in nano-Newtons. The difference between the rock and clay surrounded shafts is also shown in the plot. Similarly, the waveforms collected in access tube #3 are shown in the lower graph.

Since the rock has only a slightly higher density and stiffness than concrete, the reflected compression arrival has slightly higher amplitude than the soil reflection. This study is primarily concerned with the first arrival, as velocity determination using CSL uses only first arrival information. This example indicates that important information about the shaft outside of the reinforcement cage and the environment surrounding the shaft is contained in the full waveform, and can be extracted using model inversion techniques.

The surrounding environment can have a large effect on first arrivals during the curing phase. Since initial CSL measurements are acquired during and shortly after the second hydration phases of concrete curing, this is an important factor to take into consideration. The effects of the surrounding environment on concrete temperature and CSL velocity are presented later in this study.
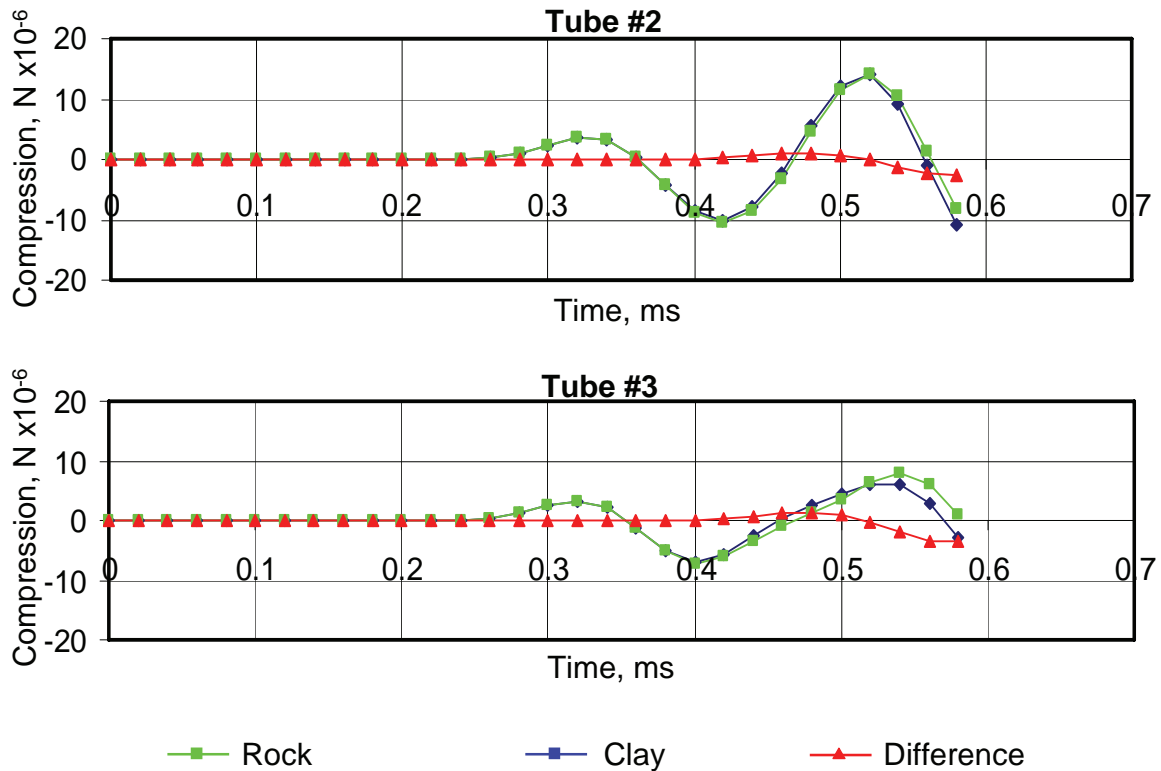

Figure 4.9. Chart. CSL Signals from Rock vs. Clay, between Access Tubes 1 and 2 (Top), and Tubes 1 and 3 (Bottom)

4.5   CSL Wave Interaction with Rebar

Figures 4.10 – 4.15 compare CSL signals from a drilled shaft with no rebar with signals from a typical shaft with rebar. The purpose is in part to test the claim that rebar scatters and disrupts the signal, requiring access tubes be located inside the rebar cage.

Figure 4.10 shows the compression wave propagating from the top access tube after 20 µs. The concrete has lower density and stiffness than the rebar, resulting in the reverse-polarity difference shown in the difference plot. The actual reflection is the same polarity, but is shown reversed because of the order of the difference.
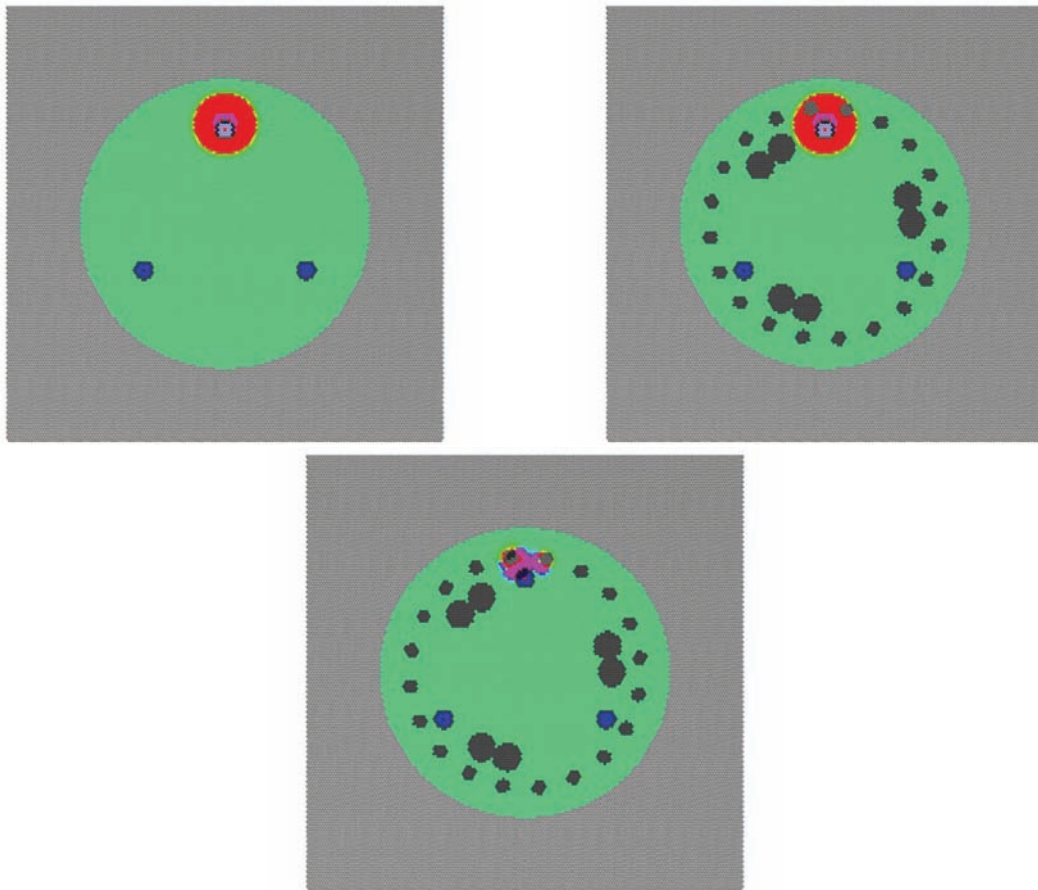

Figure 4.10. Plot. No Rebar (Top Left) vs. Rebar (Top Right) at 20 µs, with Difference (Bottom)

Figure 4.11 shows the compression wave at 60 µs, as the wave first interacts with the surrounding ground. The rebar slightly deforms the wavefront, but the scattering does not destroy the compression wave entirely. The difference plot highlights the effects of the rebar.
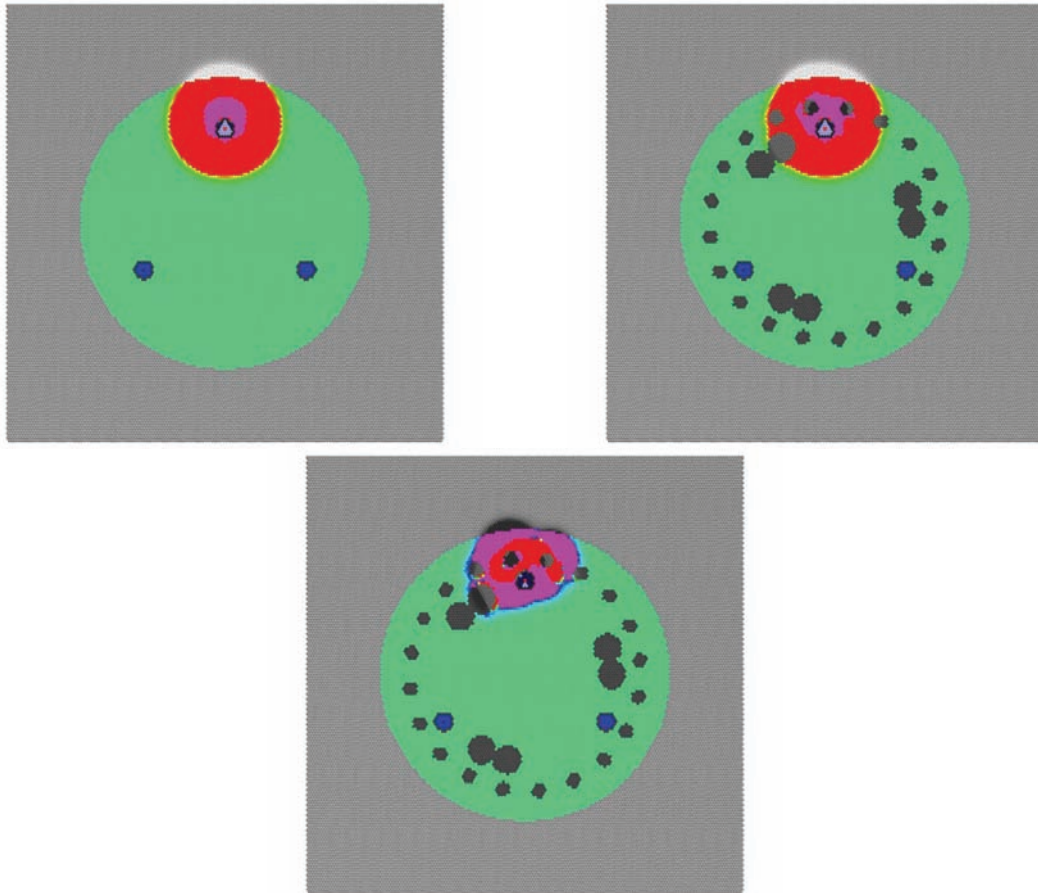

Figure 4.11. Plot. No Rebar (Top Left) vs. Rebar (Top Right) at 20 µs, with Difference (Bottom)

Figure 4.12 shows the compression wave at 120 μs, as the first tension wave interacts with the surrounding ground. The top plots show that the signal propagating into the rock is not noticeably affected after passing through the rebar.
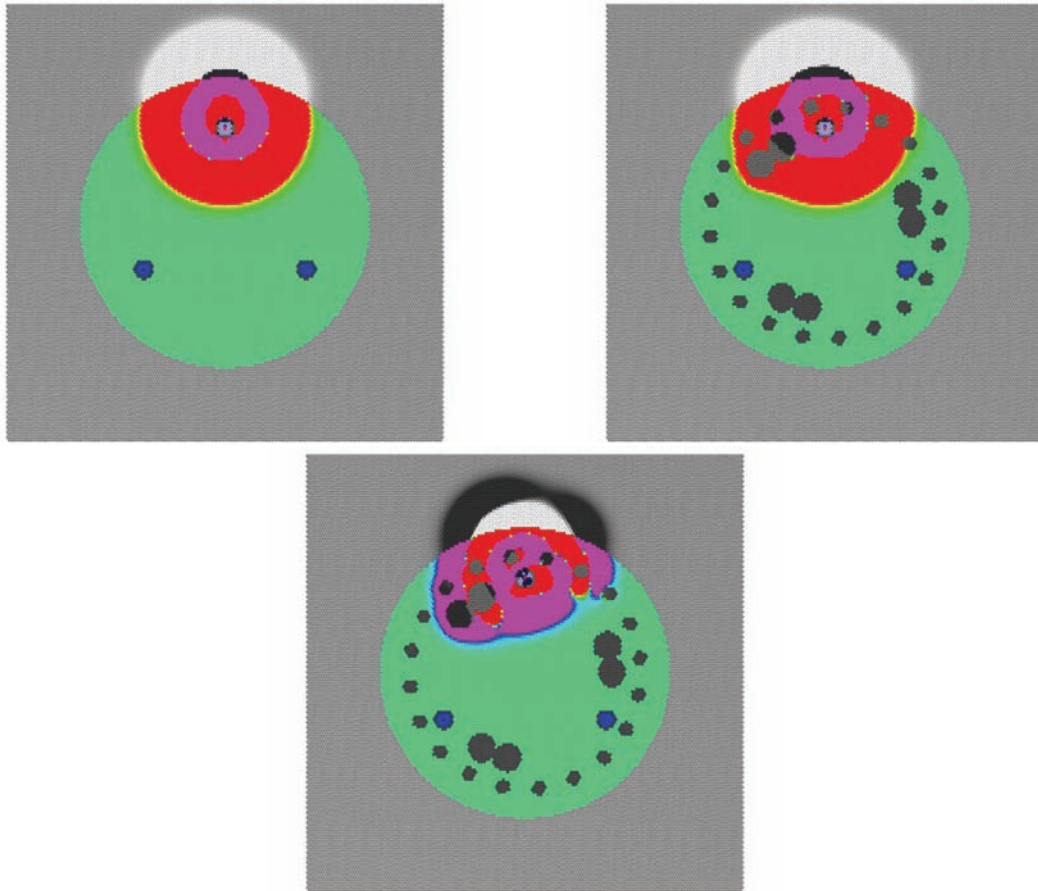

Figure 4.12. Plot. No Rebar (Top Left) vs. Rebar (Top Right) at 120 μs, with Difference (Bottom)

Figure 4.13 shows the compression wave at 300 μs, as the first compression wave reaches the access tubes. The arrival is practically identical for both access tubes. The difference plot shows the rebar does have a slight effect on the amplitude of the arrival, and will affect the rest of the waveform.
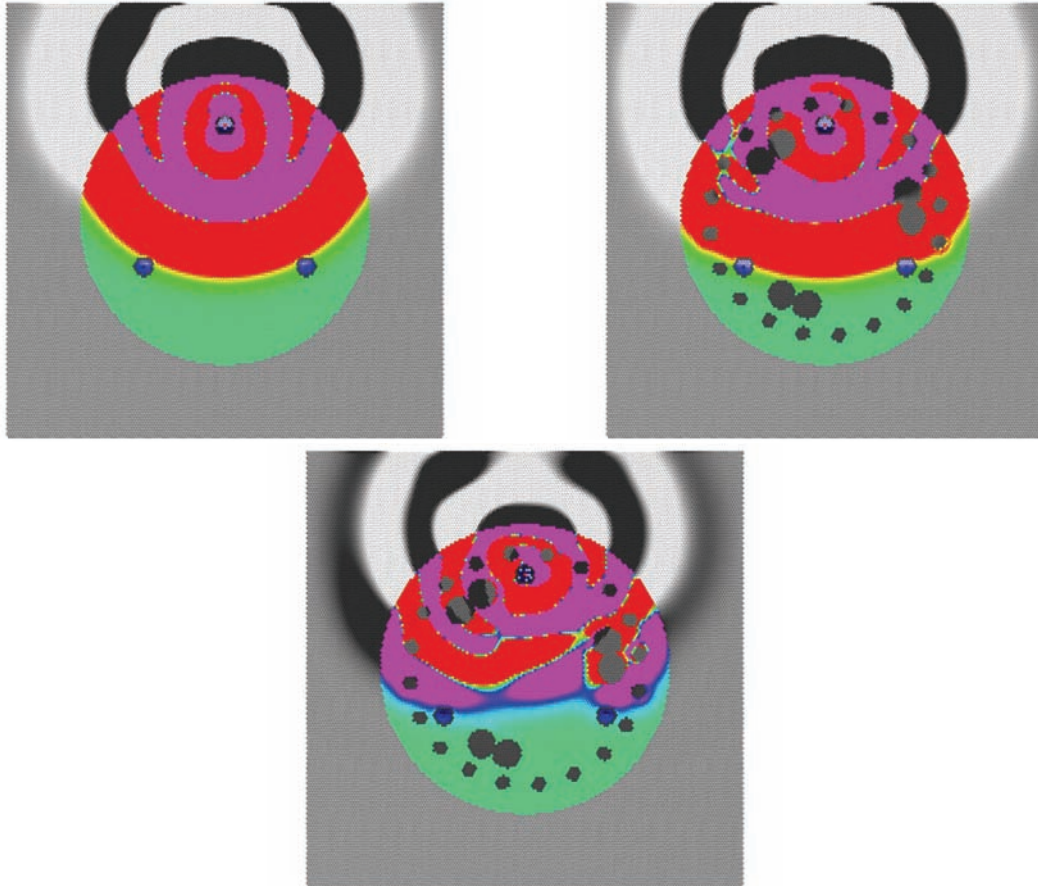

Figure 4.13. Plot. No Rebar (Top Left) vs. Rebar (Top Right) at 300 μs, with Difference (Bottom)

Figure 4.14 shows the compression wave at 500 μs, as the first tension wave reaches the access tubes. The first tension wave arrivals are essentially the same. The rebar does distort the wavefront, but the scattering is not significant for CSL purposes.
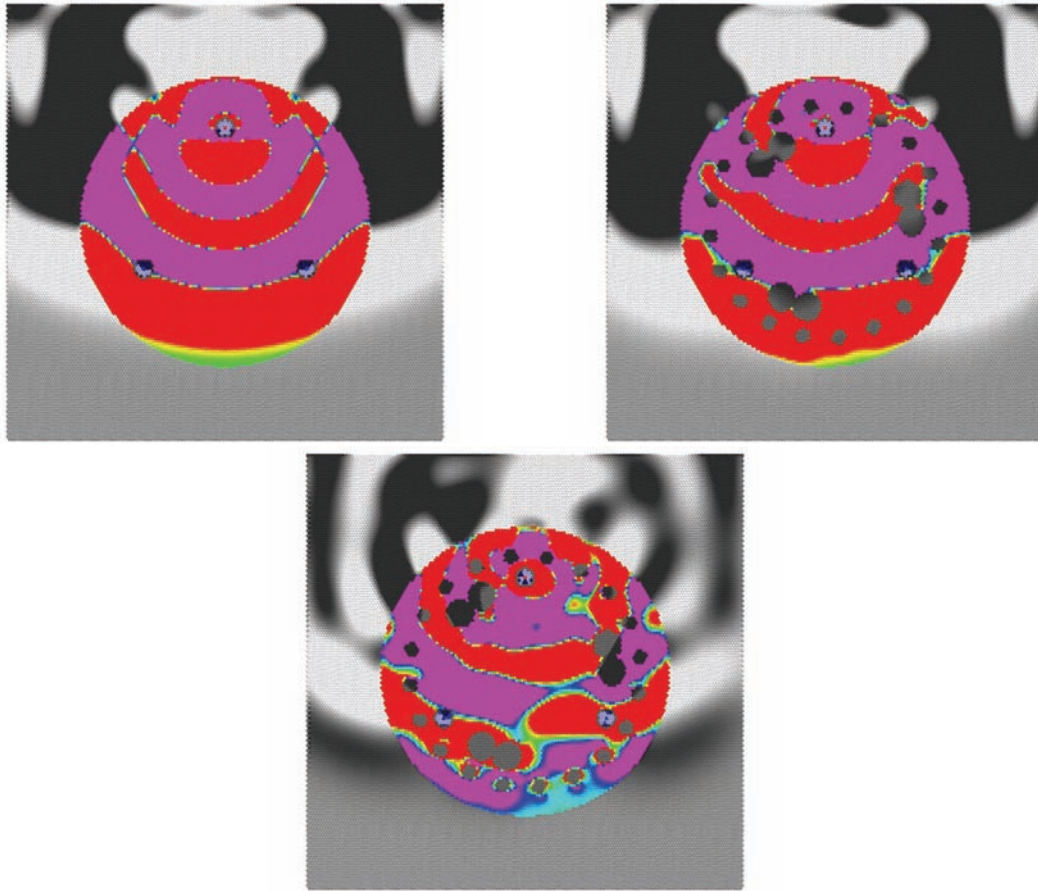

Figure 4.14. Plot. No Rebar (Top Left) vs. Rebar (Top Right) at 500 μs, with Difference (Bottom)

Figure 4.15 compares the waveforms collected in the access tubes. Although the rebar theoretically does not influence the first arrival, the waveforms show that the rebar has a large enough effect on the subsequent waveform that it could affect the first arrival pick, depending on the person making manual picks, or on the picking algorithm if performed automatically. For CSL systems that simply plot the raw data, the effect of rebar could affect interpretation.
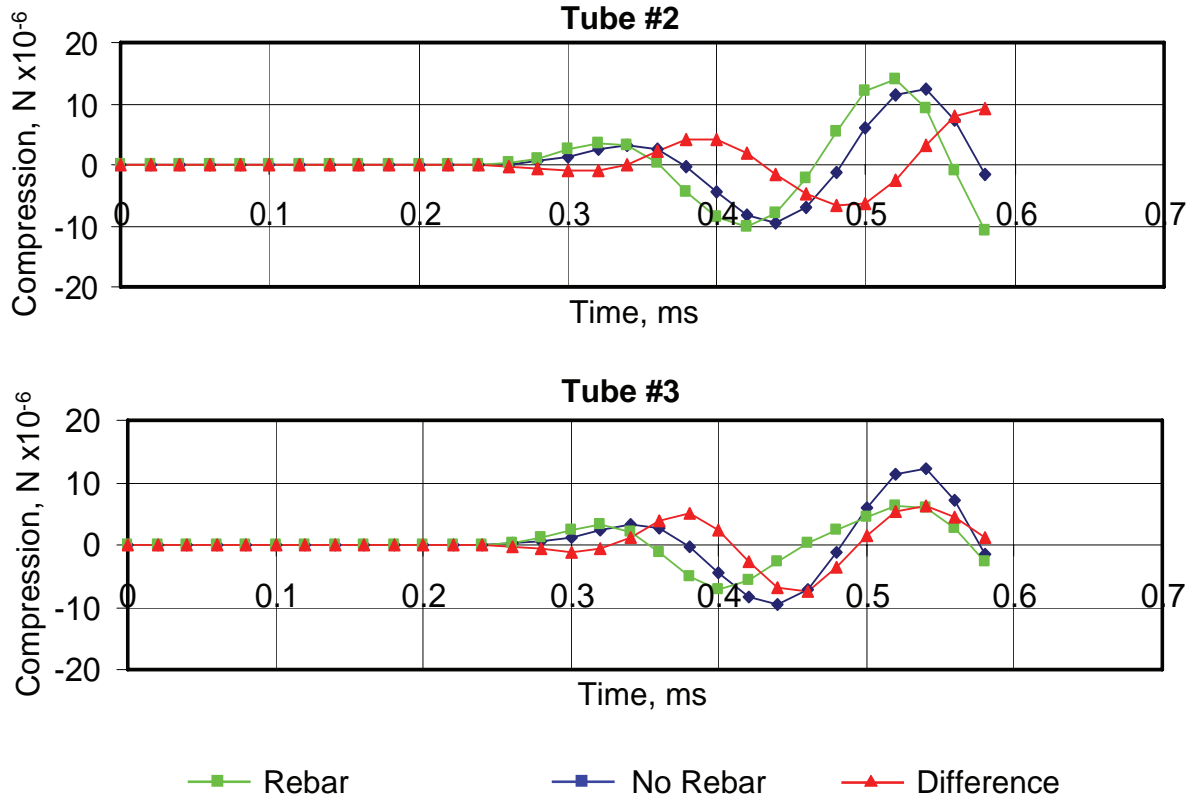

Figure 4.15. Chart. CSL Signals from No Rebar vs. Rebar, between Access Tubes 1 and 2 (Top), and Tubes 1 and 3 (Bottom)

4.6   Tube Effects

Access tubes can affect CSL velocity and energy in various ways. Numerical modeling can be used to quantify these effects. Different tube materials such as steel and PVC, with different thicknesses, can result in different waveforms. The effect of tube bending is significant. Tube deviation surveys are critical for eliminating these errors.

Tubes form a discontinuity in the concrete shaft. When filled with water or air, the tubes create a region of lower velocity that, unlike solid concrete, does not propagate shear waves. However, the previous numerical model study of the effects of rebar suggests that the tubes have minimal influence on the wave, and will not result in pronounced wave distortion, diffusion, reflection, or scatter.

Errors in the source and receiver location increase the probability of false defect classification, especially with tomographic reconstructions. Concrete is injected through the center of the drilled shaft during placement, and the pressure and flow of the concrete mix tends to displace tubes outward from the center. Eddy currents within the mix, together with vibrations during placement, can displace tubes unpredictably. Tubes may be bent prior to placing the mix due to the weight of the rebar support cage itself. This often results in unpredictable tube bending in the bottom of the shaft. Tubes also can bend near the surface, resulting in inaccurate measurements of tube separations deeper in the shaft.

When tubes bend away from the center, the tubes are farther apart than assumed. This increase in distance results in an increase in travel time and a corresponding decrease in observed velocity. Methods used to correct for these errors can be problematic as actual low-velocity regions may be eliminated unintentionally.

One technique to adjust for unexpected low-velocity readings is to adjust the tube separation measurements to produce a more acceptable result. Arrival picks may also be individually adjusted, or massaged, to remove unwanted artifacts. Other techniques, such as Tomographic Velocity Equalization[1], may be incorporated to correct for "cycle skipping" pick errors, or to account for tube bending.

Adjustment techniques such as these, no matter how sophisticated, cannot guarantee accurate results in every case. Tube bending can be accurately determined in some cases assuming the concrete is consistent. However, there are cases when tube bending and inconsistent concrete are indistinguishable. For example, suppose one competent drilled shaft has a pressure surge at a certain depth, bending all the tubes away from the center. Suppose another defective shaft has a bad slurry mix resulting in a lower velocity defect at a certain depth. Both sets of arrival time picks for these shafts could be identical. Both sets of density data and temperature measurements could be identical, because the tubes in the former shaft would be bent outward. Both shafts would be either rejected or accepted by these adjustment techniques. This could result in additional cost to determine that the competent shaft had bent tubes, or could result in an undetected defect.

The solution is not to modify arrival picks, guess at tube bending, or construct more sophisticated statistical analysis techniques. The solution is to incorporate more data, such as tube deviation measurements, into CSL surveys.

4.6.1   Tube Material: PVC versus Steel Tubes

Access tubes are generally made of steel or PVC. PVC is used primarily for superior signal quality.

---

[1] Defects in Drilled Shaft Foundations, (2000) FHWA CFLHD publication, February, pp 17-19.

Figures 4.16 – 4.21 compare CSL signals from a drilled shaft with PVC access tubes to signals from a shaft with steel tubes. This comparison requires a 3-D model to properly analyze the effects.

Figure 4.16 shows the compression wave propagating from the source access tube on the upper right after 20 μs. The PVC model, with light blue access tubes, is on the left. The model with steel access tubes is on the right.
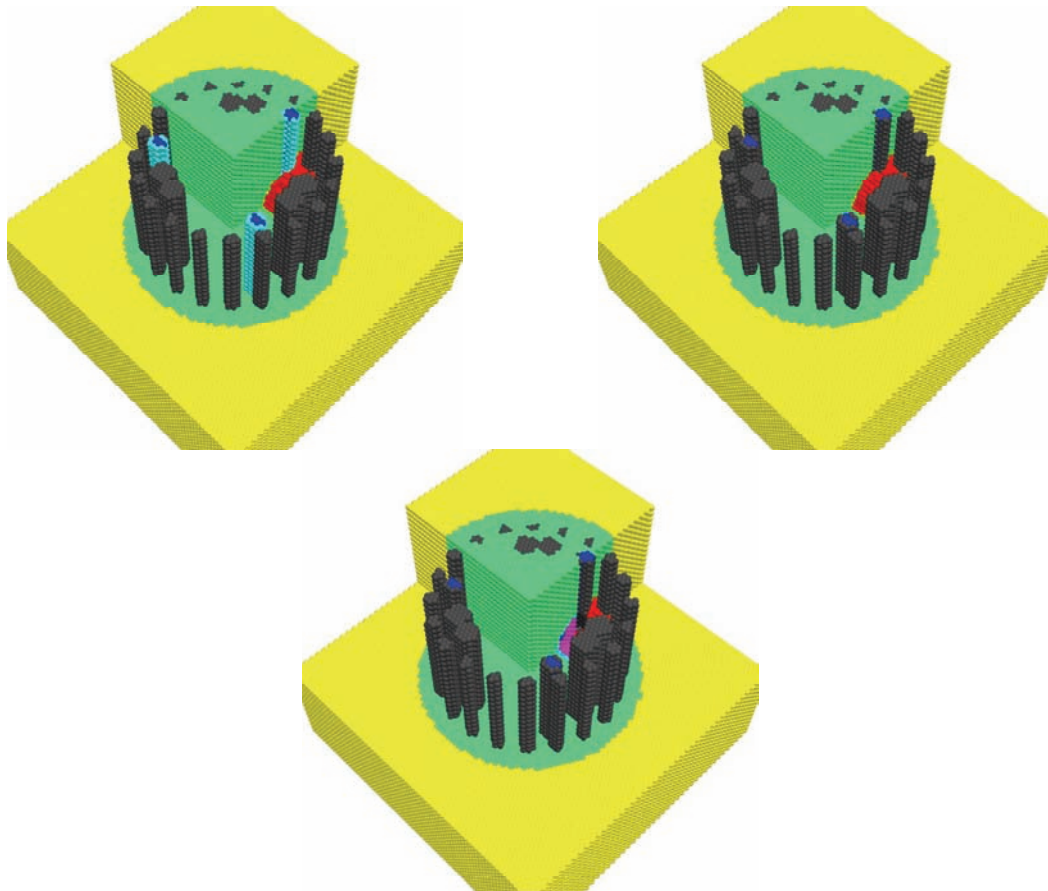

Figure 4.16. Plot. PVC (Top Left) vs. Steel (Top Right) Access Tubes at 20 μs, with Difference (Bottom)

Figure 4.17 shows the compression wave at 60 µs, as the wave first interacts with the surrounding ground. Both wavefronts appear similar, and differ only in amplitude.

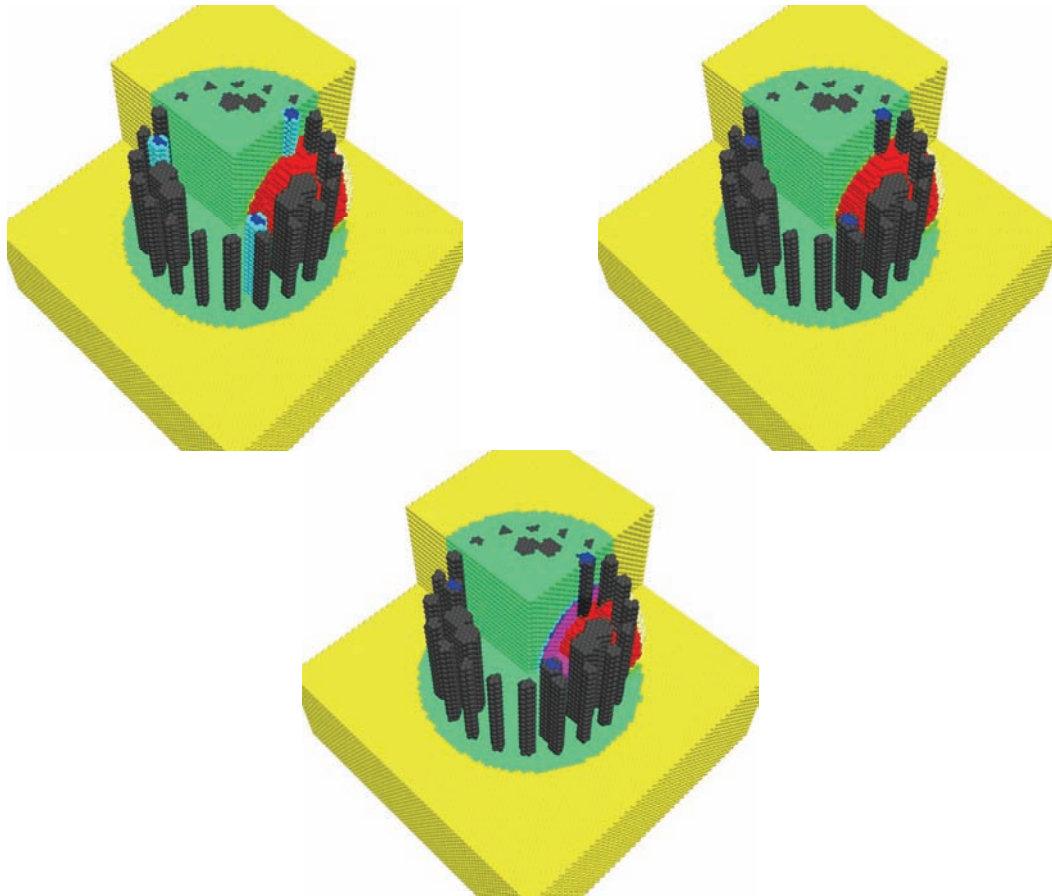**Figure 4.17. Plot. PVC (Top Left) vs. Steel (Top Right) Access Tubes at 20 µs, with Difference (Bottom)**

Figure 4.18 shows the compression wave at 120 µs, as the compression wave approaches the receiver access tubes. The wavefronts are virtually identical in shape.

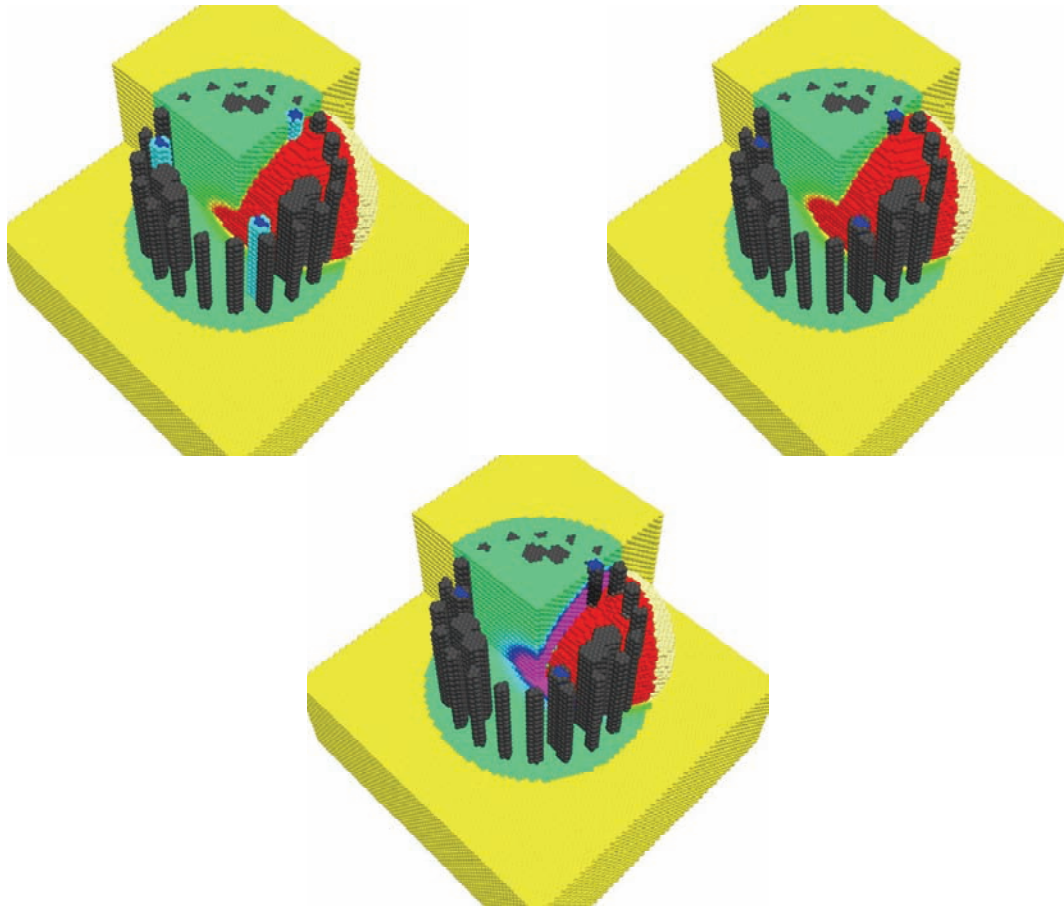**Figure 4.18. Plot. PVC (Top Left) vs. Steel (Top Right) Access Tubes at 120 µs, with Difference (Bottom)**

Figure 4.19 shows the compression wave at 300 μs, as the first compression wave reaches the receiver access tubes. The arrival is practically identical for both models.

Figure 4.19. Plot. PVC (Top Left) vs. Steel (Top Right) Access Tubes at 300 μs, with Difference (Bottom)

Figure 4.20 shows the compression wave at 500 μs, as the first tension wave reaches the access tubes. The amplitude of the signal from the steel tubes is significantly less, but the wavefront shape remains similar.
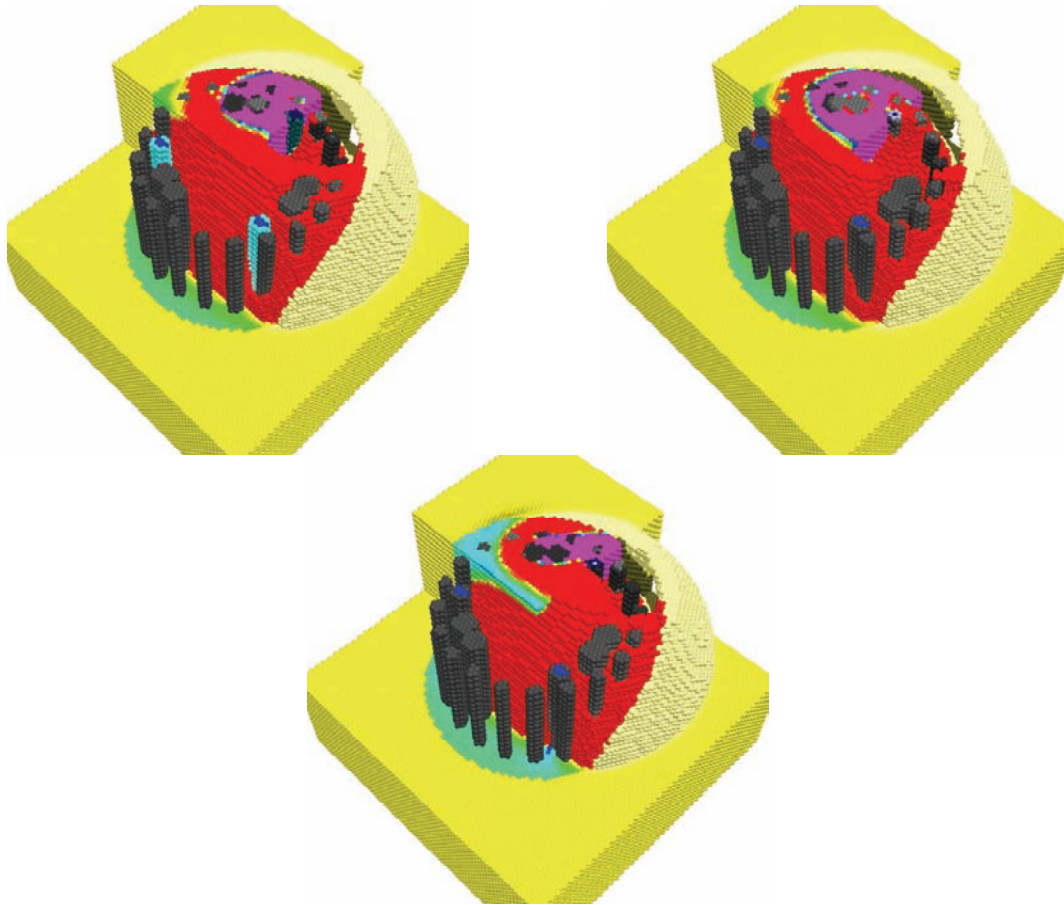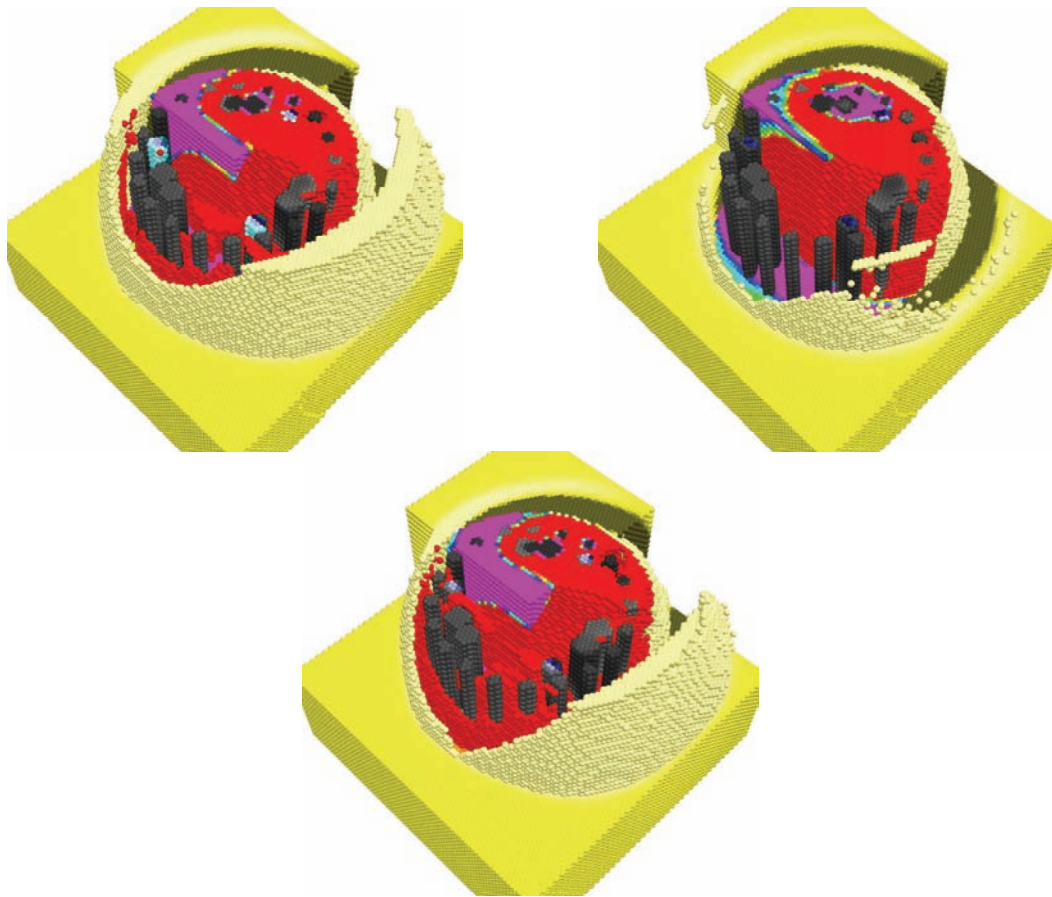

Figure 4.20. Plot. PVC (Top Left) vs. Steel (Top Right) Access Tubes at 500 μs, with Difference (Bottom)

Figure 4.21 compares the waveforms collected in the access tubes. The signal amplitude using PVC tubes is at least five times higher than steel. A larger portion of the compression wave energy is absorbed by the steel and transmitted up the tube rather than into the concrete, resulting in lower amplitude signals measured at the receiver. The first arrivals are the same, but the peak of the first compression wave is significantly different. The peak from the steel access tube arrives approximately 50 µs before the peak from the PVC. This phenomenon will have significant effects on arrival picks based on the first compression peak.
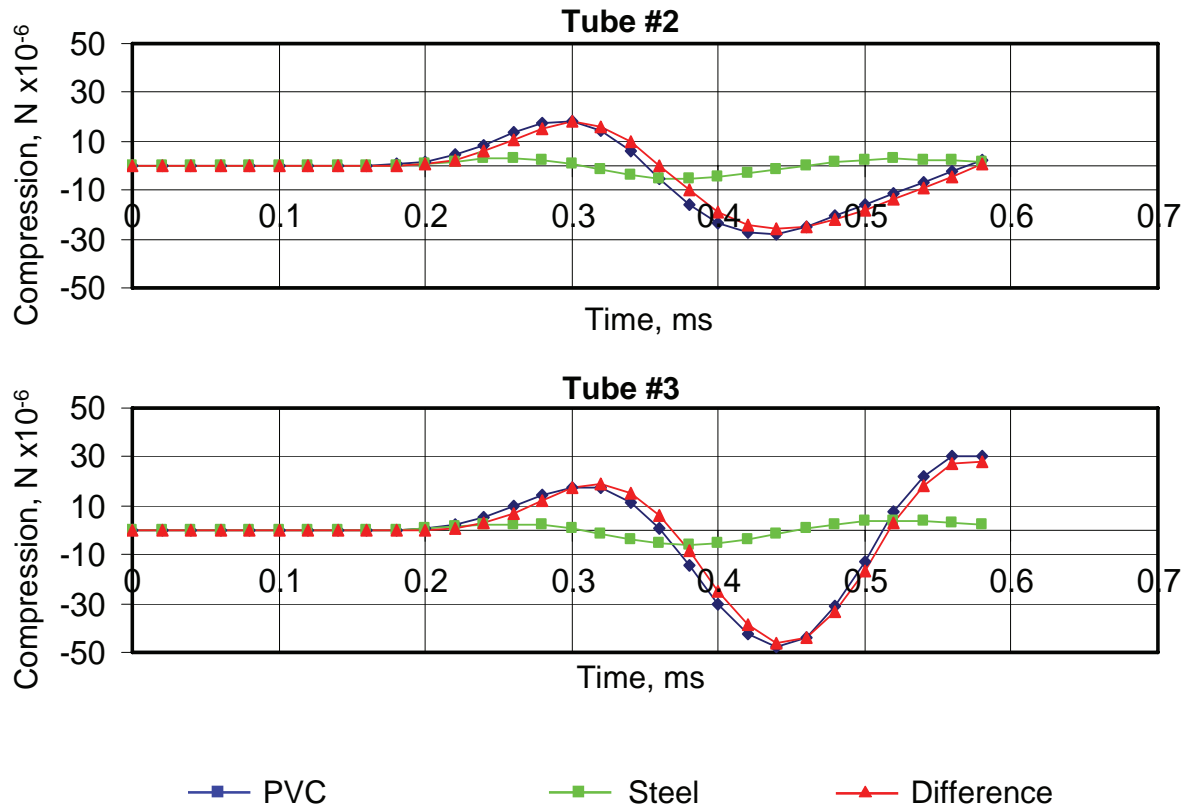

Figure 4.21. Chart. CSL Signals from PVC vs. Steel Access Tubes, between Tubes 1 and 2 (Top), and Tubes 1 and 3 (Bottom)

Although PVC transmits a higher amplitude signal, PVC is easily broken during concrete placement, preventing CSL surveys from being conducted. PVC also has a thermal expansion five times higher than steel, as shown in Table 4.3. For this reason, the use of PVC often results in tube debonding in a short period of time as the shaft cools. PVC is more brittle than steel, and occasionally is broken during placement. PVC also can be crushed by the shrinking concrete during the curing process. Some agencies still use PVC, but because of the disadvantages of using PVC, and because steel tubes are becoming more widely used, the remainder of the models in this study will use steel access tubes.

Table 4.3 Thermal Expansion of PVC and Steel (inches/100 ft)[2]

Temperature Change °F	PVC	Steel
25	0.9	0.18
50	1.8	0.36
75	2.7	0.54
100	3.6	0.72
150	5.4	1.08

4.6.2   Tube Debonding

Debonding conditions between the tubes and the concrete occasionally occur in a shaft for various reasons. One common cause is initial tube expansion during the curing process due to heat from concrete hydration, followed by contraction of the tube as the concrete cools. The vertical expansion is much greater than the radial expansion, causing tubes to slide vertically, breaking contact bonds at the tube/concrete interface. Since tubes usually are anchored in the bottom of the shaft due to initial concrete placement, the largest vertical displacement will occur in the upper portion of the shaft. Tubes disturbed after concrete placement can also result in tube debonding in the upper portion of the shaft. However, the most common cause of tube debonding is due to thermal expansion, especially when PVC access tubes are used.

Tube debonding in upper regions can also be caused by mechanically induced stress, such as bending or impacting the access tubes. Tube debonding can also occur even when tubes are not disturbed during the curing process. If the top of the shaft is not well insulated or the tubes are not filled with water immediately after concrete placement, large temperature gradients can form within the concrete. The gradient is especially severe in the region of the tubes because the tubes readily transmit heat to the surface. Large temperature gradients may also result in severe micro cracking and reduce the strength of concrete in the foundation.

Tubes should be filled with clean drinking water before or shortly after concrete placement. Filling tubes with water inhibits the debonding of the concrete from the tube. Tube debonding occurs when heat is dissipated too quickly, creating a large temperature gradient surrounding the tube. A large temperature gradient results in cracking, not only from added stresses from tube shrinkage, but also from internal cooling induced stresses in the concrete. Water has a higher specific heat than air and provides the necessary insulation to reduce the temperature gradient to acceptable levels. A rule of thumb in construction practice is to add water to the tubes within one hour after concrete placement. However, the first hydration phase of the curing process completes within the first 15 minutes, so water should be added before or as soon as possible after concrete placement.

Stress on the tubes before curing can also cause tube debonding. Excess torque or impacts during removal or replacement of tube caps or plugs can result in stresses that break the bond between the tubes and the concrete, even deep within the drilled shaft. So, care must be taken to avoid this problem.

---

[2] http://www.engineeringtoolbox.com/thermal-expansion-pvc-14_782.html

Tube debonding can significantly attenuate signals at both the source and receiver, resulting in reduced velocity measurements or lost data. Examining only the first arrival and signal amplitude is not adequate for distinguishing tube debonding from actual defects. Full waveform inversion techniques should be employed to accurately reconstruct the occurrence and extent of tube debonding.

Although initial tube debonding may appear harmless, the micro-cracks provide an inlet for future contaminants to enter and corrode the internal structure of the concrete and rebar support. Tube debonding can form and extend long after concrete curing, due to shaft deformation from loading stresses, ground settlement, freeze-thaw cycles, exposure to contaminants, and thermal expansion and contraction of the shaft and the surrounding environment.

The concrete in the shaft should normally be allowed to cure at least 1-2 days prior to testing. If PVC tubes are used, testing should be done within 10 days after the placement of concrete due to possible tube-concrete debonding. If steel tubes are used, testing can be done within 45 days after concrete placement as the steel tubes bond better than PVC tubes over a longer time.

Although CSL does require installation of tubes that could compromise the durability and performance of concrete in the long term, the same debonding issues apply to rebar within the concrete. In any event, care should be taken to avoid detrimental long-term effects.

Extreme tube debonding should be a serious concern. However, very slight tube debonding can be difficult to detect, but still can result in serious long-term effects.

Figures 4.22 – 4.27 compare CSL signals from a drilled shaft with tube debonding defects to signals from a shaft with no defect. This comparison requires a 3-D model to properly analyze the effects. A 0.5 m tube debonding defect is placed around the source access tube 1 and tube 2. The defect extends 0.25 m above and below the source and receiver.

Figure 4.22 shows the compression wave propagating from the source access tube on the upper right after 20 µs. The debonding defect significantly blocks wave propagation at the source.
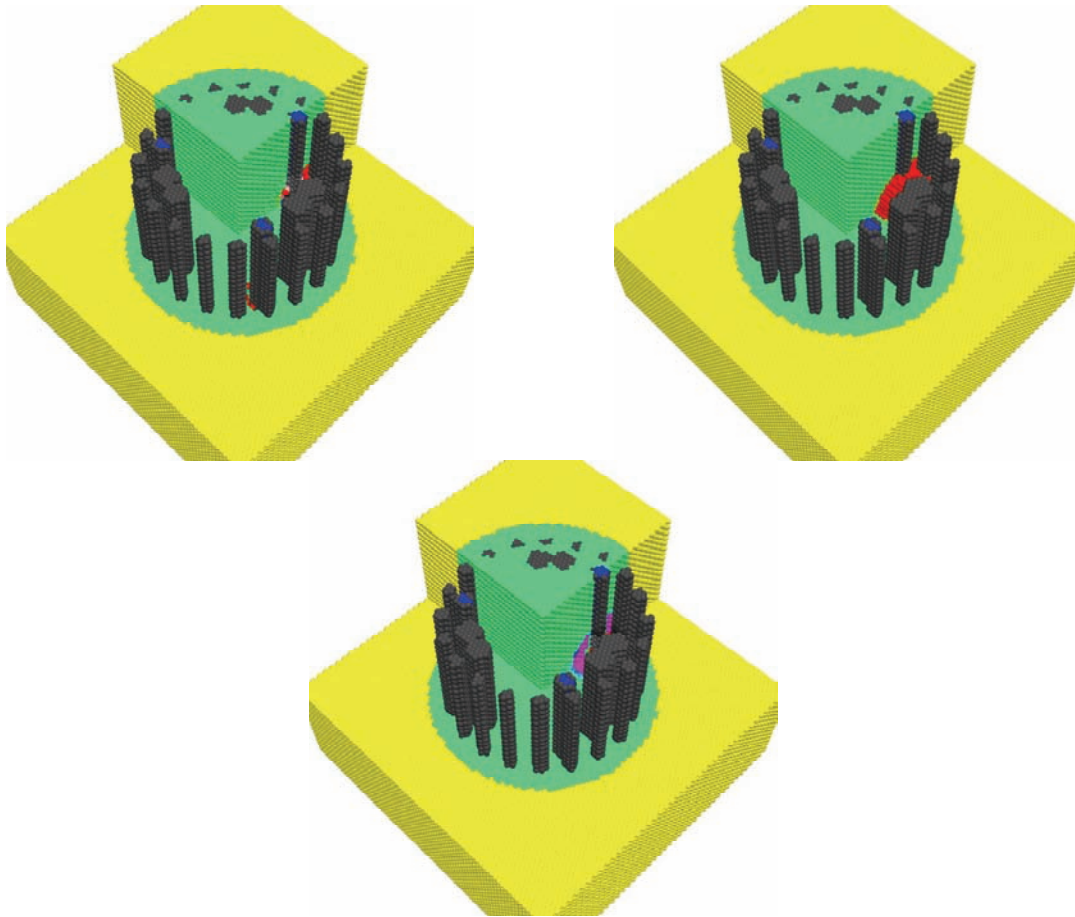

Figure 4.22. Plot. Tube Debonding (Top Left) vs. No Tube Debonding (Top Right) at 20 µs, with Difference (Bottom)

Figure 4.23 shows the compression wave at 60 μs, as the wave first encounters the surrounding ground. The signal as been significantly delayed and attenuated by tube debonding.

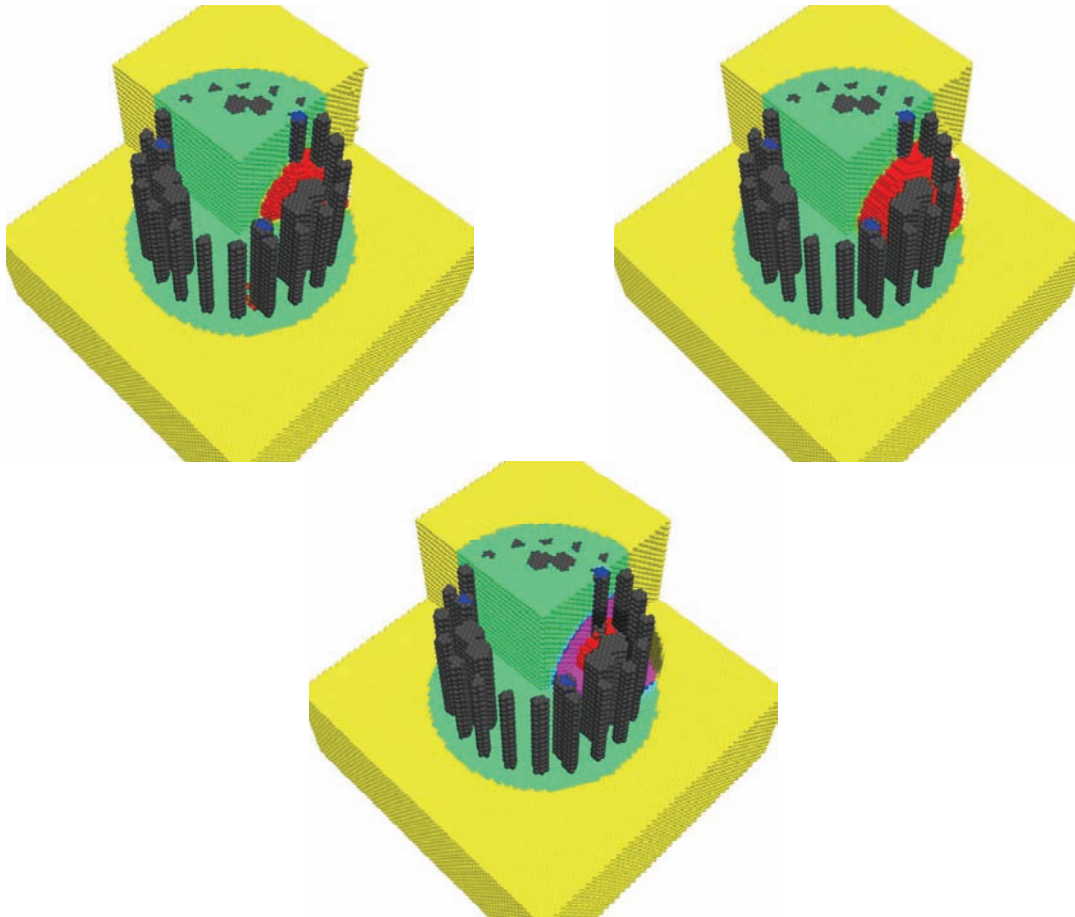**Figure 4.23. Plot. Debonding (Top Left) vs. No Tube Debonding (Top Right) at 20 μs, with Difference (Bottom)**

Figure 4.24 shows the compression wave at 120 μs, as the compression wave approaches the receiver access tubes. The debonding defect had distorted the shape of wavefront, as much of the wave must travel along the tube and around the defect.
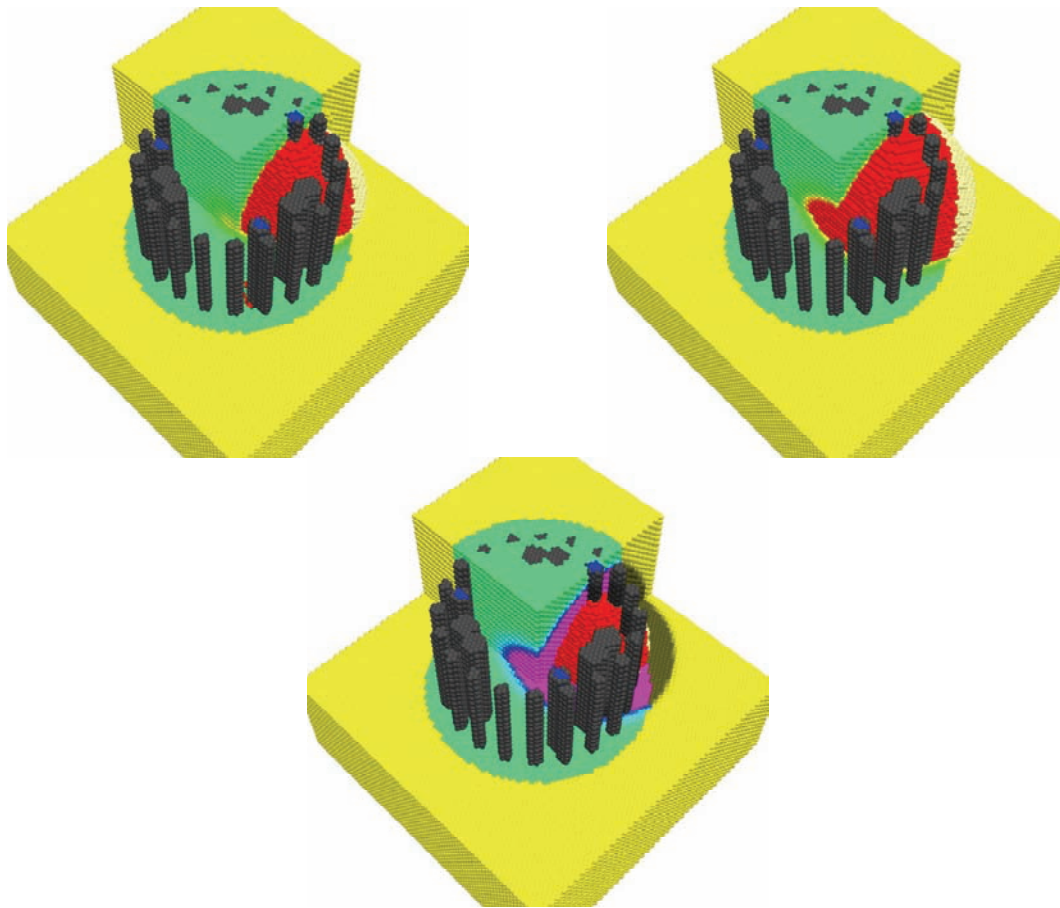

Figure 4.24. Plot. Debonding (Top Left) vs. No Tube Debonding (Top Right) at 120 μs, with Difference (Bottom)

Figure 4.25 shows the compression wave at 300 μs, as the first compression wave in the shaft with no tube debonding reaches the receiver access tubes. The first compression wave in the defective shaft is delayed, but has grown significantly higher in amplitude.
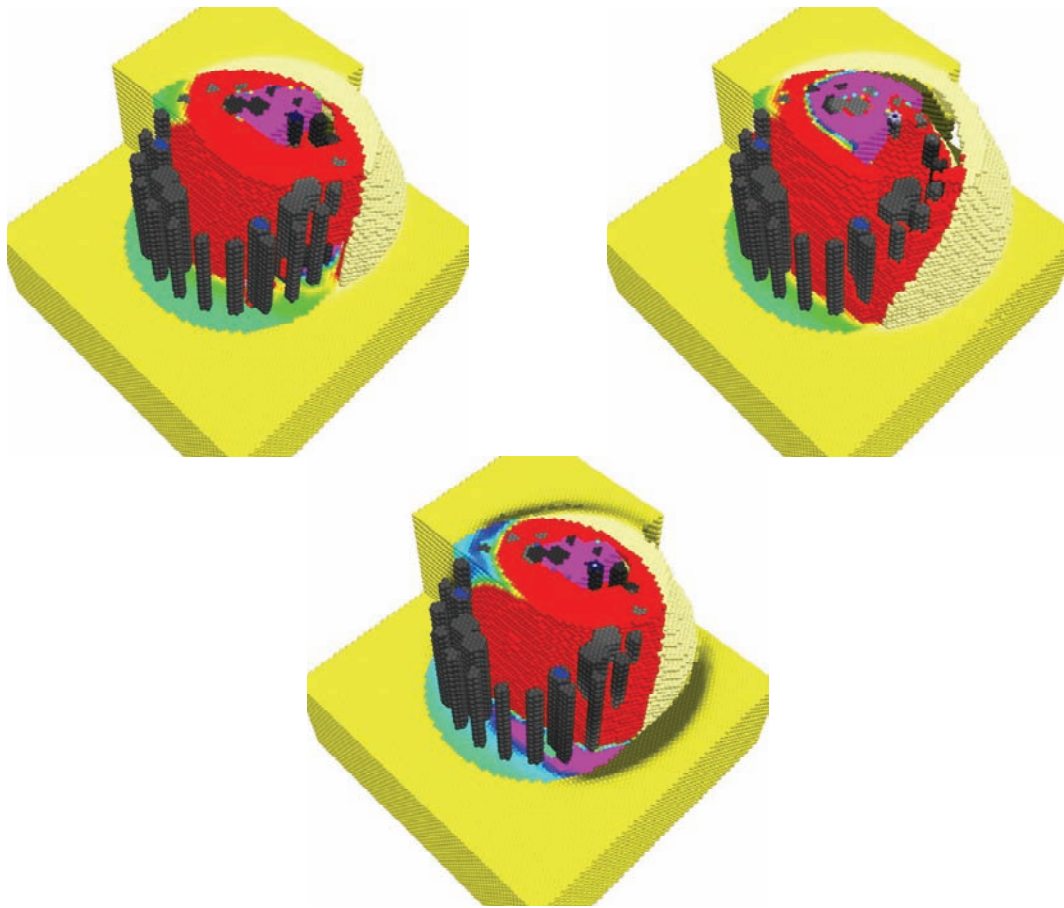

Figure 4.25. Plot. Debonding (Top Left) vs. No Tube Debonding (Top Right) at 300 μs, with Difference (Bottom)

Figure 4.26 shows the compression wave at 500 μs, as the first tension wave reaches the access tubes in the shaft with no debonding defect. The peak of the first compression wave now appears to have reached the access tubes in the defective shaft.
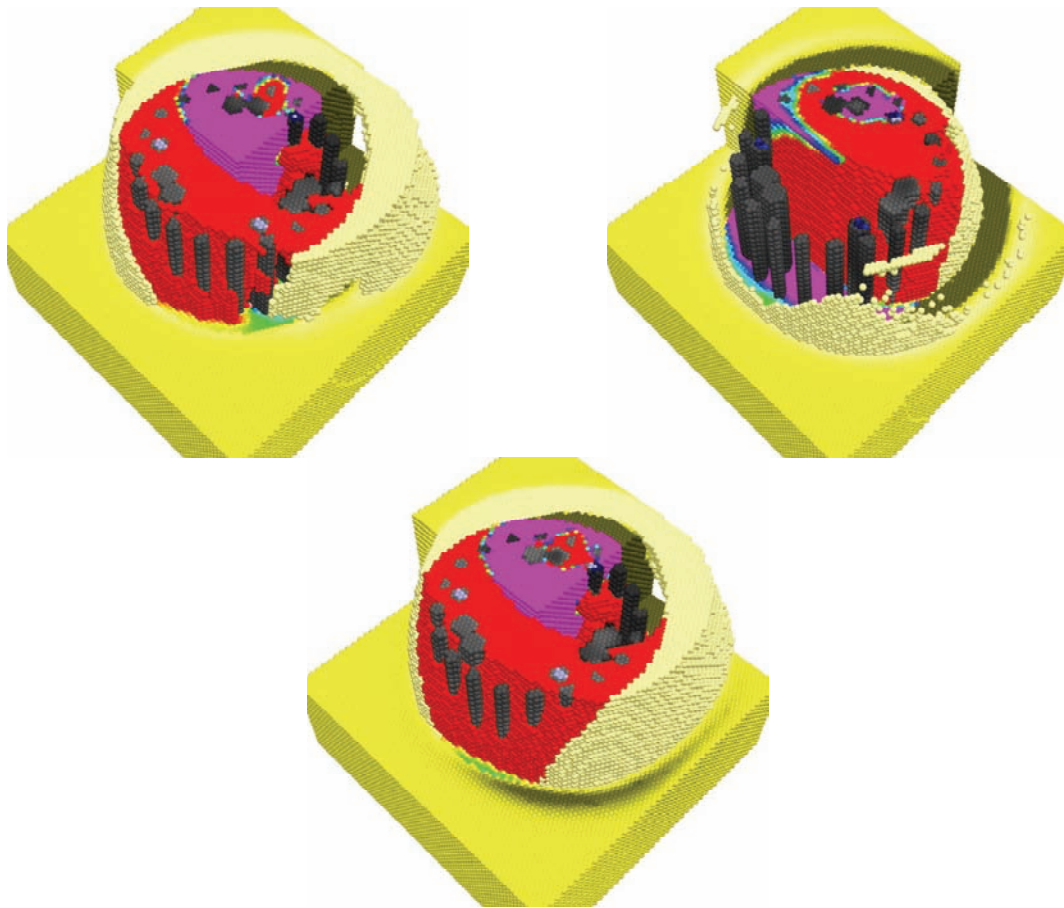

Figure 4.26. Plot. Debonding (Top Left) vs. No Tube Debonding (Top Right) at 500 μs, with Difference (Bottom)

Figure 4.27 compares the waveforms collected in the access tubes. The top graph shows that the signal almost completely attenuates with tube debonding around both the source and receiver access tubes. The bottom graph shows a significant delay in the first compression peak from the source tube debonding. However, the amplitude of the signal in the tube with the debonding defect is significantly higher for some reason.
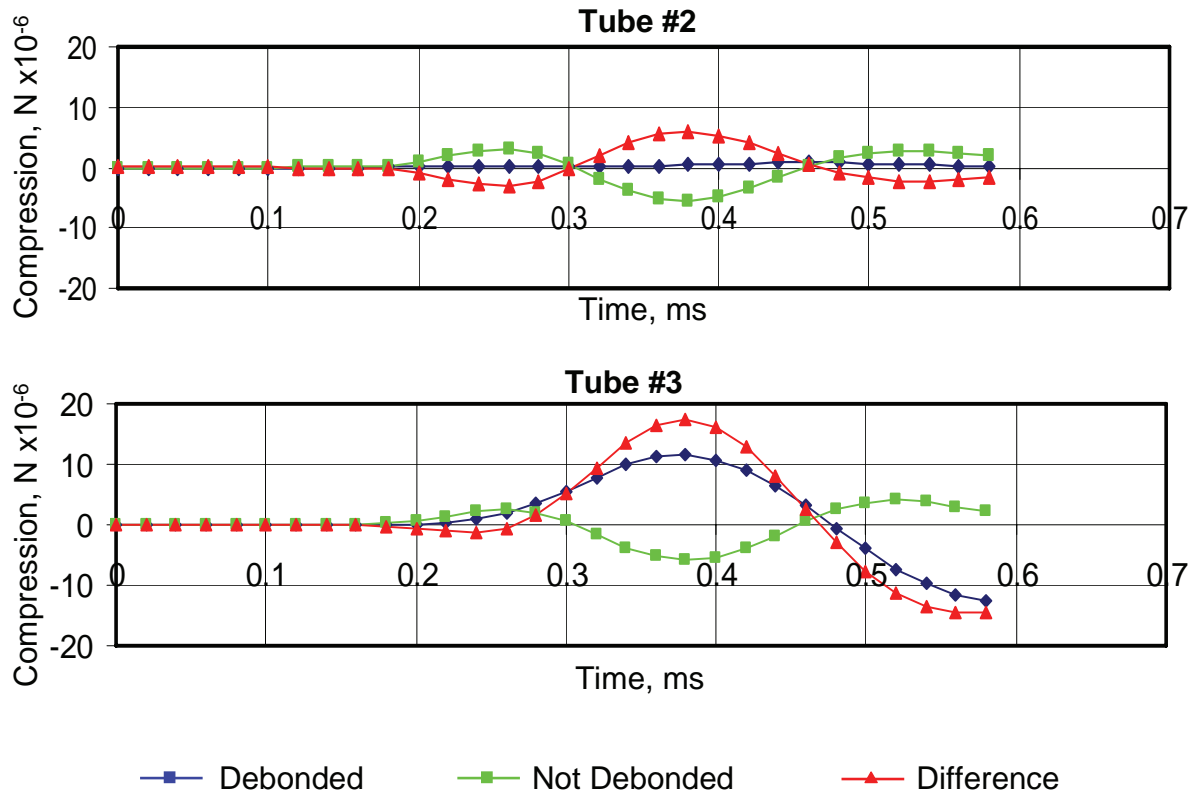

Figure 4.27. Chart. CSL Signals with Tube Debonding vs. No Tube Debonding, between Access Tubes 1 and 2 (Top), and Tubes 1 and 3 (Bottom)

4.6.3 Sensor Drift within the Access Tubes

Source and receiver position and orientation within the access tubes can have a significant effect on arrival time. The compression wave velocity of water is much lower than the velocity of concrete, so very small changes in the source or receiver position or rotation within the access tube can have a large effect on the arrival time. The numerical model estimates changes in velocity at levels up to 20% for only a 2 cm difference in source and receiver position.

Figures 4.28 – 4.33 compare CSL signals from a drilled shaft with the source and receivers displaced in the access tube 1 cm to the outside of the shaft, to a model with the source and receivers displaced 1 cm toward the center of the shaft. In this scenario, the signals travel a total difference of 4 cm through water.

Figure 4.28 shows the compression wave propagating from the top access tube after 20 μs. The model on the left, with the outside sensor drift, has an initial wavefront that is offset slightly higher than the model with inside sensor drift.

Figure 4.28. Plot. Outside Sensor Drift (Top Left) vs. Inside Sensor Drift (Top Right) at 20 μs, with Difference (Bottom)

The subsequent wavefront propagation is shown in Figures 4.29-4.32. The wavefront is slightly delayed in the model with outside sensor drift. The delay increases as the compression wave interacts with the water in the access tube.

Figure 4.29. Plot. Outside Sensor Drift (Top Left) vs. Inside Sensor Drift (Top Right) at 20 μs, with Difference (Bottom)

Figure 4.30. Plot. Outside Sensor Drift (Top Left) vs. Inside Sensor Drift (Top Right) at 120 μs, with Difference (Bottom)
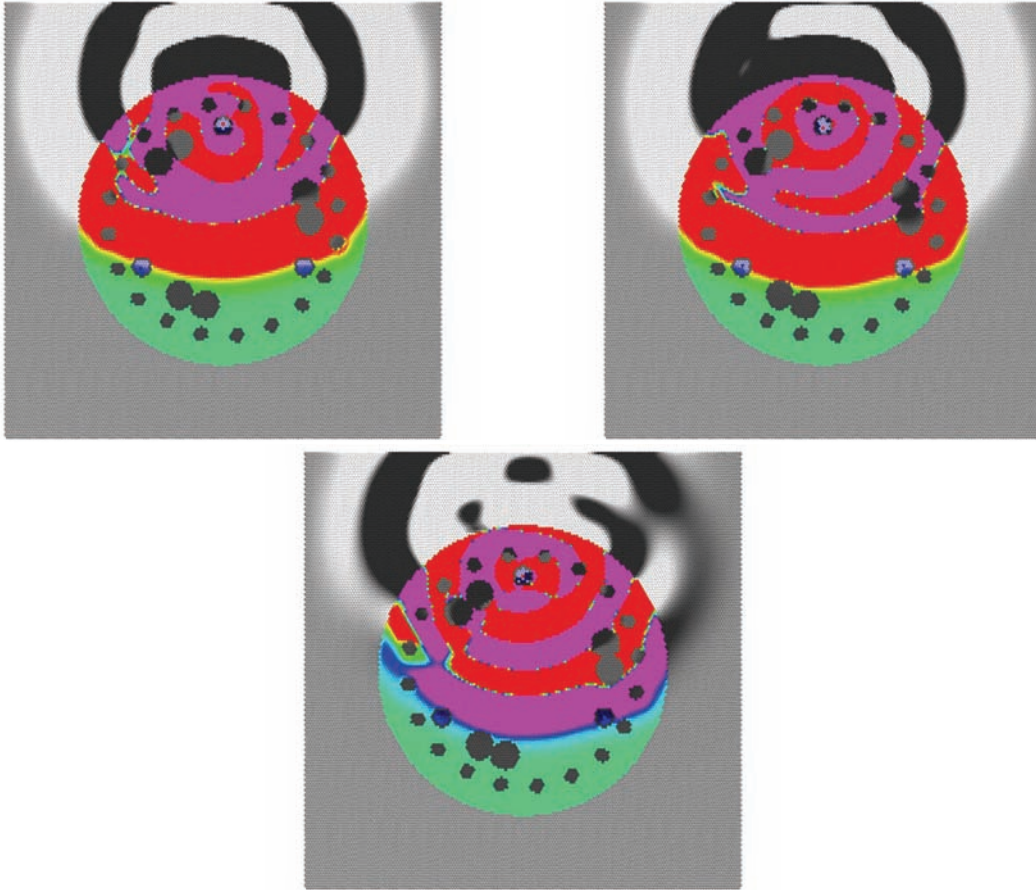
Figure 4.31. Plot. Outside Sensor Drift (Top Left) vs. Inside Sensor Drift (Top Right) at 300 µs, with Difference (Bottom)

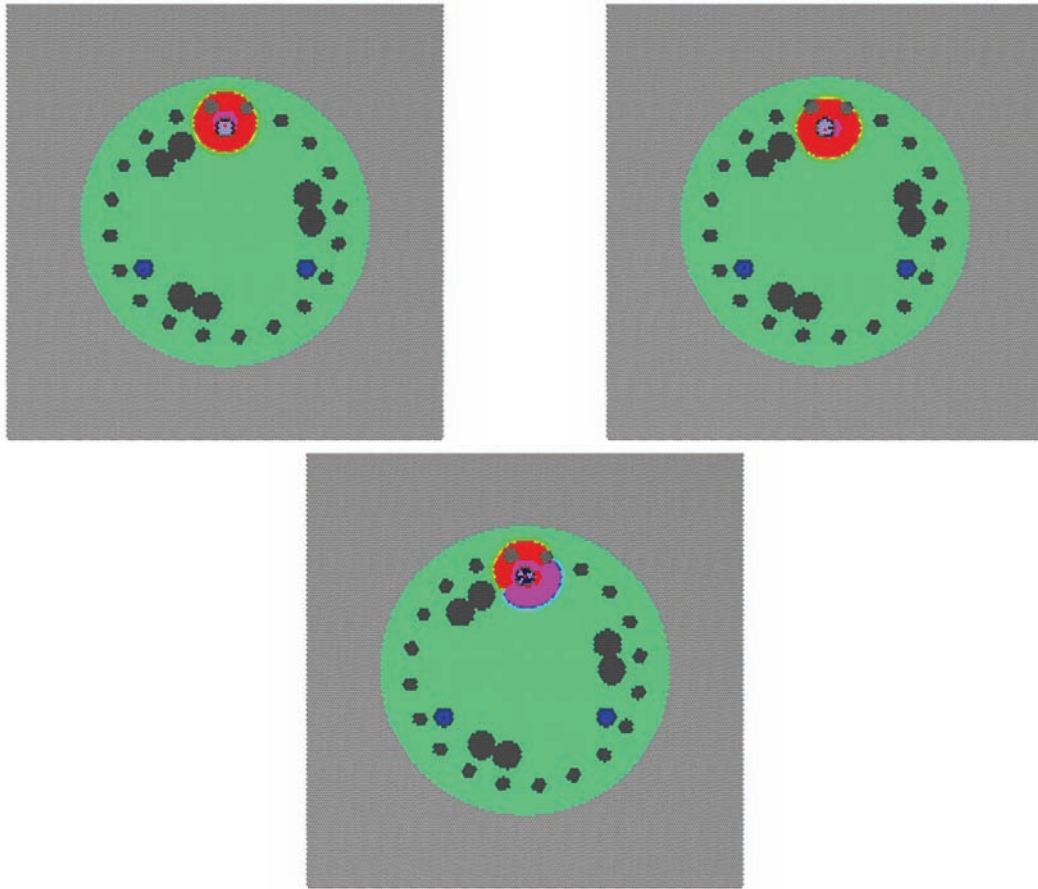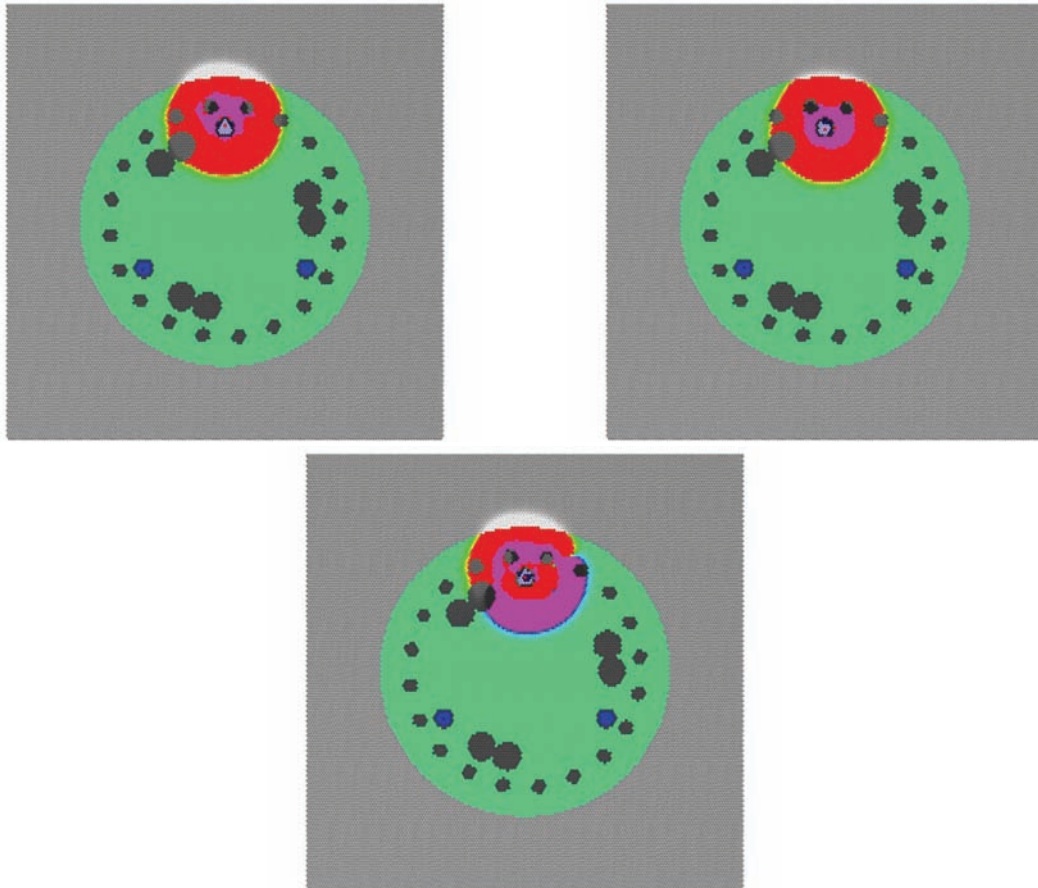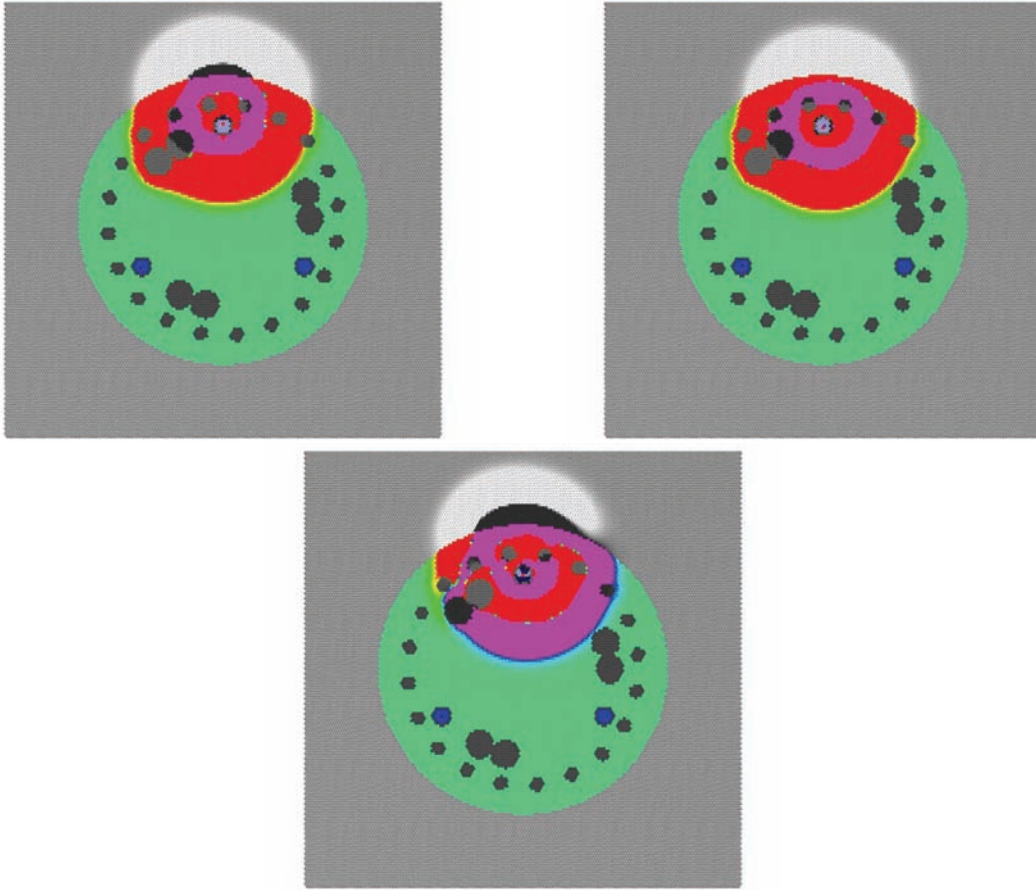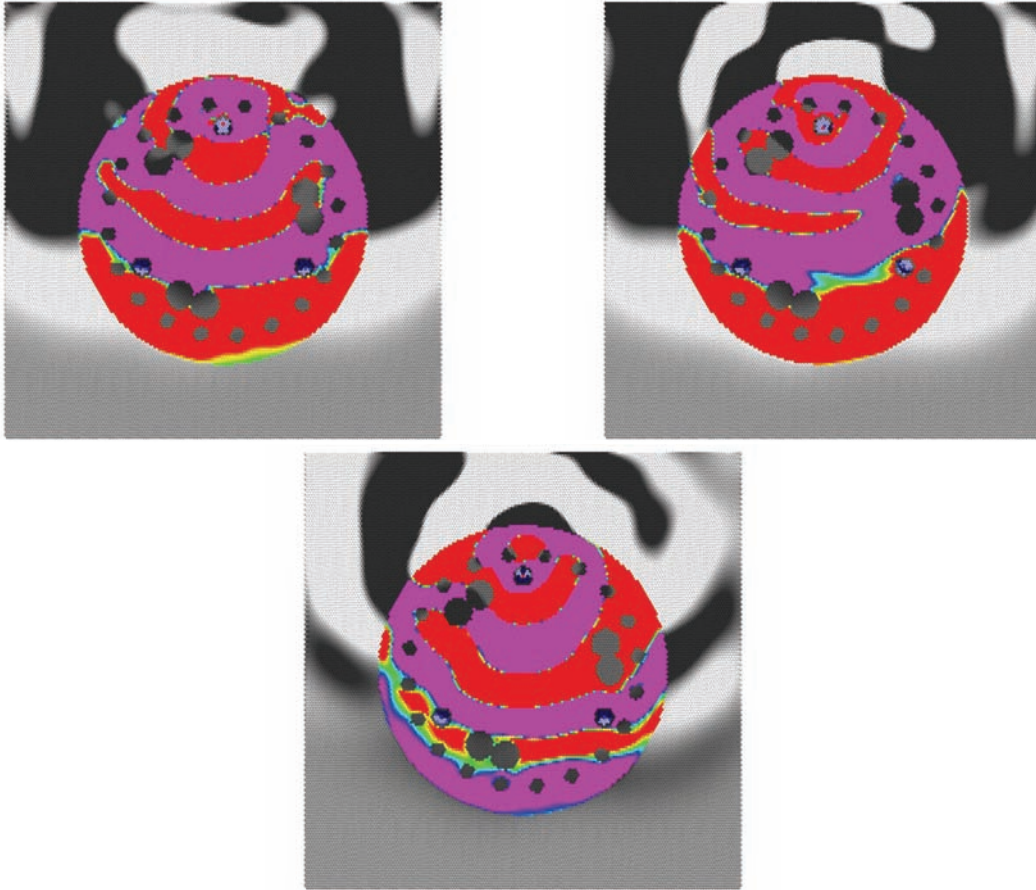**Figure 4.32. Plot. Outside Sensor Drift (Top Left) vs. Inside Sensor Drift (Top Right) at 500 μs, with Difference (Bottom)**

Figure 4.33 compares the waveforms collected in the access tubes. The top graph shows significant delay in the signal with outside sensor drift. The signal is also lower in amplitude and lower in frequency, due to the longer distance. This example shows the importance of carefully specifying tolerances in CSL data collection equipment if accurate measurements are desired.
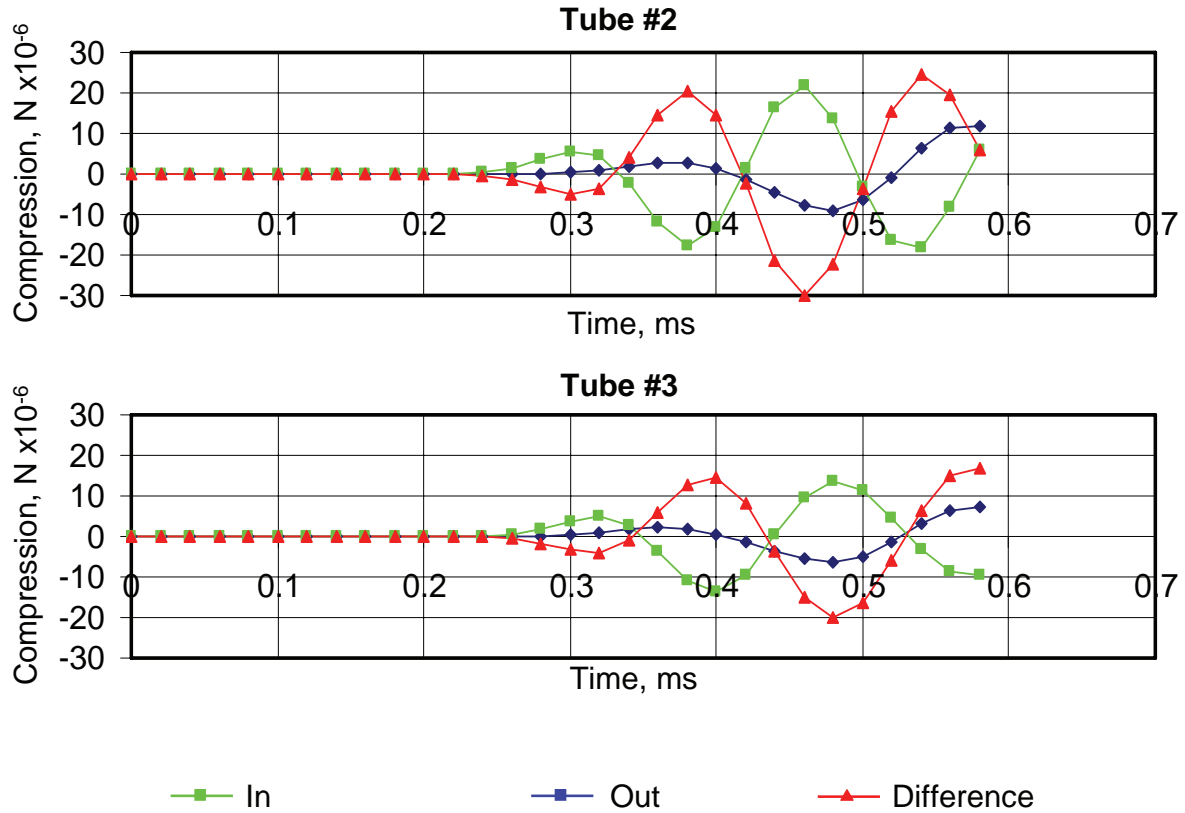
Figure 4.33. Chart. CSL Signals with Outside Sensor Drift vs. Inside Sensor Drift, between Access Tubes 1 and 2 (Top), and Tubes 1 and 3 (Bottom)

4.7 Concrete Cracking Effects

The inherently brittle nature of concrete makes cracking the most observable and characteristic defect of concrete structures. However, cracking can pass undetected using CSL first arrival and signal energy measurements in the field. Ultrasonic Pulse Velocity (UPV) lab tests are also not significantly affected by cracking, resulting in the characteristically poor ability of the test to predict concrete strength.

The effect of cracking on compression wave velocity is important to consider. When cracks are closed and under compression, and the compression wave is unable to open the crack, the velocity will not change. When the compression wave is unable to close an open crack, the wave will not propagate across the crack. If the wave can travel around the crack, the velocity will appear slower. When the compression waves is able to both open and close the crack, then the velocity will increase, and the amplitude of the first compression arrival will increase. This may seem counterintuitive, but logically follows because cracks under this condition do not contribute the same tensile force as intact material.

Figures 4.34 – 4.39 compare CSL signals from a drilled shaft with a cracking defect, shown in red, to a shaft with no defect. The cracking defect has the same compression wave velocity, modeled with 90% of the springs broken.

Figure 4.34 shows the compression wave propagating from the source access tube after 20 μs.
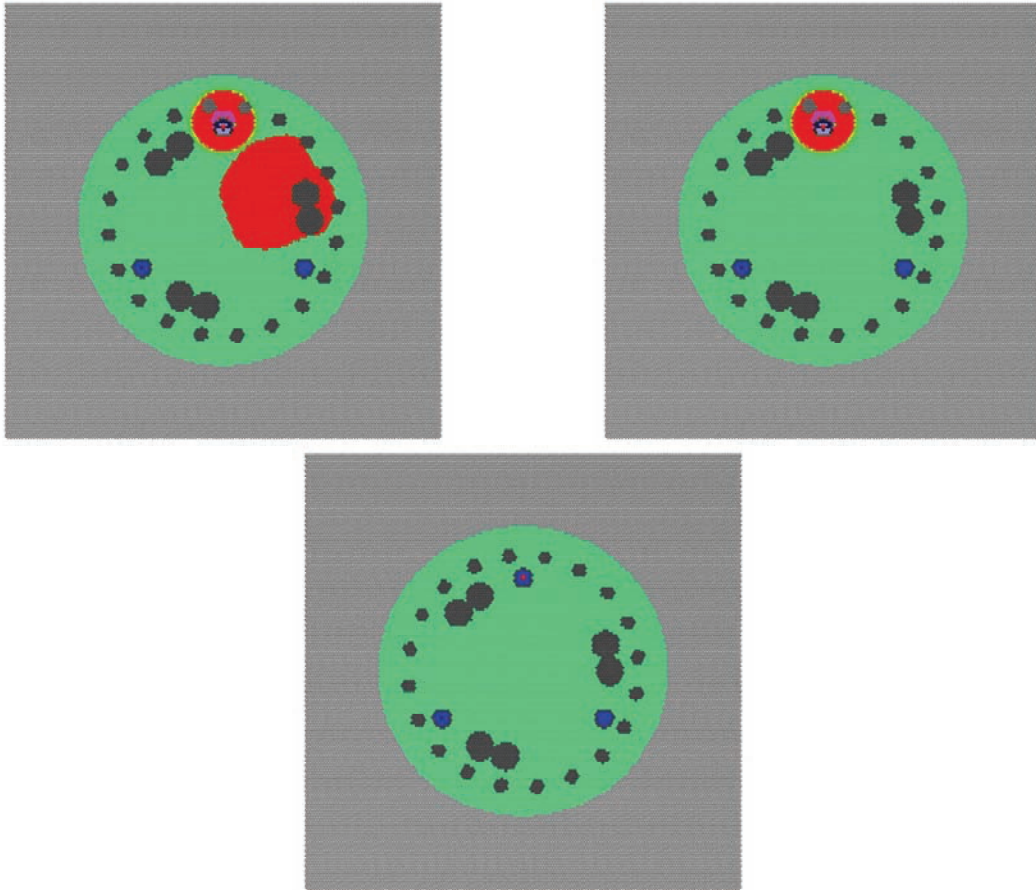
Figure 4.34. Plot. Cracking Defect (Top Left) vs. No Defect (Top Right) at 20 μs, with Difference (Bottom)

The wavefront first encounters the cracking defect in Figure 4.35 at 60 μs. The difference plot shows the effect of the cracking on the compression wave.

Figure 4.35. Plot. Cracking Defect (Top Left) vs. No Defect (Top Right) at 20 μs, with Difference (Bottom)

Figure 4.36 shows the compression wave at 120 μs, as the compression wave passes half way through the cracking defect. The amplitude of the compression wave is higher through the cracking defect, as shown in the difference model. This is the case because no tension forces "pull back" elements that are cracked, resulting in a higher degree of compression on the wave front.

Figure 4.36. Plot. Cracking Defect (Top Left) vs. No Defect (Top Right) at 120 μs, with Difference (Bottom)

Figure 4.37 shows the compression wave at 300 μs, as the compression wave reaches the receiver access tubes. The compression wave reaches the access tubes in both models at essentially the same time.

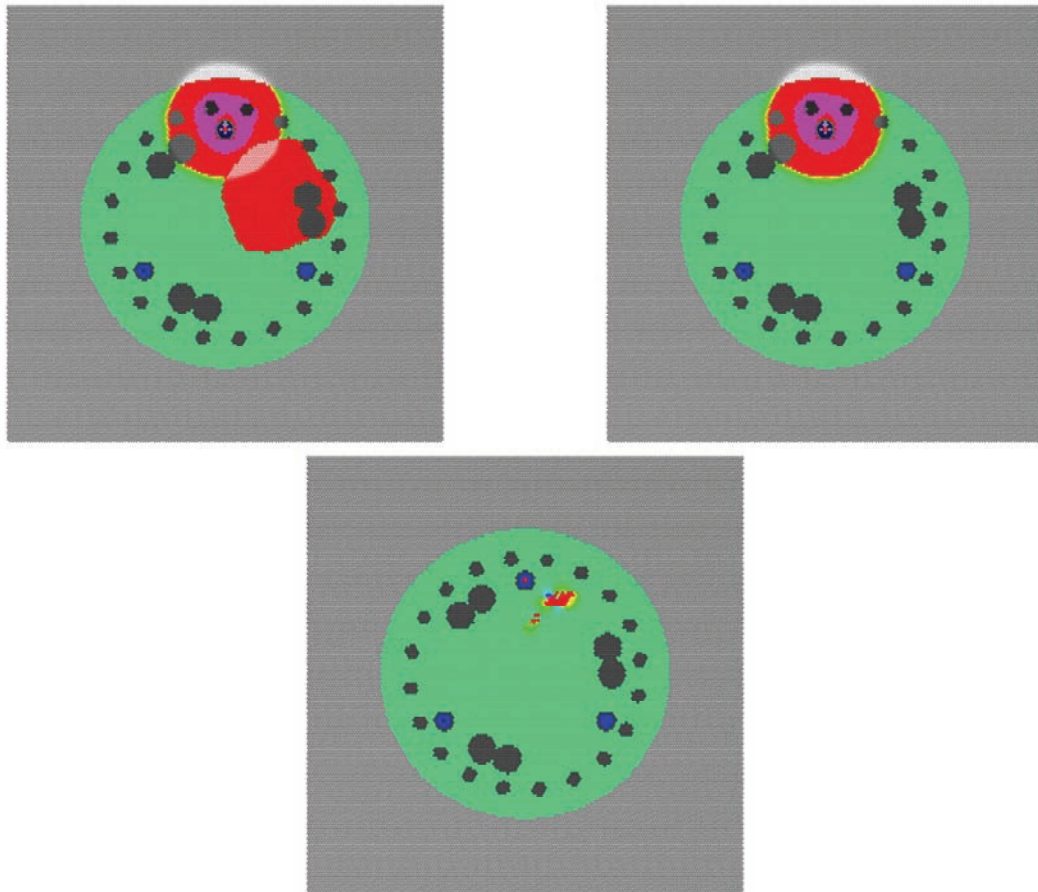**Figure 4.37. Plot. Cracking Defect (Top Left) vs. No Defect (Top Right) at 300 μs, with Difference (Bottom)**

Figure 4.38 shows the compression wave at 500 µs, as the peak of the first tension wave crosses the access tubes in the shaft with no defect. The tension wave in the shaft with cracking defect is almost non-existent at the access tube.
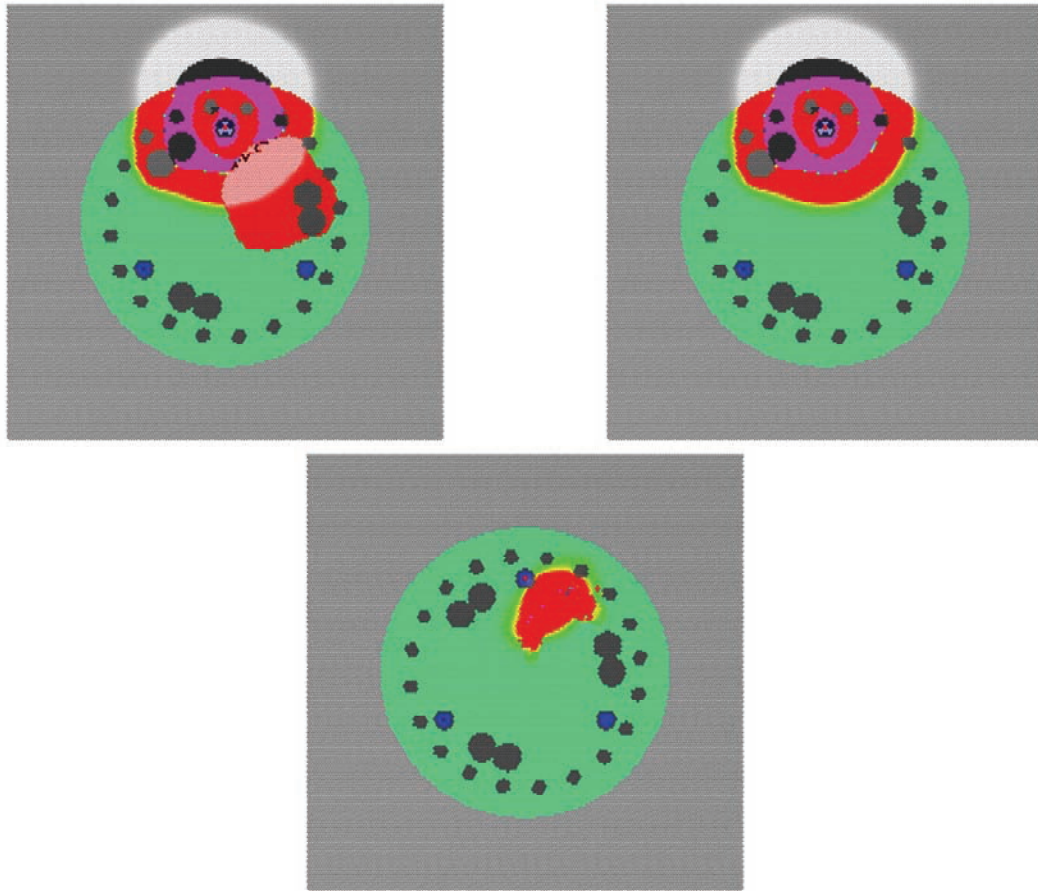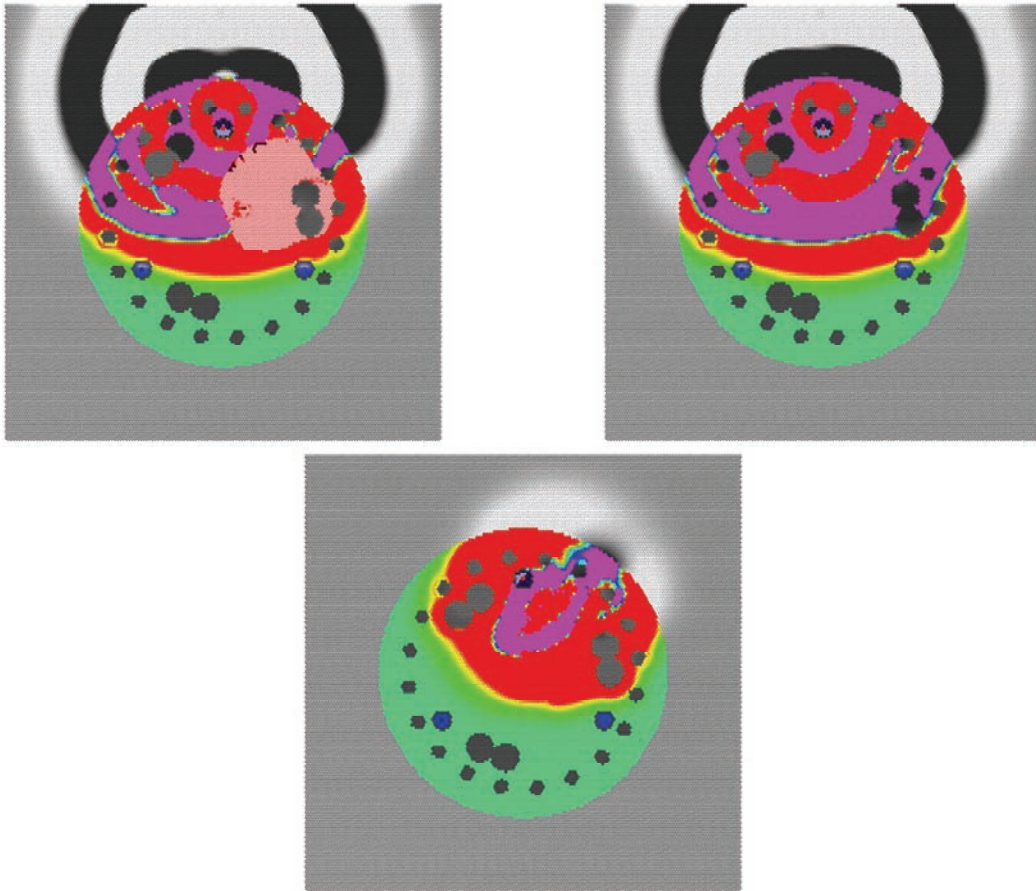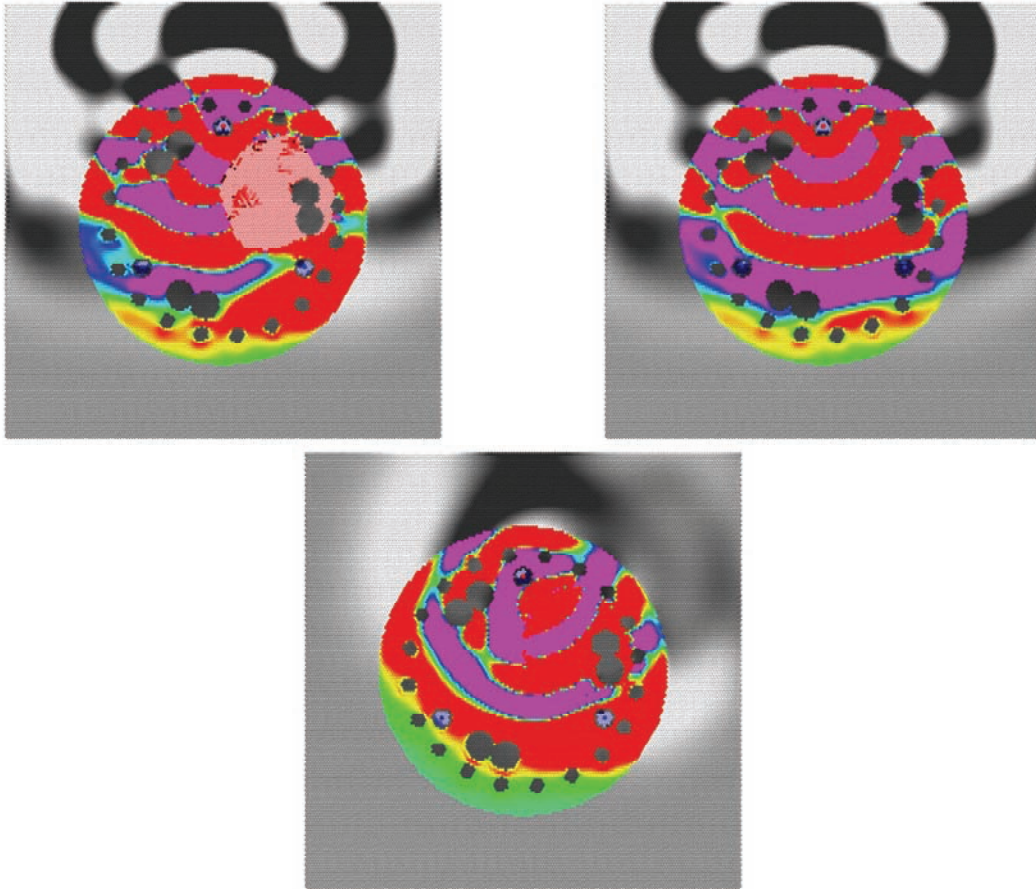

Figure 4.38. Plot. Cracking Defect (Top Left) vs. No Defect (Top Right) at 500 µs, with Difference (Bottom)

Figure 4.39 compares the waveforms collected in the access tubes. Since the cracking defect is between tubes 1 and 2, the top graph shows a much greater effect in the signal. No tension wave was propagated through the cracking defect.

Cracking does result in a significant difference in the full waveform. However, this difference does not appear in the first arrival portion of the signal, and does not significantly affect signal energy. This confirms the observation that UPV lab tests cannot measure cracking or predict specimen strength, in turn suggesting that CSL surveys will fail to detect these defects as well.

Micro-cracking readily allows propagation of compression waves, but severely attenuates and resists propagation of tension waves. Figure 4.39 shows little effect on the first arrival time, but a significant change in the amplitude of later portions of the signal at the receiver.

Figure 4.39. Chart. CSL Signals with a Cracking Defect vs. No Defect, between Access Tubes 1 and 2 (Top), and Tubes 1 and 3 (Bottom)

4.7.1 Concrete Strength Reduction

Since by its chemical nature concrete is not as thermodynamically stable as natural stone, concrete is susceptible to various forms of physical and chemical deterioration. A number of different factors can result in concrete deterioration from physical and chemical weathering. Deterioration from sunlight can cause heat-induced surface cracking. Abrasion also can affect surfaces. F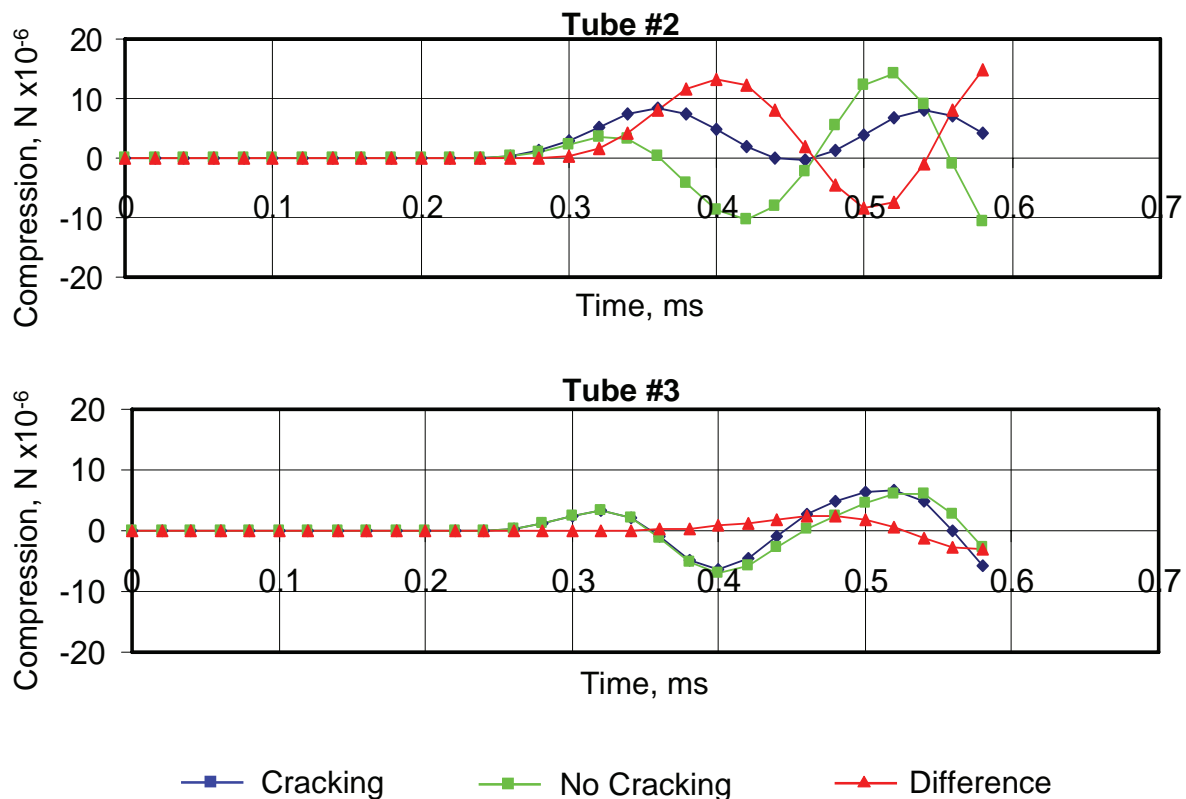or large concrete structures, chemical weathering is more significant, as damage can occur deep within the concrete structure.

Various chemical agents in the environment can cause chemical weathering or corrosion due to the reactive nature of cement. Carbon dioxide at normal atmospheric concentrations is the source of carbonic acid, which naturally reacts with and breaks down cement. This process is accelerated by acid rain, which also contains more reactive compounds such as sulfuric acid. Other sources of corrosion include the ingress of sulfates in ground water, which readily attack cement and lead to corrosion.

Reinforcing steel that is encased in concrete is naturally protected from corrosion (i.e. oxidation) because the concrete provides a highly alkaline environment. The pH of concrete including that of the pore solution is about 12.5. At a pH of 11.5 and higher, a passivating oxide film will form on the steel surfaces in contract with the concrete. As long as the passivating oxide film forms, and the high pH environment is maintained, the reinforcing steel will be protected from corrosion.

Concrete surfaces exposed to the atmosphere (CO_2) carbonate (i.e. the pH will be reduced from 12.5 to about 8.5). With time, the carbonation will progress as a front from the exposed surfaces inward toward the reinforcing steel. When the carbonation front reaches reinforcing steel or serves to reduce the pH of the pore solution sufficiently, the rebar will corrode. In concrete of low cover and permeability, this process takes decades. In concrete of high permeability, the process can take a few years.

Corrosion can also initiate in voids that interface with the steel, particularly in instances where the rebar has not been properly encased with concrete and numerous voids exist. At the void-steel interface, the passivating oxide film may have never formed or be very unstable. The voids also harbor water and oxygen, which further fuels corrosion in a low pH environment. Additionally, the chloride ion is attracted to corroding sites. It can be present in the environment surrounding the structure and ingress inward through voids and cracks in the concrete to further destroy the passivating oxide film surrounding the rebar. Wetting (provided by rain or a fluctuating water table) and subsequent drying can replenish and concentrate salts on the concrete surface leading to continual attack and deterioration. Corrosion products are more voluminous (about twice the size) of the original parent material. As they continue to expand, they cause additional cracking and deterioration of the concrete matrix.

Deterioration over time can cause large areas of weakness and cracking in the concrete, lowering bearing capacity below design specifications. The progression of chemical weathering is closely related to a basic chemical defect of concrete: the tendency to crack. The ingress of chemical

agents into concrete is directly proportional to the initial permeability of the concrete, and permeability is directly proportional to cracking. Cracking allows a pathway for corrosive agents of all kinds to penetrate deep within the concrete. Crack prevention is a key factor in improving concrete durability and resistance to deterioration.

The strength and performance of the concrete is dependent on the cracking extent within the structure. Cracking does cause a substantial decrease in both Poisson's Ratio and the stiffness of the concrete. However, cracking does not, in and of itself, necessarily result in major impacts on strength. This is especially true for concrete structures reinforced with rebar. Cracking affects the stability of tensile load behavior of concrete more than any other characteristic, so failure strength is reduced substantially in non-reinforced concrete structures by only moderate levels of cracking. Steel reinforces the tensile strength of the concrete structure so that moderate levels of cracking do not compromise structural capacity in the short term. However, the effects of cracking are a significant issue for long-term stability and durability.

4.8   Honeycombs Effects

Honeycombs are regions in concrete with a high concentration of small void areas, with a small degree of cracking. The grainy consistency in some cases can be compared with common cinder blocks sold in hardware stores. Honeycombs can be formed by using an improper cement mixture, inadequate vibration of the mixture, improper placement, by the presence of oversized aggregate, or by too tight of a spacing of the reinforcement as compared to the maximum aggregate size. For example, a portion of the sidewall of the drilled shaft could fall into the shaft during concrete placement and form a region of honeycombed concrete. The cement volume is inadequate to fill in all the gaps between the aggregate, resulting in a cluster of small voids resembling a honeycomb in appearance. Concrete strength is significantly reduced in areas of concrete affected by honeycombing. Honeycombed defects are modeled by randomly replacing a certain percentage of concrete with a void material and specifying a small percentage of cracking.

Figures 4.40 – 4.45 compare CSL signals from a drilled shaft with a honeycomb defect, shown in red, to a shaft with no defect. The honeycomb defect has slightly slower compression wave velocity, with 10% of the springs broken, and is 20% void.

Figure 4.40 shows the compression wave propagating from the source access tube after 20 μs.
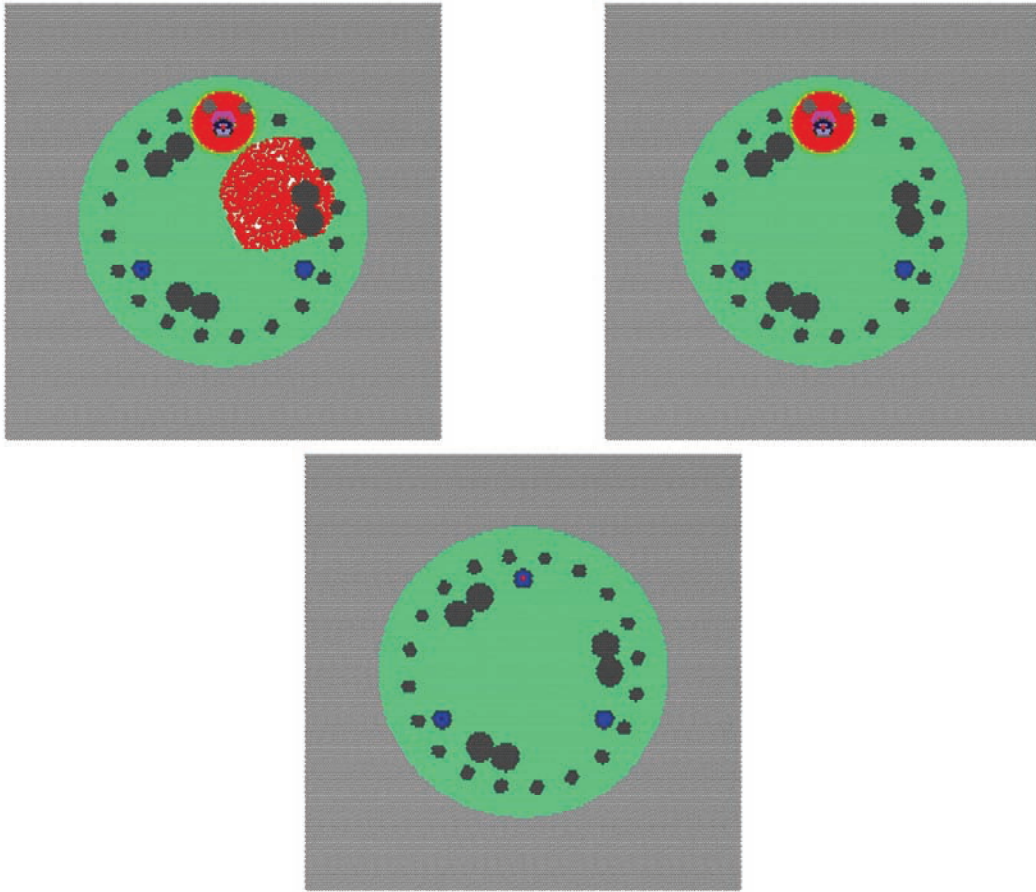
Figure 4.40. Plot. Honeycomb Defect (Top Left) vs. No Defect (Top Right) at 20 μs, with Difference (Bottom)

The wavefront first encounters the honeycomb defect in Figure 4.41 at 60 μs. The difference plot shows the effect of the honeycomb defect on the compression wave.

Figure 4.41. Plot. Honeycomb Defect (Top Left) vs. No Defect (Top Right) at 20 μs, with Difference (Bottom)

Figure 4.42 shows the compression wave at 120 μs, as the compression wave passes half way through the honeycomb defect. The voids inside the honeycomb defect delay and attenuate the wavefront.

Figure 4.42. Plot. Honeycomb Defect (Top Left) vs. No Defect (Top Right) at 120 μs, with Difference (Bottom)

Figure 4.43 shows the compression wave at 300 μs, as the compression wave reaches the receiver access tubes in the shaft with no defect. The compression wave is significantly delayed by the honeycomb defect.

Figure 4.43. Plot. Honeycomb Defect (Top Left) vs. No Defect (Top Right) at 300 μs, with Difference (Bottom)

Figure 4.44 shows the compression wave at 500 μs, as the peak of the first tension wave crosses the access tubes in the shaft with no defect. A small attenuated compression wave is crossing tube 2 in the shaft with the honeycomb defect.
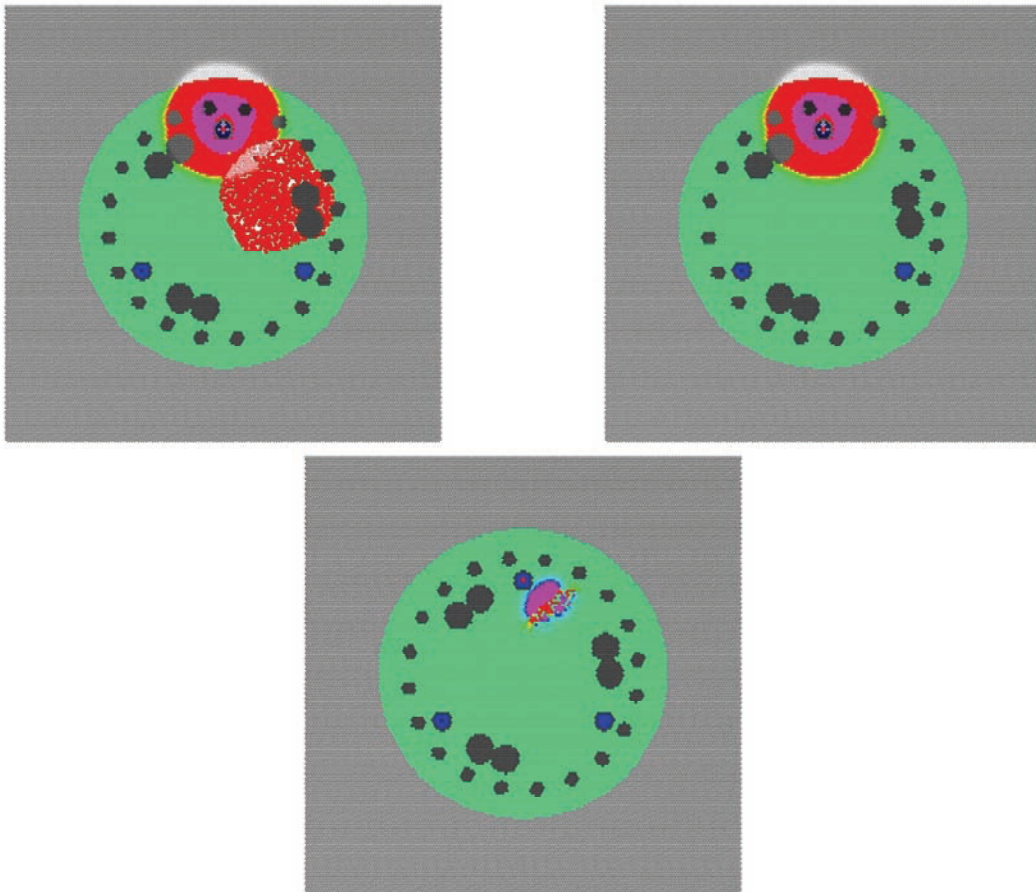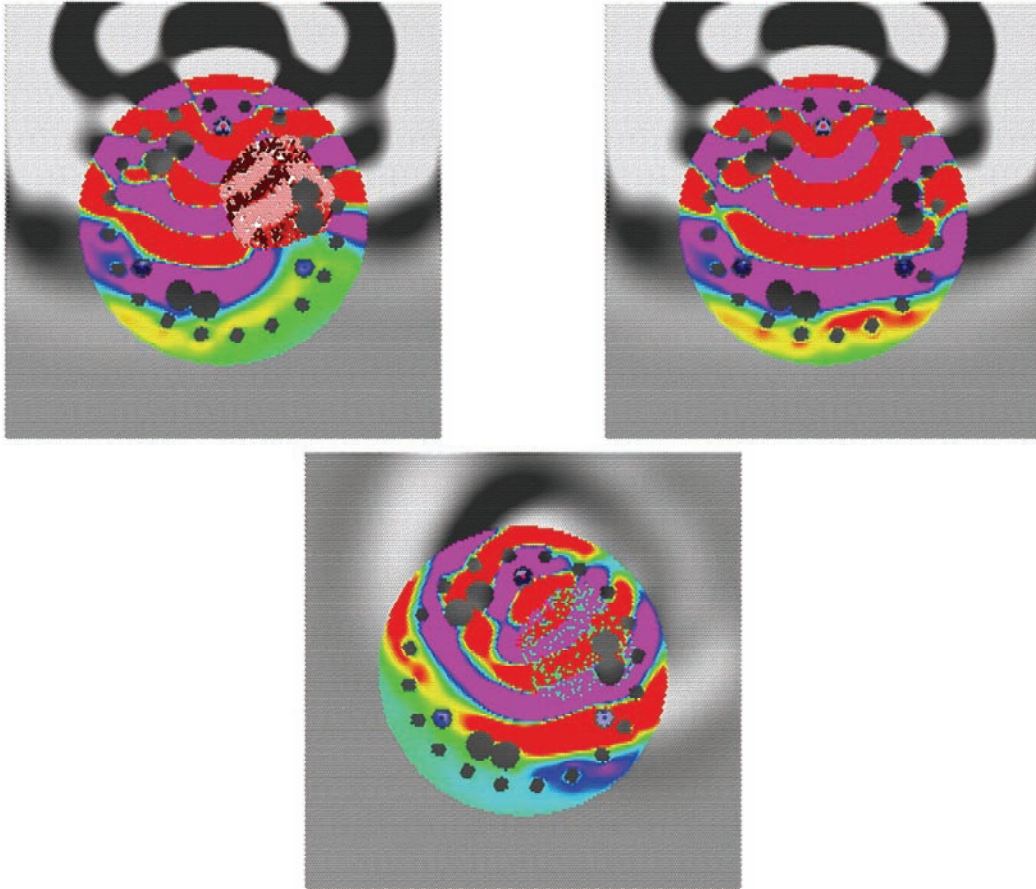

Figure 4.44. Plot. Honeycomb Defect (Top Left) vs. No Defect (Top Right) at 500 μs, with Difference (Bottom)

Figure 4.45 compares the waveforms collected in the access tubes. The top graph shows that the honeycomb defect almost entirely attenuates the signal between tubes 1 and 2.
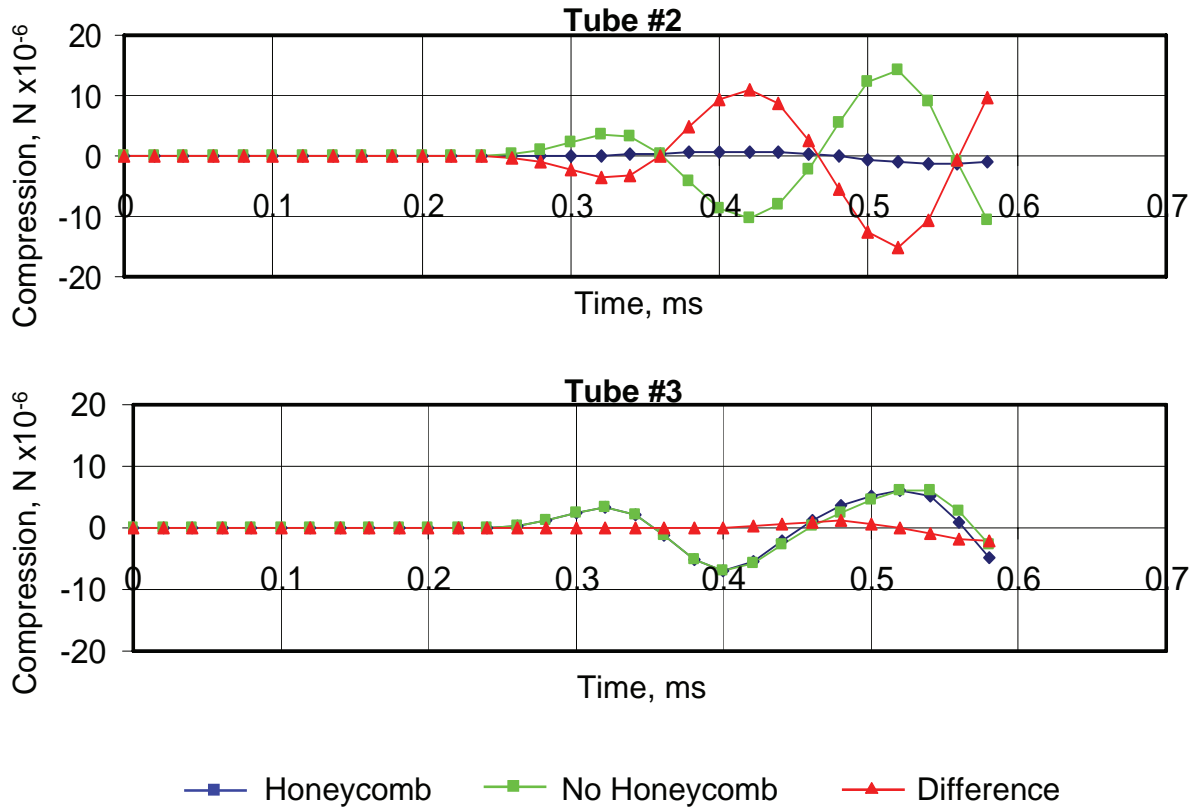
Figure 4.45. Chart. CSL Signals with a Honeycomb Defect vs. No Defect, between Access Tubes 1 and 2 (Top), and Tubes 1 and 3 (Bottom)

4.9   Effect of Voids

Occasionally concrete can be displaced by water or debris, resulting in fluid-filled voids. The voids may be filled with air or water, depending on conditions. Air-filled voids are more easily detected, so a water-filled void will be investigated instead. Figure 4.38 shows the source activation in a shaft with a water-filled void with the same size, shape, and location as the honeycomb and cracking defects previously examined.

Figures 4.46 – 4.51 show the effect of the void on the compression waves. The void is the same size as the cracking and honeycomb defects.

Figure 4.46 shows the compression wave propagating from the source access tube after 20 μs.
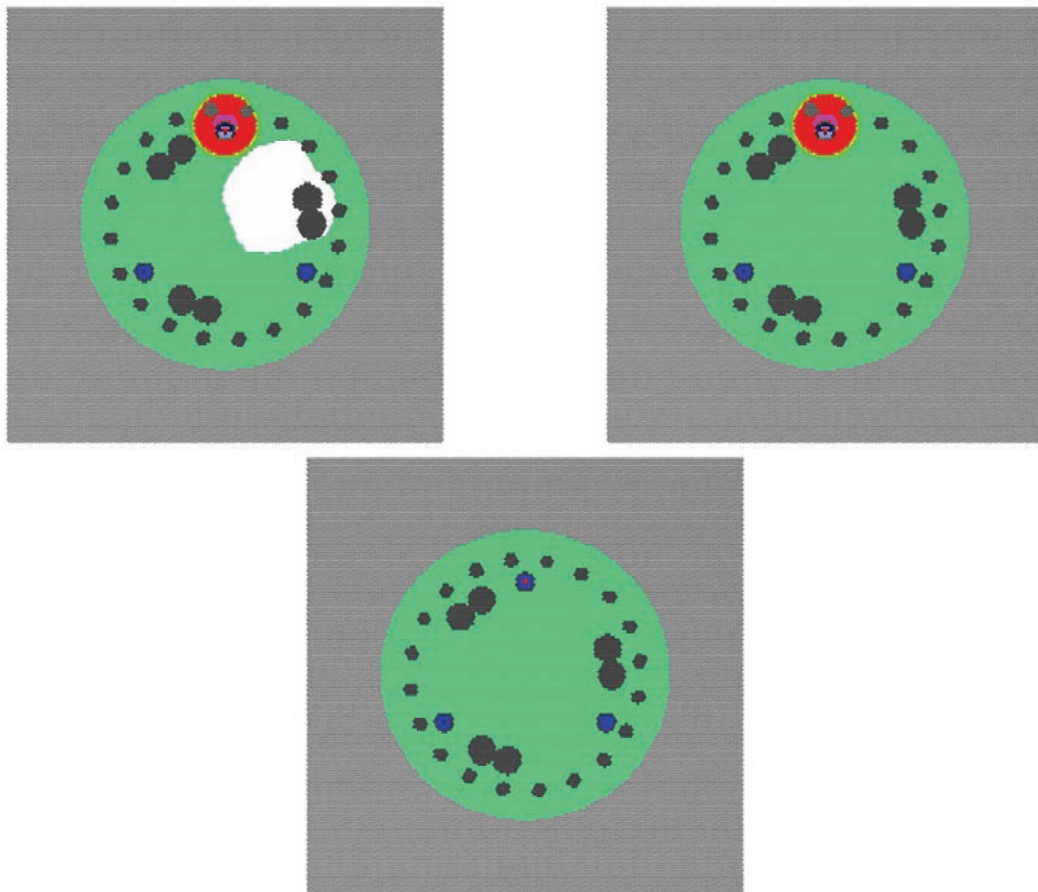
Figure 4.46. Plot. Void Defect (Top Left) vs. No Defect (Top Right) at 20 μs, with Difference (Bottom)

The wavefront first encounters the void in Figure 4.47 at 60 µs. The difference plot shows the reflection of the compression wave from the void.
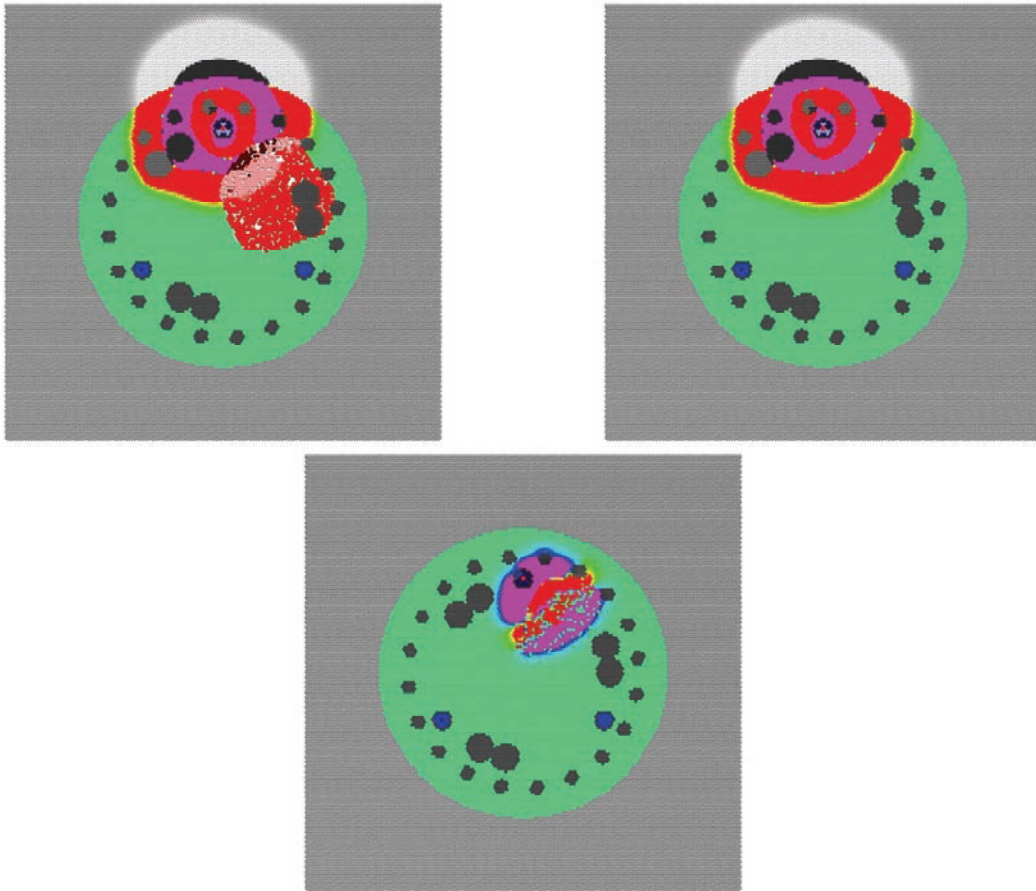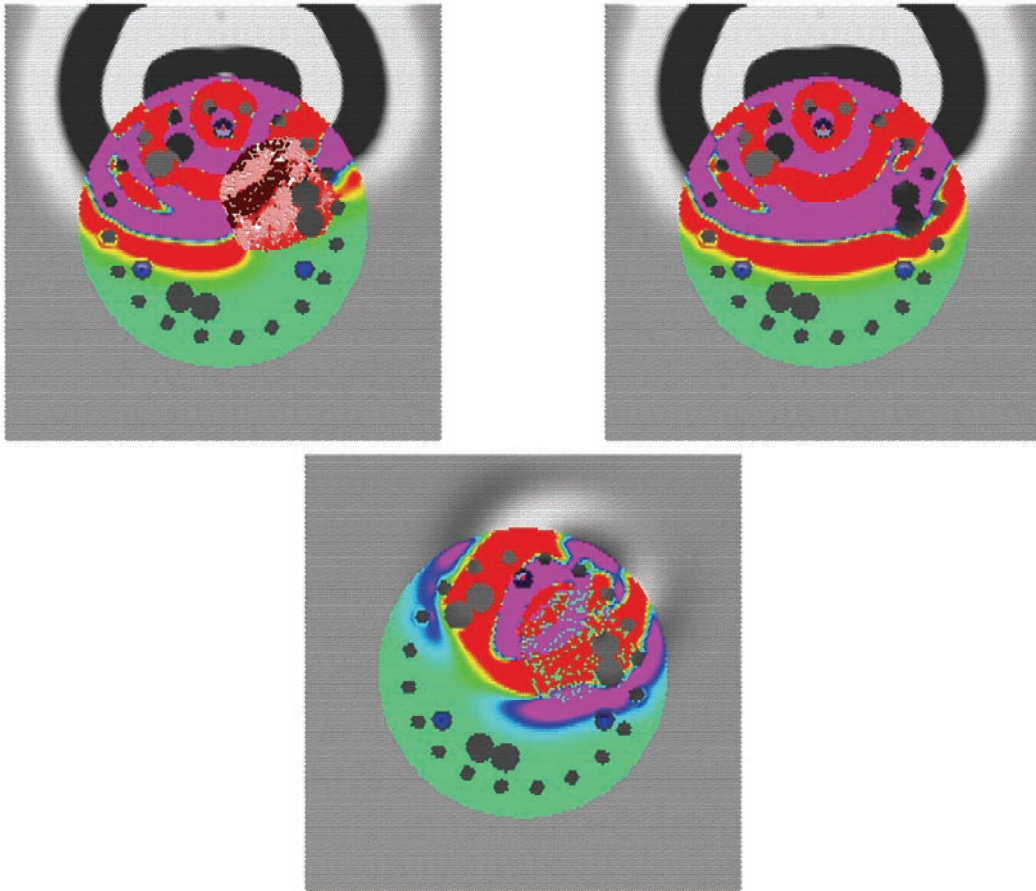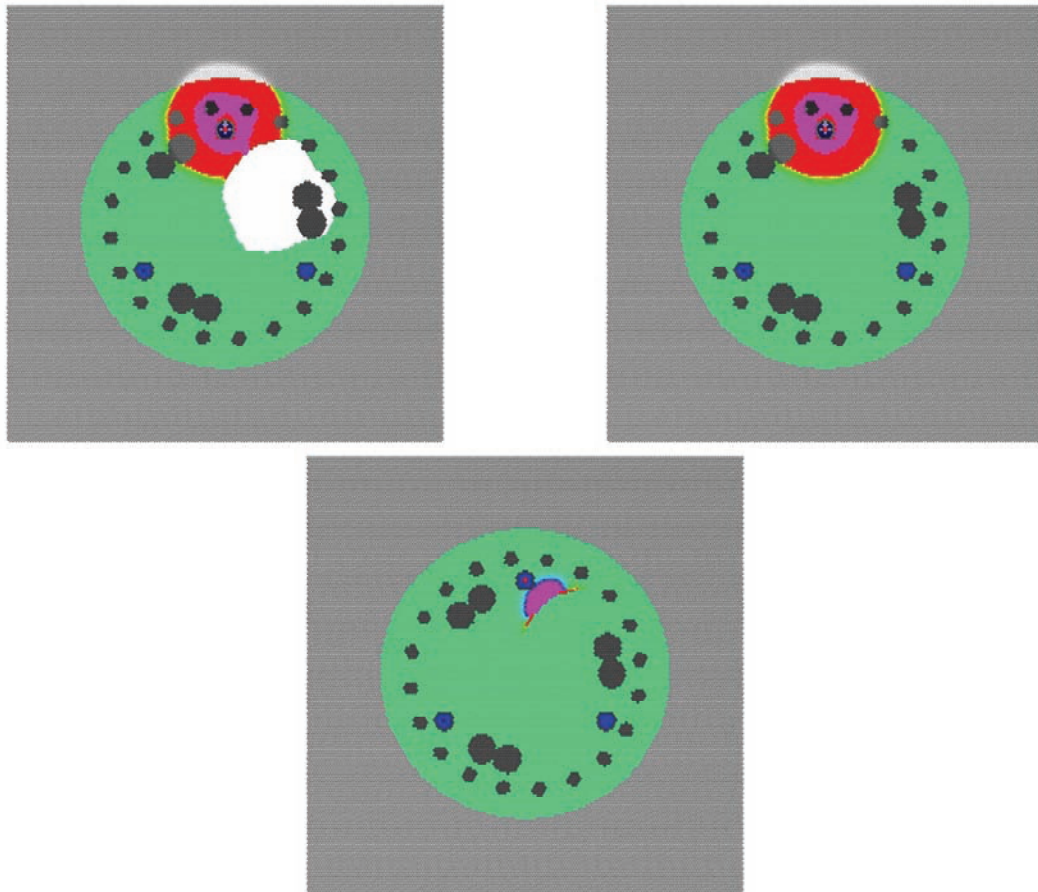

Figure 4.47. Plot. Void Defect (Top Left) vs. No Defect (Top Right) at 20 µs, with Difference (Bottom)

Figure 4.48 shows the compression wave at 120 µs, as the compression wave passes half way around the void.
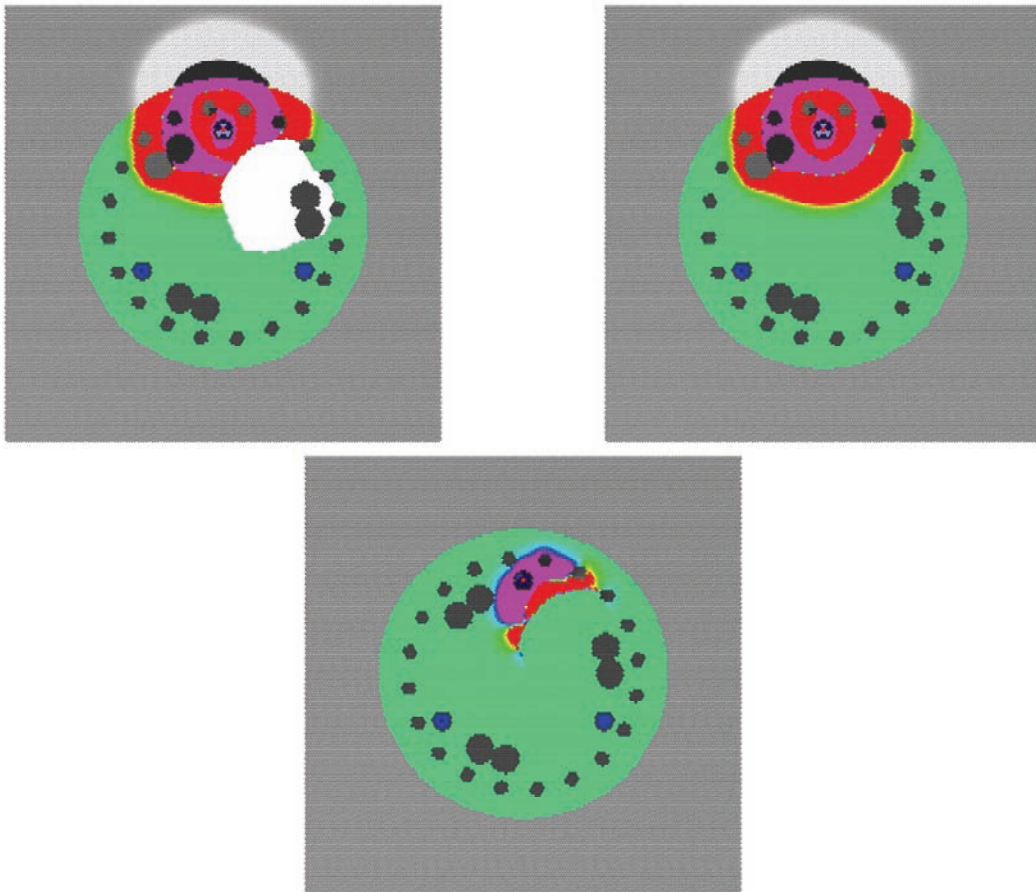
Figure 4.48. Plot. Void Defect (Top Left) vs. No Defect (Top Right) at 120 µs, with Difference (Bottom)

Figure 4.49 shows the compression wave at 300 µs, as the compression wave reaches the receiver access tubes in the shaft with no void. The compression wave has not quite encircled the void.
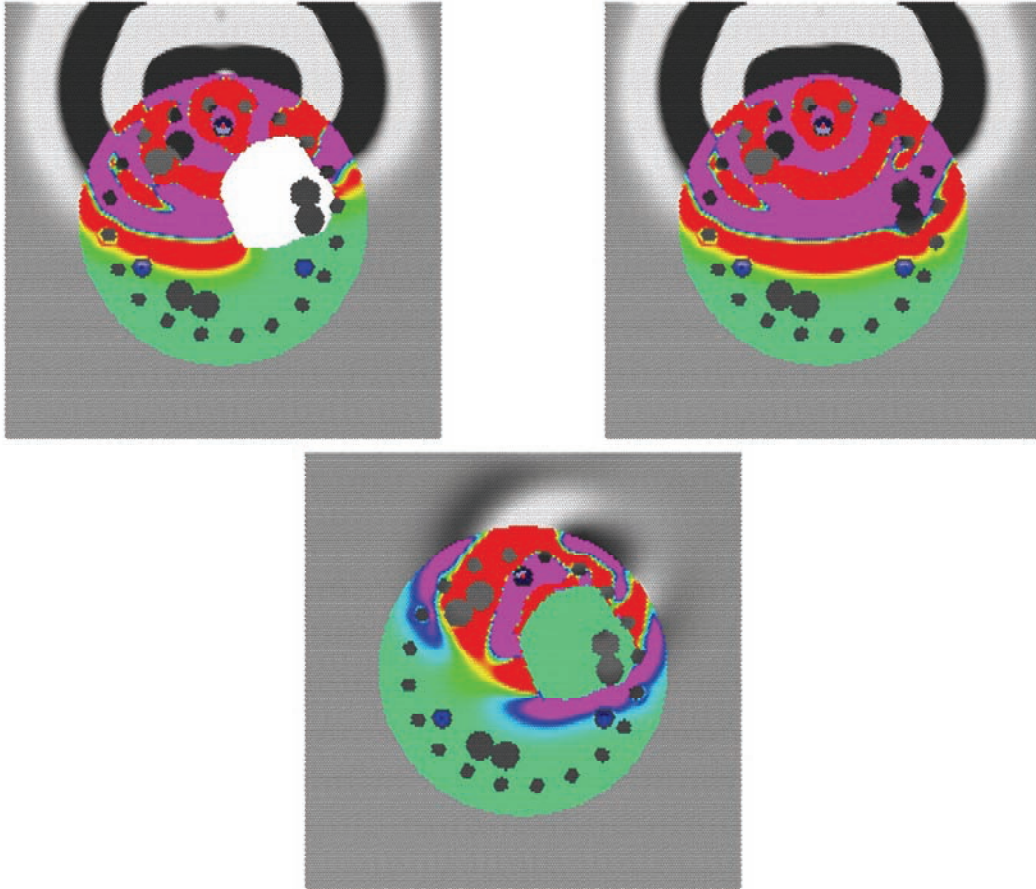
Figure 4.49. Plot. Void Defect (Top Left) vs. No Defect (Top Right) at 300 µs, with Difference (Bottom)

Figure 4.50 shows the compression wave at 500 μs, as the peak of the first tension wave crosses the access tubes in the shaft with no void. The void has almost completely attenuated the first compression wave.

Figure 4.50. Plot. Void Defect (Top Left) vs. No Defect (Top Right) at 500 μs, with Difference (Bottom)

Figure 4.51 compares the waveforms collected in the access tubes. The void significantly blocks the signal between tubes 1 and 2.
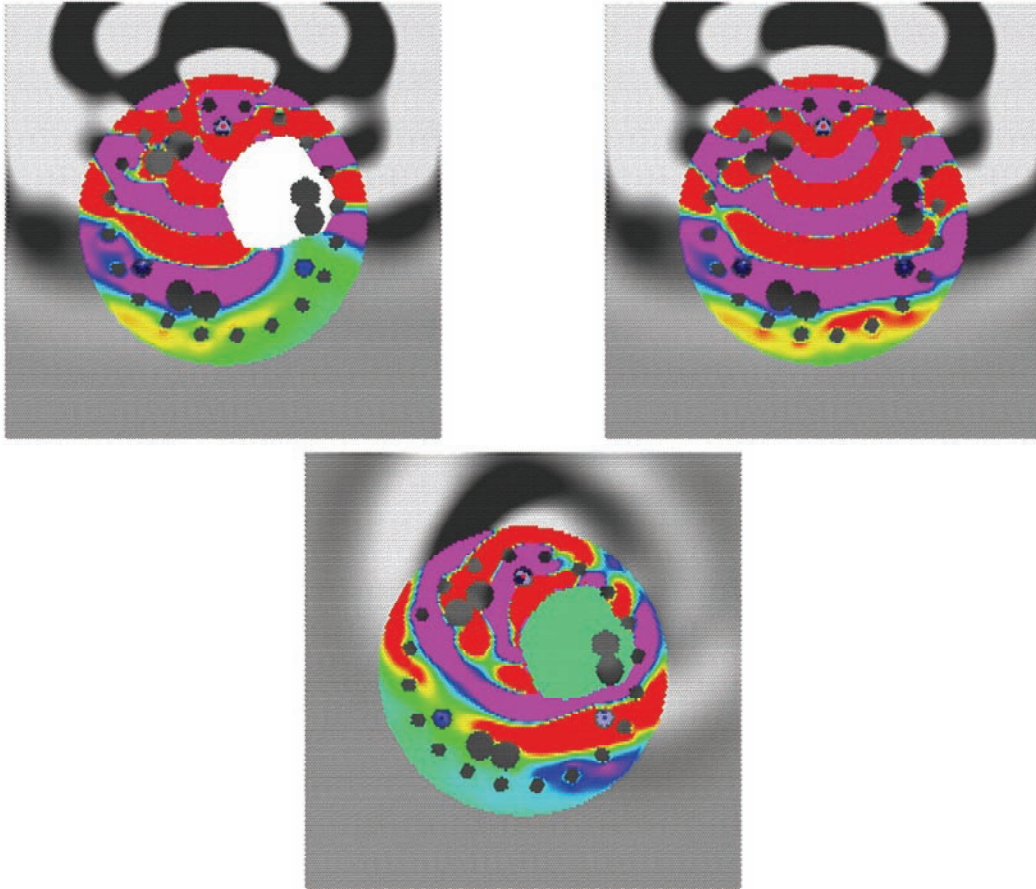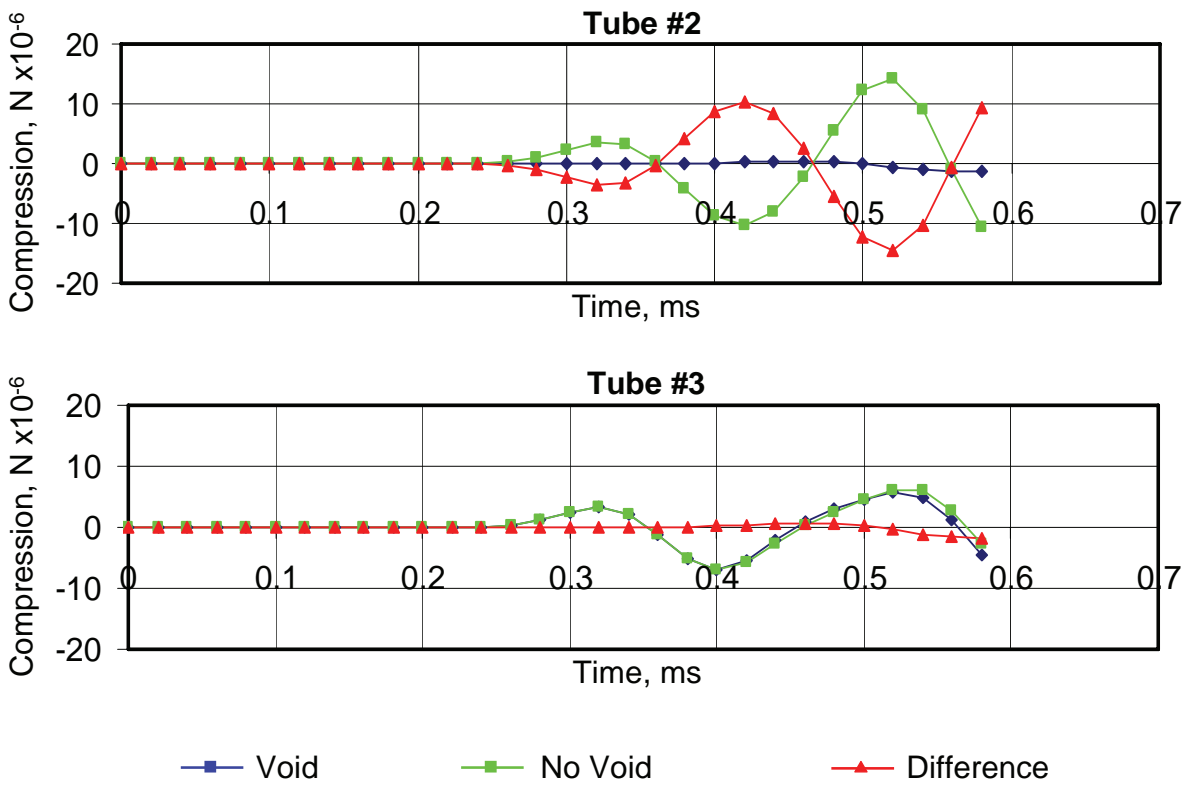

Figure 4.51. Chart. CSL Signals with a Void vs. No Defect, between Access Tubes 1 and 2 (Top), and Tubes 1 and 3 (Bottom)

CHAPTER 5.   NUMERICAL MODELING OF CONCRETE CURING

Concrete curing involves complex interactions of numerous variables. The numerical model in this section varies thermal conductivity, tension strength, modulus, heat generation, hydration phases, and volume expansion. Resulting compression stresses, cracking, and temperature are computed, which in turn affect the material properties and chemical reactions.

The following study compares a drilled shaft surrounded by rock to a drilled shaft surrounded by clay. All other factors are identical. The surrounding ground temperature is set to 10° C. The concrete is initially placed at 45° C. A very warm concrete temperature is used to encourage cracking. The first five days of concrete curing is simulated. This is sufficient time due to the high temperatures and high rates of hydration caused by the high initial concrete temperature. High placement temperatures are not recommended, as this study will show.

Rock and clay have different thermal conductivities, but the thermal effects on cracking are less pronounced in this scenario. A lower initial concrete temperature would show sharper differences in curing rates, cracking, and internal stress due to differences in thermal conductivity of the surrounding environment. For this reason, chemical modeling should be seriously considered to study complex interactions of variables for various scenarios, beyond the case presented in this study.

5.1   Empirical Curing Model Method

Figure 5.1 plots the heat of hydration curves used in the model. These curves can be obtained empirically for a particular concrete mix by measuring heat generation under isothermal conditions.

Table 5.1 lists the actual coefficients used in the model. The high temperature curve in Figure 5.1 corresponds to 50° C in the table. The average temperature corresponds to 30° C, and the low temperature corresponds to 10° C. All the curves have a rapid initial hydration phase that quickly completes within the first few minutes of concrete placement, depending on the temperature of the concrete. According to Table 5.1, the first hydration phase releases heat during first half hour at a concrete temperature of 10° C, but generates the same heat in the first 12 minutes at a higher temperature of 50° C. The curves in Figure 5.1 produce the same heat at different rates, depending on the concrete temperature, assuming that all the cement hydrates according to the same chemical reactions. This is not always the case, and should be validated empirically by isothermal lab tests. The shape of the curves corresponds to the different hydration reactions that concrete typically undergoes throughout the curing process.
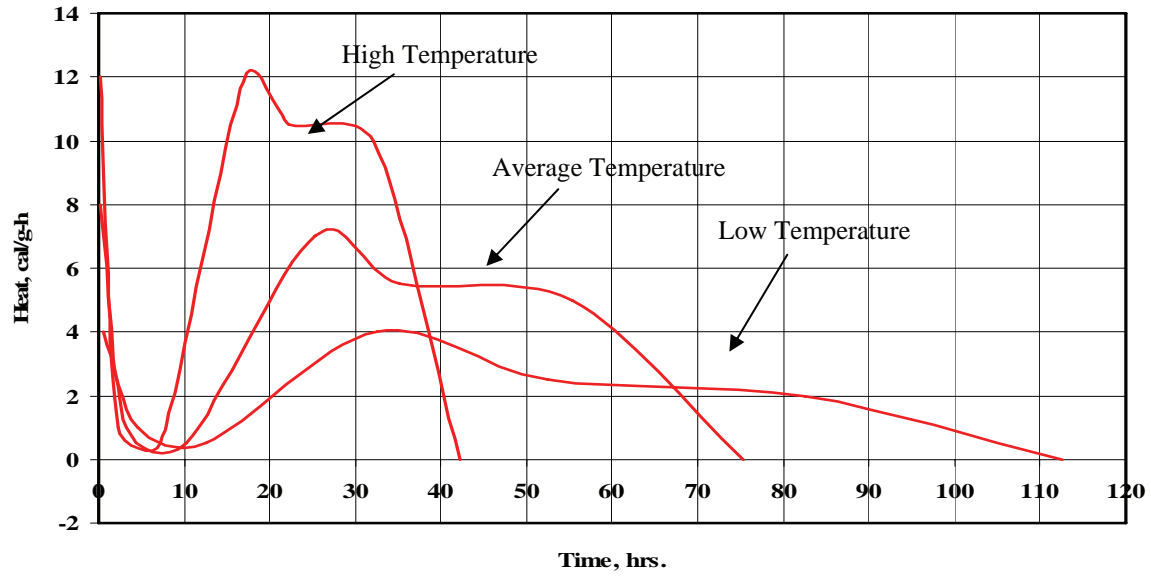
Figure 5.1. Chart. Rate of Heat Generation (Cal/hr) used in the Numerical Mode

The concrete curing model interpolates model parameters from Table 5.1 depending on the concrete temperature and hydration phase for each concrete particle element in the model. The rate of change of the hydration phase is also interpolated from the table, and updated for each concrete element. Thermal conductivity, strength, modulus, and particle volume are updated in a similar fashion. This allows the model to simulate complex interactions of parameters at a fundamental level, using empirical values tabulated from straightforward lab tests.

Table 5.1 Curing Model Coefficients

Temperature (C)	Hydration %	Heat	Time (hrs)	Thermal Conductivity	Strength	Stiffness	Radius
10	0	4	0.5	0.25	0.25	0.25	1
10	17	1	4	0.3	0.5	0.5	0.99
10	33	0.5	8	0.35	0.6	0.6	0.98
10	50	4	20	0.4	0.7	0.7	0.97
10	67	2.5	20	0.45	0.8	0.8	0.96
10	83	2	30	0.5	0.9	0.9	0.95
10	100	0	30	0.55	1	1	0.94
30	0	8	0.25	0.25	0.25	0.25	1
30	17	1	3	0.3	0.5	0.5	0.99
30	33	0.5	7	0.35	0.6	0.6	0.98
30	50	7	15	0.4	0.7	0.7	0.97
30	67	5.5	10	0.45	0.8	0.8	0.96
30	83	5	20	0.5	0.9	0.9	0.95
30	100	0	20	0.55	1	1	0.94
50	0	12	0.2	0.25	0.25	0.25	1
50	17	1	2	0.3	0.5	0.5	0.99
50	33	0.5	5	0.35	0.6	0.6	0.98
50	50	12	10	0.4	0.7	0.7	0.97
50	67	10.5	5	0.45	0.8	0.8	0.96
50	83	10	10	0.5	0.9	0.9	0.95
50	100	0	10	0.55	1	1	0.94

5.2   Curing Model Presentation

The following figures display various properties at different stages in the concrete curing process. All the figures show the drilled shaft in rock on the left, the drilled shaft in clay in the center, and the difference on the right. Many of the difference scales have been amplified for display purposes. See section 6.1 for details on the color schemes, property scales, and model parameters used in this simulation.

Certain properties are displayed for discussion purposes, but are not exhaustive. Compression, fracture extent, heat generation, hydration phase, and temperature are shown, while other properties such as material tensile strength, modulus, and thermal conductivity are not shown. Changes in element volume and displacement are shown indirectly.

Figures 5.2 - 5.5 show the compression effects of concrete curing. The compression is defined as the average force exerted on an element by attached springs. A zero compression value does not mean the element is not under compression, but that the sum of all compression and tension forces averages to zero. Initial compression was set to zero to show the effects of concrete curing. This is a reasonable assumption, since shaft excavation relieves lateral compression in clay.

Figures 5.6 - 5.9 show the fracture extent. Initially, no cracks are introduced in the concrete. This is a valid assumption, as concrete slowly changes from a fluid to a solid state. The surrounding clay is randomly initialized with 5% cracking, to simulate more realistic conditions. Each element color is determined from the number of non-broken springs attached to the element. This scheme has the effect of magnifying crack severity for display purposes, and should be taken into account when interpreting the images. A single broken spring will affect the display of two elements. Crack propagation can be traced by comparing images at different times.

Figures 5.10 - 5.13 show the heat of hydration generated from the chemical reactions. Each concrete element in the model will release basically the same amount of heat during the curing process, but potentially at different rates, depending on the temperature of the concrete. The temperature is a function of heat generation and heat transfer over time, which in turn may be affected by cracking and shrinkage of the concrete, and deconsolidation of the clay. It is important to keep in mind the many complex interactions are involved in the modeling.

Figures 5.14 - 5.17 show the hydration phase of each concrete element in the model, as a percentage of completion. Other properties, such as thermal conductivity, modulus, strength, and shrinkage often are closely correlated to the hydration phase. As the concrete changes chemical composition, the material properties of the concrete are affected correspondingly. For this reason, material properties such as thermal conductivity, modulus, strength, and shrinkage are not included in the plots.

Figures 5.18 - 5.21 show the resulting temperature of each element in the model, generated from the chemical reactions and transferred by conduction and convection. Conduction is modeled in a traditional fashion, depending on contact and thermal conductivity coefficients. Convection is modeled by retaining spring connections after fracture. Heat is allowed to transfer across springs that are broken, at a reduced rate, depending on the separation. Spring connections greater than two times the element radius are eliminated, so convection is not modeled across large crack separation. Radiation was not considered a significant factor in this study, so was not modeled.

5.3   Curing Model Simulation

The following discussion may require observation of several figures at once, due to complex interaction of various parameters during the curing phase. To minimize confusion, each parameter will be discussed individually throughout the curing process.

5.3.1 Compression

The top row of Figure 5.2 shows the compression after 4 hours. At this stage, the first hydration phase has completed, and the second hydration phase is in a very early stage.

The concrete has started to shrink slightly after the initial hydration phase. The top left image shows that the concrete is under relatively high tension at this stage, shown in magenta. This is because the concrete has not debonded from the rock, and has a very low modulus at this early stage. The rock shows no change in stress, because the rock has a much higher stiffness. The top center image shows that the clay surrounding the concrete starts to deconsolidate as the shaft shrinks. Clay has a much lower stiffness than rock, so tension forces allow more deformation in the clay. The cohesion forces and interlocking between the clay and the concrete are strong enough at this stage to cause deformation and deconsolidation of the clay, rather than debonding from the concrete. The entire shaft is still under tension, but the tension is less around the perimeter of the shaft, due to the deformation of the clay. This difference is more pronounced in the difference image at the top right. This shows that the tension in the center of the shaft is the same for both models, but slightly lower in the outer portions of the shaft around the rebar cage, due to the deformation in the clay.

The tension stress in the shaft is large enough to overcome cohesion forces bonding the rebar and access tubes to the concrete. This debonding affects the compression stresses in the shaft. Careful observation indicates that the tension forces are lower in regions near the rebar and access tubes. These lower tensions are a result of the different thermal expansion rates between steel and concrete, and also due to the differences in initial temperature and thermal conductivity. The steel was initialized at 10° C, while the concrete was placed at 45° C. The difference in temperature as heat transfers from the warm concrete to the cool steel results in a different hydration rate in the vicinity of the rebar, causing lower initial stiffness and lower initial strength in the adjacent concrete. These property changes result in lower tension in these regions, but because of the lower strength, slight debonding begins to occur even at this very early stage in the curing process. The debonding between steel and concrete is slightly more pronounced in the shaft surrounded by rock, because of the higher tension forces in the perimeter of the shaft.

After 8 hours, as shown in the bottom row of Figure 5.2, the second hydration phase is beginning to generate heat in warmer regions of the concrete. The concrete continues to shrink, expanding the region of clay deconsolidation, and reducing tension around the rebar. Tension in the concrete around the rebar in the shaft surrounded by rock has reached zero, in some regions. The difference plot shows much lower tension forces in the shaft surrounded by rock in regions around the rebar, but higher tension forces along the perimeter. The higher tension forces along the perimeter are due to the high stiffness of the rock.
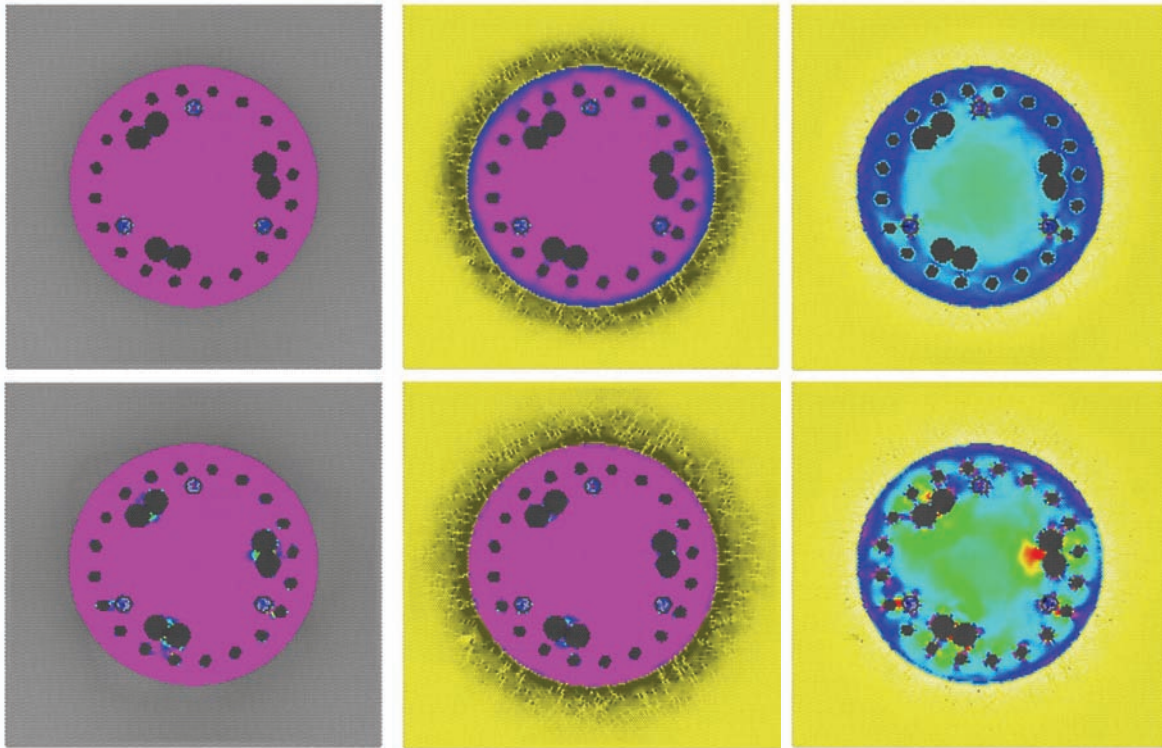
115

Figure 5.2. Plot. Curing Compression. Top: 4 hours. Bottom: 8 hours. Left: Rock. Middle: Clay. Right: Difference

The large differences in tension stress are a result of the stiffness of the surrounding ground, not due to differences in thermal conductivity. This is an important factor which is easily overlooked in the analysis of thermal cracking. This factor is more pronounced for higher concrete placement temperatures, but is still a major contributing factor in thermal cracking in other scenarios as well.

The top row of Figure 5.3 shows the compression stress condition at 12 hours, as more heat is generated from the second hydration phase. Careful observation of the image on the left shows a release in tension forces in the rock at the left of the shaft, as tension forces in the strengthening concrete begin to overcome the cohesion and interlocking forces bonding the concrete to the rock. Tension forces remain lower in the perimeter of the shaft surrounded by clay. The tension forces in the center of the shaft are basically the same for both cases.

The bottom row of Figure 5.3 shows the compression stress condition at 24 hours, at the peak of the second hydration phase. The shaft on the left exhibits a sharp decrease in tension forces along the perimeter of the shaft, after the concrete fully debonds from the surrounding rock. However, the high variations in compression in the vicinity of the rebar are a result of cracking,
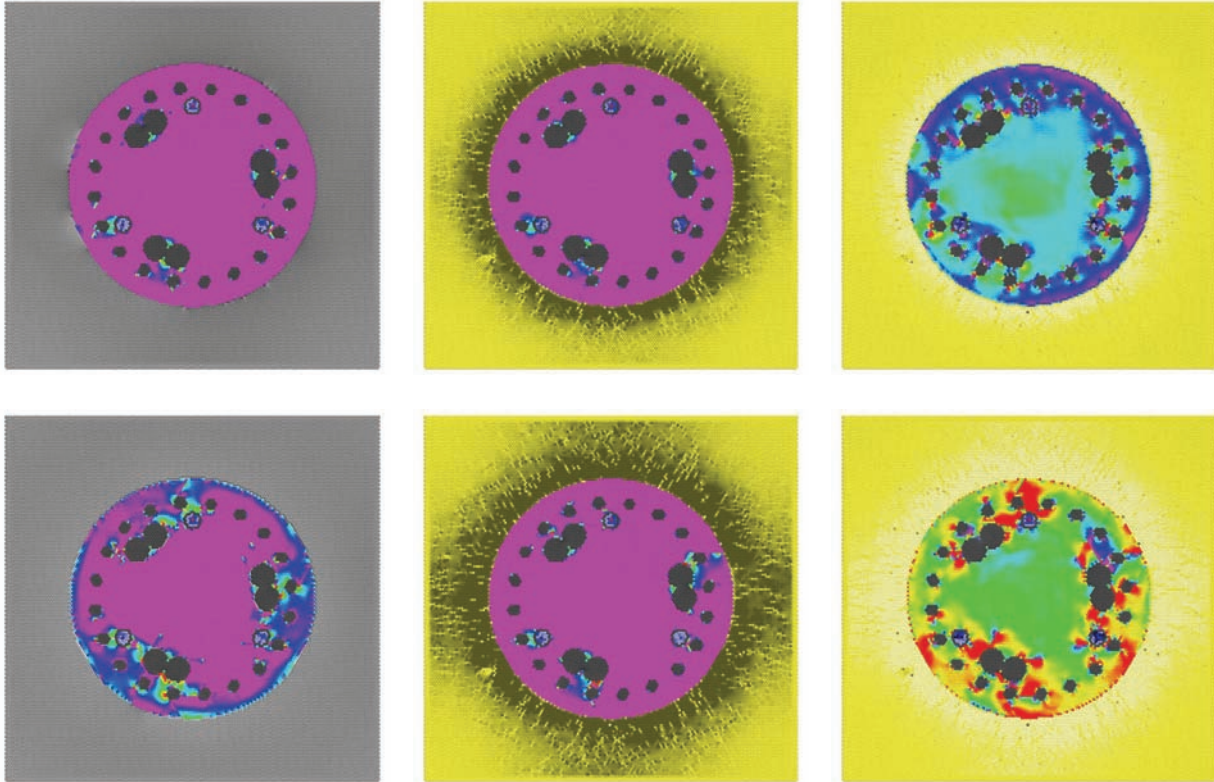
Figure 5.3. Plot. Curing Compression. Top: 12 hours. Bottom: 24 hours. Left: Rock. Middle: Clay. Right: Difference

due to the high tensile stresses formed before debonding with the rock. The clay has not debonded, so the clay continues to deconsolidate as the shaft shrinks.

The top row of Figure 5.4 shows the compression stress condition at 2 days, at the peak of the third hydration phase. Compression stress continues to build in the shaft on the left in the region of the rebar. The rock now has no effect on compression stress, except indirectly through convection cooling. Tension stresses in the clay have increased to the point of initiating slight debonding between the clay and the concrete. Debonding appears to occur first in the regions adjacent to the rebar. The compression stress does not clearly indicate why debonding occurs first in this region. However, internal compression stress has increased to positive levels for the first time in some regions. The compression stress has reached levels capable of deforming the access tubes.

The thickness of the access tube is only one element at this resolution, and is unable to provide the proper shear resistance force. The difference image on the right has some very interesting features. As micro-cracks propagate, regions of high stress concentrate at the point of the crack. Two of these regions can be seen near the center of the shaft. The bottom row of Figure 5.4 shows the compression stress condition at 3 days, at the end of the third hydration phase. Very little additional heat is generated after this point, but the shaft continues to cool, shrink, and
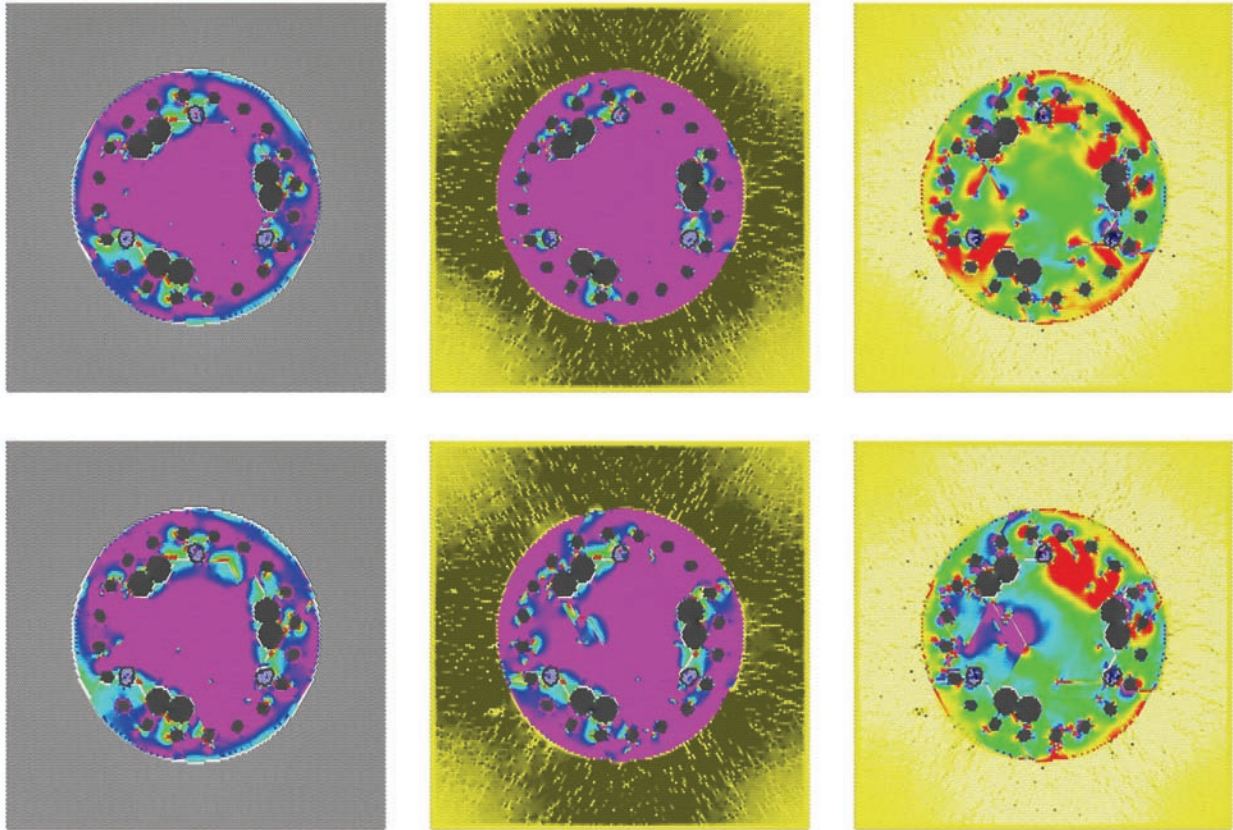
Figure 5.4. Plot. Curing Compression. Top: 2 days. Bottom: 3 days. Left: Rock. Middle: Clay. Right: Difference

crack. Compression stress at this stage is closely correlated to rebar and tube debonding, and internal cracking of the shaft.

After 4 days, the shaft compression stress has stabilized, as shown in Figure 5.5. The overall internal stress in the shaft surrounded by rock is nearly zero, but with pockets under high tension and compression. The high tension at the perimeter of the shaft is of concern, because of a higher future cracking potential that could weaken the shaft and expose the rebar to corrosives. The surrounding rock is unaffected, but the clay has deconsolidated to greater than one radius away from the shaft. This is a serious concern, because soil near the surface contributes significant support to the foundation. Reduction in the consolidation of the surrounding ground due to excavation and concrete shrinkage can lower the shaft capacity.

The internal stresses in the shaft surrounded by clay are more pronounced, especially in tension. These stresses will persist in the shaft, unless disrupted by additional cracking. Regions under tension are most likely to crack under future loading. Although both cases have similar fracture extent, the shaft surrounded by clay is much weaker, due to trapped pockets of internal tension.
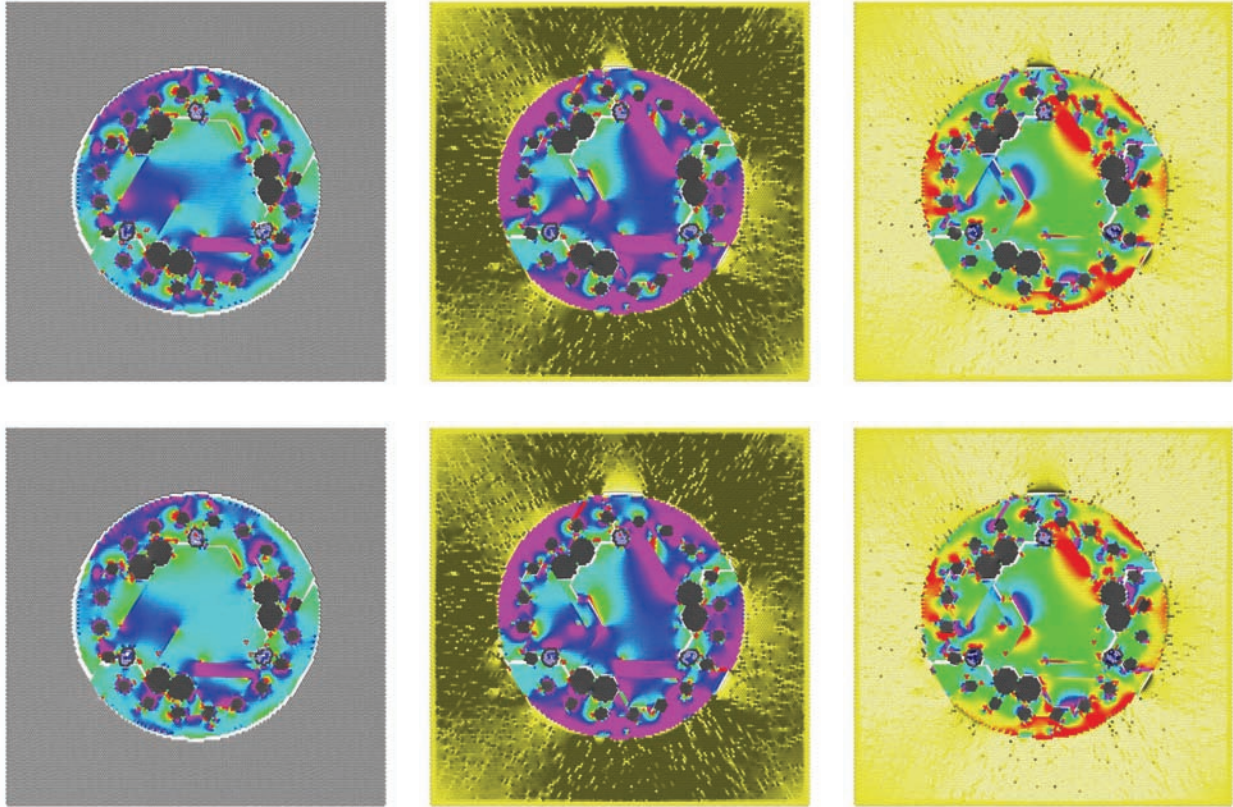
Figure 5.5. Plot. Curing Compression. Top: 4 days. Bottom: 5 days. Left: Rock. Middle: Clay. Right: Difference

5.3.2 Cracking

The top row of Figure 5.6 shows the cracking extent 4 hours after concrete placement. Slight cracking can be observed around access tubes. Although debonding occurs at an early stage, NDE techniques such as CSL can only detect debonding at later stages after significant separation. The bottom row of Figure 5.6 shows the cracking extent 8 hours after concrete placement, between the first and second hydration phases. At this stage, micro-cracks have formed in the concrete completely around all access tubes and rebar in the shaft surrounded by rock. The higher tension forces pull the concrete away from the steel, breaking the weak cohesive bonds. Due to cooler temperatures surrounding the steel, the concrete in these regions is not as mature as concrete in warmer portions of the shaft. The shaft surrounded by clay shows more debonding around the large rebar. The higher thermal conductivity and greater volume of the rebar has the effect of reducing the temperature of adjacent concrete.

Lower temperatures slow hydration, which in turn delay development of concrete strength and stiffness. Narrow regions of concrete between closely spaced rebar, and between rebar adjacent to access tubes, begins to crack at this stage.
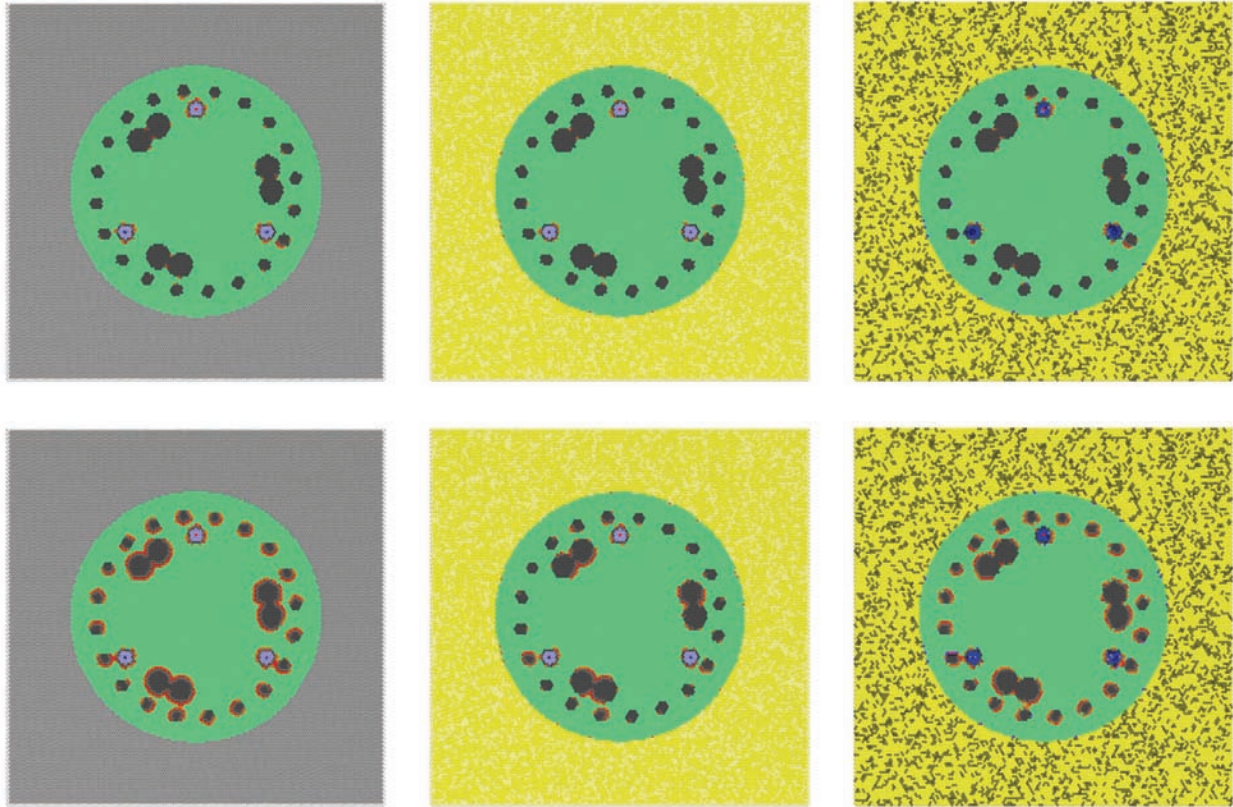
119

Figure 5.6. Plot. Curing Fracture. Top: 4 hours. Bottom: 8 hours. Left: Rock. Middle: Clay. Right: Difference

The top row of Figure 5.7 shows the fracture extent at 12 hours, as more heat is generated from the second hydration phase. Early stages of debonding can be detected between the concrete and the surrounding rock. The lower clay stiffness results in higher displacements, allowing the clay to deconsolidate before debonding from the shaft. Internally, cracks begin to propagate from the rebar in the shaft surrounded by rock, generally parallel to the perimeter of the shaft where tension forces are greatest. A small crack can be seen extending from the rebar toward the debonded rock in the lower left of the image. It is interesting to note that thermal cracking propagates from the inside of the shaft out, and initiates at the rebar.

The bottom row of Figure 5.7 shows the fracture extent at 24 hours, at the peak of the second hydration phase. Cracks surrounding the shaft on the left indicate complete debonding between the concrete and surrounding rock. More cracks have formed along the perimeter of the shaft between the rebar and access tubes. Cracks have also developed from the rebar to the outside of the shaft.
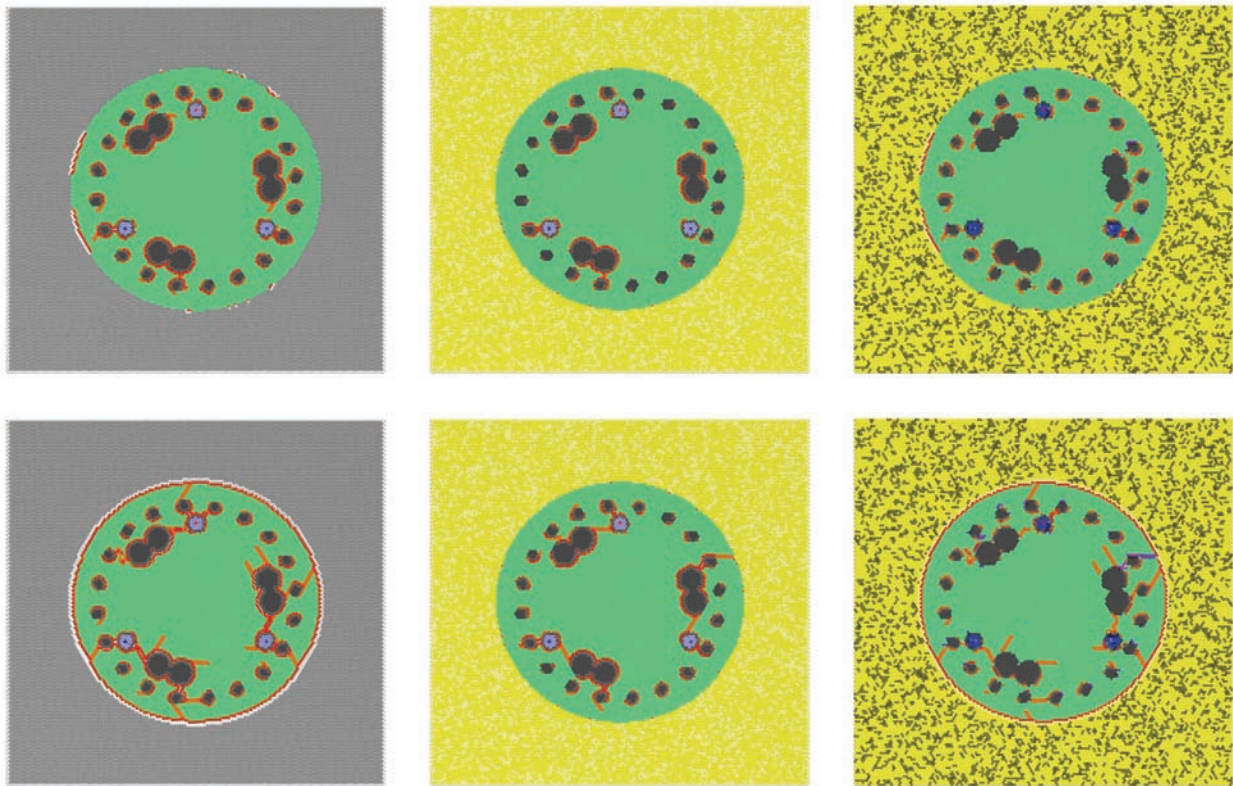

Figure 5.7. Plot. Curing Fracture. Top: 12 hours. Bottom: 24 hours. Left: Rock. Middle: Clay. Right: Difference

The top row of Figure 5.8 shows cracking extent at 2 days, at the peak of the third hydration phase. Cracks in both cases have extended almost entirely around the shaft in the region of the rebar cage. Cracks in the shaft surrounded by clay also extend across the central regions of the shaft.

The bottom row of Figure 5.8 shows cracking extent at 3 days, at the end of the third hydration phase. No additional cracking is observed, indicating that cracking has stabilized after 2 days. Figure 5.9 verifies this stabilization, as no change in cracking is observed after day 4.
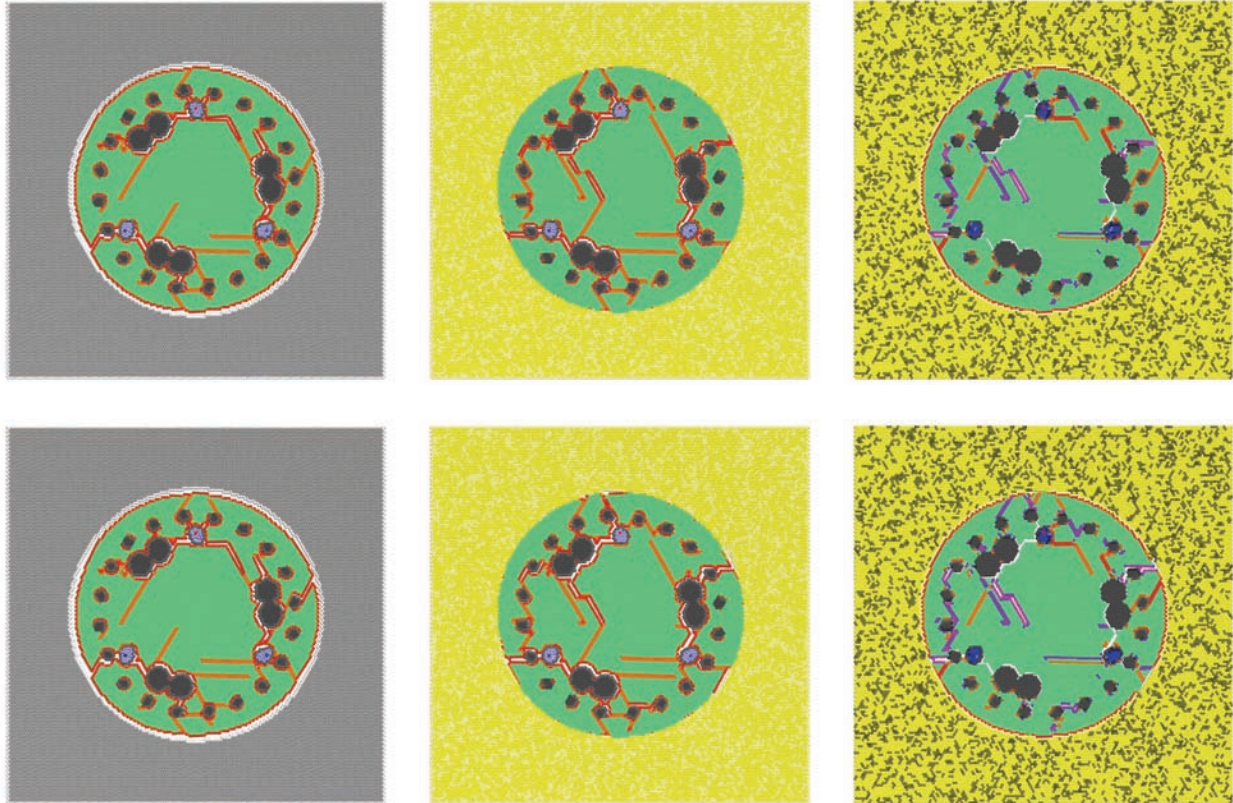

Figure 5.8. Plot. Curing Fracture. Top: 2 days. Bottom: 3 days. Left: Rock. Middle: Clay. Right: Difference
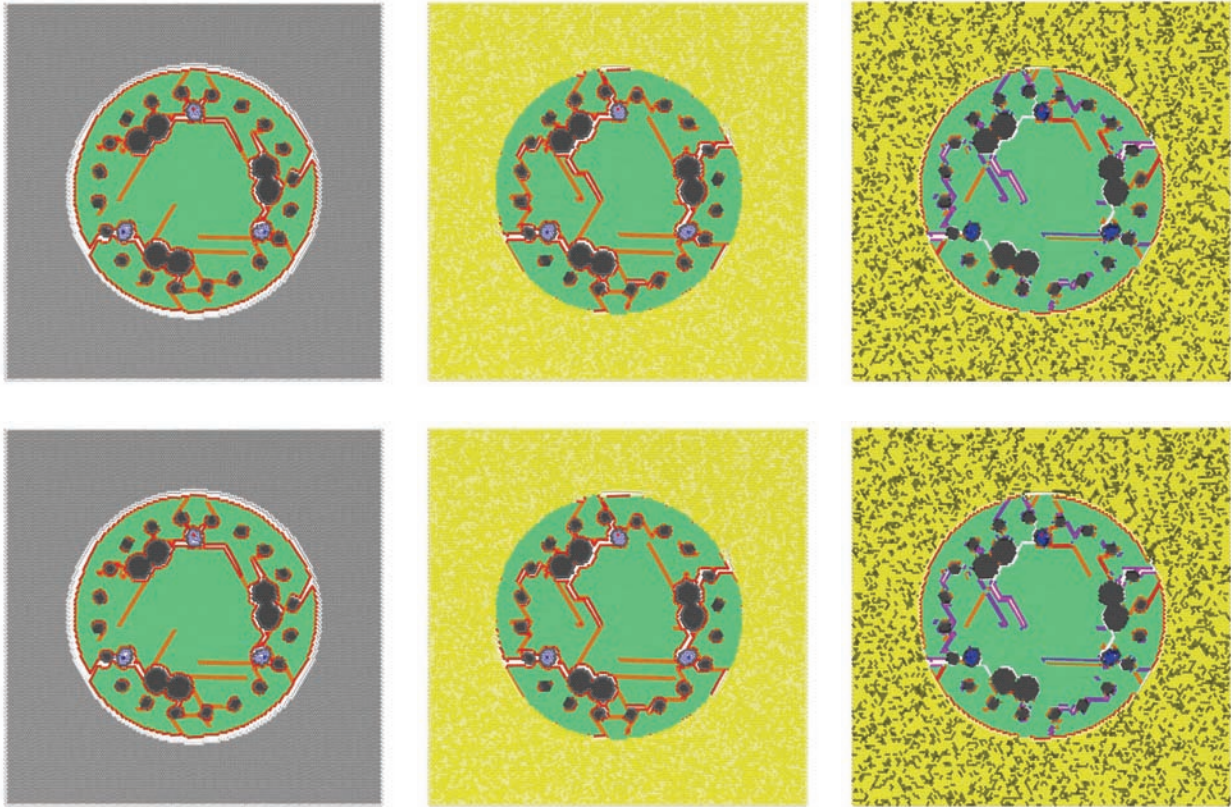
Figure 5.9. Plot. Curing Fracture. Top: 4 days. Bottom: 5 days. Left: Rock. Middle: Clay. Right: Difference

5.3.3 Heat

The top row of Figure 5.10 shows the heat generated from hydration 4 hours after concrete placement. This is the stage between the first and second hydration phases, so no heat is generated in either case.

The bottom row of Figure 5.10 shows the heat generated from hydration 8 hours after concrete placement. Most of the concrete is in early stages of the second hydration phase. Regions around the rebar and the perimeter of the shaft have cooler temperatures due to heat transfer, so this concrete has not yet entered the second hydration phase. The combination of cooler temperatures and delayed heat generation result in further delay of concrete curing in these regions. Less heat is generated in concrete adjacent to the clay because of the difference in thermal conductivity between the clay and the rock. Clay has higher thermal conductivity, so more heat is transferred into the surrounding clay than into the rock. These lower temperatures result in delayed hydration around the perimeter.

Figure 5.10. Plot. Curing Heat. Top: 4 hours. Bottom: 8 hours. Left: Rock. Middle: Clay. Right: Difference

The top row of Figure 5.11 shows the heat generated at 12 hours. The center of the shaft has reached the peak of the second hydration phase, due to the high placement temperature, and sustained high temperatures. Concrete in the region of the rebar, where temperatures are cooler, is at the beginning of the second hydration phase.

The bottom row of Figure 5.11 shows the heat generated at 24 hours. Heat generation is more uniform throughout the shaft, although the concrete is not at the same maturity level.
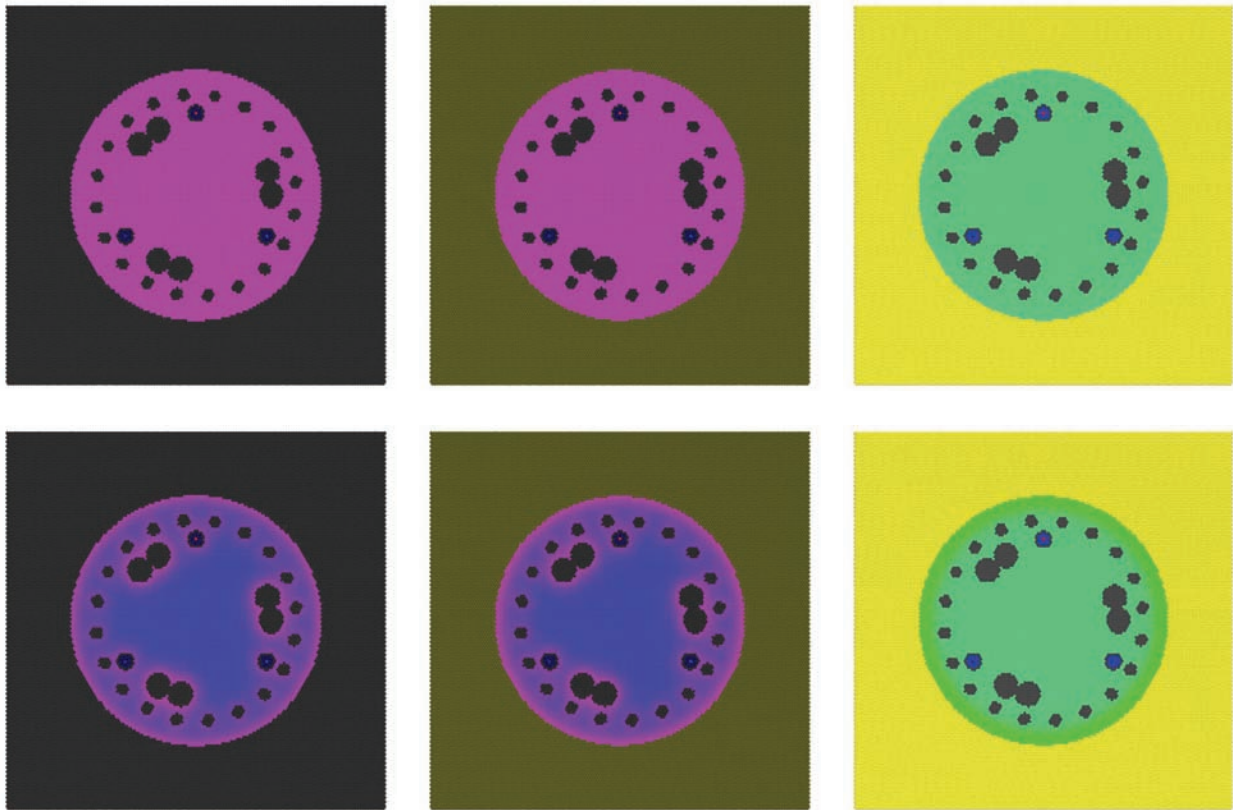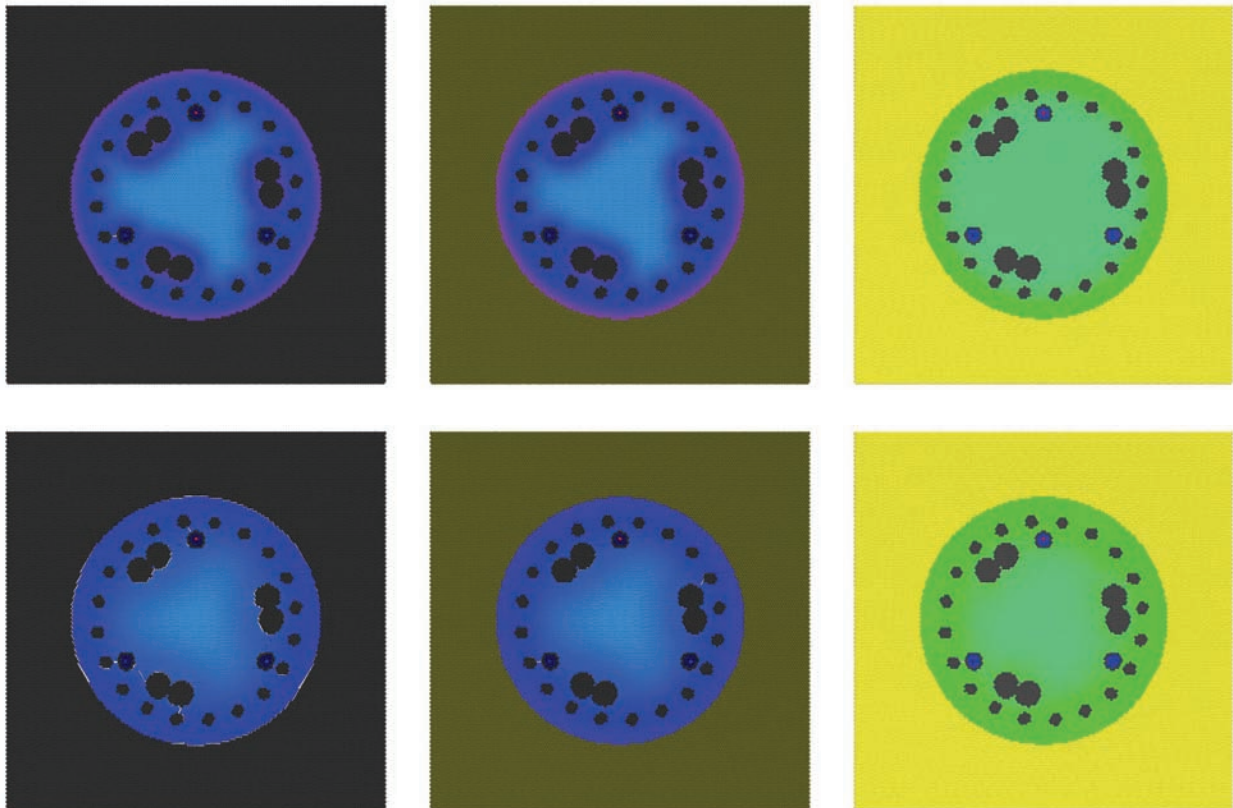

Figure 5.11. Plot. Curing Heat. Top: 12 hours. Bottom: 24 hours. Left: Rock. Middle: Clay. Right: Difference

The top row of Figure 5.12 shows heat generation at 2 days. The center of the shaft has fully cured, and has stopped generating additional heat. The concrete in the rock is slightly more mature than the concrete surrounded by clay, as shown in the difference plot.

The bottom row of Figure 5.12 shows heat generation at 3 days. Almost all the concrete has ceased heat generation, except for a very thin section around the perimeter of the shaft surrounded by clay, as shown in the difference plot.
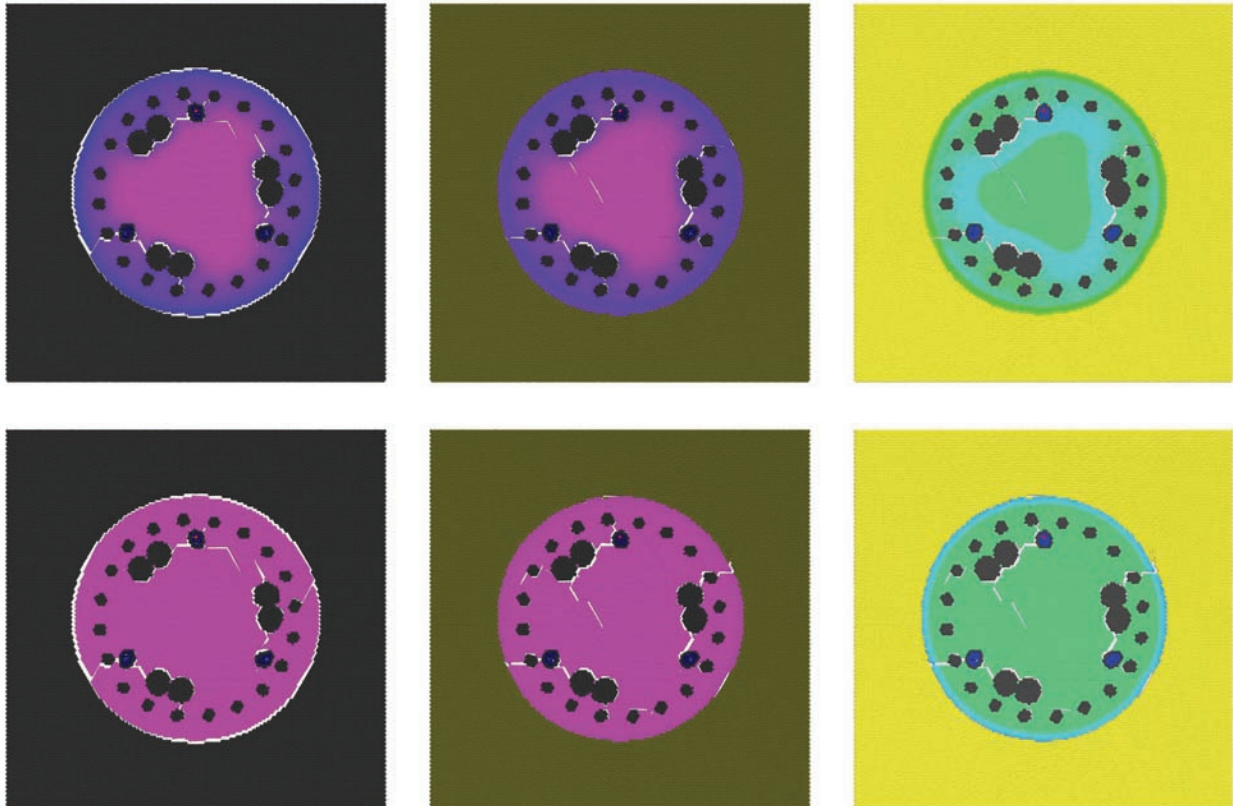
Figure 5.12. Plot. Curing Heat. Top: 2 days. Bottom: 3 days. Left: Rock. Middle: Clay. Right: Difference

Figure 5.13 shows that no additional heat is generated after day 4.

Figure 5.13. Plot. Curing Heat. Top: 4 days. Bottom: 5 days. Left: Rock. Middle: Clay. Right: Difference

5.3.4 Hydration

The top row of Figure 5.14 shows the hydration phase 4 hours after concrete placement. This is the stage between the first and second hydration phases, and is essentially the same for both drilled shafts. The bottom row of Figure 5.14 shows that the concrete from both shafts begins the second hydration phase at the same time.

**Figure 5.14. Plot. Curing Hydration. Top: 4 hours. Bottom: 8 hours. Left: Rock. Middle: Clay. Right: Difference.**

Figure 5.15 shows the hydration phase after 12 hours and 24 hours. A more pronounced difference in concrete maturity appears after 24 hours between the inside and outside portions of the shaft, but the surrounding rock and clay have little effect on the hydration phases. Figure 5.16 shows that the center of the shaft reaches maturity before the perimeter, and then stabilizes, as shown in Figure 5.17. Material stiffness, strength, thermal conductivity, and expansion volume follow a similar pattern.

Figure 5.15. Plot. Curing Hydration. Top: 12 hours. Bottom: 24 hours. Left: Rock. Middle: Clay. Right: Difference

Figure 5.16. Plot. Curing Hydration. Top: 2 days. Bottom: 3 days. Left: Rock. Middle: Clay. Right: Difference
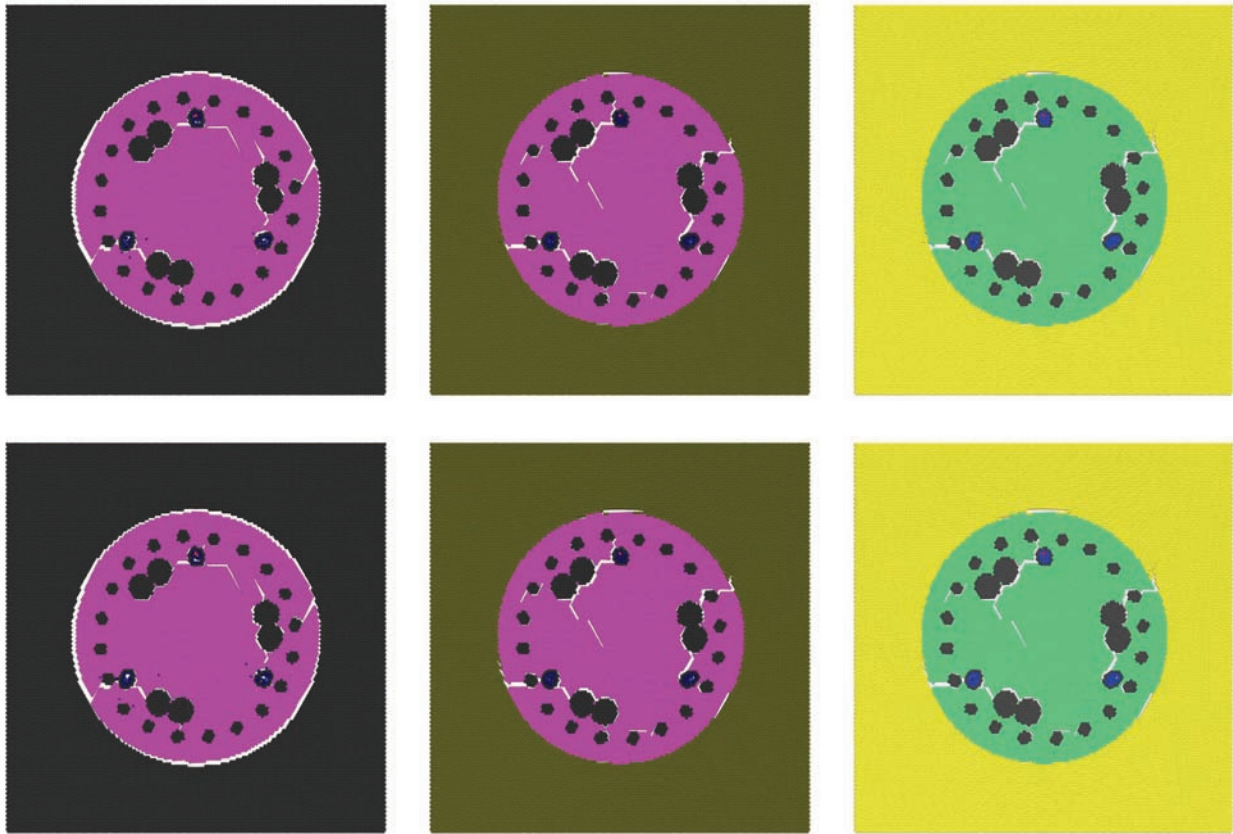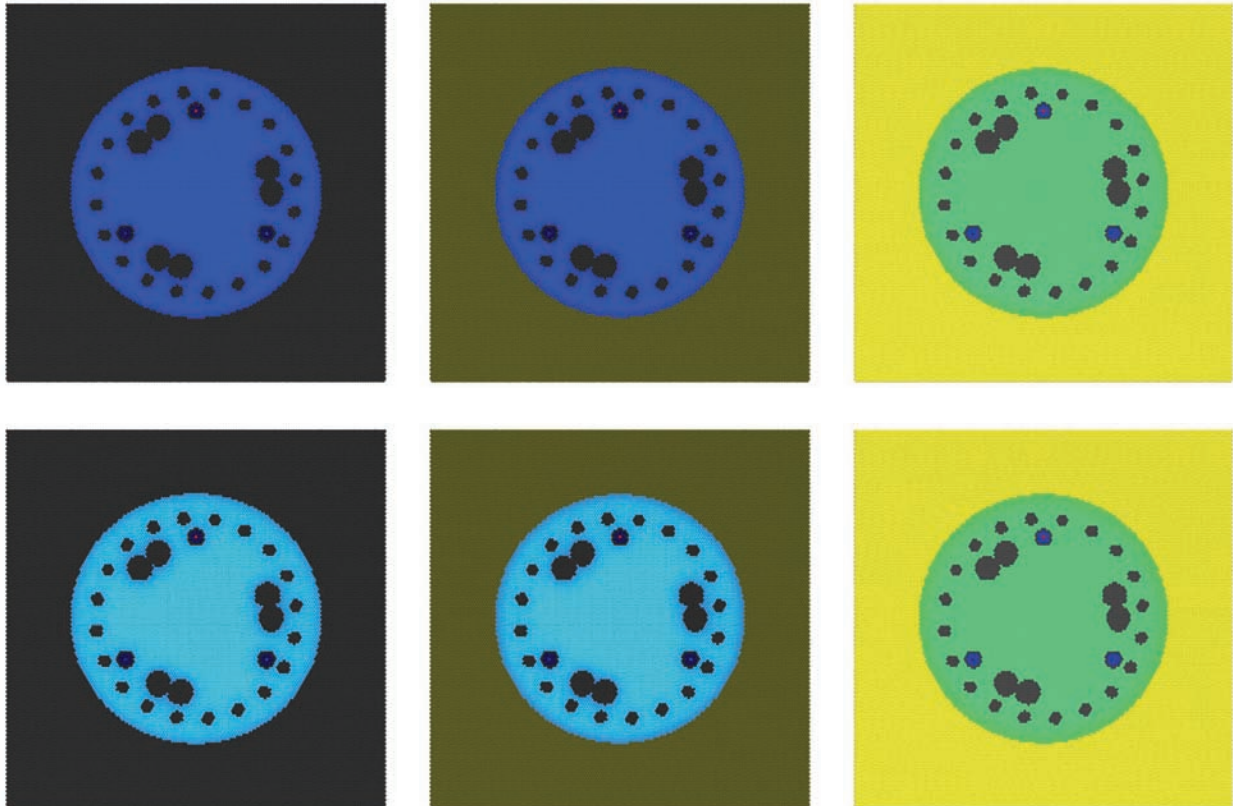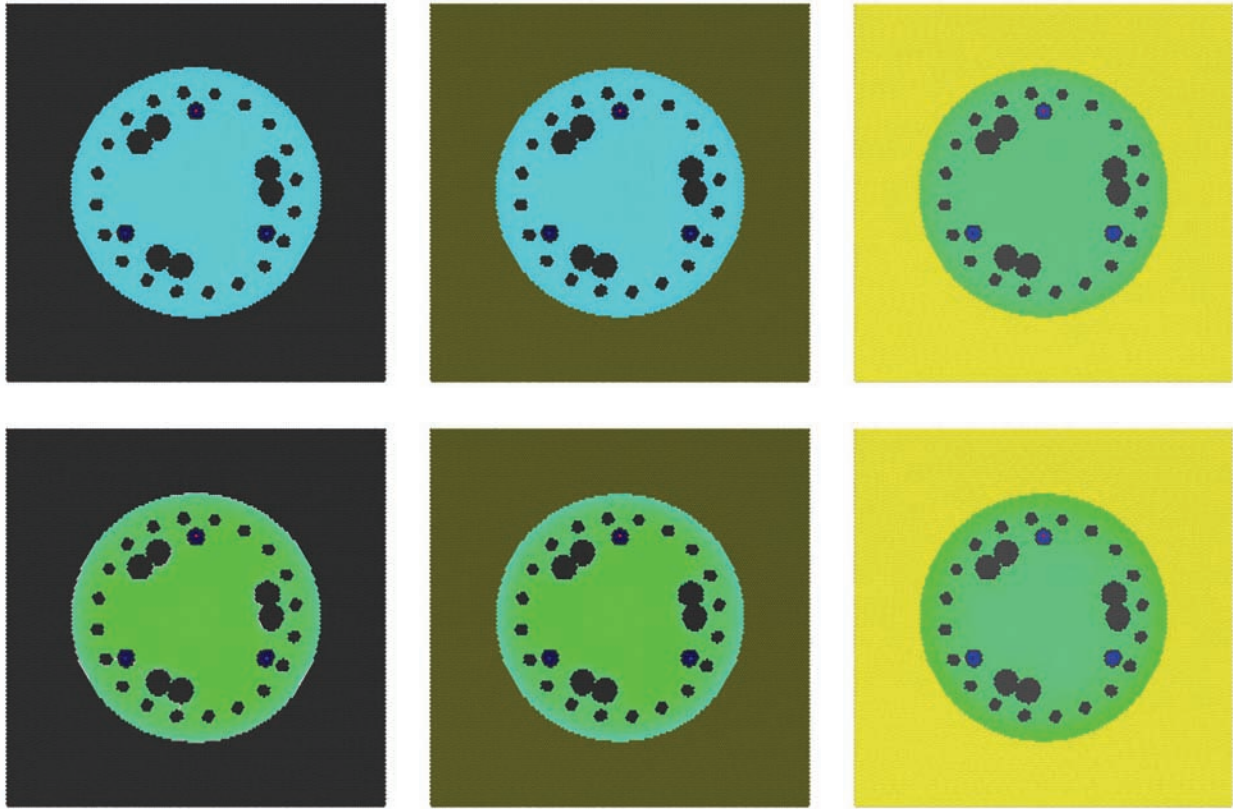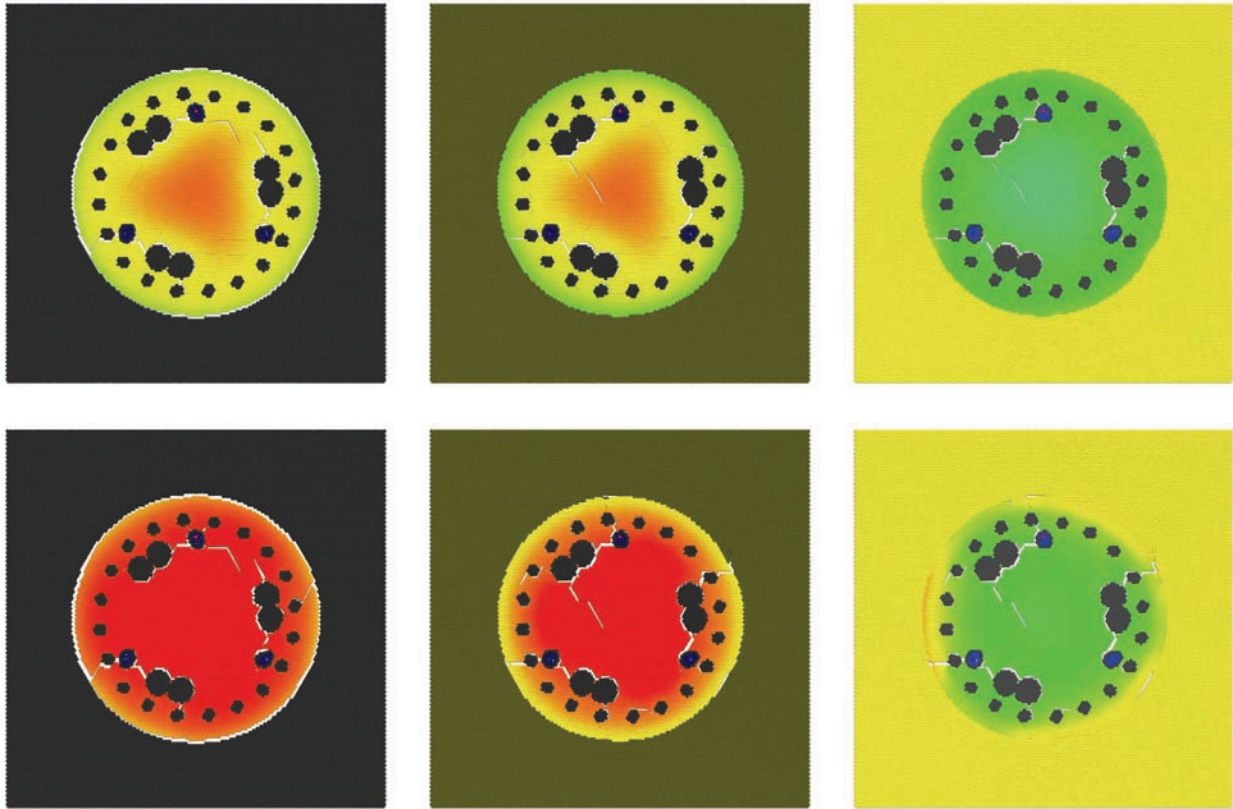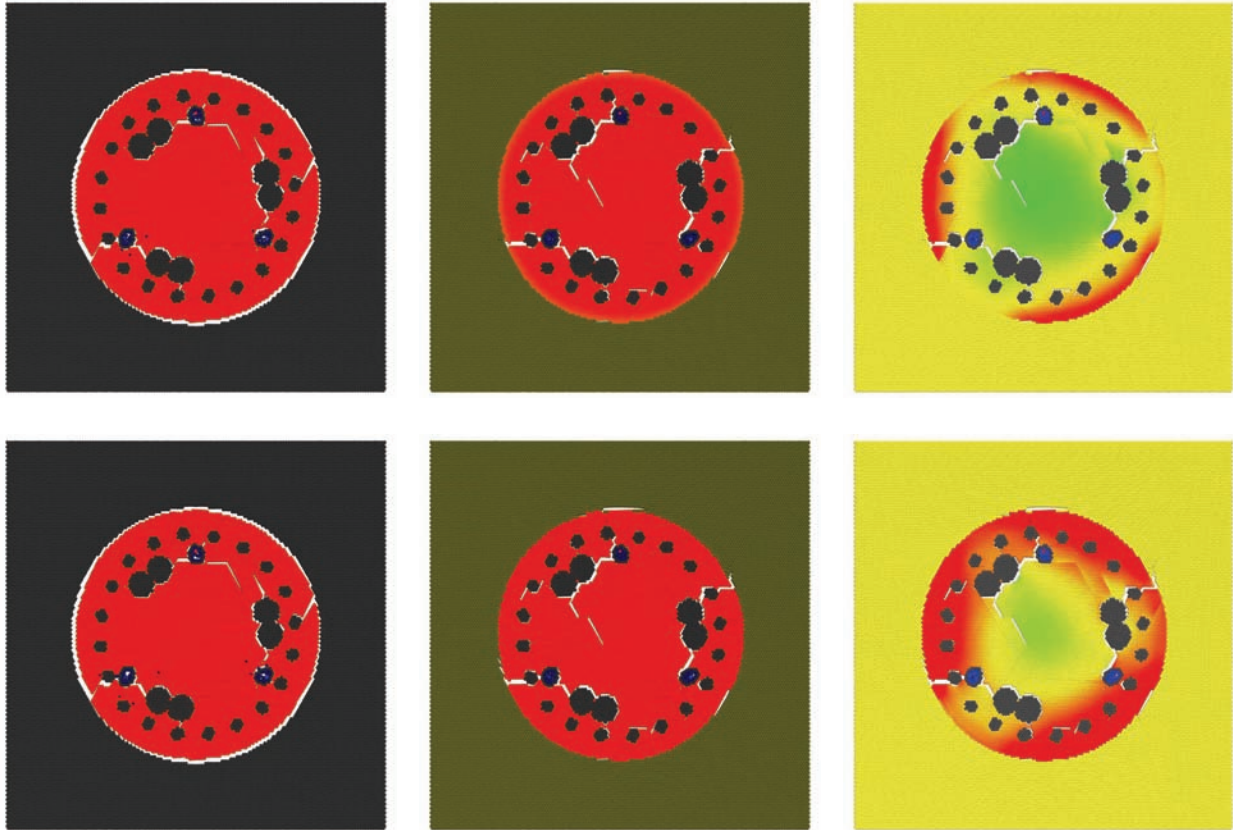
Figure 5.17. Plot. Curing Hydration. Top: 4 days. Bottom: 5 days. Left: Rock. Middle: Clay. Right: Difference

5.3.5 Temperature

The top row of Figure 5.18 shows the temperature after 4 hours. At this stage, the first hydration phase has completed, and the second hydration phase is in a very early stage. The temperature of the shaft remains high due to the high placement temperature. The temperature is lower in regions around the rebar and access tubes, as heat readily transfers from the warmer concrete to the cooler steel. The halo around the perimeter of difference plot indicates that the temperature of the rock adjacent to the concrete is higher than the temperature of the clay at this location. The temperature of the concrete adjacent to the rock is also at a higher temperature, due to the lower thermal conductivity of the rock. Even though the rock is at a higher temperature, the total amount of heat transferred into the clay is higher, distributed over a larger volume.

The bottom row of Figure 5.18 shows the temperature after 8 hours, when the second hydration phase is beginning to generate heat in warmer regions of the concrete. The temperature becomes more uniform in the perimeter of the shaft, in the region of the rebar cage.

Figure 5.18. Plot. Curing Temperature. Top: 4 hours. Bottom: 8 hours. Left: Rock. Middle: Clay. Right: Difference

The top row of Figure 5.19 shows the temperature at 12 hours, as more heat is generated from the second hydration phase. The temperature of the shaft remains high in the center, but decreases around the perimeter, as heat transfers into the surrounding ground. The temperature continues to rise in a larger volume of clay than in the rock. The bottom row shows that the temperature after 24 hours continues to cool around the perimeter of the shaft, and converge to a more stable temperature gradient.

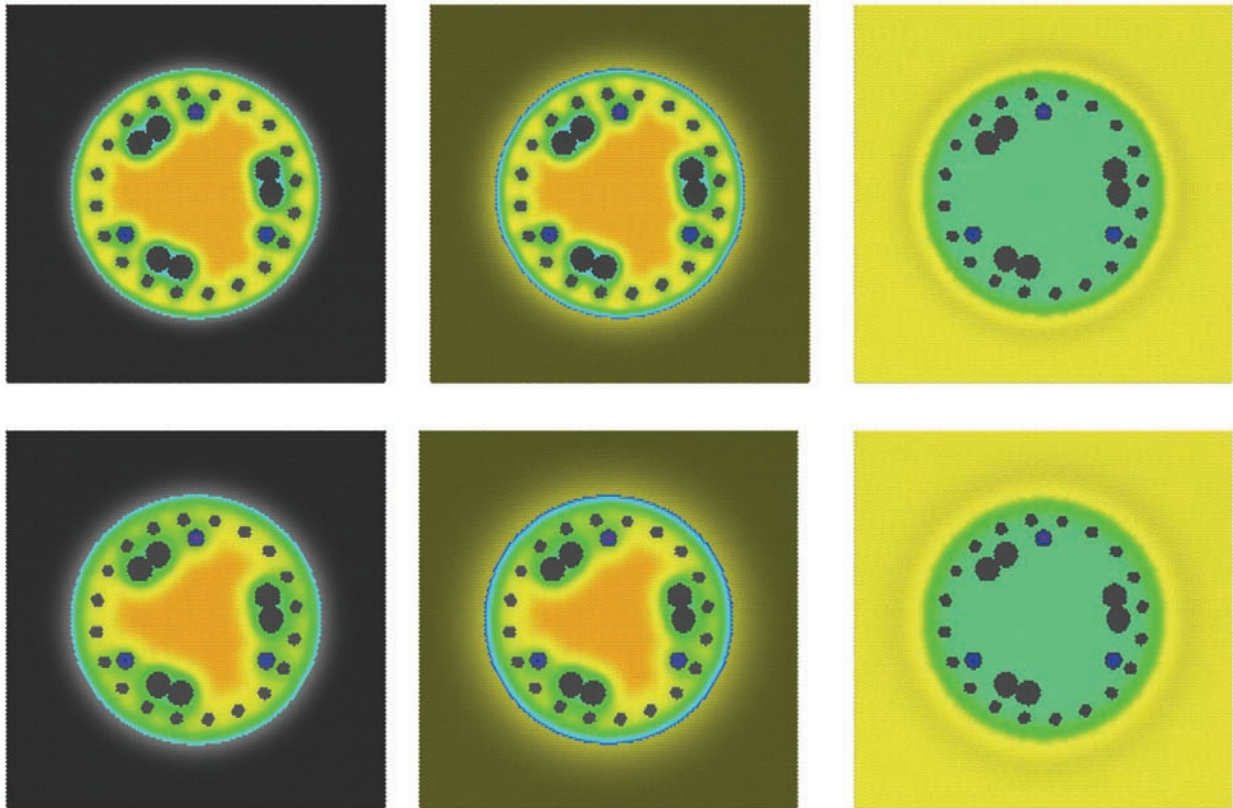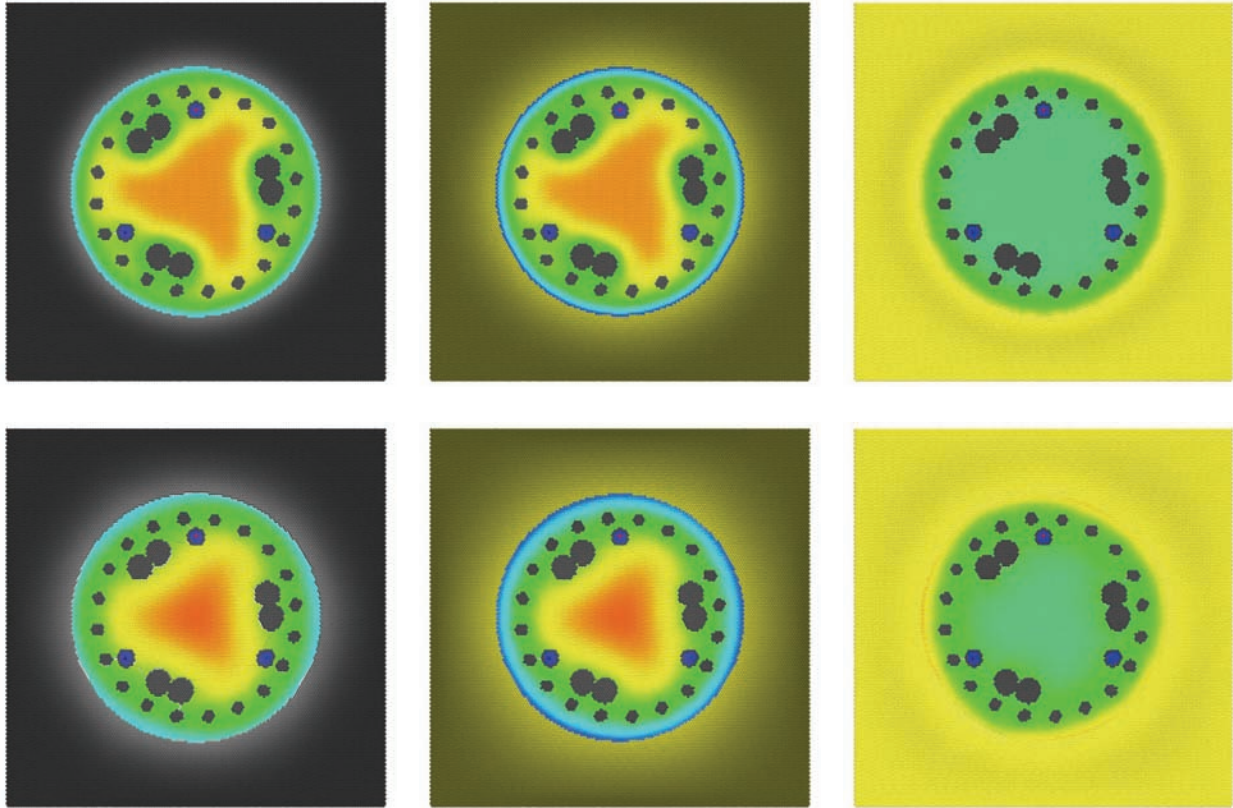**Figure 5.19. Plot. Curing Temperature. Top: 12 hours. Bottom: 24 hours. Left: Rock. Middle: Clay. Right: Difference**

The top row of Figure 5.20 shows the temperature at 2 days, at the peak of the third hydration phase. Debonding of the rock and concrete results in slight variations in the temperature distribution. Less heat is dissipated by convection, resulting in a significantly higher temperature in the shaft surrounded by rock, especially in the perimeter of the shaft, as shown in the difference figure.

The bottom row of Figure 5.20 shows the temperature at 3 days, at the end of the third hydration phase. The shaft surrounded by rock remains hot, but has a lower temperature gradient as the temperature distributes more evenly throughout the shaft. The temperature around the perimeter of the shaft surrounded by clay is significantly lower, causing a higher temperature gradient in the shaft.

Figure 5.20. Plot. Curing Temperature. Top: 2 days. Bottom: 3 days. Left: Rock. Middle: Clay. Right: Difference

After 4 days, the shaft temperature continues to decrease, as shown in Figure 5.21. Much less heat transfers by convection, so the shaft surrounded by rock remains uniformly warm. The core of the shaft surrounded by clay remains warm, and will also require significantly more time to completely cool. The difference plot shows that cracking patterns have a slight effect on temperature.
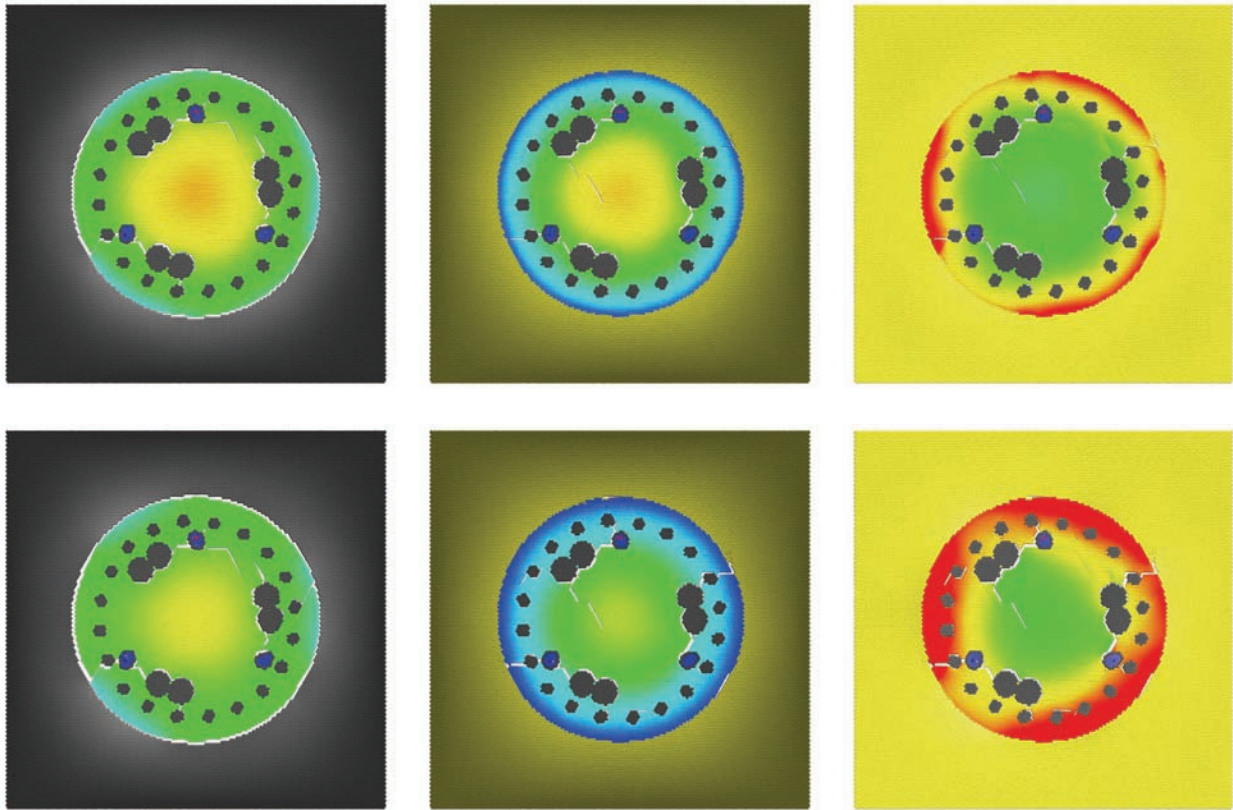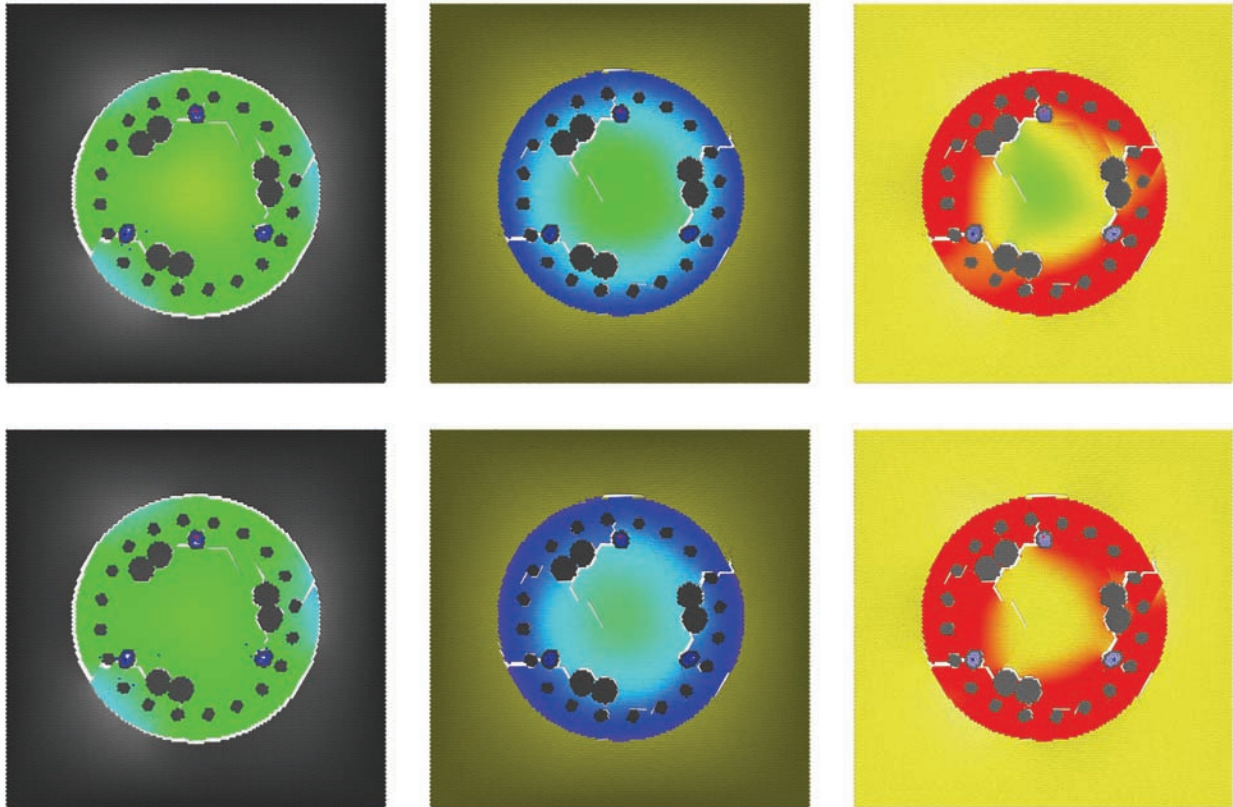

Figure 5.21. Plot. Curing Temperature. Top: 4 days. Bottom: 5 days. Left: Rock. Middle: Clay. Right: Difference

5.4   Discussion

Internal cracking between rebar is common, and likely occurs in most, if not all, drilled shafts. This is the primary reason why access tubes are placed inside the rebar cage, rather than outside. Tubes placed outside the cage allow more concrete in the shaft to be imaged for defects. CSL data from tubes outside the shaft show very high variability in arrival times and energies. This is commonly attributed to scattering by the rebar and higher signal attenuation from larger tube separation. However, these models show that the variability is actually caused by internal cracking between rebar in the rebar cage, and debonding cracks around the perimeter of the rebar. Sonic compression waves have no problem propagating through rebar and intact concrete. Also, CSL data along the perimeter of the shaft is often ignored, "corrected", or intentionally not collected on larger shafts with more access tubes, supposedly to save time and cost. CSL velocities are almost always lower along the perimeter of the shaft than through the center, even when tubes are placed inside the rebar cage. This is often attributed to differences in concrete

maturity and lower temperatures in regions along the perimeter. However, these lower velocities persist long after all the concrete in the shaft has fully cured. Since cracking is common in the region of the rebar cage, slower velocities and higher variability will result between tubes along the perimeter.

Cracks develop from the rebar to the outside of the shaft. These cracks are serious concerns for corrosion, because they provide a conduit for corrosives to reach the rebar and deteriorate the shaft. Since cracks initiate at the rebar, any cracks that extend to the outside of the shaft will lead directly to a rebar support. Since cracks extend between rebar in the support cage, more rebar is directly exposed to corrosives from a single external crack than is readily apparent.

As this study indicates, variability and reduction of CSL velocities and energies can result from cracking. Indications of internal cracks from lower velocity CSL surveys are often nerve-racking, and can result in litigation. Ignoring or side-stepping the issue is not an option.

CHAPTER 6.   NUMERICAL TESTING OF AXIAL LOAD CAPACITY OF A DRILLED SHAFT WITH ANOMALIES

Various tests and analytical methods have been developed to evaluate the axial load capacity of a drilled shaft. Design requires proper sizing of the drilled shaft for sufficient axial load capacity. Static load tests are generally performed on full-scale prototype shafts to obtain load-settlement curves. Analytical methods, based on concrete, soil, and rock properties obtained from laboratory or in-situ tests, are used to determine the ultimate load capacity of a drilled shaft. This study focuses on axial load capacity and static load tests, to demonstrate the capabilities of a modeling approach to determine the effect of anomalies on capacity. Numerical modeling can also analyze dynamic and lateral loads, which may be the control factors in certain situations.

Drilled shafts transfer applied axial loads to the ground via two mechanisms: side friction and toe bearing. Since geo-materials are highly inhomogeneous, anisotropic, non-linear, and non-elastic, the quality of the drilled shaft and interaction of the shaft and surrounding soils are major factors to control performance of the foundation. In situ prototype tests provide reliable design parameters for shaft design, but can be expensive and time consuming for many applications. Analytical methods can provide economical alternatives for simulating field conditions. With numerical modeling, site specific geology and material properties obtained from field investigations can be reproduced, and the effects of various loading conditions for drilled shaft design criteria can be analyzed.

6.1   Axial Loading Model Analysis

Concerns have recently been raised that design procedures for drilled shafts prescribed by the American Association of State Highway and Transportation Officials (AASHTO) do not incorporate the effect of soil density or cementation, specifically for end bearing shafts. In this study, common soil and rock properties encountered in highway engineering, with corresponding boundary conditions, are incorporated into a model that is socketted in bedrock for an end bearing shaft. The same defect at two different depths in the shaft is introduced into the model, to compare performance under axial loading.

In the axial loading model analysis, the drilled shaft is installed inside four different geo-materials. The order of the materials from the top to the toe of the drilled shaft is dry sand, wet sand, clay, and bedrock. The depths of each material and their relative elevations are showed in Figure 6.1. The toe of the drilled shaft is socketed 0.5 m in bedrock. The geo-material properties of this model are specified the same as other modeling this study (see section 6.1 for the specifications). The bottom of the model is constrained from displacement in the vertical (Z) direction and the surrounding boundary conditions are constrained of displacements in horizontal (X-Y) directions but vertical displacement is allowed (i.e. compaction and settlement are allowed). The ground surrounding the drilled shaft model has been expanded from 1.5 m to 2 m on a side, to reduce boundary condition effects. Elements at the base of the model are static.

Figure 6.1. Plot. Compression Stress at Initial Vertical Displacement. Top: Sand Intrusion at 1 m Depth. Bottom: Sand Intrusion 3 m Depth. Left: Compression Stress, No Defect. Center: Compression Stress. Right: Compression Stress Difference

Axial loading is applied uniformly on the top of the drilled shaft by pushing the shaft slowly downward with uniform displacement (standard displacement control test). The vertical force component is calculated from summing spring compression over the constrained elements at the top of the shaft. Two small sized defects (20% reduction in velocity) are introduced into the drilled shaft at depth of 1 m and 3 m, by replacing drilled shaft material with dry sand for comparison to a drilled shaft with no defect. Compacted and loosened conditions are also simulated to compare the effect of the density or cementation of the soil. The modeling results at the different loading/displacement stages are plotted in figures and graphs. The observations are presented and discussed in the following sections.

6.1.1 Displacement of 4 mm

The stress intensity in the drilled shaft at an initial displacement of 4 mm, measured at the top of the shaft, is plotted in Figure 6.2. Three models showing stress intensity are plotted in the figure. The left plot is the stress of the shaft without a defect. The center top and bottom plots represent the stress of the shaft with a defect at a depth of 1 m and 3 m, respectively. The right plots show the stress differences between the non-defective and the defective shafts.

The center plots show highest stress in the top of the shaft, gradually decreasing with depth. The stress is insignificant after a depth of 0.5 m. The stress build-up in the top of the shaft is a result of the friction and interlocking between the concrete and the surrounding ground. As the shaft moves, the surrounding ground compresses, resisting a significant proportion of the load. The drilled shaft is not so much compressed between the surface and the bedrock as it is compressed between the surface and the surrounding ground. In this case, the shaft experiences the most compression between the surface and the top of the wet sand.

The difference plots on the right of the figure show no change in stress from the shaft with no defect. This indicates that the defect at both depths of the shaft has no influence on the compression stress at this displacement.

6.1.2 Displacement of 4 cm

The stress intensity at a displacement of 4 cm is plotted in Figure 6.3. This is at the stage when the shaft is usually considered to have failed due to the large displacement. As seen from the plot on the left (non-defective shaft) and the plots in the center (defective shaft), the compression stress is at very high levels in the top 0.75 m of the shaft. Regions in the shaft where the stress is red have high potential to fracture. The stress abruptly decreases in the next 0.25 m, and is insignificant after a depth of 1 m. The shaft still experiences the most compression between the surface and the top of the wet sand. The wet sand layer is able to sustain slightly more load than the dry sand layer, and is most likely the cause for the abrupt decrease in stress at that depth.

The difference plot on the top right of the figure shows a slight change in stress due to the 1m defect. A region of lower stress, shown in blue, can also be seen extending 0.3 m directly above the defect. A smaller region of higher stress can be seen below the defect, extending 0.1 m.

Figure 6.2 shows the fracture extent corresponding to the compression stress plot in Figure 6.1. The dry sand has a very weak bond with the concrete. The dry sand is separated from the concrete, to a depth of 1 m. The difference plots on the right show that the defect has no influence on cracking at this stage.
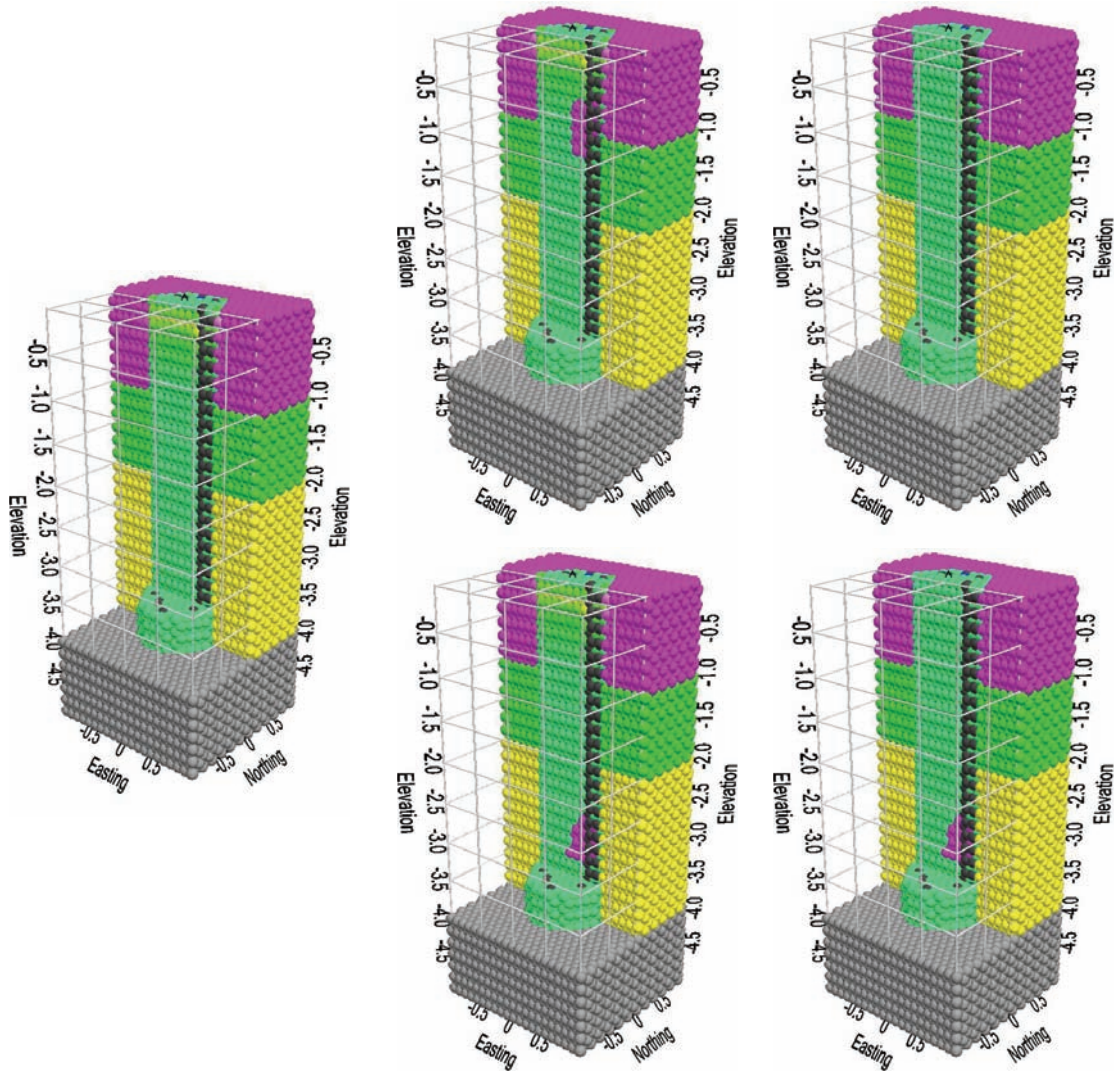
Figure 6.2. Plot. Fracture Extent at Initial Vertical Displacement. Top: Sand Intrusion at 1 m Depth. Bottom: Sand Intrusion 3 m Depth. Left: Fractures, No Defect. Center: Fractures. Right: Fracture Difference

The stress distribution in the surrounding soil is also of interest. The more the shaft settles, the more the sand and clay compact. This compaction strengthens the load bearing capacity of the ground, and ultimately of the shaft. The compaction also increases the friction and interlocking between the concrete and the ground, further improving shaft performance.

Figure 6.3. Plot. Compression Stress at 4 cm Vertical Displacement. Top: Sand Intrusion at 1 m Depth. Bottom: Sand Intrusion 3 m Depth. Left: Compression Stress, No Defect. Center: Compression Stress. Right: Compression Stress Difference

Figure 6.4 shows the fracture extent corresponding to the compression stress plot in Figure 6.3, at a displacement of 4 cm. At this stage, the concrete shows indications of significantly slipping away from the sand to a depth of 1.5 m, with separation forming between the concrete and clay to a depth of 3 m. Cracking can be seen to extend deeper in the right-most region of the shaft along the rebar. At this stage, the concrete is debonding from the rebar. On the other side of the shaft, at a region with no nearby rebar support, the concrete already shows signs of cracking at a depth of 0.5 m, indicated by a slightly lighter green color. The cracking is greatest at the outer left-hand region of the shaft, and gradually decreases to the center of the shaft. The difference plots on the right show that the defect still has no influence on cracking at this stage.
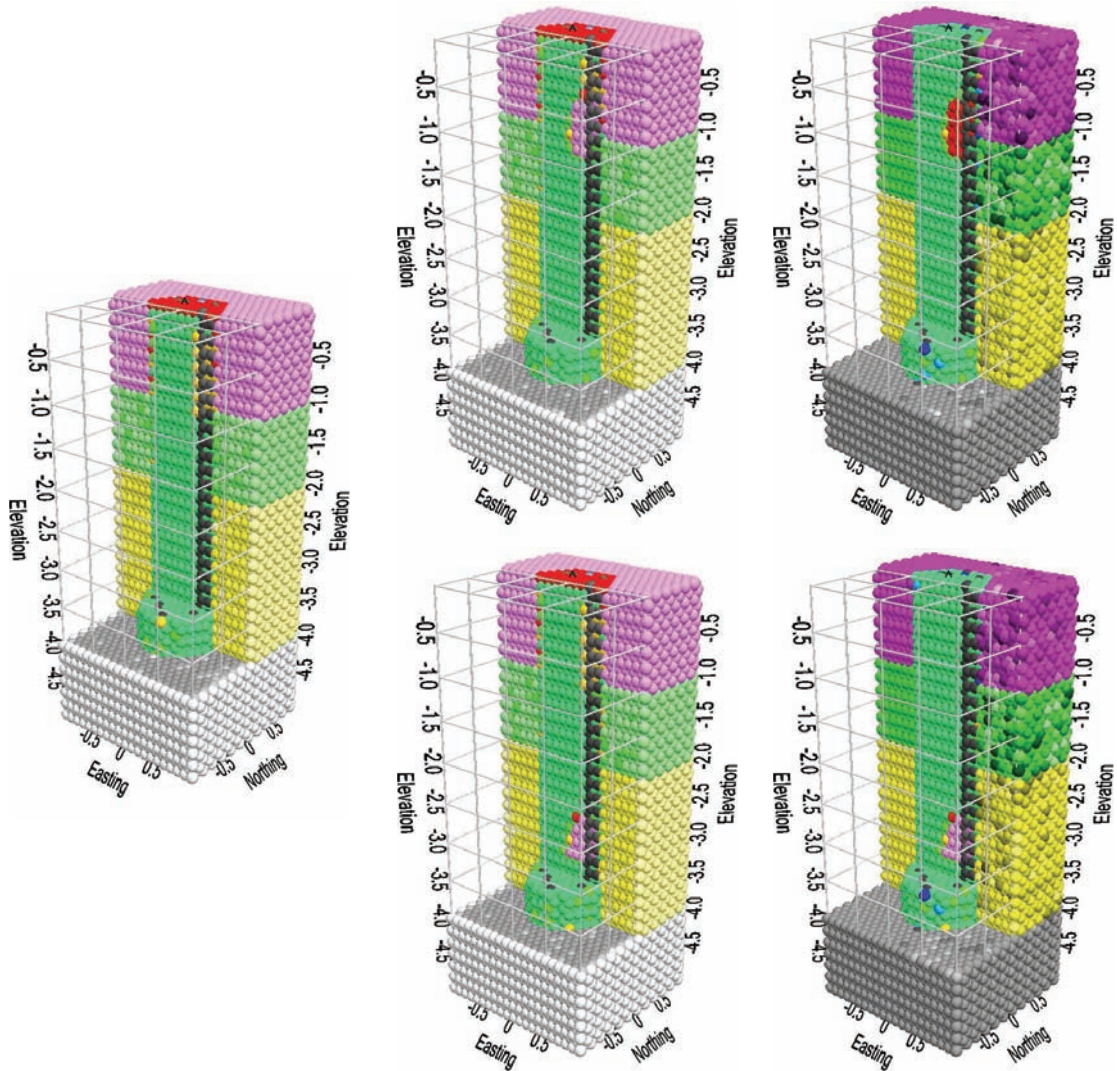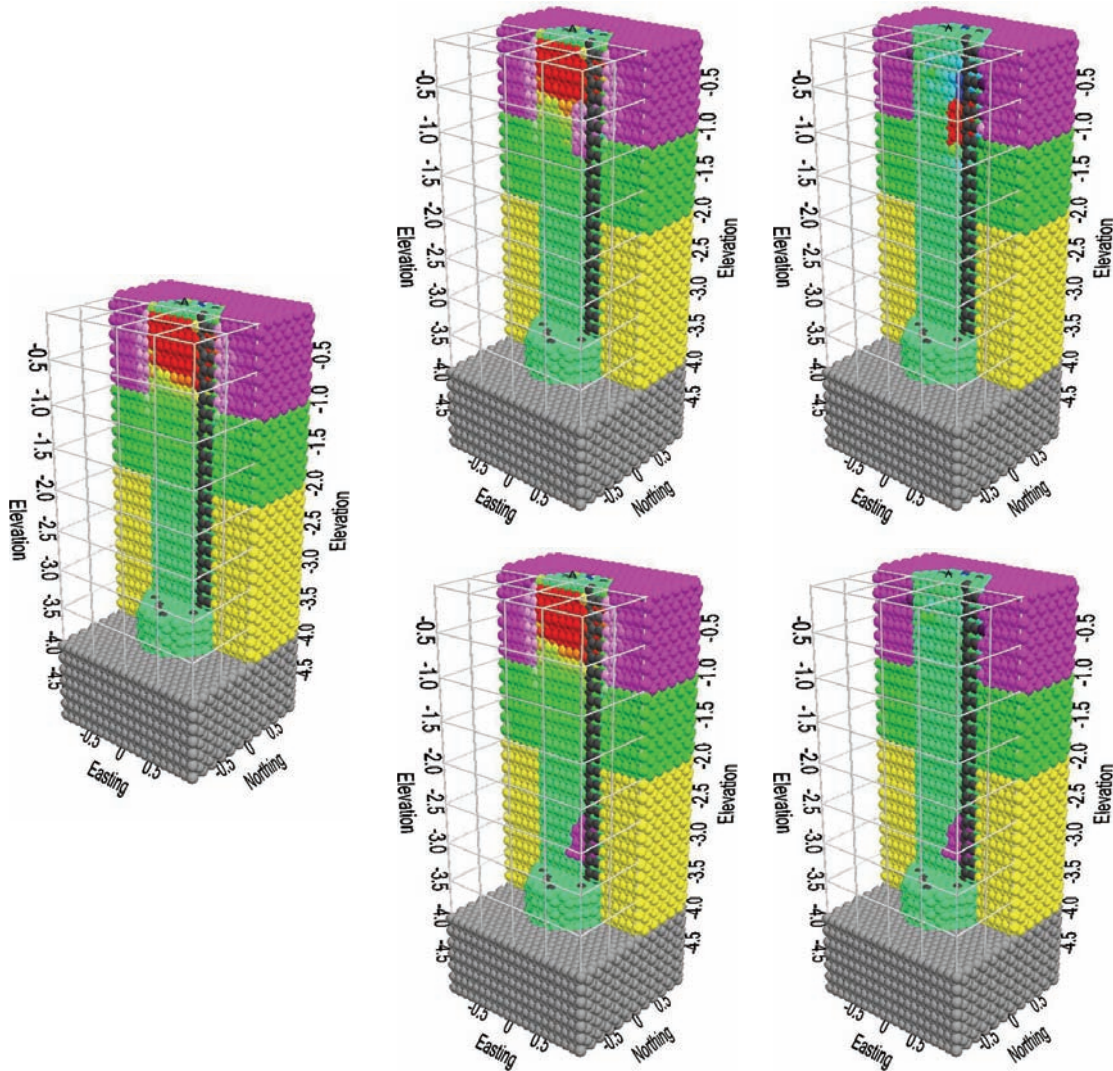
141

Figure 6.4. Plot. Fracture Extent at 4 cm Vertical Displacement. Top: Sand Intrusion at 1 m Depth. Bottom: Sand Intrusion 3 m Depth. Left: Fractures, No Defect. Center: Fractures. Right: Fracture Difference

6.1.3 Displacement of 8 cm

The stress intensity at a displacement of 8 cm is plotted in Figure 6.5. The shaft is now at peak load capacity. As seen from the plot on the left and the plots in the center, the compression stress is at very high levels in the top 1 m of the shaft. The stress abruptly decreases in the next 0.25 m, and gradually tapers off to nearly zero after a depth of 2.5 m. The shaft experiences the most compression between the surface down to 0.25 m below the top of the wet sand.

Figure 6.5. Plot. Compression Stress at 8 cm Vertical Displacement. Top: Sand Intrusion at 1 m Depth. Bottom: Sand Intrusion 3 m Depth. Left: Compression Stress, No Defect. Center: Compression Stress. Right: Compression Stress Difference

The difference plot in the top right of the figure shows a more significant change in stress due to the 1 m defect. The region of lower stress developing above the defect has both expanded in size and decreased in amplitude, shown in blue and purple. The smaller region of higher stress below the defect has significantly increased in amplitude to red, but a new region of lower stress has developed in a region extending 0.25 m below the higher stress region. There is also a small region of highly concentrated stress in the center of the shaft at a depth of 1 m shown in red, and another small region of highly concentrated stress slightly to the left of center at a depth of 0.75 m shown in orange. High concentrated stresses form as cracks develop and propagate, and these small regions of concentrated stress correspond to crack propagation, as shown in Figure 6.6.
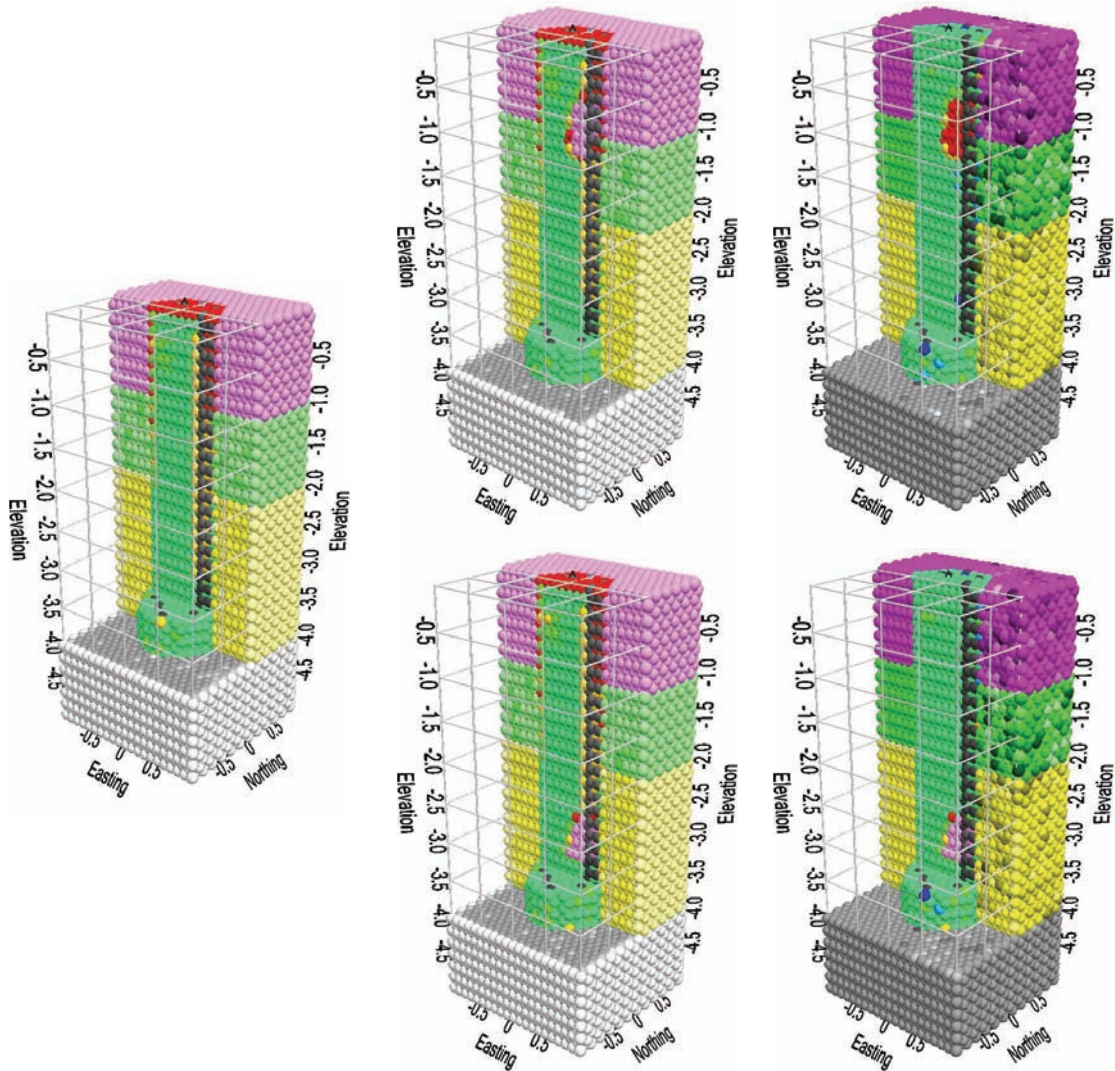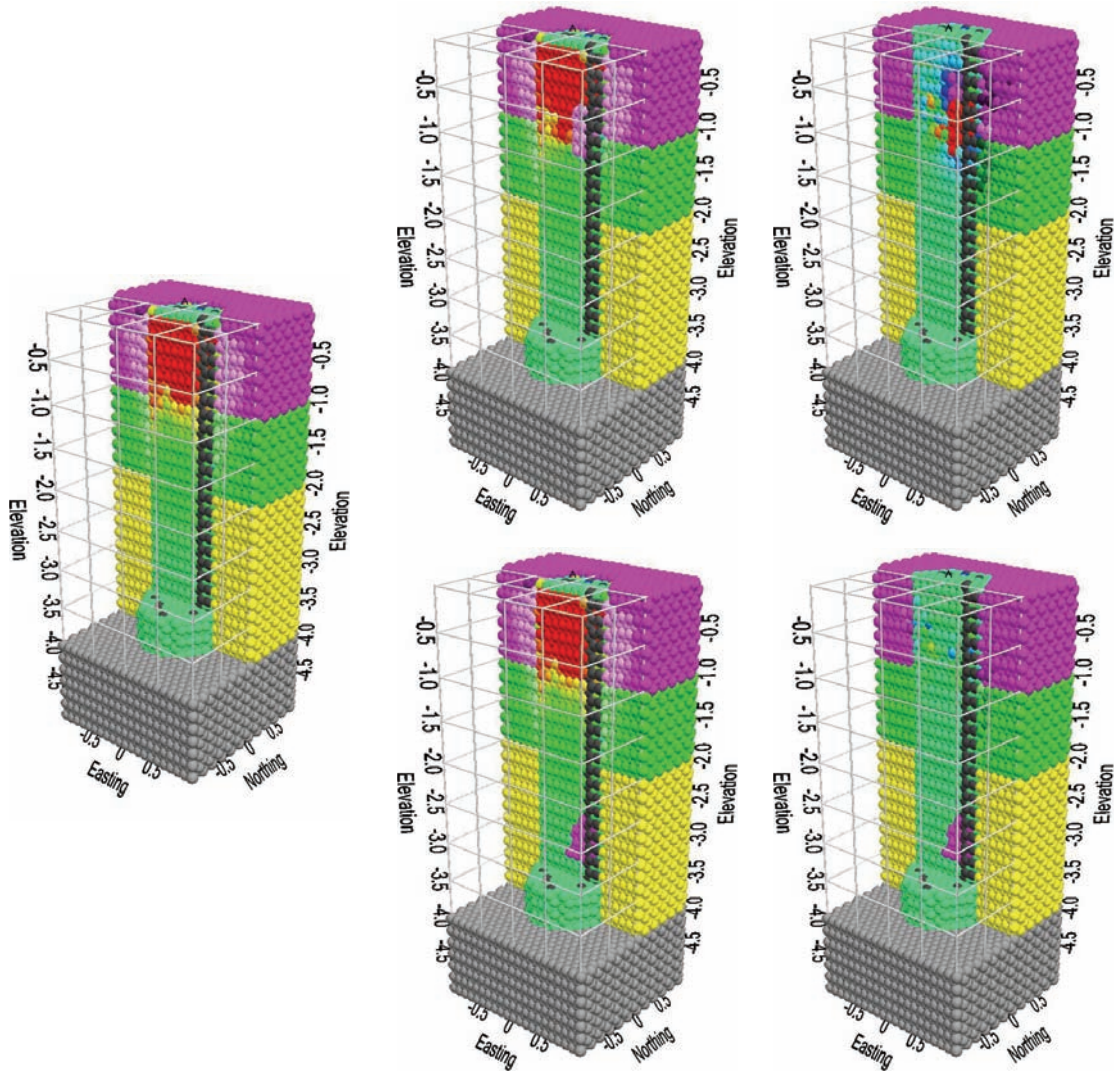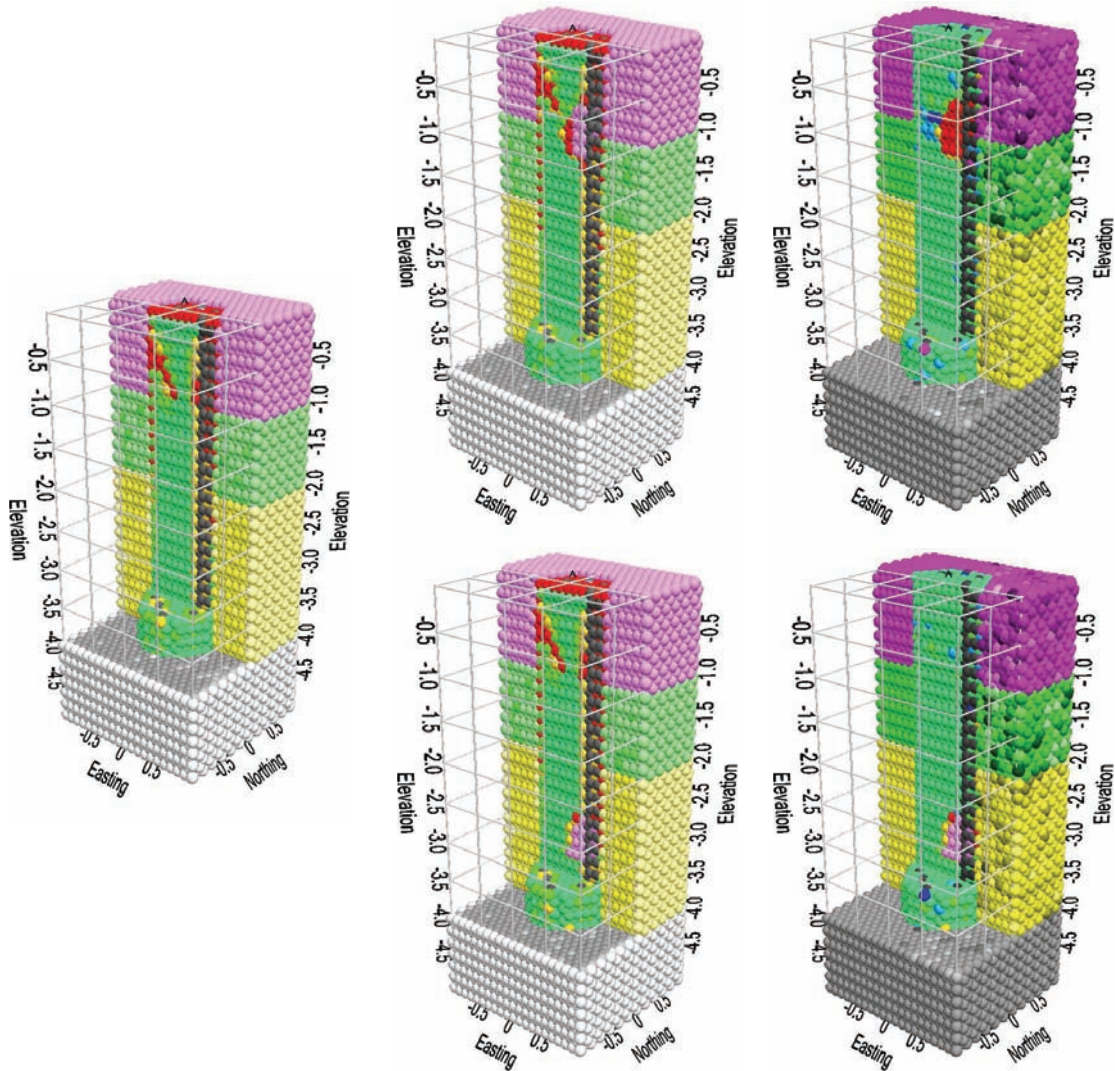
143

Figure 6.6. Plot. Fracture Extent at 8 cm Vertical Displacement. Top: Sand Intrusion at 1 m Depth. Bottom: Sand Intrusion 3 m Depth. Left: Fractures, No Defect. Center: Fractures. Right: Fracture Difference

Cracks release stress and change stress distribution. Therefore, cracks must be taken into account when attempting to understand stress behavior. The defect itself may at times acts as a large crack, redistributing stress and affecting crack propagation.

Figure 6.6 shows the fracture extent corresponding to the compression stress plot in Figure 6.5, at a displacement of 8 cm. At this stage, the concrete shows indications of significantly breaking away from the sand to a depth of 1.9 m in the shaft with no defect, 2.1 m in the shaft with the 3 m defect, and 2.25 m in the shaft with the 1 m defect. All three shafts show distinct crack development from the left side of the shaft at a depth of 0.25 m, extending to the center of the shaft at a depth of 1 m. However, the crack in the shaft with the 1 m defect appears to be at least 0.1 m shorter than the cracks in the other two shafts. This is a case of the defect altering crack

propagation. The small concentrated regions of high stress shown in the top right plot in Figure 6.5 indicate that two cracks are developing simultaneously in the shaft with the 1 m defect. One crack is propagating downward from the left side of the shaft, while another crack is propagating upward from the center of the defect. The crack from the defect changes the stress distribution, reducing the length of the downward propagating crack.

6.1.4 Displacement of 12 cm

The stress intensity at a displacement of 12 cm is plotted in Figure 6.7. The shaft is now considered to be in the plunging stage. As seen from the plot on the left and the plots in the center, the compression stress is at very high levels in the top 1.25 m of the shaft. The stress abruptly decreases, and will not significantly change with subsequent loading. At this point, the shaft has fully fractured, as shown in Figure 6.8, redistributing stress outward into the surrounding sand.

The difference plot in the top right of the figure shows an interesting change in stress due to the 1m defect. The region of lower stress still remains above the defect. However, the stress in the sand to the right of the shaft is significantly lower. This is not because the stress in the sand has decreased in the shaft with the 1 m defect, but because the stress in the sand has increased in the shaft with the 3 m defect and the shaft with no defect. This difference in stress is due to the difference in lateral displacement of the upper portion of the fractured concrete after shaft failure. The difference plot in the lower right of the figure shows a slight change in stress concentration along the fracture line. This indicates that the 3 m defect has an effect on stress in the region of the fracture, but not on the region at the surface. Therefore, the 3 m defect does not significantly affect load capacity in this scenario.

Figure 6.7. Plot. Compression Stress at 12 cm Vertical Displacement. Top: Sand Intrusion at 1 m Depth. Bottom: Sand Intrusion 3 m Depth. Left: Compression Stress, No Defect. Center: Compression Stress. Right: Compression Stress Difference

Figure 6.8. Plot. Fracture Extent at 12 cm Vertical Displacement. Top: Sand Intrusion at 1 m Depth. Bottom: Sand Intrusion 3 m Depth. Left: Fractures, No Defect. Center: Fractures. Right: Fracture Difference

6.1.5 Displacement of 16 cm and 20 cm

The stress intensity at a displacement of 16 cm is plotted in Figure 6.9. Figure 6.10 shows the fracture extent corresponding to the compression stress plot in Figure 6.9. The shaft is still considered to be in the plunging stage, after the load bearing capacity has stabilized. The upper portion of the shaft continues to bulge as it fails, and compress the surrounding sand.
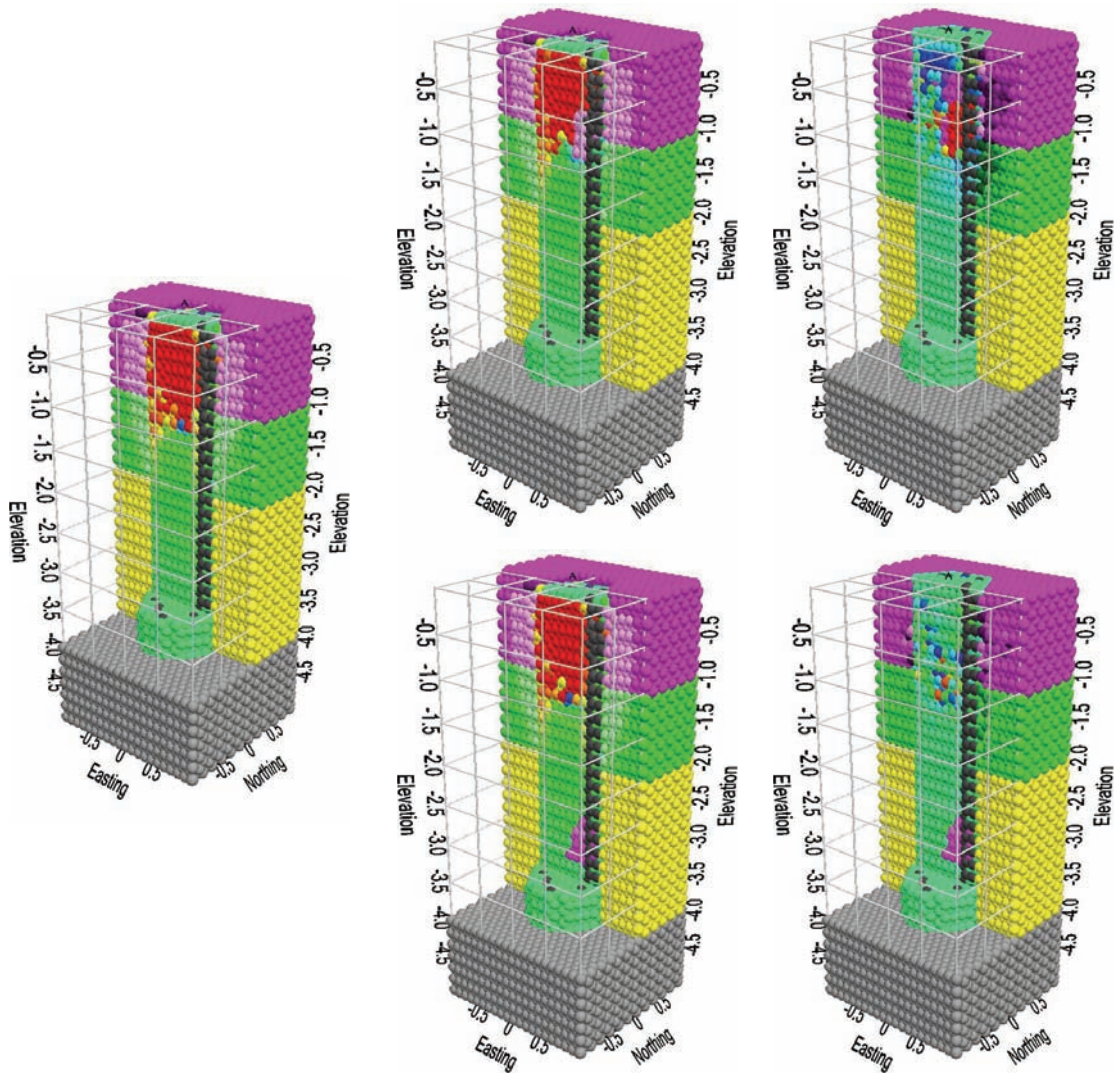
Figure 6.9. Plot. Compression Stress at 16 cm Vertical Displacement. Top: Sand Intrusion at 1 m Depth. Bottom: Sand Intrusion 3 m Depth. Left: Compression Stress, No Defect. Center: Compression Stress. Right: Compression Stress Difference
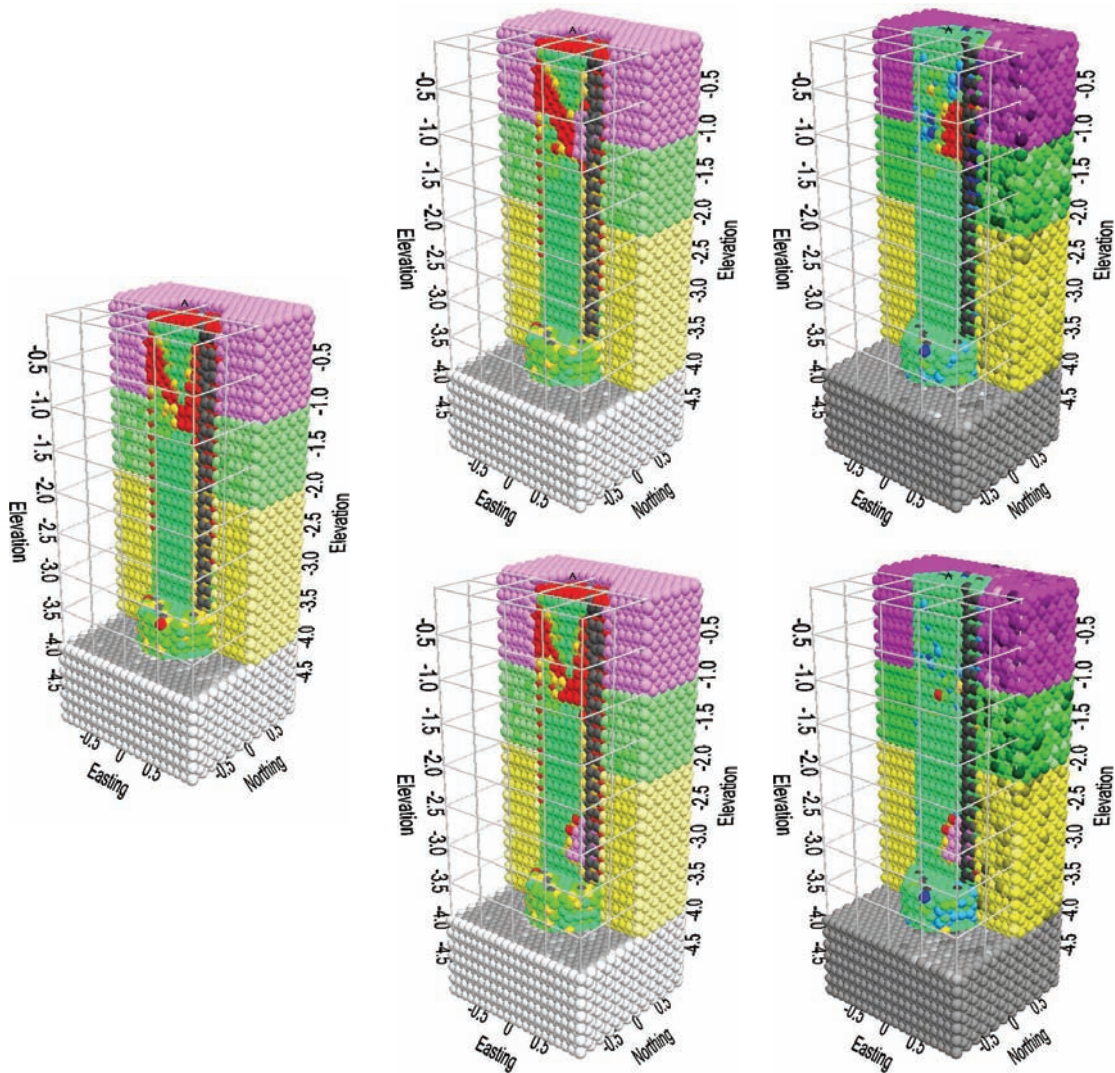
Figure 6.10. Plot. Fracture Extent at 16 cm Vertical Displacement. Top: Sand Intrusion at 1 m Depth. Bottom: Sand Intrusion 3 m Depth. Left: Fractures, No Defect. Center: Fractures. Right: Fracture Difference

The compression stress at a displacement of 20 cm is plotted in Figure 6.11. Figure 6.12 shows the fracture extent corresponding to the compression stress plot in Figure 6.11. The shaft is still considered to be in the plunging stage. The upper portion of the shaft continues to bulge as it fails, and compress the surrounding sand.
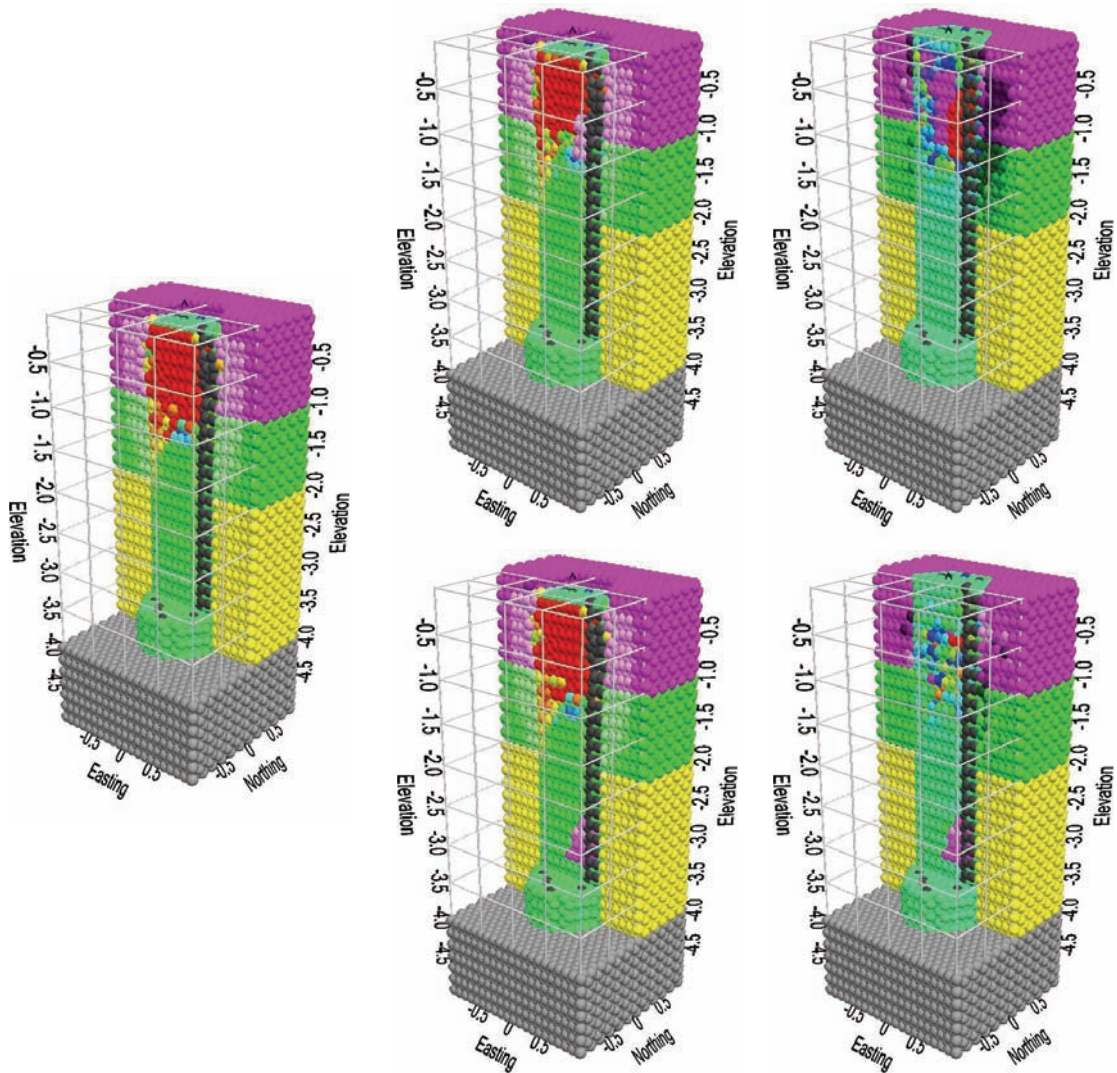
Figure 6.11. Plot. Compression Stress at 20 cm Vertical Displacement. Top: Sand Intrusion at 1 m Depth. Bottom: Sand Intrusion 3 m Depth. Left: Compression Stress, No Defect. Center: Compression Stress. Right: Compression Stress Difference
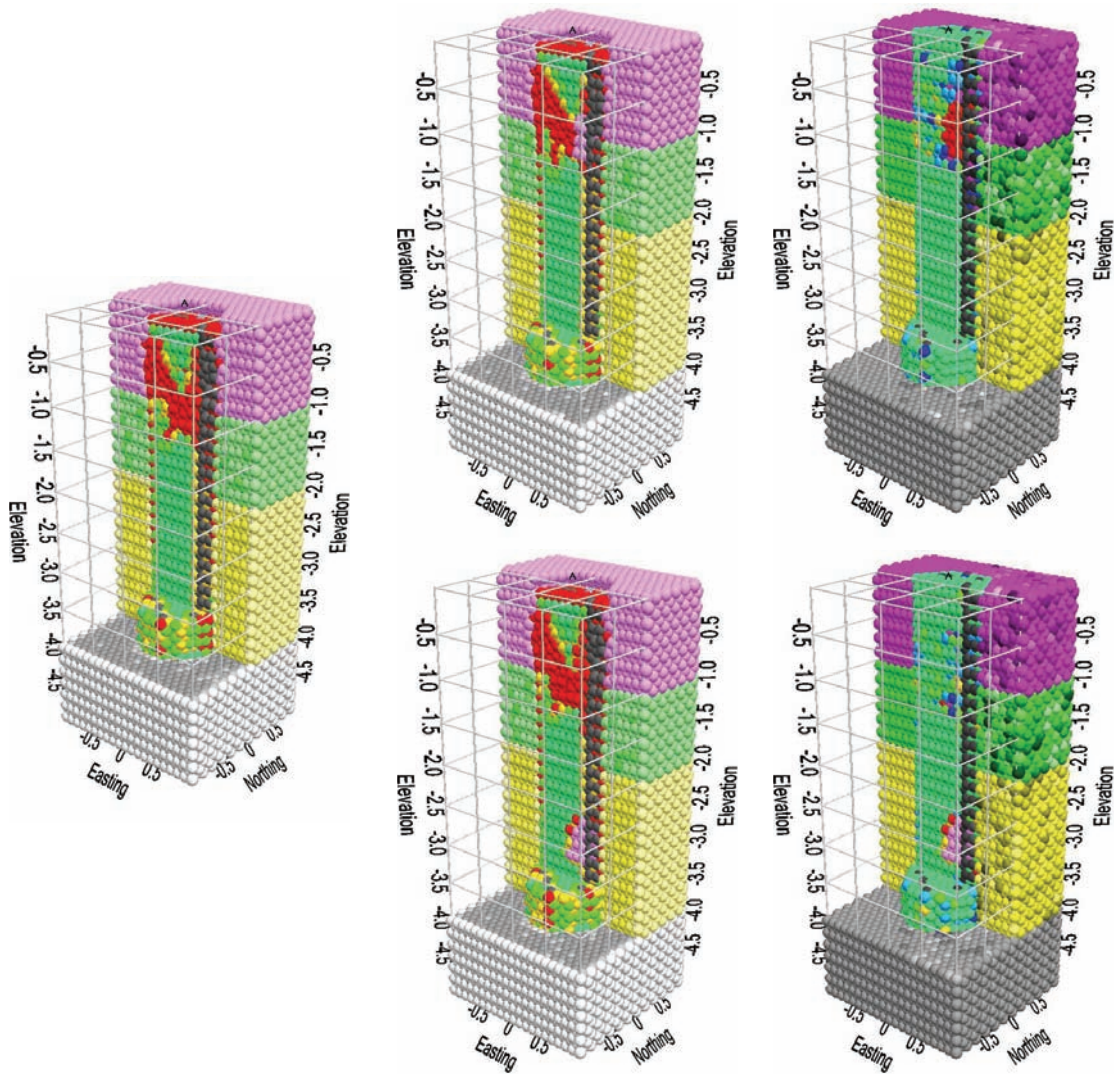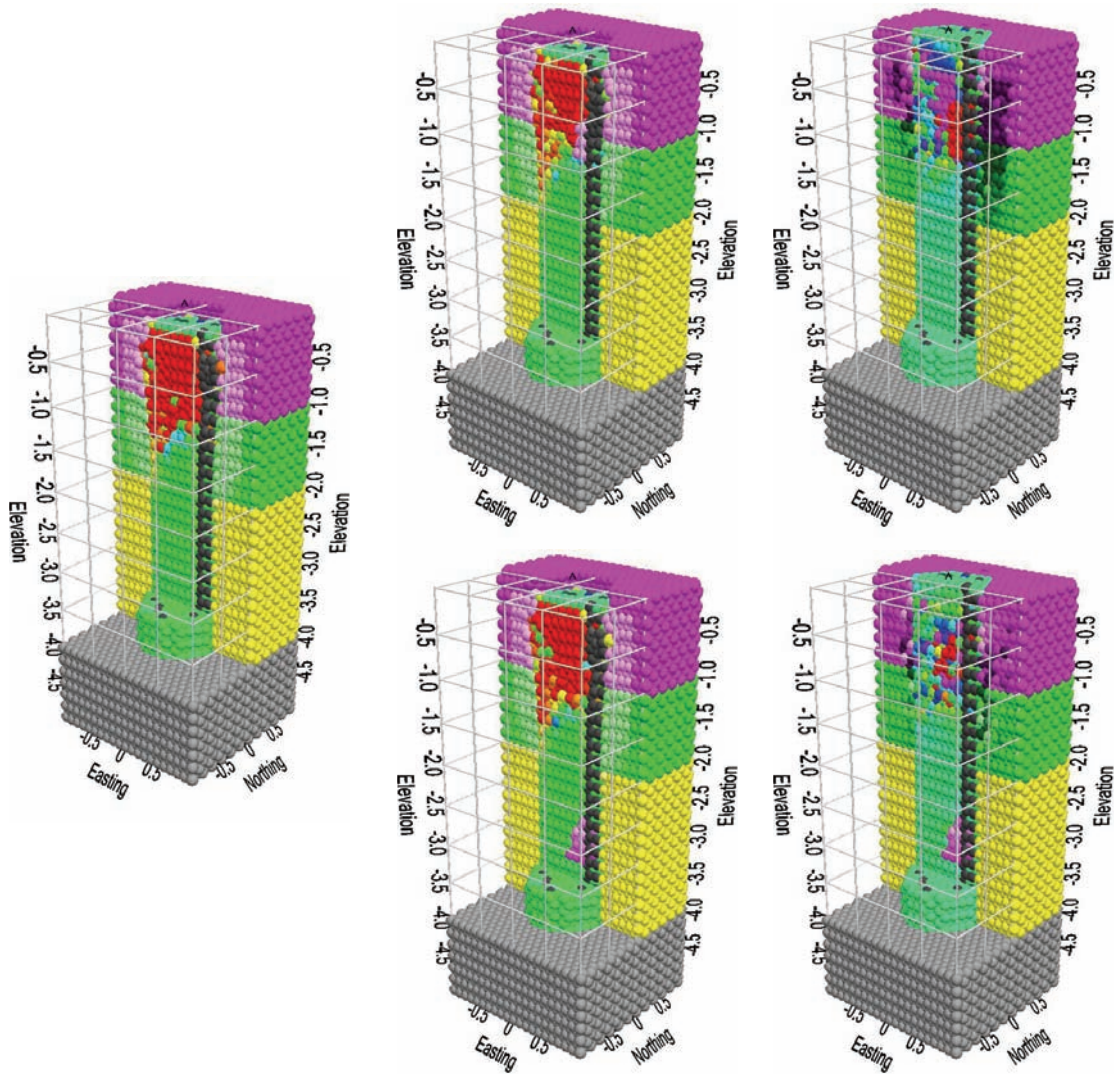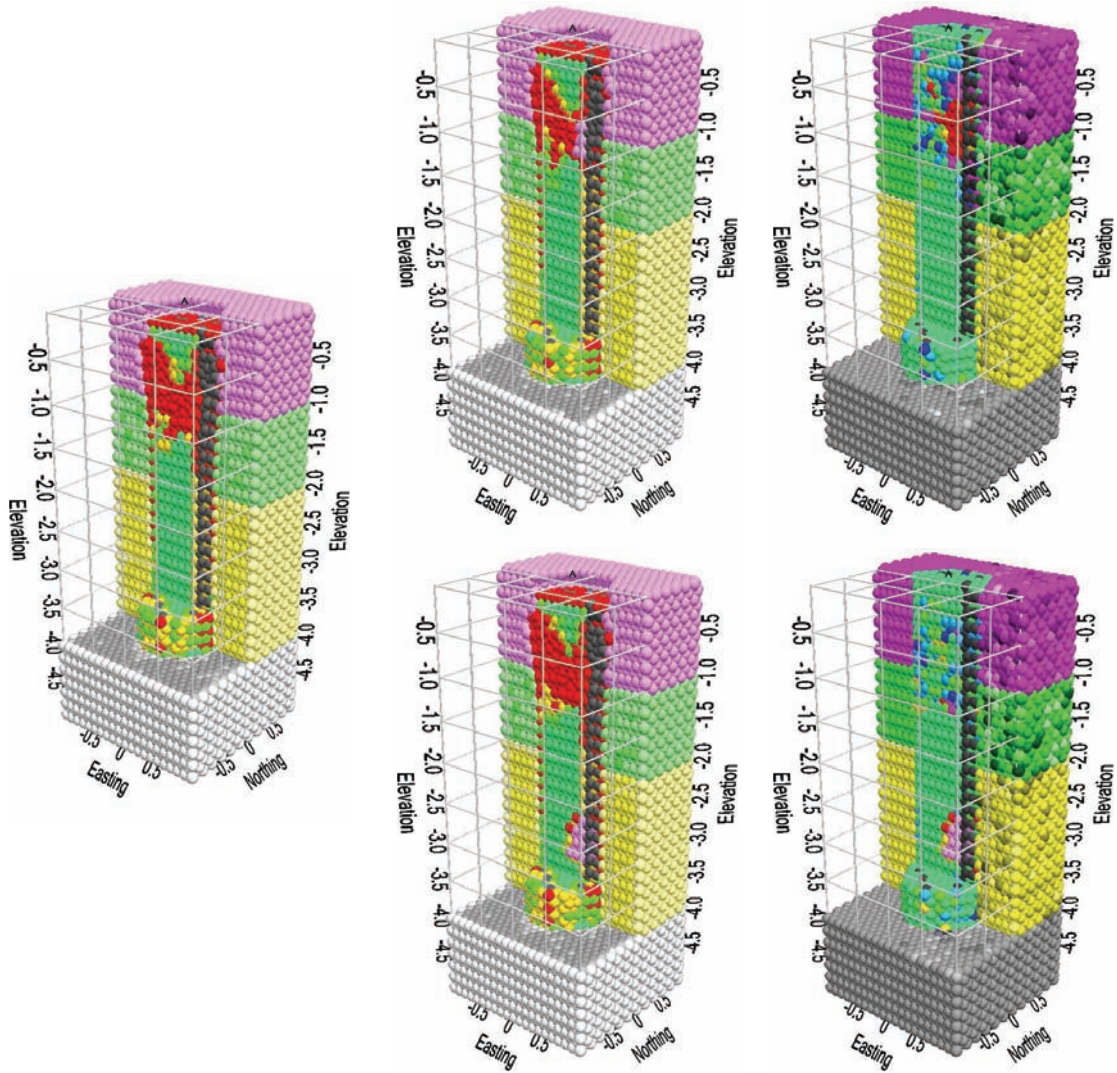
Figure 6.12. Plot. Fracture Extent at 20 cm Vertical Displacement. Top: Sand Intrusion at 1 m Depth. Bottom: Sand Intrusion 3 m Depth. Left: Fractures, No Defect. Center: Fractures. Right: Fracture Difference

6.2 Load-Settlement Curve Analysis

The load-settlement curves obtained from the numerical tests are shown in Figures 6.13 – 6.15. The figures clearly show the effects of the surrounding soil and rock. It is understood from both in situ and laboratory tests that the load-settlement curve undergoes a distinct "plunge" if the surrounding soil is soft clay, but no clear point of failure on the curve can be seen for the shaft in sands, intermediate soils, and stiff clays.
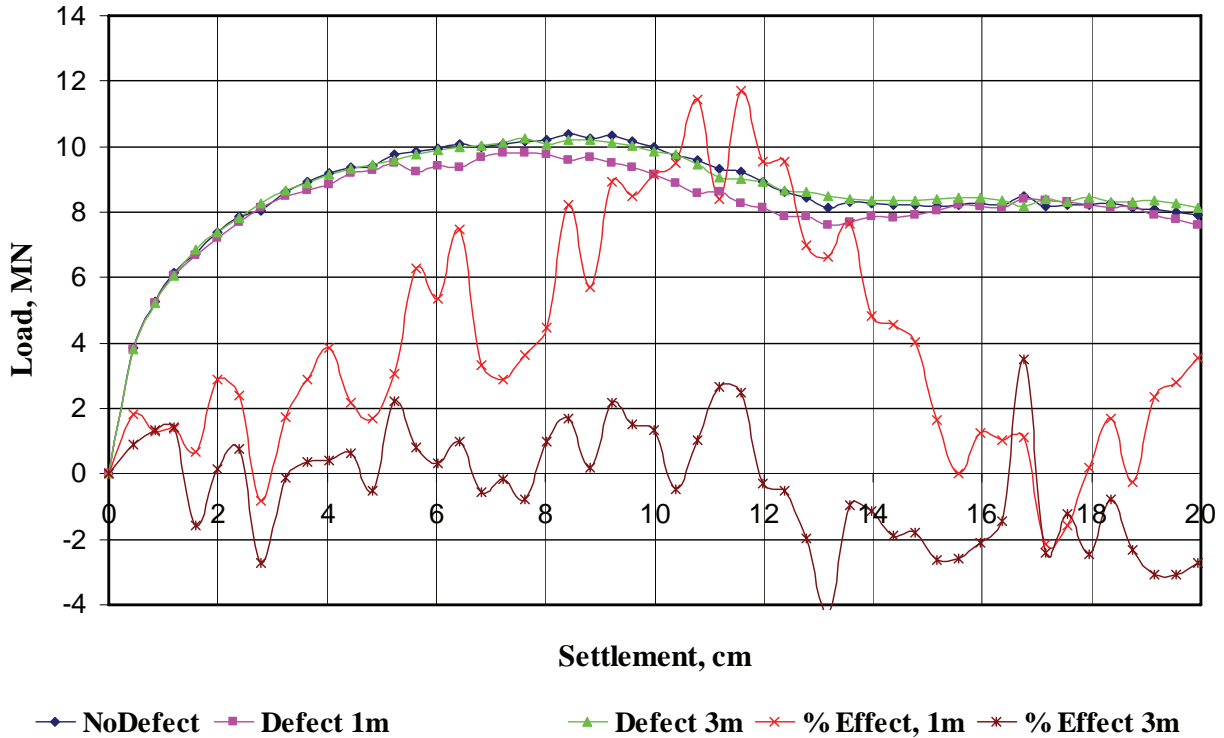
Figure 6.13. Chart. Effect of a Defect at Two Different Depths on Load Bearing Capacity

Many different methods have been proposed for interpreting this type of load-settlement curve without the plunge point. The Davisson's method is commonly recommended in specifications and procedures that defines ultimate bearing capacity at a settlement of 4 mm as:

$$P_{ult} = 4 \text{ mm} + B/120 + PD/AE \qquad (6.1)$$

where

      P_{ult} is ultimate capacity
      B is the foundation diameter
      P is applied load
      D is the foundation depth
      A is the foundation cross-sectional area
      E is the foundation elastic modulus
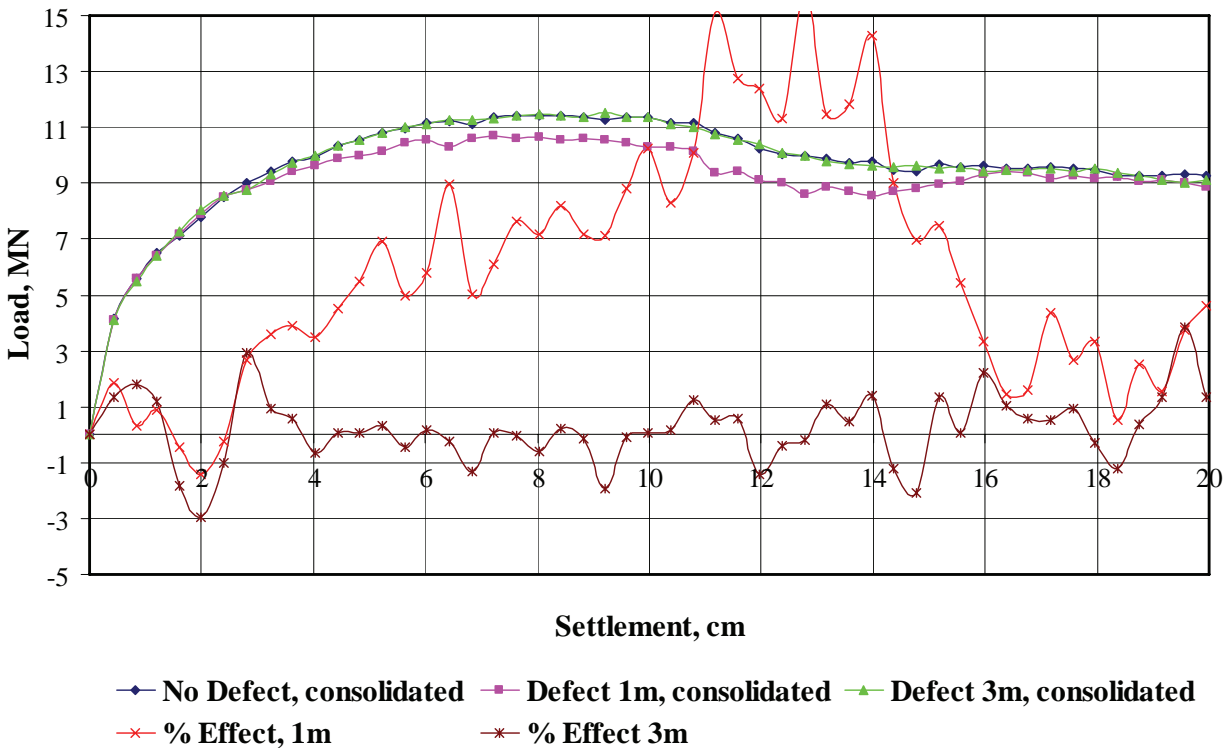
**Figure 6.14. Chart. Effect of a Defect on Load Bearing Capacity with Shaft in Compacted
Soil**

6.2.1 Loosened Soil

Figure 6.13 is a graph of the loading curves from the axial load test performed in the previous
section. The surrounding sand and clay were assumed to be loosened, a typical condition that
occurs after soil is affected by excavation and thermal contraction after concrete curing. The
load-settlement curves are typical of the ground conditions. The load initially increases sharply,
then gradually peaks at about 8 cm displacement. The plunging phase begins at approximately 5
cm displacement.

The effect on load bearing capacity from the drilled shaft with the 1 m the 3 m defect is plotted
as a percentage, compared with the shaft with no defect. The 3 m defect shows no significant
change in shaft load capacity throughout the test. Although the difference in shafts load capacity
for the 1 m defect exceeds 10%, this is at a displacement far beyond the failure criteria of 2.5 cm.
There is actually no significant change in load performance for either defective shaft in the first
2.5 cm of displacement.

Figure 6.14 is a graph of the loading curves from an axial load test performed using the same
shafts in the previous section, but with compacted sand and clay layers surrounding the drilled
shaft. This condition could be produced by compacting the ground around the shaft near the
surface, by pressurizing the concrete during placement, or by surrounding the shaft with a few

jet-grouted micro-piles or driven piles to compact the soil. Figure 6.14 is relatively equivalent to the test conducted with loosened soil, shown in Figure 6.13.

Figure 6.15 compares the loading curves from the two tests. The effect of soil compaction is far more significant than the effect of the defect. The improvement in load capacity in the first 2.5 cm reaches an average of nearly 10%. This suggests that the primary control factor is not the slight variations in concrete quality, but in the condition of the surrounding soil in the near surface.
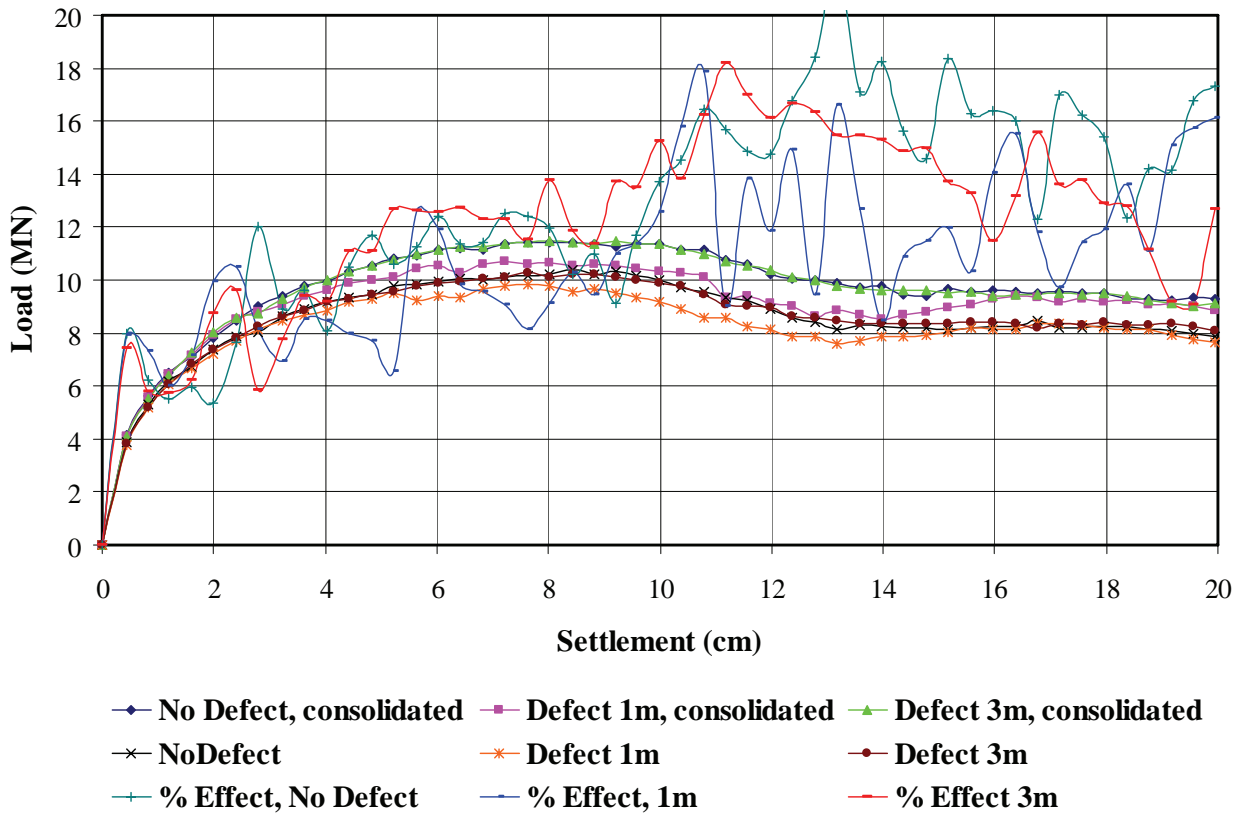
Figure 6.15. Chart. Effect of Soil Compaction on Load Bearing Capacity

6.3   Discussion

The modeling and analysis above show that the stress in the drilled shaft is not uniformly distributed through out the depth of the shaft. Soil density, friction angles of geo-materials, defects in the shaft, and compaction levels are the major control factors for stress concentration. In these stress concentration zones, local stresses may exceed the strength of the material to cause local failure within the material. In these stress concentration zones, materials may also experience large plastic deformations, which aggravate the propagation of cracks and worsen the corrosion process. Further stress analysis with fracture and non-elastic constitutive modeling in the stress concentration zones is recommended for further study.

CHAPTER 7.   SUMMARY, CONCLUSIONS, AND RECOMMENDATIONS FOR FUTURE STUDY

Several conclusions may be explicitly or implicitly inferred from this study. The modeling technique used here identifies the discrete sources that can influence the variation of measured CSL velocities. Where CSL data are shown as a cumulative result of the various factors that effect velocities over the cross-section of the drilled shaft, this method provides insight into how each one contributes to the final estimate of concrete quality. It also offers a basis for quality control engineers to use in refining and improving CSL data collection methods such that one-by-one sources of velocity variations can be eliminated, and a truer estimate of the concrete quality can be obtained.

This study suggests that current techniques for generating CSL data plots of velocity and energy are fairly reliable for estimating concrete consistency, as CSL data processing techniques have potential to detect voids and honeycomb regions. It does however, have difficulty in detecting cracking and estimating strength.

Current methods employed for first arrival determination are arbitrary and open to manipulation. Manipulation of arrival picks can result in velocity artifacts, or can eliminate existing defects. Lack of tolerances in CSL data collection equipment is also a problem, which may result in arrival pick variations. Poor quality CSL data collection equipment results in poor quality, noisy, and unreliable data. For tomography purposes, failure to account for tube bending results in velocity artifacts. Failure to account for sensor position and orientation in access tubes can result in velocity artifacts. PVC access tubes transmit higher amplitude signals than steel. Steel access tubes are more resistant to breaking and bending during concrete placement and curing. Steel access tubes reduce tube de-bonding due to lower thermal expansion. The thermal expansion of PVC is 10 times higher than steel. Thermal expansion of access tubes results in tube de-bonding in the upper portions of the shaft, further complicating data interpretation. Access tubes transport heat from the shaft, and can result in concrete cracking. The resulting CSL data can be misinterpreted as tube de-bonding, but it can be accurately noted as cracking as it also is more likely to occur in the upper portions of the shaft where tubes are exposed to the surface. Filling tubes with water prior to concrete placement reduces this effect.

Concrete cures as a result of chemical hydration processes, and does not dry by loss of moisture. Surrounding ground conditions affect curing rates and temperature gradients. Temperature gradients above a certain level result in cracking. Stress in the drilled shaft is not uniformly distributed throughout the depth of the shaft. Soil density, friction angles of geo-materials, defects in the shaft, and consolidation levels are the major control factors for stress concentration. Failure to account for variations in curing rates, shaft temperatures, heat transfer, stress, cracking, and the surrounding environment will likely result in velocity artifacts. This may be an issue if the CSL data is collected too soon, that is before the conventional 48-hour cure time.

Concrete cures as a result of chemical hydration processes, and does not dry by loss of moisture. Surrounding ground conditions affect curing rates and temperature gradients. This includes lithology, ground water, and surface exposure. Temperature gradients above a certain level

155

result in cracking. Stress in the drilled shaft is not uniformly distributed through out the depth of the shaft. Soil density, friction angles of geo-materials, defects in the shaft, and compaction levels are the major control factors for stress concentration.

Full shaft tomography should not be done unless all the deviations have been identified. Quantitative processing techniques, such as tomography, should not be used on CSL data that has not been quantitatively acquired or processed. With quantitative data collection, numerical inversion and analysis has potential to improve data processing and interpretation for CSL, providing objective, automated techniques for evaluating the data. This includes in situ measurement of concrete properties, shaft evaluation outside of the reinforcement cage, shaft cohesion with the surrounding ground, shaft bulging or necking, and cracking defects. Numerical analysis can evaluate effects of shaft defects, estimate load capacity, account for variations in curing rates, and estimate cracking. Numerical analysis can also estimate long term effects such as corrosion and scouring, with further study.

RECOMMENDATIONS FOR THE FUTURE

Recommendations for future improvement are to supplement CSL with a more quantitative NDE and emerging technique. We propose the installation of embedded sensors as opposed to access tubes. These sensors should be distributed throughout the shaft, connected serially by a single cable for power and data communication. This cable may be connected to a power source and computer at the surface, and be accessible for the life of the shaft. Each sensor should be capable of generating a seismic source. The sensors should measure three-component particle acceleration within the concrete, of sources generated by other embedded sensors within the same shaft, from adjacent shafts, from vertical or horizontal impacts at the top of the shaft, or impacts at the surface on surrounding ground. Each sensor should measure the temperature of the concrete. The sensors should be capable of accurate and automatic self location and orientation. Data from the sensors should be processed and analyzed to reconstruct an image of the entire shaft, inside and outside the rebar cage, as well as the surrounding ground. The bearing capacity of the entire support structure, including adjacent shafts and surround ground, should be evaluated by numerical analysis.

The system could be fully automated, and accommodate additional manual surveys if desired. Automated surveys should be conducted monthly for the first half year, and annually after that, to show changes in the shafts or surrounding ground over time. This system would be effective for on-demand monitoring to determine the drilled shafts condition for instance after catastrophic events of scour events or earthquakes. Until this proposed embedded sensor system is developed and validated, the CSL systems should still be employed.

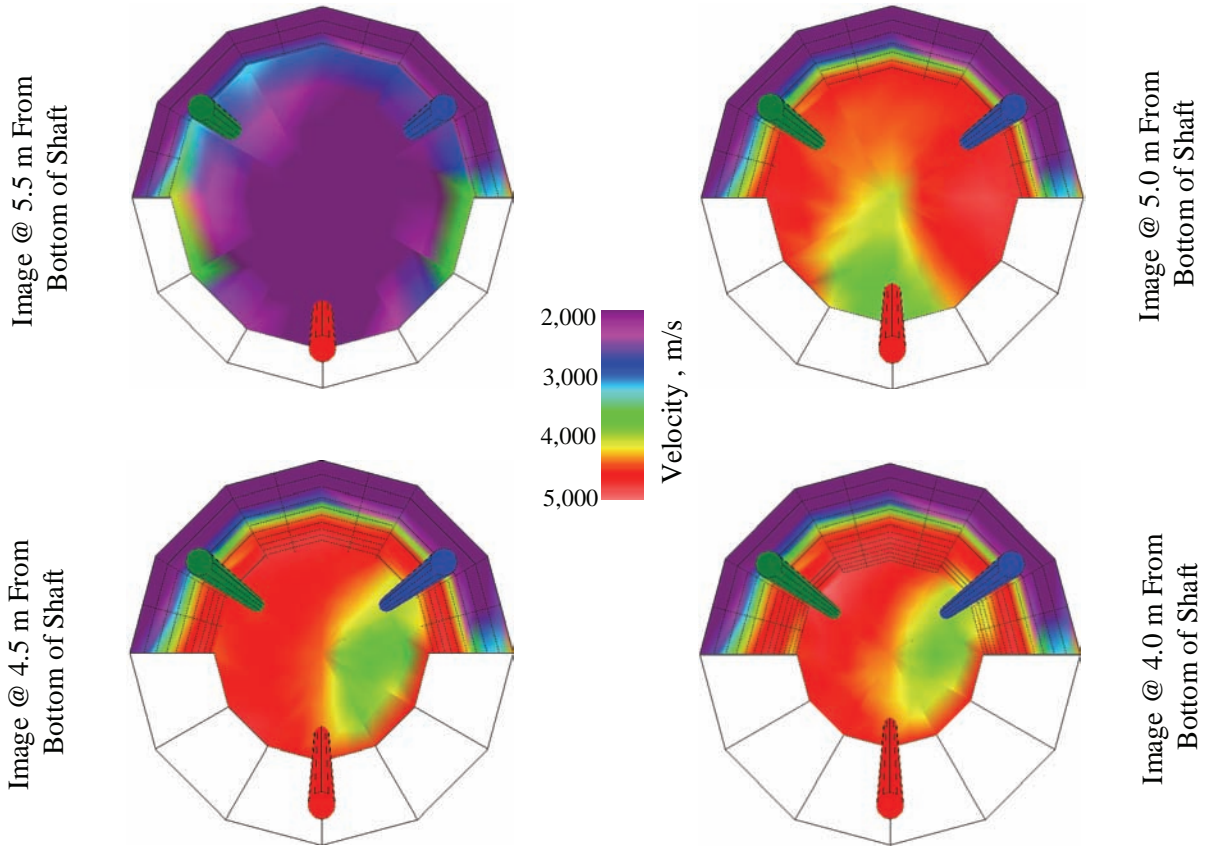156

APPENDIX A – SITE #1 VERTICAL CROSS SECTIONS

Figure A1. Plot. Site #1 Abutment 1 Shaft 2 Vertical Cross Sections Looking from the Top
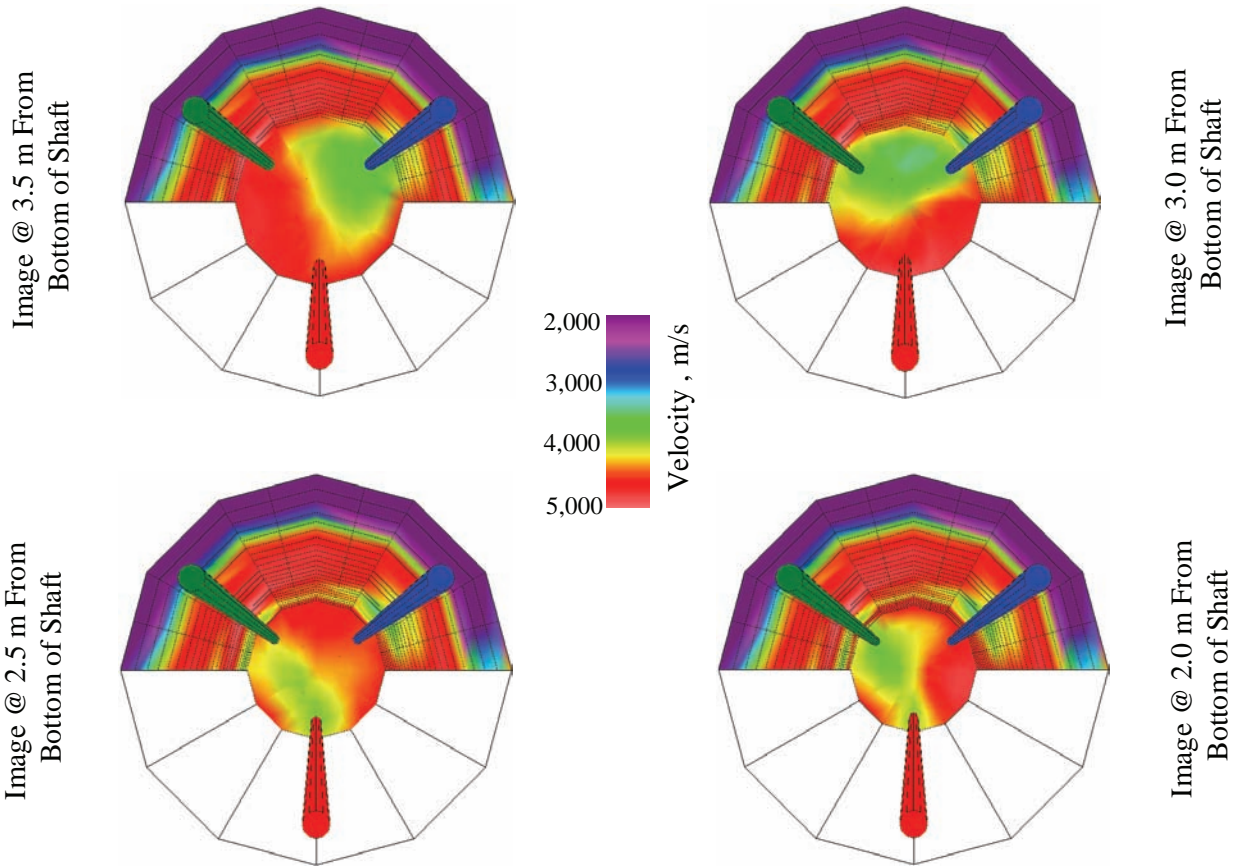
Figure A2. Plot. Site #1 Abutment 1 Shaft 2 Vertical Cross Sections Looking from the Top
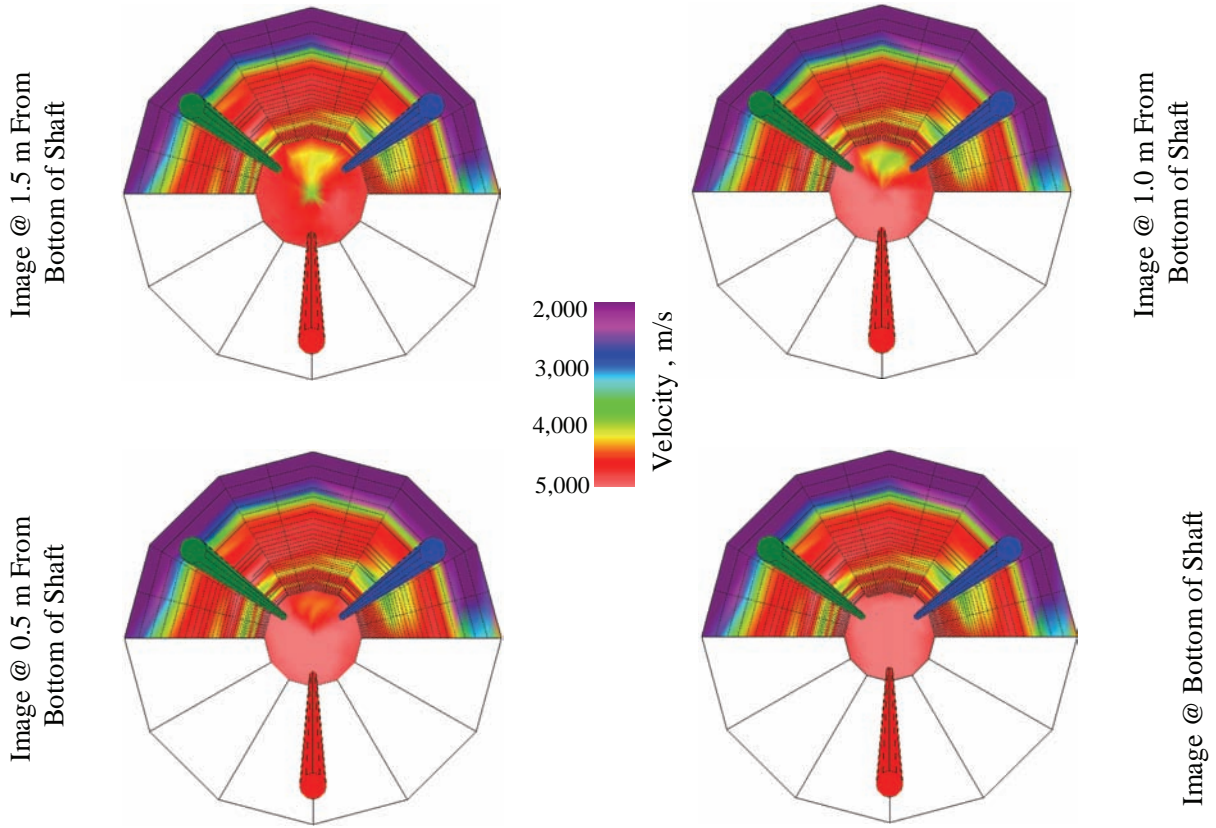
Figure A3. Plot. Site #1 Abutment 1 Shaft 2 Vertical Cross Sections Looking from the Top

REFERENCES

Amir, E. I., and J. M. Amir: (1998) Recent Advances in Ultrasonic Pile Testing, Proc. 3rd Intl Geotechnical Seminar on Deep Foundation on Bored and Auger Piles, Ghent.

Amir, E. I., and J. M. Amir: (1998) Testing Piles with Virtual Instruments Proc DFI 7th Intl Conf on Piling and Deep Foundations, Vienna.

Amir, J. M.: (1988) Wave Velocity in Young Concrete, Proc 3rd Intl Conf on Application of Stress-wave Theory to Piles, Ottawa.

Amir, J. M.: (1999) Caveat Emptor or a Buyer's Guide to Integrity Testing, Proc DFI Annual Conf, Dearborn

Amir, J. M.: (2002) Single-Tube Ultrasonic Testing of Pile Integrity, ASCE Deep Foundation Congress, Vol. 1 pp. 836-850, Orlando

Amir, J. M., E. I. Amir, and C. W. Felice: (2004) Acceptance Criteria for Bored Piles by Ultrasonic Testing, Proc. Intl. Conf on Application of Stress Wave Theory to Piling, Kuala Lumpur

ASTM C597-83: "Standard Test Method for Pulse Velocity through Concrete," Annual Book of ASTM Standards, Vol. 04.02, Philadelphia.

Bardet, J. P. and J. Proubet: (1991) *Adaptative Dynamic Relaxation for Statics of Granular Material*, Computer & Structures, Vol. 39, No 3.4 pp 221-229

Bazant, Z.P. (1977) Viscoelasticity of Solidifying Porous Material – Concrete. Journal of The Engineering Mechanics Division ASCE, Vol. 103, No EM6, Dec. 1977: 1049-1067

Braja, M. Das: (1992) *Principle of Soil Dynamics*, PWS-KENT Publishing Company

Brown, D.: (2004) "Zen and the Art of Drilled Shaft Construction: The Pursuit for Quality." Geo-support Conference: Innovation and Cooperation in the Geo-industry, Drilled Shafts, Micro-piles, Deep Mixing, Remedial Methods, and Specialty Foundation System, American Society of Civil Engineers, Reston, VA.

Bungey, J. H.: (1980) "Validity of Ultrasonic Pulse Velocity Testing of In-Place Concrete for Strength," Nondestructive Testing International, Volume 13, No. 6, December.

CenGel, Yunus A. and Robert H. Turner (2001) *Fundamentals of Thermal-Fluid Sciences*, McGRAW-HILL Higher Education

Chung, H.W. (1978) "Effect of Embedded Steel Bars upon Ultrasonic Testing of Concrete" Magazine of Concrete Research, London, 30(102), 19.

Davis, A. G., and C. S Dun: (Dec. 1975). From Theory to Field Experience with the Non-Destructive Vibration Testing of Piles Proceedings, Institute of Civil Engineering, Part 2, pp. 571-593.

Department of Materials Science and Engineering, Scientific Principle- Concrete, MAST, University of Illinois Urbana-Champaign

Devaney, A. J., (1980) Geophysical diffraction tomography, IEEE Trans. And Geoscience and Remote Sensing, v. GE-22, no. 1, pp. 3-13.

DiMaggio, J. (2004) "Developments in Deep Foundation Highway Practice – The Last Quarter Century" Foundation Drilling Magazine - The International Association of Foundation Drilling (ADSC), Vol. 24, No. 2, pp. 16-22.

Dines, K. A., and R. J. Lytle: (1979) "Computerized Geophysical Tomography", Proc. IEEE, and Vol. 67, pp. 1065-1073.

Ealy, C., M. Iskander, M. Justason, D. Winters, and G. Mullins (2002) "Comparison between Statnamic and Static Load Testing of Drilled Shafts in Varved Clay" Proc. 9'th International Conference on Piling and Deep Foundations, Nice, June 3-5, 2002.

Emborg, M and Bernander, (1994) S; Assessment of the risk of thermal cracking in hardening concrete, Journ. Of Struc. Eng (ASCE). 120 (10), October.

Felice, C. W., and J. M. Amir (2005) Observational Method and Drilled Shaft Acceptance Criteria, Proc. Dallas

Fung, Y. C., and Pin Tong: (2001) *Classical and Computational Sold Mechanics*, World Scientific Publishing Co.

Gajda, J., and M. VanGeem: (2002) "Controlling Temperatures in Mass Concrete," Concrete International, pp. 59-61.

Gassman, S. L.: (1997) "Impulse response Evaluation of Inaccessible Foundations", Evanston, Illinois.

Hanley-Wood, (2001) Concrete Construction Magazine, Are Temperature Requirements in Mass Concrete Reasonable?, October, 68-70.

Herman, G. T.: (1980) "Image Reconstruction from Projections, the Fundamentals of Computerized Tomography" (Academic Press, Inc.).

Hertlein, Bernard H.: (1996) "NDT Methods for Dams and Waterside Structures" - Michigan Department of Environmental Quality Seminar on Dam Safety - Higgins Lake Michigan.

InfraSeis, Inc.: Nondestructive testing of Soils and Civil Infrastructures, Products and Services– network advertisement.

Instruction Manual for MODEL C-4902 and MODEL C-4901 V-meter. James Instruments, Inc., Non Destructive Testing Systems, January 1980.

Iskander M., Roy, D., Ealy, C., Kelley, S.. (2000) "Class-A Prediction of Construction Defects in Drilled Shafts". Submitted to TRB 2001 Session on Drilled Shaft Capacity & Defects in Varved Clay.

Ivansson, S. (1986) "Seismic Borehole Tomography- Theory and Computation Methods" Proc. IEEE, Vol 74, pp. 328-338.

Jones, R. (1954) "Testing of Concrete by an Ultrasonic Pulse Technique" RILEM International Symposium on Nondestructive Testing of Materials and Structures. Paris, Vol 1, Paper no. A-17, 137. RILEM Bull. No. 19, 2nd part, November.

Jones, R., and I. Facaoaru: (1969) "Recommendations for Testing Concrete by the Ultrasonic Pulse Method" Materials and Structures Research and Testing (Paris), 2(19), 275.

Komornik, A., and J.M. Amir: (1994) Quality Control at Pier NB-2, Proc. 5th Intl. Conf. DFI, Bruges.

Kosmatka, S H et.al: (2002) Design and Control of Concrete Structures, Portland Cement Association, Skokie, Ill, pp. 41-42.

Litke, S. S. (2005) Drilled Shafts: Commitment to Delivering a Quality Product, GEO3-Construction QA/QC Conference Proceedings, ADSC meeting, Dallas, TX

Lokhorst, S.J. and Breugal, K. van. (1993) The Effect of Microstructural Development on Creep and Relaxation of Hardening Concrete. Creep and Shrinkage of Concrete: Proceedings of the Fifth International RILEM Symposium, Spain: 145-150

MacGregor, J. G. (1997) "Reinforced Concrete, Mechanics and Design, "Third Edition.

MATLAB 11 (1998) Partial Differential Equations Toolbox. Mathworks, Inc., Natick, MA.

Nilson, A. H., and G. Winter: (1986) Design of Concrete Structures, McGraw-Hill Book Company, p.35

Nolet, G. (1987) "Seismic Wave Propagation and Seismic Tomography", in Seismic Tomography with Applications in Global Seismology and Exploration Geophysics, ed. G. Nolet (D. Reidal Publishing Co.), pp. 1-23.

NSA Engineering, Inc. International Geotechnical Engineering and Ground Imaging Consultants, Products and Services – network advertisement.

Olson Engineering, Inc., Freedom NDT PCTM Family of Instruments, Products and Services – network advertisement.

O'Neil, W. M., Reese, C. L. (1999) Drilled Shafts: Construction Procedures and Design Methods. Publication No. FHWA-IF-99-025.

Pidwirny, M. Introduction to the Hydrosphere, (2000). Throughflow and Groundwater Storage, Chapter 8: PhysicalGeography.net | Fundamentals Of Physical Geography, Okanagan

Piletest.com: Pile Integrity Sonic Analyzer and Cross-hole Ultrasonic Analyzer, Products and Services – network advertisement.

Santamarina, Carlos J., and Dante Fratta: (2005) *Discrete Signals and Inverse Problems: An Introduction for Engineers and Scientists*, John Wiley & Sons Ltd.

Saul, A.G.A. (1951) "Principles Underlying the Steam Curing of Concrete at Atmospheric Pressure*" Magazine of Concrete Research*, 2(6), 127.

Scales, J. A. (1987) "Tomographic Inversion via the Conjugate Gradient Method" *Geophysics,* Vol 52, pp. 179-185.

Sheriff, Robert E. (1978) *A First Course in Geophysical Exploration and Interpretation.* International Human Resources Development Corporation, Boston.

Sheriff, R. E., and L. P. Geldart: (1995) *Exploration Seismology*, second edition, Cambridge Univ. Press, 1982, 1995.

Sims, F. (1999) *Engineering Formulas,* Industrial Press,

Springenschmid, R. and R. Breitenbucher: (1998) Influence of Constituents, Mix Proportions, and Temperature on Cracking Sensitivity of Concrete, in: R. Springenschmid (Ed.), Prevention of Thermal Cracking in Concrete at Early Ages, E & FN Spon, London, pp 40-50.

Stain, R. T. (1982) "Integrity Testing" *Civil Engineering*, pp.53-72.

Tufenkjian, M.R. (2003) Nondestructive Testing for Quality Assurance and Quality Control of drilled Shafts at state Department of Transportation. California State University, LA, CA. 49 pp.

Van Breugel, K. (1998) Prediction of Temperature Development in Hardening Concrete, in: R. Springenschmid (Ed.), Prevention of Thermal Cracking in Concrete at Early Ages, E & FN Spon, London, pp. 51- 75

Van Koten, H. and P. Middendorp (1981) "Testing of Foundation Piles", Heron, joint publication of the Department of Civil Engineering of Delft University of Technology, Delft, The Netherlands, and Institute TNO for Building Materials and Sciences, Rigswijk (ZH), The Netherlands, Vol. 26, no. 4.

Welty, J., C. E. Wicks, R. E. Wilson., and G. L. Rorrer (1984) Fundamentals of Mass, Momentum, and Heat Transfer, 3rd ed., Wiley and Sons.

Wood, David M. (2004) *Geotechnical Modeling*, Spon Press

Yuan, D., S. Nazarian, and A. Medichetti:(2003) "A Methodology for Optimizing Opening of PCC Pavements to Traffic" Texas Department of Transportation Report No. 4188-2, p.29.

Zhang, Runing. (1996) *Discrete Element Modeling of Granular Materials under Biaxial Conditions*, A thesis submitted to the Faculty of the Graduate School of the University of Colorado in partial fulfillment of the requirements for the degree of Doctor of Philosophy